



TECHNISCHE UNIVERSITÄT
CHEMNITZ

Synthese von Indacenodithiophen-basierten Copolymeren mittels direkter C-H-Arylierungspolykondensation

Von der Fakultät für Naturwissenschaften der Technischen Universität Chemnitz
genehmigte Dissertation zur Erlangung des akademischen Grades

doctor rerum naturalium

(Dr. rer. nat.)

vorgelegt von

M. Sc. Desiree Adamczak

geboren am 04.02.1991 in Eberbach

eingereicht am 23.07.2021

Gutachter: Prof. Dr. Michael Sommer,

Prof. Dr. Ullrich Scherf

Tag der Verteidigung: 18.11.2021

<https://nbn-resolving.org/urn:nbn:de:bsz:ch1-qucosa2-769551>

„memento moriendum esse“

-lateinische Phrase

BIBLIOGRAPHIC DESCRIPTION ARRANGEMENT AND RETRIEVAL

Desiree Adamczak

Synthese von Indacenodithiophen-basierten Copolymeren mittels direkter C-H-Arylierungspolykondensation

Technische Universität Chemnitz, Fakultät für Naturwissenschaften

Dissertation, 2021, 187 Seiten

Organic semiconducting polymers are widely employed in organic electronics such as organic photovoltaics (OPVs), organic field-effect transistors (OFETs) and organic light emitting diodes (OLEDs). Their remarkable mechanical and charge transport properties as well as solution processability allow low-cost fabrication of light-weight and flexible devices. Among them indacenodithiophene (IDT)-based materials are promising candidates for application in organic electronics. Due to their low energetic disorder, extended conjugation and high electron density IDT-based polymers show high field-effect mobilities and high absorption coefficients. However, their synthesis suffers from long reaction sequences and is often accomplished using toxic materials. Commercialization requires development of more efficient and sustainable reaction pathways to ease tailoring of structures and to limit molecular defects.

Herein, the development of new synthetic pathways towards IDT-based polymers is presented in which all C-C coupling steps are achieved by C-H activation – an atom-economic alternative to conventional transition-metal catalyzed cross couplings. Two different strategies were established to synthesize a series of well-defined IDT-based homo- and copolymers with different side chain patterns and varied molecular weights. The first way starts by synthesis of a precursor polymer and subsequent cyclization affording IDT homopolymers. In the second approach, cyclized IDT monomers were prepared first and then polymerized using direct arylation polycondensation (DAP) yielding IDT homo- and copolymers. The synthetic pathways were optimized in terms of maximizing molecular weights and limiting defect structures. While the first pathway enables synthesis of well-defined homopolymers, the latter is the method of choice for preparation of IDT-based copolymers in high yields and adjustable molecular weights. The polymers were further characterized in detail by optical, thermal, electrical and morphological analyses. OFETs as well as all-polymer solar cells (all-PSCs) were fabricated to investigate the influence of structural modifications and molecular weight on their optoelectronic performance. Thus, this thesis provides a comprehensive study of the structure-property correlations of IDT-based polymers and simplified synthetic protocols for the design and preparation of donor-acceptor copolymers in the future.

Keywords: Indacenodithiophene (IDT), direct arylation polycondensation (DAP), homopolymers, donor-acceptor copolymers, structure-property correlations, solar cells, organic field-effect transistors (OFETs).

Table of contents

BIBLIOGRAPHIC DESCRIPTION ARRANGEMENT AND RETRIEVAL	V
Abbreviations.....	IX
Preamble	XIV
I. Introduction.....	17
1. Conjugated materials for organic electronics	17
1.1. Organic field-effect transistors	18
1.2. Organic solar cells	19
1.3. Indacenodithiophene – a building block for organic photovoltaic materials ...	23
1.3.1. Indacenodithiophene-based small molecules as non-fullerene acceptors.....	24
1.3.2. Design and synthesis of indacenodithiophene-based conjugated polymers .	25
1.4. Direct arylation polycondensation – synthesis of π -conjugated polymers.....	29
2. Overview of thesis	34
3. References	38
II. Indacenodithiophene homopolymers via direct arylation: direct polycondensation versus polymer analogous reaction pathways	47
III. Influence of synthetic pathway, molecular weight and side chains on properties of indacenodithiophene-benzothiadiazole copolymers made by direct arylation polycondensation	88
IV. Temperature-dependent morphology-electron mobility correlations of naphthalene diimide-indacenodithiophene copolymers prepared via direct arylation polymerization	133
V. Indacenodithiophene-based copolymers for application in all-polymer solar cells	161
VI. Summary and outlook	179
VII. Acknowledgement.....	184
VIII. Selbstständigkeitserklärung.....	185
IX. Curriculum vitae.....	186
X. Publications and poster distributions	187

Abbreviations

A	acceptor
ACN	acetonitrile
Al	aluminium
Ar	aryl
BDD	Benzodithiophene-4,8-dione
BHJ	bulk heterojunction
BT	2,1,3-Benzothiadiazole
BTBr ₂	4,7-Dibromo-2,1,3-benzothiadiazole
BTz	2,2'-Bithiazole
Ca	calcium
CbzBr ₂	2,7-Dibromo-9-(1-octylnonyl)-9 <i>H</i> -carbazole
CDT	cyclopentadithiophene
CHCl ₃	chloroform
CN	1-chloronaphthalene
CT	charge transfer
CV	cyclic voltammetry
Đ	dispersity
D	donor
DA	direct arylation
D-A	donor-acceptor
DAP	direct arylation polycondensation
DCI	1,1-Dicyanomethylene-3-indanone
DCNBT-IDT	Poly(5,6-dicyano-2,1,3-benzothiadiazole- <i>alt</i> -indacenodithiophene)
DFT	density functional theory
DIO	1,8-Diiodooctane
DMAc	<i>N,N</i> -dimethylacetamide
DMF	<i>N,N</i> -dimethylformamide
DMIDT	4,9-Bis(bis(4-hexylphenyl)methylene)-4,9-dihydro- <i>s</i> -indaceno [1,2- <i>b</i> :5,6- <i>b'</i>]dithiophene
DPP	diketopyrrolopyrrole
DSC	differential scanning calorimetry

ABBREVIATIONS

EQE	external quantum efficiency
F4	1,2,4,5-Tetrafluorobenzene
F4Br ₂	1,4-Dibromo-2,3,5,6-tetrafluorobenzene
Fc	ferrocene
FF	fill factor
FSC	flash scanning calorimetry
GIWAXS	grazing-incidence wide-angle X-ray scattering
HOMO	highest occupied molecular orbital
IDT	Indaceno[1,2- <i>b</i> :5,6- <i>b'</i>]dithiophene
IDTT	Indacenodithienothiophene
IEIC	2,2'-((2 <i>Z</i> ,2' <i>Z</i>)-((5,5'-(4,4,9,9-Tetrakis(4-hexylphenyl)-4,9-dihydro- <i>s</i> -indaceno[1,2- <i>b</i> :5,6- <i>b'</i>]dithiophene-2,7-diyl)bis(4-(2-ethylhexyl)thiophene-5,2-diyl))bis(methanylylidene))-bis(3-oxo-2,3-dihydro-1 <i>H</i> -indene-2,1-diylidene))dimalononitrile
INCN	2-(3-Oxo-2,3-dihydro-1 <i>H</i> -inden-1-ylidene)malononitrile
IR	infrared
IT-4F	(3,9-Bis(1-oxo-2-methylene-3-(1,1-dicyanomethylene)-5,6-difluoro-indanone)-5,5,11,11-tetrakis(4- <i>n</i> -hexylphenyl)-dithieno[2,3- <i>d</i> :2',3'- <i>d'</i>]- <i>s</i> -indaceno[1,2- <i>b</i> :5,6- <i>b'</i>]dithiophene)
ITIC	3,9-Bis(2-methylene-(3-(1,1-dicyanomethylene)-indanone))-5,5,11,11-tetrakis(4-hexylphenyl)-dithieno[2,3- <i>d</i> :2',3'- <i>d'</i>]- <i>s</i> -indaceno[1,2- <i>b</i> :5,6- <i>b'</i>]dithiophene)
ITO	indium tin oxide
J51	Poly[(5,6-difluoro-2-octyl-2 <i>H</i> -benzotriazole-4,7-diyl)-2,5-thiophenediyl[4,8-bis[5-(2-hexyldecyl)-2-thienyl]benzo[1,2- <i>b</i> :4,5- <i>b'</i>]dithiophene-2,6-diyl]-2,5-thiophenediyl]
J_{sc}	short-circuit current
Li	lithium
LPPP	ladder-type poly(<i>p</i> -phenylene)
LUMO	lowest unoccupied molecular orbital
Me	methyl
Mes	mesitylene
M_n	number average molecular weight

M_w	weight average molecular weight
MW	molecular weight
N2200	Poly{[<i>N,N'</i> -bis(2-octyldodecyl)-naphthalene-1,4,5,8-bis(dicarboximide)-2,6-diyl]- <i>alt</i> -5,5'-(2,2'-bithiophene)}
<i>n</i> -Bu	<i>n</i> -butyl
NBu ₄ PF ₆	tetrabutylammonium hexafluorophosphate
NDI	naphthalene diimide
NFA	non-fullerene acceptor
NFSMA	non-fullerene small molecule acceptor
NIR	near infrared
NMR	nuclear magnetic resonance
<i>o</i> -DCB	<i>ortho</i> -dichlorobenzene
OFET	organic field-effect transistor
OPV	organic photovoltaic
OSC	organic solar cell
oxDAP	oxidative direct arylation polycondensation
P3AT	Poly(3-alkyl)thiophene
P3HT	Poly(3-hexyl)thiophene
PBDB-T	Poly[(2,6-(4,8-bis(5-(2-ethylhexyl)thiophen-2-yl)-benzo[1,2- <i>b</i> :4,5- <i>b'</i>]dithiophene))- <i>alt</i> -(5,5-(1',3'-di-2-thienyl-5',7'-bis(2-ethylhexyl)benzo[1',2'- <i>c</i> :4',5'- <i>c'</i>]dithiophene-4,8-dione)]
PBDB-T-SF	Poly[(2,6-(4,8-bis(5-(2-ethylhexylthio)-4-fluorothiophen-2-yl)-benzo[1,2- <i>b</i> :4,5- <i>b'</i>]dithiophene))- <i>alt</i> -(5,5-(1',3'-di-2-thienyl-5',7'-bis(2-ethylhexyl)benzo[1',2'- <i>c</i> :4',5'- <i>c'</i>]dithiophene-4,8-dione)]
PBDTTT-C-T	Poly[[4,8-bis[5-(2-ethylhexyl)-2-thienyl]benzo[1,2- <i>b</i> :4,5- <i>b'</i>]dithiophene-2,6-diyl][2-(2-ethyl-1-oxohexyl)thieno[3,4- <i>b</i>]thiophenediyl]]
P-BNBP-fBT	Poly[[μ-[3,3'-bis[(2-octyldodecyl)amino-κ <i>N</i>][2,2'-bipyridine]-5,5'-diyl-κ <i>N</i> ¹ : <i>N</i> ^{1'}]](3,3'-difluoro[2,2'-bithiophene]-5,5'-diyl)bis(difluoroboron)complex]
PC ₇₀ BM	[6,6]-Phenyl-C71-butyric acid methyl ester
PCE	power conversion efficiency

ABBREVIATIONS

PCy3 Pd G2	Chloro[(tricyclohexylphosphine)(2'-aminobiphenyl-2-yl) palladium(II)
Pd ₂ dba ₃	Tris(dibenzylideneacetone)dipalladium(0)
PDINO	2,9-Bis[3-(dimethyloxidoamino)propyl] <i>anthra</i> [2,1,9- <i>def</i> :6,5,10- <i>d'e'f'</i>]diisoquinoline-1,3,8,10(2 <i>H</i> ,9 <i>H</i>)-tetrone
Pd(OAc) ₂	Palladium(II) acetate
PDS	photothermal deflection spectroscopy
PEDOT	Poly(3,4-ethylenedioxythiophene)
PffT2-FTAZ-2DT	Poly[(5,6-difluoro-2-propyl-2 <i>H</i> -benzotriazole-4,7-diyl)[3,3'''-bis(2-decyltetradecyl)-3'',4'-difluoro[2,2':5',2'':5'',2'''-quaterthiophene]-5,5'''-diyl]]
PhanQ	phenanthrenequinoxaline
PIDTBT	Poly(indacenodithiophene- <i>alt</i> -benzothiadiazole)
PIDTF4	Poly(indacenodithiophene- <i>co</i> -tetrafluorobenzene)
PL	photoluminescence
PM6	Poly[(2,6-(4,8-bis(5-(2-ethylhexyl-3-fluoro)thiophen-2-yl)-benzo[1,2- <i>b</i> :4,5- <i>b'</i>]dithiophene))- <i>alt</i> -(5,5-(1',3'-di-2-thienyl-5',7'-bis(2-ethylhexyl)benzo[1',2'- <i>c</i> :4',5'- <i>c'</i>]dithiophene-4,8-dione)]
PNDIBTz	Poly{[<i>N,N'</i> -bis(2-octyldodecyl)-naphthalene-1,4,5,8-bis(dicarboximide)-2,6-diyl]- <i>alt</i> -5,5'-(2,2'-bithiazole)}
P(NDI-IDT)	Poly(naphthalene diimide- <i>alt</i> -indacenodithiophene)
PNDIT2	Poly{[<i>N,N'</i> -bis(2-octyldodecyl)-naphthalene-1,4,5,8-bis(dicarboximide)-2,6-diyl]- <i>alt</i> -5,5'-(2,2'-bithiophene)}
PPV	Poly(<i>p</i> -phenylene vinylene)
PSC	polymer solar cell
PSS	Poly(styrenesulfonate)
PTB7-Th	Poly([2,6'-4,8-di(5-ethylhexylthienyl)benzo[1,2- <i>b</i> ;3,3- <i>b</i>]dithiophene]{3-fluoro-2[(2-ethylhexyl)carbonyl]thieno[3,4- <i>b</i>] thiophenediyl})
PTzBI	Poly(1,3-bis(thiophene-2-yl)-benzo[1,2- <i>c</i> :4,5- <i>c'</i>]dithiophene-4,8-dione,4,8-di(thien-2-yl)-6-octyl-2-octyl-5 <i>H</i> -pyrrolo[3,4- <i>f</i>] benzo-triazole-5,7(6 <i>H</i>)-dione)
r.t.	room temperature
SEC	size exclusion chromatography

T2	2,2'-Bithiophene
TBT	4,7-Bis(4-hexyl-2-thienyl)-2,1,3-benzothiadiazole
TGA	thermogravimetric analysis
THF	tetrahydrofuran
Tol	toluene
TPD	Alkyl[3,4- <i>c</i>]thienopyrrole-4,6-dione
TT	Thieno[3,2- <i>b</i>]thiophene
UV-vis	ultraviolet-visible
V_{oc}	open-circuit voltage
Y6	2,2'-((2Z,2'Z)-((12,13-bis(2-ethylhexyl)-3,9-diundecyl-12,13-dihydro-[1,2,5]thiadiazolo[3,4- <i>e</i>]thieno[2'',3'':4',5']thieno [2',3':4,5]pyrrolo[3,2- <i>g</i>]thieno[2',3':4,5]thieno[3,2- <i>b</i>]indole-2,10-diyl)bis(methanylylidene))bis(5,6-difluoro-3-oxo-2,3-dihydro-1 <i>H</i> -indene-2,1-diylidene))dimalononitrile

Preamble

The dissertation is structured in six chapters. The first chapter serves as an introduction to constitute the state of knowledge and to give a short overview of the following chapters. The scientific results were obtained in collaboration with others and are presented in chapters II-V. Chapter II and III are already published in international journals and chapter IV has been submitted for publication. Chapter V shows unpublished results in which the synthesized materials are applied in organic photovoltaics. The last chapter summarizes all results and gives a short outlook.

The contributions of all coauthors to each chapter are listed below.

Chapter II: “Indacenodithiophene homopolymers via direct arylation: direct polycondensation versus polymer analogous reaction pathways”

D. Adamczak, H. Komber, A. Illy, A. Scaccabarozi, M. Caironi, M. Sommer, *Macromolecules*, **2019**, 52 (19), 7251-7259.

I synthesized all monomers, homopolymers as well as model compounds and characterized them by ¹H NMR, SEC, IR spectroscopy, UV-vis and PL spectroscopy, TGA as well as DSC analyses. Further, I wrote the first draft of the publication. The NMR analyses of the polymers were performed by Hartmut Komber (Leibniz-Institut für Polymerforschung Dresden e.V.) Anna Illy aided monomer synthesis under my supervision. Alberto Scaccabarozi and Mario Caironi (Istituto Italiano di Tecnologia, Center for Nano Science and Technology @PoliMi) carried out mobility measurements. Michael Sommer designed and supervised the work. All authors were involved in revising the manuscript.

Chapter III: “Influence of synthetic pathway, molecular weight and side chains on properties of indacenodithiophene-benzothiadiazole copolymers made by direct arylation polycondensation”

D. Adamczak, A. Perinot, H. Komber, A. Illy, S. Hultmark, B. Passarella, W. L. Tan, S. Hutsch, D. Becker-Koch, C. Rapley, A. D. Scaccabarozi, M. Heeney, Y. Vaynzof, F. Ortmann, C. R. McNeill, C. Müller, M. Caironi, M. Sommer, *J Mater C*, **2021**, 9 (13), 4597-4606.

I synthesized all monomers, polymers as well as model compounds and characterized them by ¹H NMR, SEC, IR spectroscopy, UV-vis and PL spectroscopy, cyclic voltammetry, TGA as well as DSC analyses. Further, I wrote the first draft of the publication. Andrea Perinot, Bianca

Passarella, Alberto Scaccabarozzi and Mario Caironi (Istituto Italiano di Tecnologia, Center for Nano Science and Technology @PoliMi) executed the mobility measurements. Hartmut Komber (Leibniz-Institut für Polymerforschung Dresden e.V.) performed NMR spectroscopy of the polymers. Anna Illy aided initial polymer syntheses *via* route A under my supervision. Sandra Hultmark and Christian Müller (Chalmers University of Technology, Department of Chemistry and Chemical Engineering) carried out the FSC experiments. Wen Liang Tan and Christopher R. McNeill (Monash University, Department of Materials Science and Engineering) characterized the polymers by GIWAXS analysis. Sebastian Hutsch and Frank Ortmann (Technische Universität München, Department of Chemistry) executed the DFT calculations. David Becker-Koch and Yana Vaynzof (Technische Universität Dresden, Integrated Centre for Applied Physics and Photonic Materials and Centre for Advancing Electronics Dresden (cfaed)) performed PDS measurements. Charlotte Rapley and Martin Heeney (Imperial College London, Department of Chemistry and Centre for Processable Electronics) provided the C12-IDT monomer. Michael Sommer designed and supervised the work. All authors were involved in revising the manuscript.

Chapter IV: Temperature-dependent morphology-electron mobility correlations of naphthalene diimide-indacenodithiophene copolymers prepared via direct arylation polymerization

D. Adamczak, B. Passarella, H. Komber, D. Becker-Koch, O. Dolynchuk, S. B. Schmidt, Y. Vaynzof, M. Caironi and M. Sommer, **submitted**.

I synthesized the polymers and characterized them by SEC, UV-vis and PL spectroscopy, cyclic voltammetry, TGA as well as DSC analyses. Further, I wrote the first draft of the manuscript. Simon Schmidt provided PNDIT2 as reference material. Bianca Passarella and Mario Caironi (Istituto Italiano di Tecnologia, Center for Nano Science and Technology @PoliMi) characterized the polymers in organic field-effect transistors. Hartmut Komber (Leibniz-Institut für Polymerforschung Dresden e.V.) analysed the polymers by high-temperature NMR spectroscopy. David Becker-Koch and Yana Vaynzof (Technische Universität Dresden, Integrated Centre for Applied Physics and Photonic Materials and Centre for Advancing Electronics Dresden (cfaed)) performed PDS experiments. Oleksandr Dolynchuk (Martin Luther University Halle-Wittenberg, Experimental Polymer Physics) carried out the GIWAXS measurements. Michael Sommer designed and supervised the work. All authors were involved in revising the manuscript.

Chapter V: Indacenodithiophene-based copolymers for application in all-polymer solar cells

I synthesized the donor materials and characterized all materials by SEC, UV-vis and NMR spectroscopy as well as cyclic voltammetry. Further, I fabricated as well as characterized the solar cell devices and summarized the results in this chapter. The acceptor materials were provided by Younghun Shin, Rukiya Matsidik and Simon Schmidt. Hartmut Komber (Leibniz-Institut für Polymerforschung Dresden e.V.) recorded NMR spectra of PIDTF4. Solar cell preparation and characterization was performed in the laboratories of Prof. Dr. Carsten Deibel (TUC, Physics Department).

I. Introduction

1. Conjugated materials for organic electronics

Organic electronics such as displays for high-end smartphones, lighting panels, curved television screens as well as portable solar cells are already an essential part of our daily life. The demand of high performance, printable, flexible and sustainable technology has drawn the attention towards so-called π -conjugated materials.¹⁻⁴ In contrast to inorganic materials they possess several advantages such as easy solution processability, light-weight and the ability to precisely tailor the properties by structural modification.^{3,5} Their semiconducting behavior arises from an alternating single and double bond structure. The sp^2p_z configuration with a maximal p-orbital overlap lead to an optimal delocalization of the π -electrons.⁶⁻⁸ However, their charge carrier mobility and conductivity lag behind inorganic materials. Since the discovery of electric conductive polyacetylene in 1977⁹ and the pioneer work of *MacDiarmid*, *Heeger* and *Shirakawa*,¹⁰⁻¹² researchers all over the world developed new design structures of π -conjugated materials to improve their optoelectronic properties and increase device performances.^{3,5,13,14} In initial stages, the most prominent materials were based on polyphenylene vinylene (PPV)^{15,16} and poly(3-alkylthiophene) (P3AT).^{17,18} Nowadays, the state-of-the-art materials are based on small molecules and polymers with a donor (D)-acceptor (A) structure.^{19,20} Such materials possess small and largely tunable energy band gaps resulting from an alternating arrangement of electron-rich and electron-deficient moieties. Thus, the mixing of the molecular orbitals leads to a higher lying HOMO and lower lying LUMO energy level (Figure I-1a). While the HOMO is determined by the donor, the LUMO is mainly dictated by the acceptor unit. Tuning of the band gap by adjusting the electron pushing and pulling strength of the corresponding units is an important feature to design appropriate materials for various applications.^{21,22} For instance, materials with a deep LUMO are favored for the use in thermoelectrics^{23,24} while a higher lying LUMO level and hence, smaller band gap is required for application in organic photovoltaics (OPVs).^{25,26} Depending on the nature of the D and A units, the conjugated polymers show either hole, electron or ambipolar transport characteristics exceeding mobility values of $10 \text{ cm}^2 \text{ V}^{-1} \text{ s}^{-1}$.²⁷⁻²⁹ In combination with their broad absorption range those materials are excellent candidates not only for application in organic field-effect transistors (OFETs)^{30,31} but also in OPVs.³²⁻³⁴ Examples of common D-A copolymers are shown in Figure I-1b.

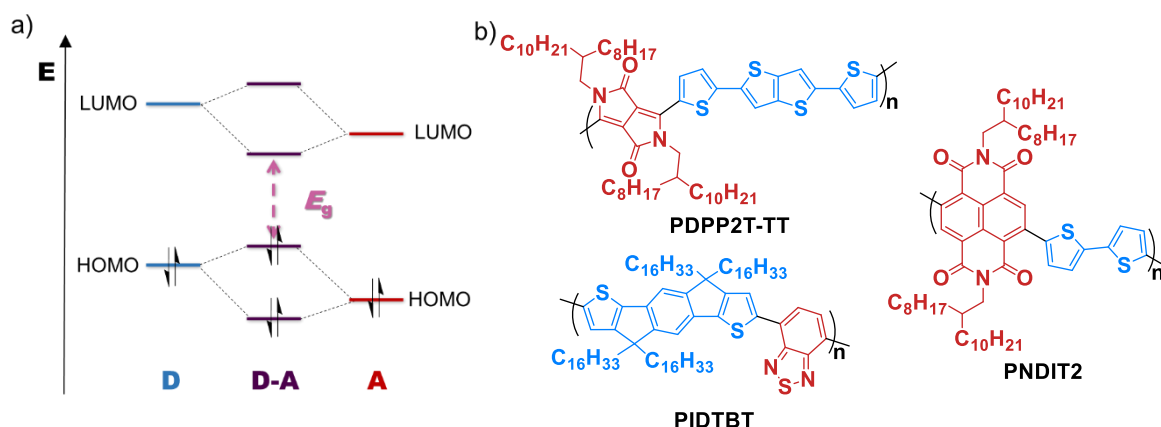


Figure I-1. a) Molecular orbital diagram of D-A unit and b) chemical structures of common D-A conjugated polymers.

1.1. Organic field-effect transistors

Besides their application in sensors, flexible displays and electronic papers, organic field-effect transistors (OFETs) are an important instrument to characterize the charge transport properties of π -conjugated materials. A significant parameter is the field-effect mobility μ which describes the carrier transfer rate under an external field. An OFET device consists of an organic semiconductor as active layer, a dielectric layer as well as the source and the drain electrodes. According to the arrangement of the layers there are four different device architectures (Figure I-2, a-d). While bottom-gate configurations are primary used for fundamental studies, top-gate type devices are chosen in practical applications.^{30,31,35} Free charges can be induced at the interface between the semiconductor and the dielectric layers by applying a voltage at the gate electrode. At the same time a current I_{DS} between the drain and source electrode is generated which can be controlled by the gate voltage V_G .

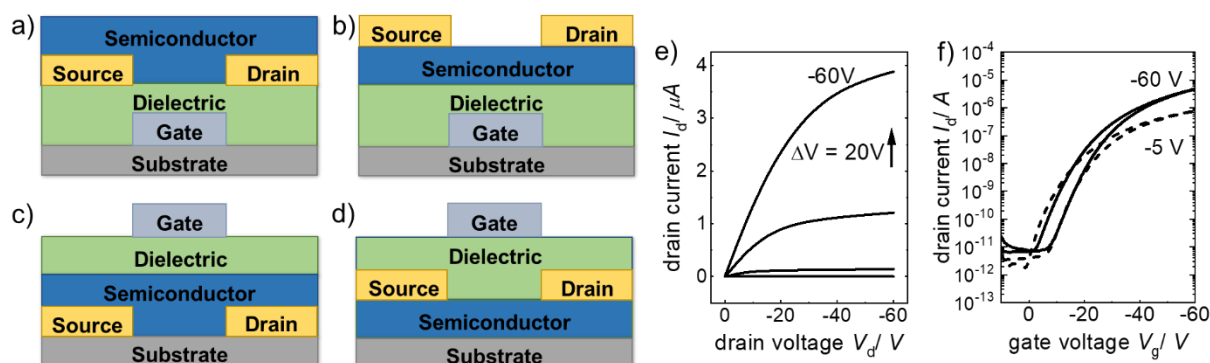


Figure I-2. OFET configurations: a) bottom-gate bottom-contact, b) bottom-gate top-contact, c) top-gate bottom-contact, d) top-gate top-contact; e) typical output curve and f) transfer curve of a p-type material. Adapted from Ref.³⁵

Depending on the nature of the charge carriers the transistors are categorized as p-channel (holes) and n-channel (electrons), respectively.^{31,36,37} The characteristic relationship between current and voltage of an OFET is represented in so-called output (constant V_G /sweeping I_{DS}) and transfer curves (constant I_{DS} /sweeping V_G) (Figure I-2, e-f).^{36,37} The most important parameter that can be obtained from the transfer measurements is the field-effect mobility μ . The mobility describes the drift velocity of the charge carrier per unit applied electric field. It is used to probe the performance of OFET devices and to define electrical properties of a material.^{31,35} In the last decades a lot of effort was made to improve the device performances of OFETs. In addition to appropriate fabrication techniques such as interface engineering, device geometry and processing techniques,^{31,38,39} high charge mobility as well as electronic stability in air of the semiconducting active layer plays a crucial role for high-performance OFETs. In particular n-channel OFETs often suffer from poor stability in air. When operating under ambient conditions, the formed anions of organic semiconductors can undergo common redox reactions with water and oxygen that have diffused into the film.^{40–42} One prominent class of materials for application in OFETs are π -conjugated polymers due to their intrinsic flexibility and solution-processability. Common materials are based on diketopyrrolopyrrole (DPP)^{43,44}, indacenodithiophene (IDT)^{45,46}, naphthalene diimide (NDI)^{47,48} and cyclopentadithiophene (CDT)^{49,50} with mobilities μ between 1-20 cm² V⁻¹ s⁻¹.^{35,51,52} The charge carrier transport can occur through π -orbitals in two directions along the backbone (intrachain) and in π - π stacking direction of the polymer chains (interchain); the first one is faster and dominant whereas the latter occurs only *via* hopping.⁵³ Hence, key factors for high mobilities are solid-state aggregation, appropriate polymer chain length and alignment as well as crystallinity of the polymer films. To enhance the charge transport a number of design strategies for D-A polymers were developed.^{30,35} One approach is to lower the energetic disorder^{54,55} by increasing planarity and rigidity of the conjugated backbone. Such structural resilience can be achieved by incorporating fused aromatic building blocks with extended π -conjugation into the system.^{56,46} Further methods involve side chain engineering to improve intermolecular packing⁵⁷ and increasing molecular weights (MW).⁵⁸

1.2. Organic solar cells

The continuously increasing demand for clean and renewable energy resulted in a rapid growth of solar energy technologies. Since the development of the first bilayer organic solar cell (OSC) by *Tang* in the 1980s⁵⁹ organic photovoltaics (OPVs) have attracted a tremendous

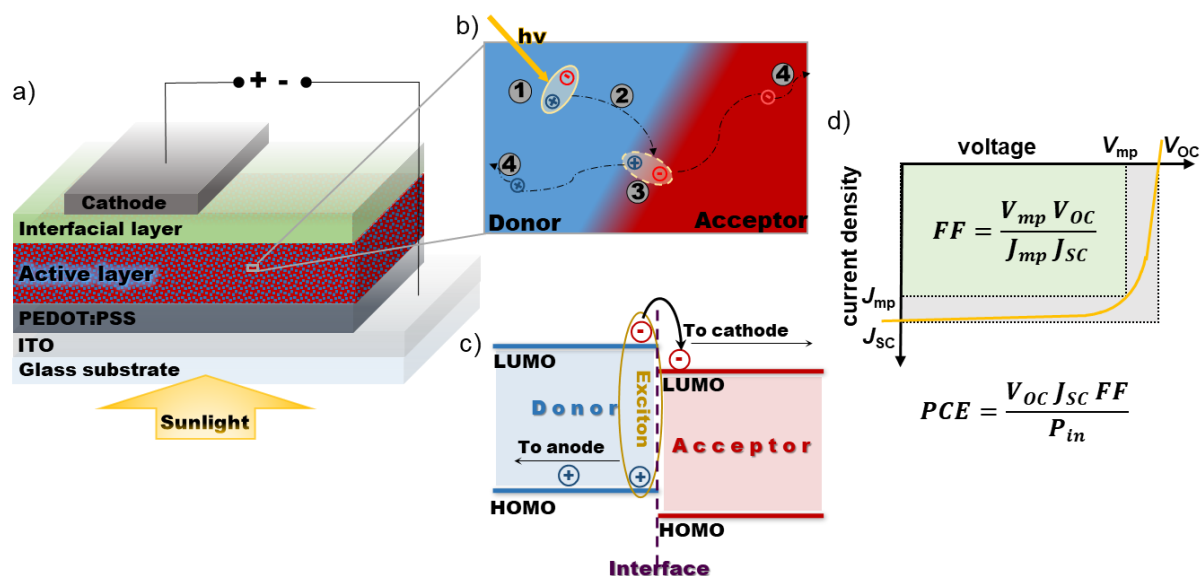


Figure I-3. a) Device architecture of a bulk heterojunction OSC. b) Operation principles and c) energy diagram of OSCs. d) Figures of merit including short-circuit current density (J_{sc}), open-circuit voltage (V_{oc}), fill factor (FF) and power conversion efficiency (PCE). Adapted from Refs.^{64,65}

interest in the field of research.^{34,60,61} The photoactive layer of a bulk heterojunction (BHJ) organic solar cell consists of a continuous blend film of electron donor and electron acceptor inserted between a PEDOT/PSS-modified ITO anode and a low work function metal cathode (Figure I-3a).^{62,63} The conversion process of solar energy into electricity can be divided into four steps (Figure I-3b and c): (1) absorption of photons by donor and acceptor materials in the active layer followed by generation of so-called excitons (electron-hole pairs), (2) diffusion of the excitons to D/A interfaces, (3) dissociation of excitons into free charges and (4) transport of the free charges to anode and cathode through the donor and acceptor domains. Subsequently, the free charge carriers are collected at the electrodes and a photocurrent is generated in the external circuit. Recording of current density-voltage ($J-V$) correlations allow the extraction of the OSC characteristics (Figure I-3d).^{64–66} Here, the maximum current passing through the device is ascribed to the short-circuit current (J_{sc}) and the maximum voltage which occurs at zero current is defined as open-circuit voltage (V_{oc}). The solar cell performance is determined by the light-to-charge power conversion efficiency (PCE) which is proportional to V_{oc} , J_{sc} and the fill factor (FF) (Figure I-3d).^{64,66} The device parameters are strongly dependent on the optoelectronic and morphological characteristics of the blend film. Thus, molecular design of suitable D-type and A-type materials for the photoactive layer is essential to enhance the PCE .^{62,67} A critical requirement is the appropriate alignment of HOMO and LUMO energy levels of donor and acceptor materials. J_{sc} is influenced by the light harvesting ability, dissociation efficiency and charge carrier transport properties of the active layer. Enhancement

of J_{sc} can be achieved by reducing the band gap to enable a broad absorption of light. At the same time the offset energies of donor and acceptor (Δ_{LUMO} and Δ_{HOMO}) ideally exceed the exciton binding energy, which is in the range of 0.1–0.3 eV^{64,68} to afford efficient charge separation. On the other hand, V_{oc} arises from the splitting of hole and electron quasi-Fermi levels and hence, increases with increasing band gap E_g . Therefore, it is key to balance J_{sc} and V_{oc} by energy level tuning and molecular design.^{62,64,66,69} Furthermore, an optimal morphology of the blend film including small domain sizes, domain purity as well as domain connectivity is necessary to ensure efficient charge separation and transport.^{62,70}

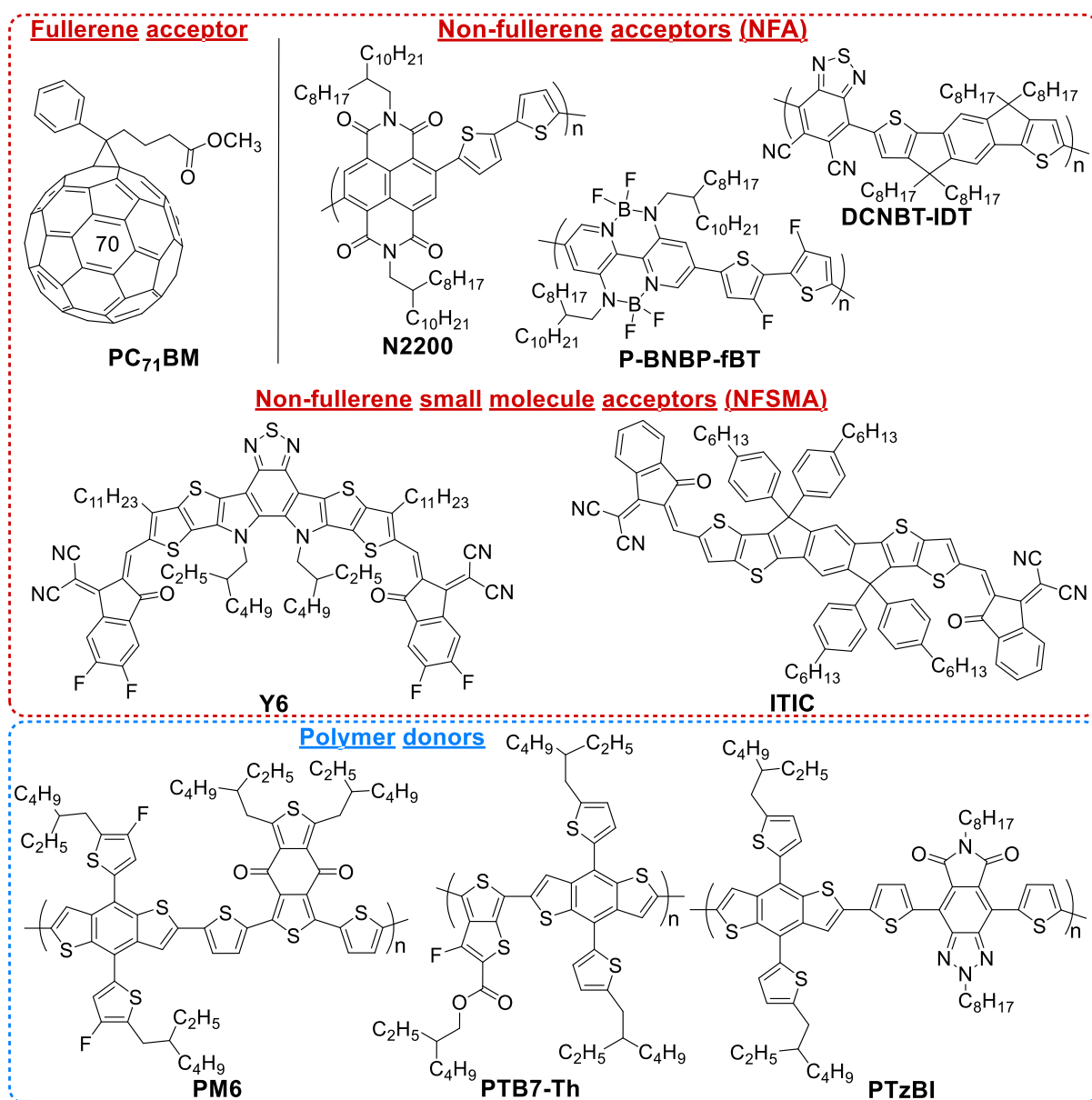


Figure I-4. Chemical structures of common A-type and D-type conjugated semiconducting materials for OSCs.

The establishment of fullerene derivatives such as phenyl-C₇₁-butyric acid methyl ester (PC₇₁BM) (Figure I-4) as acceptor materials blended with p-type polymers and small molecules, respectively, as donors pushed PCEs of OSCs up to 12%.^{64,71,72} Despite their high electron affinity, high charge mobility, isotropic charge transport and favorable blend morphology with donor materials fullerene acceptors possess several disadvantages. High synthetic costs, insufficient absorption in the visible and near infrared spectral ranges, poor morphological stability as well as challenging chemical and energetic modification limit the enhancement of high-performing OSCs.^{33,68,73} Alternatively, several polymers^{33,34,66} as well as small molecules^{60,63,68} were developed (Figure I-4). Such materials are meanwhile termed non-fullerene acceptors (NFAs) and non-fullerene small molecule acceptors (NFSMAs), respectively. NFAs benefit from strong absorption with high molar extinction coefficients, high morphological stability as well as easy structural modification allowing tunable optical and electronic properties.⁶⁸ High-performing NFSMA materials are based on perylene diimide (PDI), NDI, DPP and IDT building blocks usually blended with donor polymers with complementary absorption spectra. Molecular optimization of NFSMAs could achieve devices with PCEs exceeding 16%.^{60,74–77} Compared with small molecules, polymers possess improved morphological stability and superior mechanical flexibility that are important characteristics for application in wearable electronics.^{78,79} A widely used polymer acceptor is poly{[N,N'-bis 2-octyldodecyl)-naphthalene-1,4,5,8-bis(dicarboximide)-2,6-diyl]-*alt*-5,5'-(2,2'-bithiophene)} (PNDIT2) known as N2200 owing to its easy synthetic accessibility and good electron mobility. In combination with a siloxane-functionalized poly(*N*-alkyl-5,5'-bithiazole-4,4'-dicarboximide) PTzBI as donor polymer a single-junction all-polymer solar cell (all-PSC) with a record PCE of 11.76% could be fabricated.^{33,64,80–82} Nevertheless, a major challenge is related to the morphological characteristic of the BHJ blend film such as control over phase separation, molecular packing and interfacial orientation of donor and acceptor polymers. The reduced entropic contribution of the polymer chains promotes large-scale phase separation leading to recombination processes due to a limited diffusion length of excitons (~ 10 nm).^{33,34,70,73} Control over domain size and the degree of phase separation can be achieved by the adjustment of M_n of the donor as well as acceptor polymer.^{83–86} For instance, studies on N2200 based all-PSCs have shown that intermediate M_n values for both polymers result in blend films with a high degree of miscibility and intermixed features affording both, well balanced charge carrier generation and transport ability. Cells with higher M_n polymers can further reduce domain sizes and enhance miscibility leading to higher J_{sc} but, at the same time also promote charge carrier

recombination.⁸³ The crystalline properties are also influenced by side chains, torsion and structure of the π -conjugated polymers.^{34,73,87} Thus, side chain engineering^{88,89} and backbone modification^{90,91} can improve inter- and intrachain interactions and hence, enhance the device performance. In addition to the material design, the processing conditions can also have a great impact on the performance of the solar cells.^{73,92,93} For instance, the morphology of the active layer can be influenced by the nature of the processing solvent,^{82,94,95} solvent additives⁹⁶ as well as solvent and thermal annealing.⁷⁰ Further studies regarding device stability as well as efficiency concern device engineering such as conventional or inverted architecture,^{33,97} the choice of electrode and interlayer materials.^{98,99} Another tool to boost the PCE values is the construction of advanced device structures. So-called tandem solar cells consisting of two subcells with complementary absorption and incorporation of ternary blends based on two compatible acceptors and one donor into the active layer surpassing PCEs of 13%.^{33,100,101}

1.3. Indacenodithiophene – a building block for organic photovoltaic materials

Since its first introduction¹⁰² indacenodithiophene (IDT) is widely used as electron-rich chromophore in small molecules as well as D-A polymers. The fused aromatic ring system has several desirable features such as a preserved coplanarity, maximized π -orbital overlap as well as reduced conformational energetic disorder, an extended conjugation and a high electronic density. Moreover, the broad range of strategies to modify the IDT core gives access to broadly tunable materials.^{103–105} The different possibilities to functionalize the IDT molecule are shown in Figure I-5. Side chain engineering is a common tool to modify chemical structures. It affects not only solubility but also morphology and molecular packing. IDT can be classified into (i) aliphatic-substituted and (ii) aromatic-substituted materials. The first class gives rise to materials with excellent charge transport properties which, however, are strongly dependent on the side chain length. The second class leads to materials with high absorption coefficients and

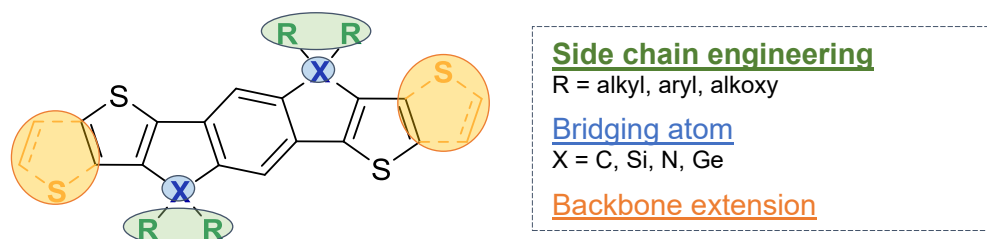


Figure I-5. Modification of the indacenodithiophene unit. Adapted from Ref.⁴⁶

easy processability but induce steric hindrance, thus, corrupting molecular packing.^{104,105} Additionally, the choice of bridging atom is critical to the morphological properties. Incorporation of various heteroatoms like carbon, silicon, germanium and nitrogen can influence the planarity of the attached side chains, solubility and optoelectronic properties of the materials.^{103,106} A further strategy to tune the planarity, intermolecular interactions and electronic properties is the extension of the conjugated unit by replacing the thiophene moieties with two thieno[3,2-b]thiophene (TT) units.^{103–105} Even though IDT-based compounds suffer from tedious synthetic pathways,^{56,107} the appealing and tunable properties led to the development of a wide variety of promising semiconducting materials for application in OPVs (based on IDT).

1.3.1. Indacenodithiophene-based small molecules as non-fullerene acceptors

The typical design strategy of NFAs is built on an A-D-A structure. A major breakthrough of the development of novel NFA materials was the incorporation of IDT derivatives as donor unit. In contrast to fullerene-based acceptors, IDT-based NFAs benefit from their excellent electron transport properties, easy purification and strong absorption in visible-NIR region. The easy functionalization of the IDT core allows adjustment of the optoelectronic properties to adapt their use in combination with donor polymers. Recently, such NFSMA solar cells exhibit PCEs over 13% surpassing fullerene-based devices.^{60,74,75,108}

One of the first A-D-A-type small molecules based on IDT contained 1,1-dicyanomethylene-3-indanone (DCI) as acceptor moieties and thiophene as π -bridges. Incorporation of π -bridges is used as extension of the backbone conjugation and at the same time to enhance the planarity. As result, a red-shift of the absorption spectrum and a narrowing of the bandgap E_g is observed. Blended with PBDTTT-C-T as donor polymer BHJ PSC devices yielded PCEs of 3.93%.^{75,109} The development of IEIC, in which the thiophene spacer is modified with 2-ethylhexyl side chains, and usage of the low bandgap donor polymer PTB7-Th boosted the device efficiency to 6.31%. The good performance of this novel NFA is attributed to its strong absorption in visible region with high absorption coefficients, high electron mobilities and deep LUMO levels similar to those of fullerene derivatives. The choice of the medium bandgap polymer PffT2-FTAZ-2DT with a complementary absorption spectrum, more suitable energy levels and a favorable blend morphology with IEIC led to an enhanced solar cell performance.^{75,110,111} Further improvements were obtained by attaching alkoxy instead of alkyl side chains on the π -

bridges. The noncovalent S \cdots O interactions and stronger electron-donating character of the alkoxy side chains led to an up-shifted HOMO level with a narrowed bandgap E_g . Thus, a broader absorption and improved morphology were attained resulting in PCEs over 8%.^{75,112}

At present, state-of-the-art NFAs are based on ITIC derivatives (Figure I-4) containing indacenodithieno[3,2-*b*]thiophene (IDTT) as donor and 2-(3-oxo-2,3-dihydroinden-1-ylidene)malononitrile (INCN) as acceptor unit. Owing to the extended backbone with additional thiophene rings ITIC possesses strong absorption, low LUMO and HOMO energy levels, high charge mobility as well as good miscibility with various donor polymers.^{74,108,113,114} One efficient method to modify the core structure and, hence, to tune the physicochemical properties is altering of the side chains. The alkylphenyl side chains ensure solubility and processability but at the same time reduce the intermolecular interactions. Isomerization of the side chains resulted in *meta*-alkylphenyl substituted ITIC with improved electron mobility due to an increased face-on crystalline orientation and higher absorptivity.¹¹⁵ In addition, employment of novel side chain patterns such as alkyl, thienyl and asymmetric substitution could also reduce steric hindrance. The higher crystallinity promotes an efficient and balanced charge transport.^{116–118} Such PSC devices showed broad absorption and a good tolerance to film thickness leading to high fill factors and enhanced PCEs up to 11.9%.^{75,108,115–118} A further common strategy to improve photovoltaic performance is the fluorination of acceptor as well as donor material. The small electronegative fluorine lowers the energy levels and improves crystallinity due to noncovalent F \cdots H/S \cdots F interactions. Fluorination of the electron-withdrawing end groups of ITIC and inclusion of fluorine atoms in the corresponding donor polymer established a new system, known as IT-4F:PBDB-T-SF. The BHJ blend layer displayed a broad absorption range and increased absorption coefficients leading to remarkable OPV device performance with a PCE over 12% even at higher film thickness.^{74,75,108}

1.3.2. Design and synthesis of indacenodithiophene-based conjugated polymers

IDT-based copolymers are counted among the most promising p-type materials for photovoltaic applications owing to their excellent optoelectronic properties. A huge effort was made to tune energy levels, charge transport properties and optical band gaps. Copolymerization with different electron deficient acceptors (Figure I-6) and modification of the backbone such as side chain engineering, backbone extension and incorporation of electron-

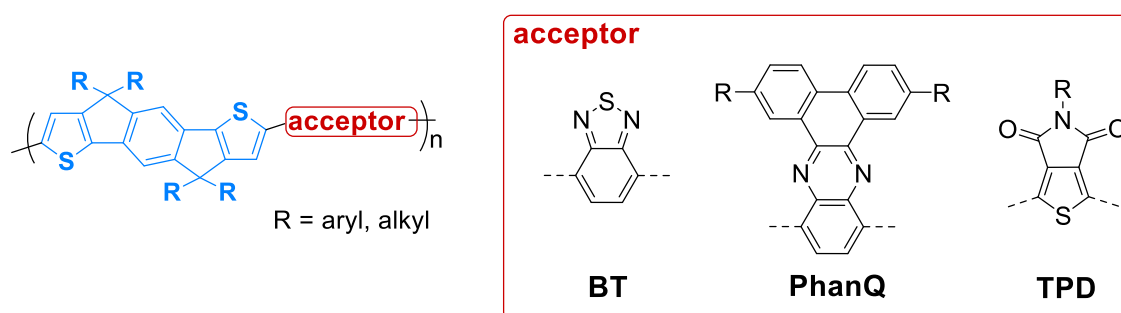


Figure I-6. Chemical structures of common acceptor units in IDT-based copolymers.

withdrawing groups gave access to a wide variety of IDT-based semiconducting materials.^{103–105} To this date, OPVs comprising IDT copolymers blended with fullerene as acceptor yielded efficiencies over 8% for single-junction and over 11% for tandem devices, respectively.^{119,120}

Many state-of-the-art IDT copolymers contain a benzothiadiazole (BT) derivative as acceptor unit. Due to its high electron affinity, stability and optoelectronic properties, the corresponding copolymers exhibit long wavelength absorption with low band gaps. At the same time the quasi-quinoidal BT structure promotes intermolecular interactions and preserves a planar conformation of the polymer backbone.^{104,105} As result, PIDTBT exhibits excellent charge transport properties. Alkyl-substituted PIDTBT copolymers achieved field-effect mobilities up to $10 \text{ cm}^2 \text{ V}^{-1} \text{ s}^{-1}$ despite their lack of long-range order.^{28,45,56} The largely torsion-free backbone with a low degree of energetic disorder enables close contact interchain interactions allowing additional interchain transport.^{45,54} Yet, charge transport properties are strongly dependent on the nature of the side chain. While aliphatic side chains benefit from formation of short contact distances, alkylphenyl side chains induce steric hindrance resulting in reduced hole mobilities.^{46,121} The advantage of aryl-substituted PIDTBT polymers are their easier synthesis, higher solution-processability, high absorption coefficients and higher V_{oc} s compared to their alkyl analogues.¹⁰⁵

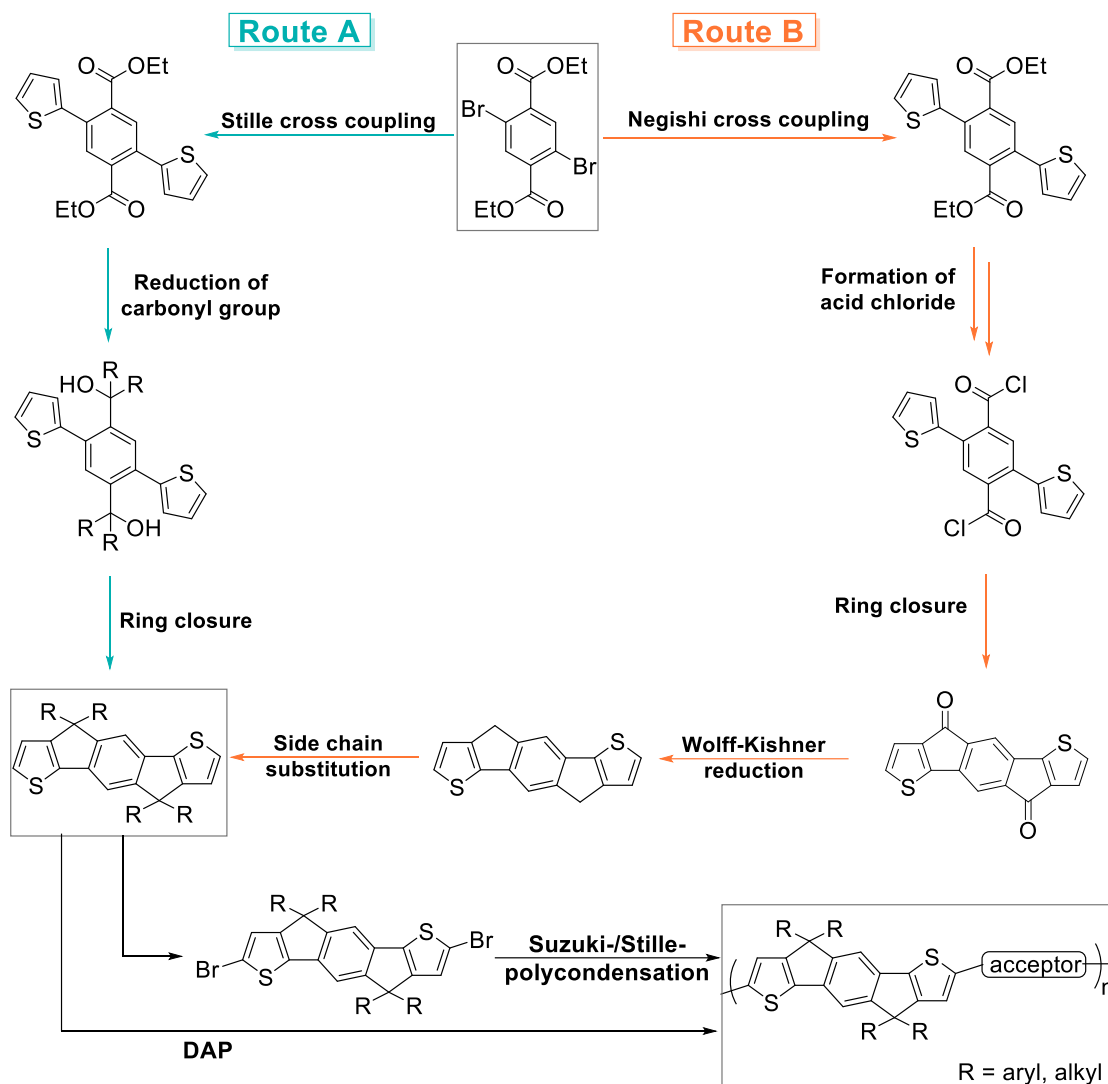
Due to their interesting properties aryl-substituted PIDTBTs are promising candidates for applications in PSCs. Several attempts to optimize the morphology such as backbone extension of the IDT unit¹²², replacement of sulfur by selenium¹²³ as well as incorporation of π -bridges¹¹⁹ could enhance the planarity of the polymer backbone and hence, the charge mobility. Fabrication of PSCs containing PIDTBT:PC₇₁BM blends as active layer achieved efficiencies up to 8.15%.^{104,105,119,122,123}

Another widely used electron deficient comonomer is the quinoxaline unit which is known for its easy synthesis and modification. Copolymerization of a fused quinoxaline moiety (PhanQ; Figure I-6) and IDT yielded materials with good intermolecular packing and charge transport properties. Blends with PC₇₁BM showed good performances in BHJ solar cells without post-treatments.^{104,105,124,125} Even higher PCEs over 7% could be achieved using a thiophene-quinoxaline-thiophene building block.^{104,105,126,127}

The development of a novel two-dimensional (2D) conjugated polymer comprising a methylene-modified IDT (DMIDT) donor unit and thieno[3,4-*c*]pyrrole-4,6-dione (TPD; Figure I-6) as acceptor established a new class of IDT-based p-type polymers. The introduction of sp²-hybridized carbon atoms flanked with four phenyl rings in the IDT core improves interchain π - π overlapping as well as charge mobility and broadens the absorption spectrum. In addition, steric hindrance of the phenyl side chains can be reduced and the more planar backbone can be locked due to S...O interactions with TPD. A PCE of 8.26% for a fullerene-based device and a PCE of 6.88% for a non-fullerene PSC could be obtained.¹²⁰

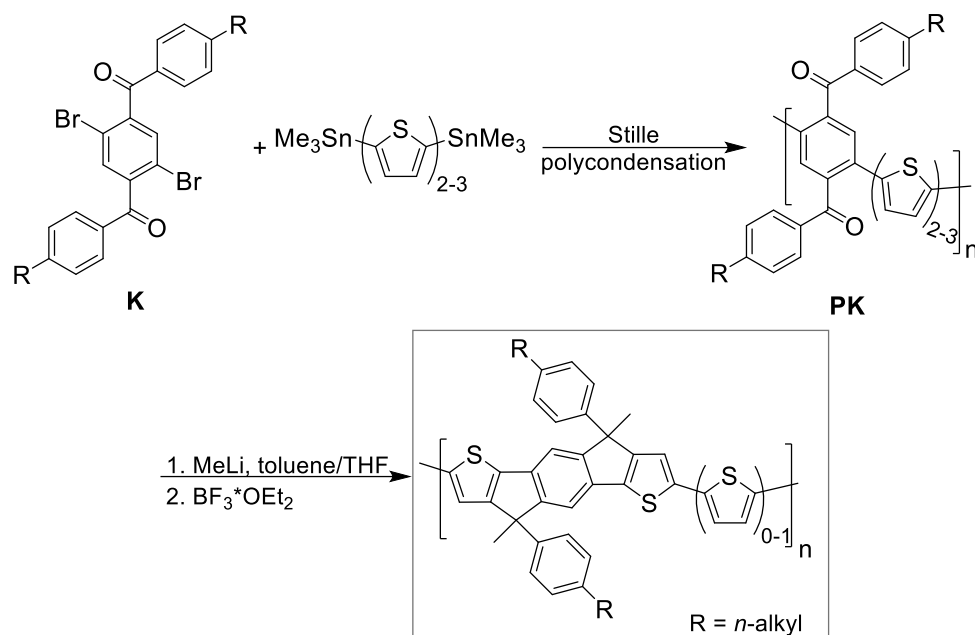
Further acceptors such as NDI^{128,129}, DPP¹³⁰ and BDD¹³¹ could be polymerized with IDT allowing a wide variety of semiconducting materials with fine-tuned properties. Besides the application in PSCs and OFETs, IDT-based polymers are also implemented as n-type acceptors in all-polymer solar cells^{128,129}, as hole-transporting material in Perovskite solar cells¹³¹, in organic photodetectors¹³² as well as in stretchable electronics¹³³.

Despite their promising features and variable field of applications, IDT-based polymers suffer from tedious reaction pathways. IDT monomer synthesis involves multiple reaction and purification steps reducing the overall yield and economic efficiency which leads to an increased production cost. State-of-the-art synthesis of IDT monomers and polymers is presented in Scheme I-1. Depending on the nature of the side chain on the IDT unit, two different synthetic procedures are employed. Both pathways start with cross coupling of 2,5-dibromo-terephthalic acid diethyl ester and thiophene using Stille or Negishi reactions. Preparation of aryl-substituted IDT is done according to Route A in four reaction steps, while alkyl-substituted IDT is prepared in six reaction steps *via* Route B. The final polymerization is usually carried out using Stille or Suzuki polycondensation.^{56,103,104,107,124} To date, few protocols have been reported that utilize atom-economic direct arylation polycondensation (DAP) to synthesize IDT-based (co)polymers.^{107,133,134}



Scheme I-1. Synthetic routes towards IDT-based (co)polymers with aromatic side chains (Route A) and aliphatic side chains (Route B), respectively.

Inspired by the preparation of soluble ladder-type poly(*p*-phenylene)s (LPPPs)¹³⁵ Scherf *et al.* reported the synthesis of IDT-based polymers *via* a polymer analogous reaction pathway (Scheme I-2).^{136,137} Here, polymerization between a ketone-functionalized phenylene **K** and thiophene derivatives using Stille polycondensation yield single-stranded polyketones **PKs** in the first step. Then, transformation into the final IDT-based polymer is accomplished by two polymer analogous cyclization steps. Firstly, polymer analogous reductions of the keto groups with methyl lithium and secondly, polymer analogous ring closure by intramolecular Friedel-Crafts alkylation.¹³⁶ Major challenges of this post-polymerization sequence concern high solubility of the polymeric intermediates (to ensure further transformation), quantitative conversion of the functional groups and suppressing of side reactions resulting in crosslinking and/or structural defects. Yet, multiple conjugated ladder-type polymers could be successfully



Scheme I-2. Synthetic route towards IDT-based polymers by Scherf et al.

prepared by choosing appropriate reaction conditions.^{138–141} In terms of IDT-based materials, this method is quite interesting since the complex monomer synthesis could be avoided. At the same time, IDT-based materials with an asymmetric substitution pattern at the IDT unit could be prepared which may allow fine-tuning of thermal, morphological and optoelectronic properties.

1.4. Direct arylation polycondensation – synthesis of π -conjugated polymers

Efficient syntheses of π -conjugated systems often rely on transition-metal catalyzed cross couplings such as *Migita-Stille*^{142,143}, *Suzuki-Miyaura*^{144,145}, *Negishi*^{146,147} and *Kumada-Tamao*^{148,149}. Yet, the couplings of heteroaryl-halides with organometallic-heteroarenes are accompanied by additional preparation steps which render synthesis pathways lengthy and costly. A further disadvantage is the stoichiometric formation of by-products like the highly toxic tin compounds formed in Stille reactions.^{150–152} An attractive and more sustainable alternative to these conventional synthetic methods is the so-called direct arylation (DA). Here, the metal-catalyzed formation of the C-C-bond is the result of the condensation between an activated C-H bond of (hetero)aryl derivatives and an arylhalide. So-called oxidative direct arylation even enables coupling of two C-H type substrates. By eliminating the need for organometallic reagents direct arylation benefits from fewer synthetic steps, simpler purification of reactants, more benign by-products and potentially broader substrate scope

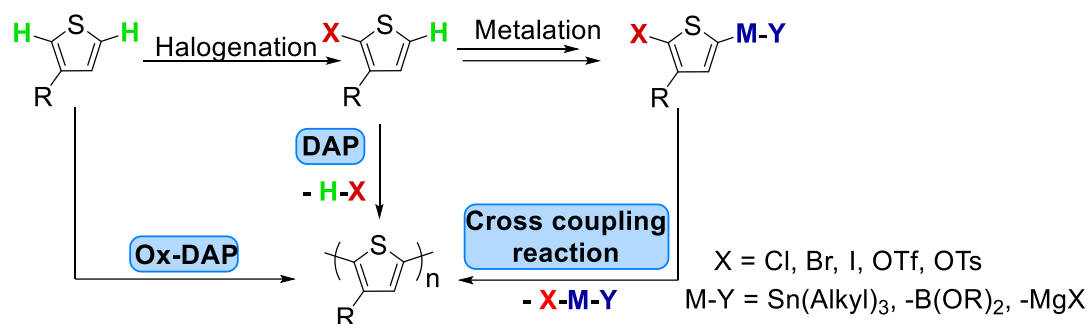


Figure I-7. Comparison of polymerization of P3HT by traditional cross coupling reactions with direct arylation. Adapted from Ref.¹⁵⁶

(Figure I-7).^{153–157} While C-H activation methods are known for several years^{158–160} adaption to conjugated polymer synthesis was done decades later. In 1999, *Lemaire et al.*^{161,162} reported the first polymer synthesis *via* direct arylation polycondensation (DAP). P3AT was polymerized directly from 2-iodo-3-alkylthiophenes using palladium(II) acetate ($\text{Pd}(\text{OAc})_2$) as catalyst, potassium carbonate (K_2CO_3) as base, stoichiometric amount of tetrabutylammonium bromide (Bu_4NBr) as phase transfer agent and *N,N*-dimethylformamide (DMF) as solvent. These reaction conditions known as *Jeffrey's* condition were chosen under the assumption that DA reactions follow a Heck-like mechanism. Though, only oligomeric materials with a regioregularity of 90% were obtained.^{161,163,164} The first successful synthesis of highly regioregular P3HT using DAP was provided by *Ozawa et al.* in 2010 and awakened interest of the research community. The *Ozawa* conditions comprise a Hermann-Beller catalyst in combination with tris(*o*-anisyl)phosphine as ligand, caesium carbonate as base and THF as solvent.^{165,166} The addition of pivalic acid (PivOH) can lower the energy of C-H bond cleavage and act as proton shuttle between the carbonate base and the catalytic species. This effect was first investigated by *Fagnou et al.* developing benzene arylation. The chosen catalytic system consisted of $\text{Pd}(\text{OAc})_2$, a bulky phosphine ligand, K_2CO_3 and PivOH in DMF as strong coordinating solvent.^{164,167,168} The first syntheses of D-A polymers *via* DAP were performed by *Kanbara et al.*¹⁶⁹ and *Leclerc et al.*¹⁷⁰ based on the pioneer work of *Ozawa* and *Fagnou*. Further modifications and optimizations of the DAP parameters, for example, catalytic systems¹⁶⁵, solvent effects¹⁷¹ and influence of additives¹⁷² were intensively investigated. To date, many successful protocols are established for the syntheses of small molecules and polymers by direct arylation.^{152,153,155,164}

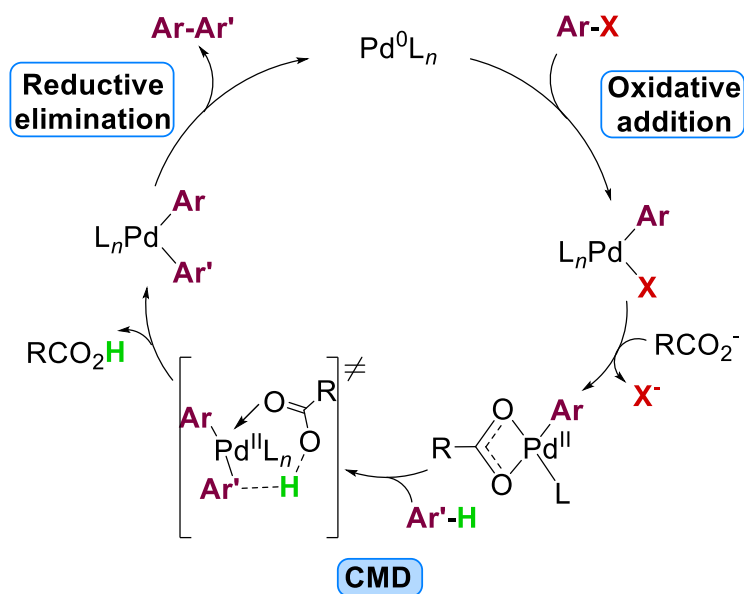


Figure I-8. Catalytic cycle of direct arylation with a carboxylate additive.

The mechanism of direct arylation depends on the nature of the substrates, the catalytic system and additives.¹⁵³ Figure I-8 illustrates the proposed catalytic cycle with a carboxylate additive. Like conventional cross coupling reactions, the process starts with oxidative addition of an arylhalide (Ar-X) to the catalyst complex (Pd^0L_n). Instead of the usually followed transmetallation, most (hetero)arenes seem to undergo a concerted metalation-deprotonation (CMD) step. Thereby, the reaction proceeds over a six-membered transition state in which a carboxylate anion coordinates with the aryl complex. At this state the Ar'-H substrate is deprotonated while simultaneously forming an Ar'-Pd bond. Finally, the Ar-Ar' coupling product is formed *via* reductive elimination.^{153,155,165} A major problem of DA reactions is the occurrence of side reactions such as homocouplings, β -couplings between unselective C-H and C-Br functionalities and chain termination reactions (Figure I-9). Especially in terms of polymerization, undesired side reactions are often troublesome resulting in low MWs and defect structures. Unlike small molecules, defect structures in polymers are embedded within the polymer chain and cannot be eliminated by purification processes. Structural defects have a strong influence on the optoelectronic as well as mechanical properties of the materials and as a consequence on the device performances. Therefore, it is crucial to optimize the reaction conditions in regard to suppressing unwanted side reactions.^{153,154} In the last years, a tremendous effort was made to investigate the effect of solvent, temperature, catalyst as well as ligand system, additives and substrate modification such as protection of the β -position on the final structure of the polymer backbone.^{153,155,173}

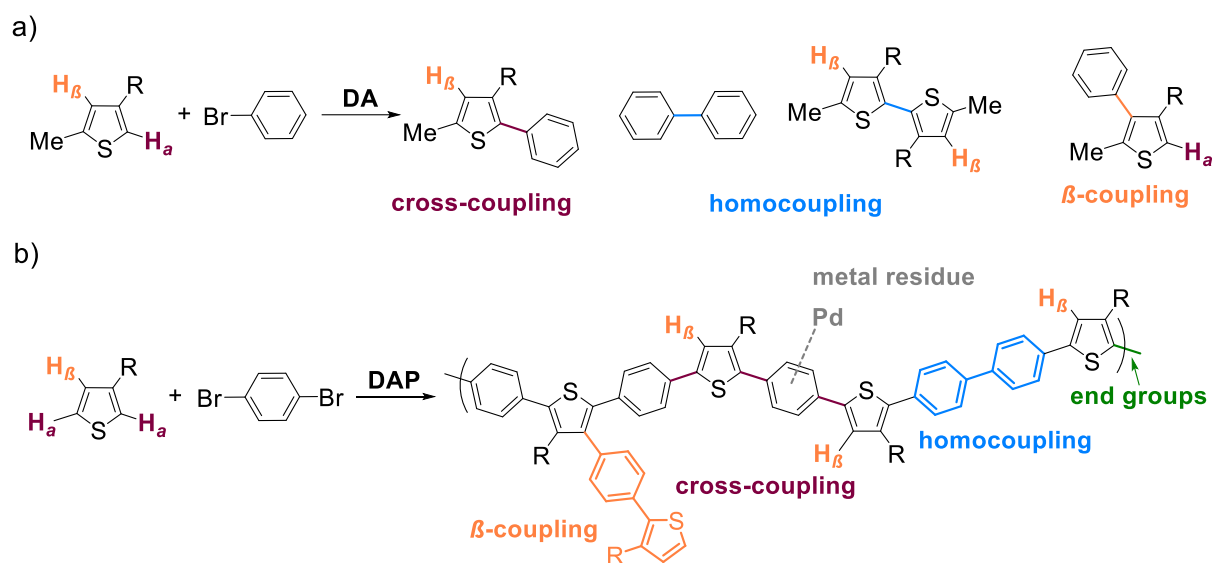


Figure I-9. Exemplary scheme of possible side reactions synthesizing small molecules by direct arylation (a) and the arising defect structures adopting direct arylation to polymer syntheses (b). Adapted from Ref.¹⁵⁵

For instance, studies of *Thompson et al.* showed that the use of bulky α -tertiary acidic additives such as neodecanoic acid (NDA) could limit unfavourable β -branching reactions yielding high molecular weight P3HT with high regioregularity.^{172–174} Not only the nature of the additives but also the choice of the ligand influences the selectivity of the catalytic centre and can improve the resulting polymer quality.^{173,175} *Sommer et al.* reported direct arylation polycondensation of 4,7-bis(4-hexyl-2-thienyl)-2,1,3-benzo-thiadiazole (TBT) and 2,7-dibromo-9-(1-octylonyl)-9*H*-carbazole (CbzBr₂). Thereby, occurring homocoupling defects could be suppressed in the presence of a bulky phosphine ligand and at a decreased reaction temperature.¹⁷⁶ Furthermore, the same group investigated the effect of monomer concentration as well as aromatic solvents on DAP of an alternating naphthalene diimide bithiophene copolymer (PNDIT2) and were able to synthesize defect-free PNDIT2 with high and controllable molecular weight.^{171,177} They reported an increase in molecular weight with increasing monomer concentration up to 0.5 M. This effect could be explained by in situ chain termination with the aromatic solvents used in polymerization *via* C-H activation. Highly substituted solvents such as mesitylene exhibit a lower C-H reactivity than less substituted solvents like toluene.^{171,177} Besides careful optimization of reaction conditions, the selection of the monomer structures is of high importance for a successful coupling by DAP. For example, the efficiency of the synthesis of an alternating copolymer containing dithienyldiketopyrrolopyrrole (DPPT_h2) and tetrafluorobenzene (F4) units depends on the monomer containing the halide function. While copolymerization of DPPT_h2 with

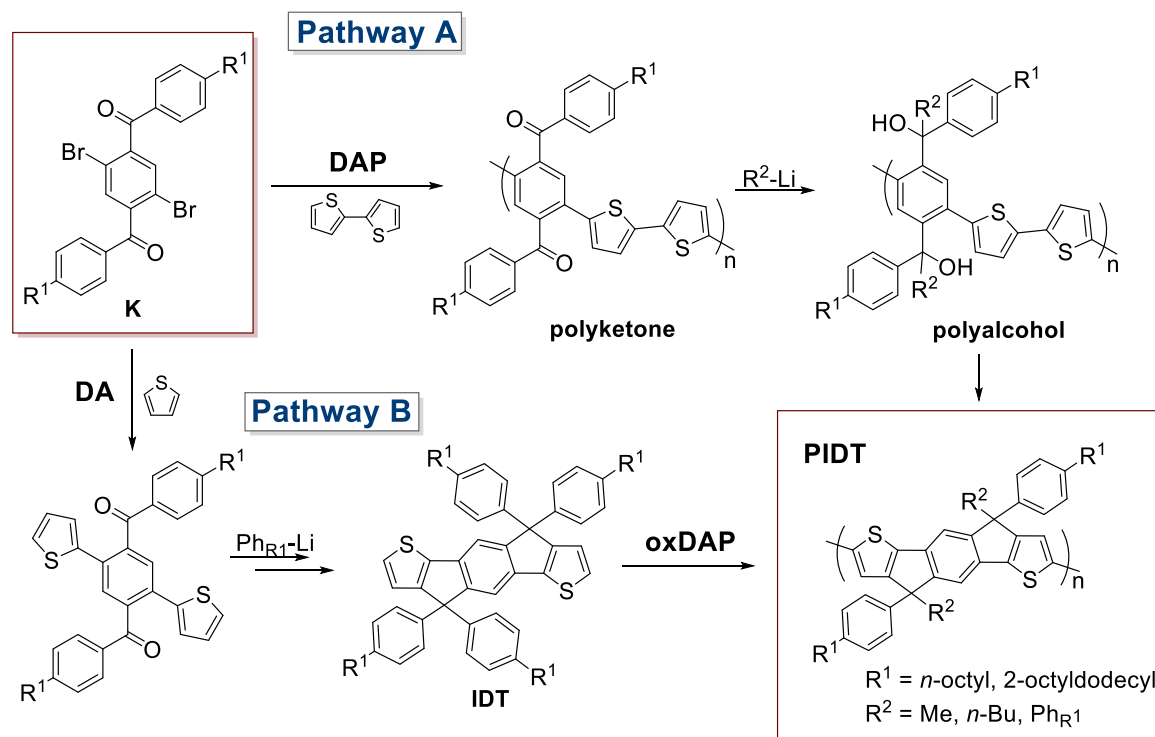
dibromotetrafluorobenzene yielded a well-defined material, coupling of a dibromo-DPPT_h2 with tetrafluorobenzene resulted in a copolymer with obvious structural defects.^{155,178,179} By now, the continuous fine-tuning of reaction conditions as well as substrates offered access to a great number of conjugated polymers *via* DAP with similar properties compared to their analogues made by conventional cross coupling methods.^{152,155,180,181}

Even though direct arylation is deemed to be an atom-economic alternative to traditional cross coupling reactions there is still a need for improvements in terms of more sustainable solvents and catalysts. Almost all solvents used in C-H activation reactions are hazardous and their production is highly energy intensive. The selection of appropriate green solvents for DAP is challenging. Solubility, stability of catalyst and base as well as propensity for side-reactions need to be considered and, to this date, only a few examples of conjugated polymers were prepared in sustainable solvents such as anisole, cyclopentyl methyl ether and 2-MeTHF.^{156,182} Further approaches to more sustainability are the replacement of palladium. A cost-efficient alternative is copper. Cu-catalyzed direct arylation requires high temperatures, amine ligands and needs to be carried out in the absence of carboxylic acid additives (due to disproportionation of Cu^I). One of the main drawbacks of Cu-DAP is the low solubility of the copper(I) salts in organic solvents as well as the limited stability of copper(I) at high temperatures. Thorough optimizations of polymerization conditions are necessary to extend the scope of Cu-DAP.^{156,183}

A highly atom-economical route towards conjugated polymers would constitute an oxidative C-H/C-H cross coupling reaction.¹⁸⁴ By eliminating the need for halogenated substrates the reaction pathway would be shortened and the overall sustainability enhanced. While this methodology is successfully established in case of small molecules^{185–187} the application to conjugated polymers is limited. The reaction is typically carried out in oxygen atmosphere and by the use of Pd(OAc)₂ as catalyst, Ag₂CO₃ as oxidant as well as acetic acid as an additive. The major problem evolves from asymmetric monomers of multiple C-H bonds with similar reactivity which is displayed in a first attempt to polymerize 3-hexylthiophene *via* oxidative DAP¹⁸⁸ resulting in P3HT with low regioselectivity and low yield. Successful examples were demonstrated by polymerization of TPD and benzodiiimidazole derivatives. The continuous development and manifold advances in the field of C-H activated reactions show the potential of DAP as a replacement technique for established methodologies and in future large scale production.^{154–156}

2. Overview of thesis

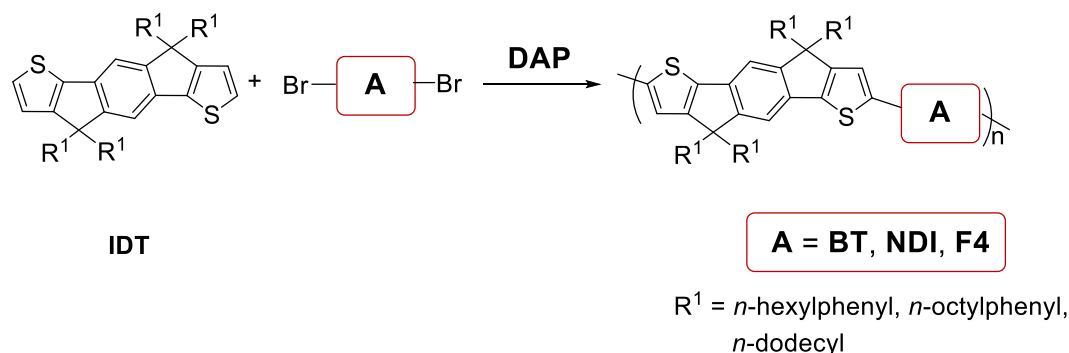
The objective of this thesis is two-fold: 1) to develop new efficient preparation pathways for IDT-based materials and 2) to investigate the influence of IDT side chain pattern and reaction pathway on the properties of the synthesized polymers. Finally, their use in OFETs and OPVs were explored. Shorter monomer and polymer synthesis was accomplished using direct arylation which will be presented in chapter II. Here, a ketone serves as starting compound offering the possibility of two different reaction pathways (Scheme I-3). Pathway A starts with the preparation of a polyketone using DAP. The isostructural element of ketone K and NDIBr₂ provides the opportunity to transfer the optimized DAP conditions of the PNDIT2 synthesis to the polymerization of K and 2,2'-bithiophene. Due to a lower reactivity of K compared to NDIBr₂ further optimization of the reaction conditions was needed to get polyketones in high yield and with sufficient molecular weights over 20 kg mol⁻¹. Cyclization to the final PIDT homopolymers occurred polymer analogously *via* a polyalcohol intermediate. Depending on the choice of the lithium compound PIDTs with a Me/alkylphenyl, *n*-Bu/alkylphenyl and alkylphenyl/alkylphenyl side chain pattern can be obtained. The progress of the polymer analogous reaction sequence was monitored by IR and UV-vis spectroscopy.



Scheme I-3. Reaction pathways towards IDT homopolymers. Pathway A illustrates the polymerization of the polyketone followed by polymer analogous cyclization and pathway B shows synthesis of the IDT monomer followed by oxidative direct arylation yielding PIDT.

Preparation of Me/alkylphenyl-PIDT and alkylphenyl/alkylphenyl-PIDT afforded well-defined homopolymers, while usage of *n*-butyl lithium caused side reactions resulting in structurally ill-defined homopolymers. In general, determination and identification of defect structures by spectroscopic analyses is quite challenging for IDT-based (co)polymers. For instance, broadening and overlapping of NMR signals impede detection of defect structures (even with the use of model compounds). In pathway B, synthesis of alkylphenyl/alkylphenyl-PIDT is achieved by oxidative direct arylation polycondensation (oxDAP) of the IDT monomer. Ketone K as starting material enables the use of DA in the first reaction step. Shorter alkyl side chains lead to a solid product facilitating purification by recrystallization. The polymerization can be carried out under ambient conditions since oxygen from air serves as co-oxidant. Due to the predominant H end groups of the homopolymers it is possible to repeat polymerization of oligomer fractions or polymer chains to get higher molecular weights. PIDTs *via* oxDAP possess similar spectroscopic properties but reduced yield and two orders of magnitude lower hole mobilities than the analogue prepared by pathway A.

In chapter III the optimized conditions of pathway A are transferred to the synthesis of poly(indacenodithiophene-*alt*-benzothiadiazole) (PIDTBT) – a well-known p-type copolymer for application in OFETs and OPVs. The reaction is limited by the polymerization of the ketone with 4,7-di(thiophene-2-yl)-2,1,3-benzothiadiazole due to the low solubility of the corresponding polyketone. Only moderate M_n s of 11 kg mol⁻¹ can be obtained. The following post-polymerization sequence led to polymers with broad and bimodal molecular weight distributions pointing to structural defects which could not be eliminated by further optimization of the reactions. In contrast, PIDTBT prepared by DAP (Scheme I-4) of IDT and 4,7-dibromo-2,1,3-benzothiadiazole (BTBr₂) afforded structurally well-defined polymers in high yields and with adjustable M_n s up to 38 kg mol⁻¹. PIDTBT bearing alkylphenyl side chains on the IDT unit are amorphous with glass transition temperatures around 90 °C and field-effect



Scheme I-4. Synthesis of IDT-based copolymers by direct arylation polycondensation.

hole mobilities around $10^{-2} \text{ cm}^2 \text{ V}^{-1} \text{ s}^{-1}$. While the absorption coefficients of these copolymers are increasing with higher molar masses, thermal and electrical properties are molecular weight independent. In comparison, PIDTBT with linear alkyl side chains possess a redshifted absorption, a weak melting endotherm and an increased order in thin films as well as lower energetic disorder leading to an order of magnitude higher hole mobilities.

In the next step, DAP was used to synthesize a n-type copolymer comprised of IDT and naphthalene diimide (NDI) which is addressed in chapter IV (Scheme I-4). The polymerization is straightforward yielding P(NDI-IDT) polymers in high yields as well as high M_n s up to 113 kg mol^{-1} , despite rapid gelation of the reaction mixtures. A series of materials with different molecular weights were investigated in detail by optoelectronic, thermal, morphological and electrical characterizations and compared to the benchmark n-type polymer P(NDIT2). The polymers have a low bandgap of 1.5 eV and a broad absorption into the near-infrared region. In contrast to P(NDIT2), the optical properties of P(NDI-IDT) are almost independent of solvent, temperature as well as end groups and show a weak aggregation in solution. Due to the stronger donor strength of IDT compared to bithiophene, the absorption maxima show a bathochromic shift of 35 nm and a LUMO energy level around -3.71 eV which is slightly higher compared to P(NDIT2). In DSC, P(NDI-IDT)s show two weak endotherms which can be assigned to side chain and main chain melting. While thin film morphologies are weakly crystalline for annealing temperatures below main chain melting, thermal annealing above the main chain melting temperature is deleterious for optical, morphological and charge transfer properties. While P(NDI-IDT) polymers seem to have a low energetic disorder with one of the lowest reported Urbach energies of $(28.2 \pm 1.0) \text{ meV}$, mobilities remain in the order of $10^{-3} \text{ cm}^2 \text{ V}^{-1} \text{ s}^{-1}$ and are chain length independent in as spun and moderately annealed films. This is probably attributed to a lack of intermolecular contacts due to the bulky hexylphenyl side chains and hence insufficient intermolecular charge transport.

In chapter V, the IDT-based polymers were finally employed in all-polymer solar cells. As acceptor materials PNDIT2 and PNDIBTz were chosen. The materials show appropriately aligned energy levels as well as complementary absorption with PIDTBT and PIDTF4 (Figure I-10). The three possible blend systems PIDTBT:PNDIT2, PIDTBT:PNDIBTz and PIDTF4:PNDIT2 were incorporated into solar cells with conventional architecture (indium tin oxide (ITO)/poly(3,4-ethylenedioxythiophene):poly(styrenesulfonate) (PEDOT:PSS)/active

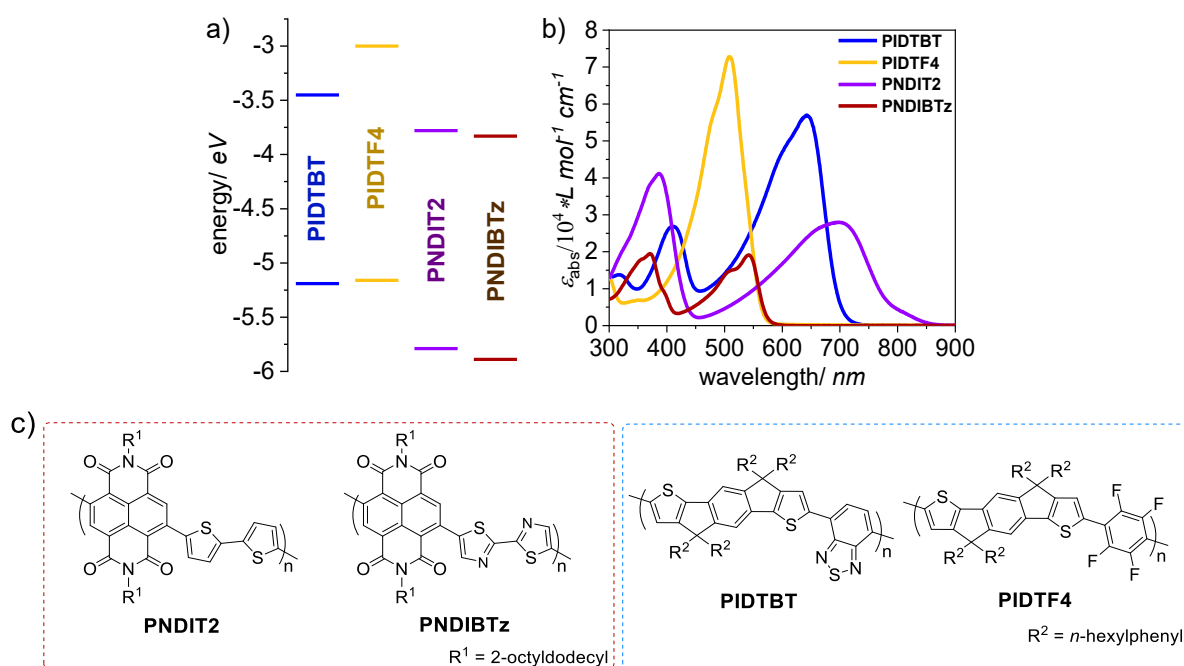


Figure I-10. Schematic energy levels (a) and absorption spectra in chloroform solution at room temperature (b) of the active materials. Chemical structures of the acceptor (PNDIT2, PNDIBTz) and donor (PIDTBT, PIDTF4) materials (c).

layer (D:A, 1:1)/Ca/Al). The first results suggest that the cell with the PIDTBT:PNDIT2 blend as active material has the greatest potential and thus, further optimization processes were focused on this system. Systematical variations of D:A ratio, processing solvent, blend concentration and molecular weight were carried out. The best performance was obtained with an 1.4:1 D:A weight ratio and a chloroform/1-chloronaphthalene mixture as processing solvent. Increasing of the blend concentration up to 12 mg mL^{-1} had a positive influence on the cell performance suggesting that even thicker films would be beneficial. In general, high V_{oc} up to 0.81 V, but low J_{sc} smaller than 1 mA cm^{-2} were achieved. Further analyses revealed a maximum EQE of 17% and decent PL quenching efficiencies below 70%. Overall, despite the complementary absorption and appropriate energy levels of donor and acceptor materials devices with power conversion efficiencies of maximum 0.2% could be obtained. All results point to a poor blend film morphology that could not be significantly improved by the attempted optimization processes. Particular, the low J_{sc} values indicate large domain sizes originating from strong demixing of the donor and acceptor polymer and result in inefficient charge generation and transport.

3. References

- (1) Y. J. Wang and G. Yu, *J. Polym. Sci. Part B Polym. Phys.*, 2019, **57**, 1557–1558.
- (2) J. de Mello, J. Anthony and S. Lee, *ChemPhysChem*, 2015, **16**, 1099–1100.
- (3) R. M. Pankow and B. C. Thompson, *Polymer*, 2020, **207**, 122874.
- (4) S. C. Rasmussen, *ChemPlusChem*, 2020, **85**, 1412–1429.
- (5) A. Facchetti, *Chem. Mater.*, 2011, **23**, 733–758.
- (6) J. L. Brédas, B. Thémans, J. G. Fripiat, J. M. André and R. R. Chance, *Phys. Rev. B*, 1984, **29**, 6761–6773.
- (7) J. L. Brédas, G. B. Street, B. Thémans and J. M. André, *J. Chem. Phys.*, 1985, **83**, 1323–1329.
- (8) W. Brütting, Ed., *Physics of organic semiconductors*, Wiley-VCH-Verl, Weinheim, 1. ed., 2. reprint., 2008.
- (9) C. K. Chiang, C. R. Fincher, Y. W. Park, A. J. Heeger, H. Shirakawa, E. J. Louis, S. C. Gau and A. G. MacDiarmid, *Phys. Rev. Lett.*, 1977, **39**, 1098–1101.
- (10) A. G. MacDiarmid, *Curr. Appl. Phys.*, 2001, **1**, 269–279.
- (11) A. J. Heeger, *J. Phys. Chem. B*, 2001, **105**, 8475–8491.
- (12) H. Shirakawa, *Angew. Chem. Int. Ed.*, 2001, **40**, 2574–2580.
- (13) K. Takimiya, I. Osaka and M. Nakano, *Chem. Mater.*, 2014, **26**, 587–593.
- (14) M. Goel, C. D. Heinrich, G. Krauss and M. Thelakkat, *Macromol. Rapid Commun.*, 2019, **40**, 1800915.
- (15) N. Zaquen, L. Lutsen, D. Vanderzande and T. Junkers, *Polym. Chem.*, 2016, **7**, 1355–1367.
- (16) T. Junkers, J. Vandenbergh, P. Adriaenssens, L. Lutsen and D. Vanderzande, *Polym Chem*, 2012, **3**, 275–285.
- (17) T. P. Kaloni, P. K. Giesbrecht, G. Schreckenbach and M. S. Freund, *Chem. Mater.*, 2017, **29**, 10248–10283.
- (18) S. Agbolaghi and S. Zenoozi, *Org. Electron.*, 2017, **51**, 362–403.
- (19) S. Holliday, Y. Li and C. K. Luscombe, *Prog. Polym. Sci.*, 2017, **70**, 34–51.
- (20) Y. Huang, D. L. Elder, A. L. Kwiram, S. A. Jenekhe, A. K. Y. Jen, L. R. Dalton and C. K. Luscombe, *Adv. Mater.*, 2019, 1904239.
- (21) M. C. Scharber and N. S. Sariciftci, *Adv. Mater. Technol.*, 2021, **6**, 2000857.
- (22) T. Marszalek, M. Li and W. Pisula, *Chem. Commun.*, 2016, **52**, 10938–10947.
- (23) Y. Lu, Z. Yu, R. Zhang, Z. Yao, H. You, L. Jiang, H. Un, B. Dong, M. Xiong, J. Wang and J. Pei, *Angew. Chem. Int. Ed.*, 2019, **58**, 11390–11394.
- (24) D. Nava, Y. Shin, M. Massetti, X. Jiao, T. Biskup, M. S. Jagadeesh, A. Calloni, L. Duò, G. Lanzani, C. R. McNeill, M. Sommer and M. Caironi, *ACS Appl. Energy Mater.*, 2018, **1**, 4626–4634.

-
- (25) L. Pandey, C. Risko, J. E. Norton and J.-L. Brédas, *Macromolecules*, 2012, **45**, 6405–6414.
- (26) C. Duan, F. Huang and Y. Cao, *J. Mater. Chem.*, 2012, **22**, 10416.
- (27) A. F. Paterson, S. Singh, K. J. Fallon, T. Hodsden, Y. Han, B. C. Schroeder, H. Bronstein, M. Heeney, I. McCulloch and T. D. Anthopoulos, *Adv. Mater.*, 2018, **30**, 1801079.
- (28) Z. A. Lamport, K. J. Barth, H. Lee, E. Gann, S. Engmann, H. Chen, M. Guthold, I. McCulloch, J. E. Anthony, L. J. Richter, D. M. DeLongchamp and O. D. Jurchescu, *Nat. Commun.*, 2018, **9**, 5130.
- (29) H.-R. Tseng, H. Phan, C. Luo, M. Wang, L. A. Perez, S. N. Patel, L. Ying, E. J. Kramer, T.-Q. Nguyen, G. C. Bazan and A. J. Heeger, *Adv. Mater.*, 2014, **26**, 2993–2998.
- (30) C. Wang, H. Dong, W. Hu, Y. Liu and D. Zhu, *Chem. Rev.*, 2012, **112**, 2208–2267.
- (31) J. Yang, Z. Zhao, S. Wang, Y. Guo and Y. Liu, *Chem*, 2018, **4**, 2748–2785.
- (32) L. Dou, J. You, Z. Hong, Z. Xu, G. Li, R. A. Street and Y. Yang, *Adv. Mater.*, 2013, **25**, 6642–6671.
- (33) Z. Genene, W. Mammo, E. Wang and M. R. Andersson, *Adv. Mater.*, 2019, **31**, 1807275.
- (34) C. Lee, S. Lee, G.-U. Kim, W. Lee and B. J. Kim, *Chem. Rev.*, 2019, **119**, 8028–8086.
- (35) M. Kim, S. U. Ryu, S. A. Park, K. Choi, T. Kim, D. Chung and T. Park, *Adv. Funct. Mater.*, 2019, 1904545.
- (36) S. Riera-Galindo, F. Leonardi, R. Pfattner and M. Mas-Torrent, *Adv. Mater. Technol.*, 2019, **4**, 1900104.
- (37) Z. A. Lamport, H. F. Haneef, S. Anand, M. Waldrip and O. D. Jurchescu, *J. Appl. Phys.*, 2018, **124**, 071101.
- (38) H. Chen, W. Zhang, M. Li, G. He and X. Guo, *Chem. Rev.*, 2020, **120**, 2879–2949.
- (39) D. Natali and M. Caironi, *Adv. Mater.*, 2012, **24**, 1357–1387.
- (40) S. Kola, J. Sinha and H. E. Katz, *J. Polym. Sci. Part B Polym. Phys.*, 2012, **50**, 1090–1120.
- (41) C. R. Newman, C. D. Frisbie, D. A. da Silva Filho, J.-L. Brédas, P. C. Ewbank and K. R. Mann, *Chem. Mater.*, 2004, **16**, 4436–4451.
- (42) A. P. Dhondge, Y.-X. Huang, T. Lin, Y.-H. Hsu, S.-L. Tseng, Y.-C. Chang, H. J. H. Chen and M.-Y. Kuo, *J. Org. Chem.*, 2019, **84**, 14061–14068.
- (43) T. Mukhopadhyay, B. Puttaraju, S. P. Senanayak, A. Sadhanala, R. Friend, H. A. Faber, T. D. Anthopoulos, U. Salzner, A. Meyer and S. Patil, *ACS Appl. Mater. Interfaces*, 2016, **8**, 25415–25427.
- (44) Y. Gao, J. Bai, Y. Sui, Y. Han, Y. Deng, H. Tian, Y. Geng and F. Wang, *Macromolecules*, 2018, **51**, 8752–8760.

- (45) X. Zhang, H. Bronstein, A. J. Kronemeijer, J. Smith, Y. Kim, R. J. Kline, L. J. Richter, T. D. Anthopoulos, H. Sirringhaus, K. Song, M. Heeney, W. Zhang, I. McCulloch and D. M. DeLongchamp, *Nat. Commun.*, 2013, **4**, 2238.
- (46) A. Wadsworth, H. Chen, K. J. Thorley, C. Cendra, M. Nikolka, H. Bristow, M. Moser, A. Salleo, T. D. Anthopoulos, H. Sirringhaus and I. McCulloch, *J. Am. Chem. Soc.*, 2020, **142**, 652–664.
- (47) R. Kim, P. S. K. Amegadze, I. Kang, H.-J. Yun, Y.-Y. Noh, S.-K. Kwon and Y.-H. Kim, *Adv. Funct. Mater.*, 2013, **23**, 5719–5727.
- (48) R. Matsidik, A. Luzio, Ö. Askin, D. Fazzi, A. Sepe, U. Steiner, H. Komber, M. Caironi and M. Sommer, *Chem. Mater.*, 2017, **29**, 5473–5483.
- (49) M. Wang, M. J. Ford, C. Zhou, M. Seifrid, T.-Q. Nguyen and G. C. Bazan, *J. Am. Chem. Soc.*, 2017, **139**, 17624–17631.
- (50) M. Khatib, T.-P. Huynh, J. J. Sun, T. T. Do, P. Sonar, F. Hinkel, K. Müllen and H. Haick, *Adv. Funct. Mater.*, 2019, **29**, 1808188.
- (51) P. Samorì and V. Palermo, *Flexible carbon-based electronics. Volume 3*, 2018.
- (52) S. Fratini, M. Nikolka, A. Salleo, G. Schweicher and H. Sirringhaus, *Nat. Mater.*, 2020, **19**, 491–502.
- (53) A. Salleo, *Mater. Today*, 2007, **10**, 38–45.
- (54) D. Venkateshvaran, M. Nikolka, A. Sadhanala, V. Lemaire, M. Zelazny, M. Kepa, M. Hurhangee, A. J. Kronemeijer, V. Pecunia, I. Nasrallah, I. Romanov, K. Broch, I. McCulloch, D. Emin, Y. Olivier, J. Cornil, D. Beljonne and H. Sirringhaus, *Nature*, 2014, **515**, 384–388.
- (55) R. Noriega, J. Rivnay, K. Vandewal, F. P. V. Koch, N. Stingelin, P. Smith, M. F. Toney and A. Salleo, *Nat. Mater.*, 2013, **12**, 1038–1044.
- (56) W. Zhang, J. Smith, S. E. Watkins, R. Gysel, M. McGehee, A. Salleo, J. Kirkpatrick, S. Ashraf, T. Anthopoulos, M. Heeney and I. McCulloch, *J. Am. Chem. Soc.*, 2010, **132**, 11437–11439.
- (57) J.-H. Dou, Y.-Q. Zheng, T. Lei, S.-D. Zhang, Z. Wang, W.-B. Zhang, J.-Y. Wang and J. Pei, *Adv. Funct. Mater.*, 2014, **24**, 6270–6278.
- (58) J. Li, Y. Zhao, H. S. Tan, Y. Guo, C.-A. Di, G. Yu, Y. Liu, M. Lin, S. H. Lim, Y. Zhou, H. Su and B. S. Ong, *Sci. Rep.*, 2012, **2**, 754.
- (59) C. W. Tang, *Appl. Phys. Lett.*, 1986, **48**, 183–185.
- (60) G. Zhang, J. Zhao, P. C. Y. Chow, K. Jiang, J. Zhang, Z. Zhu, J. Zhang, F. Huang and H. Yan, *Chem. Rev.*, 2018, **118**, 3447–3507.
- (61) H. Kim, S. Nam, J. Jeong, S. Lee, J. Seo, H. Han and Y. Kim, *Korean J. Chem. Eng.*, 2014, **31**, 1095–1104.
- (62) Y. Li, *Acc. Chem. Res.*, 2012, **45**, 723–733.
- (63) Z. Zhang, J. Yuan, Q. Wei and Y. Zou, *Front. Chem.*, 2018, **6**, 414.

-
- (64) N. Zhou and A. Facchetti, *Mater. Today*, 2018, **21**, 377–390.
- (65) K. Anagnostou, M. M. Stylianakis, K. Petridis and E. Kymakis, *Energies*, 2019, **12**, 2188.
- (66) G. Wang, F. S. Melkonyan, A. Facchetti and T. J. Marks, *Angew. Chem. Int. Ed.*, 2019, **58**, 4129–4142.
- (67) T. Tadesse, *J. Phys. Chem. Biophys.*, 2018, **08**, 1–6.
- (68) V. A., S.-W. Liu and K.-T. Wong, *Mater. Sci. Eng. R Rep.*, 2018, **124**, 1–57.
- (69) W. Yang, Y. Yao, P. Guo, H. Sun and Y. Luo, *Phys. Chem. Chem. Phys.*, 2018, **20**, 29866–29875.
- (70) C. R. McNeill, *Energy Environ. Sci.*, 2012, **5**, 5653.
- (71) J. Zhao, Y. Li, G. Yang, K. Jiang, H. Lin, H. Ade, W. Ma and H. Yan, *Nat. Energy*, 2016, **1**, 15027.
- (72) G. Zhang, K. Zhang, Q. Yin, X.-F. Jiang, Z. Wang, J. Xin, W. Ma, H. Yan, F. Huang and Y. Cao, *J. Am. Chem. Soc.*, 2017, **139**, 2387–2395.
- (73) H. Kang, W. Lee, J. Oh, T. Kim, C. Lee and B. J. Kim, *Acc. Chem. Res.*, 2016, **49**, 2424–2434.
- (74) W. Zhao, S. Li, H. Yao, S. Zhang, Y. Zhang, B. Yang and J. Hou, *J. Am. Chem. Soc.*, 2017, **139**, 7148–7151.
- (75) A. Wadsworth, M. Moser, A. Marks, M. S. Little, N. Gasparini, C. J. Brabec, D. Baran and I. McCulloch, *Chem. Soc. Rev.*, 2019, **48**, 1596–1625.
- (76) X. Xu, K. Feng, Z. Bi, W. Ma, G. Zhang and Q. Peng, *Adv. Mater.*, 2019, **31**, 1901872.
- (77) B. Fan, D. Zhang, M. Li, W. Zhong, Z. Zeng, L. Ying, F. Huang and Y. Cao, *Sci. China Chem.*, 2019, **62**, 746–752.
- (78) H. Sun, X. Guo and A. Facchetti, *Chem*, 2020, **6**, 1310–1326.
- (79) J. Choi, W. Kim, S. Kim, T.-S. Kim and B. J. Kim, *Chem. Mater.*, 2019, **31**, 9057–9069.
- (80) B. Fan, L. Ying, P. Zhu, F. Pan, F. Liu, J. Chen, F. Huang and Y. Cao, *Adv. Mater.*, 2017, **29**, 1703906.
- (81) L. Zhu, W. Zhong, C. Qiu, B. Lyu, Z. Zhou, M. Zhang, J. Song, J. Xu, J. Wang, J. Ali, W. Feng, Z. Shi, X. Gu, L. Ying, Y. Zhang and F. Liu, *Adv. Mater.*, 2019, **31**, 1902899.
- (82) Z. Li, L. Ying, P. Zhu, W. Zhong, N. Li, F. Liu, F. Huang and Y. Cao, *Energy Environ. Sci.*, 2019, **12**, 157–163.
- (83) N. Zhou, A. S. Dudnik, T. I. N. G. Li, E. F. Manley, T. J. Aldrich, P. Guo, H.-C. Liao, Z. Chen, L. X. Chen, R. P. H. Chang, A. Facchetti, M. Olvera de la Cruz and T. J. Marks, *J. Am. Chem. Soc.*, 2016, **138**, 1240–1251.
- (84) K. D. Deshmukh, R. Matsidik, S. K. K. Prasad, L. A. Connal, A. C. Y. Liu, E. Gann, L. Thomsen, J. M. Hodgkiss, M. Sommer and C. R. McNeill, *Adv. Funct. Mater.*, 2018, **28**, 1707185.

- (85) H. Kang, M. A. Uddin, C. Lee, K.-H. Kim, T. L. Nguyen, W. Lee, Y. Li, C. Wang, H. Y. Woo and B. J. Kim, *J. Am. Chem. Soc.*, 2015, **137**, 2359–2365.
- (86) P. Schilinsky, U. Asawapirom, U. Scherf, M. Biele and C. J. Brabec, *Chem. Mater.*, 2005, **17**, 2175–2180.
- (87) J. T. Ly, E. K. Burnett, S. Thomas, A. Aljarb, Y. Liu, S. Park, S. Rosa, Y. Yi, H. Lee, T. Emrick, T. P. Russell, J.-L. Brédas and A. L. Briseno, *ACS Appl. Mater. Interfaces*, 2018, **10**, 40070–40077.
- (88) H. You, D. Kim, H.-H. Cho, C. Lee, S. Chong, N. Y. Ahn, M. Seo, J. Kim, F. S. Kim and B. J. Kim, *Adv. Funct. Mater.*, 2018, **28**, 1803613.
- (89) W. Lee, C. Lee, H. Yu, D.-J. Kim, C. Wang, H. Y. Woo, J. H. Oh and B. J. Kim, *Adv. Funct. Mater.*, 2016, **26**, 1543–1553.
- (90) J. W. Jung, J. W. Jo, C.-C. Chueh, F. Liu, W. H. Jo, T. P. Russell and A. K.-Y. Jen, *Adv. Mater.*, 2015, **27**, 3310–3317.
- (91) K. D. Deshmukh, R. Matsidik, S. K. K. Prasad, N. Chandrasekaran, A. Welford, L. A. Connal, A. C. Y. Liu, E. Gann, L. Thomsen, D. Kabra, J. M. Hodgkiss, M. Sommer and C. R. McNeill, *ACS Appl. Mater. Interfaces*, 2018, **10**, 955–969.
- (92) L. Lu, T. Zheng, Q. Wu, A. M. Schneider, D. Zhao and L. Yu, *Chem. Rev.*, 2015, **115**, 12666–12731.
- (93) M. Brinkmann, E. Gonthier, S. Bogen, K. Tremel, S. Ludwigs, M. Hufnagel and M. Sommer, *ACS Nano*, 2012, **6**, 10319–10326.
- (94) B. Xie, K. Zhang, Z. Hu, H. Fang, B. Lin, Q. Yin, B. He, S. Dong, L. Ying, W. Ma, F. Huang, H. Yan and Y. Cao, *Sol. RRL*, 2020, **4**, 1900385.
- (95) C. Lee, Y. Li, W. Lee, Y. Lee, J. Choi, T. Kim, C. Wang, E. D. Gomez, H. Y. Woo and B. J. Kim, *Macromolecules*, 2016, **49**, 5051–5058.
- (96) C. McDowell, M. Abdelsamie, M. F. Toney and G. C. Bazan, *Adv. Mater.*, 2018, **30**, 1707114.
- (97) Z. Li, W. Zhang, X. Xu, Z. Genene, D. Di Carlo Rasi, W. Mammo, A. Yartsev, M. R. Andersson, R. A. J. Janssen and E. Wang, *Adv. Energy Mater.*, 2017, **7**, 1602722.
- (98) J. Yao, B. Qiu, Z.-G. Zhang, L. Xue, R. Wang, C. Zhang, S. Chen, Q. Zhou, C. Sun, C. Yang, M. Xiao, L. Meng and Y. Li, *Nat. Commun.*, 2020, **11**, 2726.
- (99) Z.-G. Zhang, B. Qi, Z. Jin, D. Chi, Z. Qi, Y. Li and J. Wang, *Energy Environ. Sci.*, 2014, **7**, 1966.
- (100) X. Ma, W. Gao, J. Yu, Q. An, M. Zhang, Z. Hu, J. Wang, W. Tang, C. Yang and F. Zhang, *Energy Environ. Sci.*, 2018, **11**, 2134–2141.
- (101) X. Che, Y. Li, Y. Qu and S. R. Forrest, *Nat. Energy*, 2018, **3**, 422–427.
- (102) K.-T. Wong, T.-C. Chao, L.-C. Chi, Y.-Y. Chu, A. Balaiah, S.-F. Chiu, Y.-H. Liu and Y. Wang, *Org. Lett.*, 2006, **8**, 5033–5036.

-
- (103) I. McCulloch, R. S. Ashraf, L. Biniek, H. Bronstein, C. Combe, J. E. Donaghey, D. I. James, C. B. Nielsen, B. C. Schroeder and W. Zhang, *Acc. Chem. Res.*, 2012, **45**, 714–722.
- (104) Y. Li, M. Gu, Z. Pan, B. Zhang, X. Yang, J. Gu and Y. Chen, *J Mater Chem A*, 2017, **5**, 10798–10814.
- (105) C. Liang and H. Wang, *Org. Electron.*, 2017, **50**, 443–457.
- (106) R. S. Ashraf, B. C. Schroeder, H. A. Bronstein, Z. Huang, S. Thomas, R. J. Kline, C. J. Brabec, P. Rannou, T. D. Anthopoulos, J. R. Durrant and I. McCulloch, *Adv. Mater.*, 2013, **25**, 2029–2034.
- (107) S. Chen, K. C. Lee, Z.-G. Zhang, D. S. Kim, Y. Li and C. Yang, *Macromolecules*, 2016, **49**, 527–536.
- (108) C. Cui, *Front. Chem.*, 2018, **6**, 404.
- (109) H. Bai, Y. Wang, P. Cheng, J. Wang, Y. Wu, J. Hou and X. Zhan, *J. Mater. Chem. A*, 2015, **3**, 1910–1914.
- (110) Y. Lin, Z.-G. Zhang, H. Bai, J. Wang, Y. Yao, Y. Li, D. Zhu and X. Zhan, *Energy Environ. Sci.*, 2015, **8**, 610–616.
- (111) H. Lin, S. Chen, Z. Li, J. Y. L. Lai, G. Yang, T. McAfee, K. Jiang, Y. Li, Y. Liu, H. Hu, J. Zhao, W. Ma, H. Ade and H. Yan, *Adv. Mater.*, 2015, **27**, 7299–7304.
- (112) H. Yao, Y. Chen, Y. Qin, R. Yu, Y. Cui, B. Yang, S. Li, K. Zhang and J. Hou, *Adv. Mater.*, 2016, **28**, 8283–8287.
- (113) W. Zhao, D. Qian, S. Zhang, S. Li, O. Inganäs, F. Gao and J. Hou, *Adv. Mater.*, 2016, **28**, 4734–4739.
- (114) N. D. Eastham, J. L. Logsdon, E. F. Manley, T. J. Aldrich, M. J. Leonardi, G. Wang, N. E. Powers-Riggs, R. M. Young, L. X. Chen, M. R. Wasielewski, F. S. Melkonyan, R. P. H. Chang and T. J. Marks, *Adv. Mater.*, 2018, **30**, 1704263.
- (115) Y. Yang, Z.-G. Zhang, H. Bin, S. Chen, L. Gao, L. Xue, C. Yang and Y. Li, *J. Am. Chem. Soc.*, 2016, **138**, 15011–15018.
- (116) S. Feng, C. Zhang, Z. Bi, Y. Liu, P. Jiang, S. Ming, X. Xu, W. Ma and Z. Bo, *ACS Appl. Mater. Interfaces*, 2019, **11**, 3098–3106.
- (117) Z. Fei, F. D. Eisner, X. Jiao, M. Azzouzi, J. A. Röhr, Y. Han, M. Shahid, A. S. R. Chesman, C. D. Easton, C. R. McNeill, T. D. Anthopoulos, J. Nelson and M. Heeney, *Adv. Mater.*, 2018, **30**, 1705209.
- (118) Y. Lin, F. Zhao, Q. He, L. Huo, Y. Wu, T. C. Parker, W. Ma, Y. Sun, C. Wang, D. Zhu, A. J. Heeger, S. R. Marder and X. Zhan, *J. Am. Chem. Soc.*, 2016, **138**, 4955–4961.
- (119) Y. Ma, S.-C. Chen, Z. Wang, W. Ma, J. Wang, Z. Yin, C. Tang, D. Cai and Q. Zheng, *Nano Energy*, 2017, **33**, 313–324.
- (120) Y. Guo, M. Li, Y. Zhou, J. Song, Z. Bo and H. Wang, *Macromolecules*, 2017, **50**, 7984–7992.

- (121) H. Bronstein, D. S. Leem, R. Hamilton, P. Woebkenberg, S. King, W. Zhang, R. S. Ashraf, M. Heeney, T. D. Anthopoulos, J. de Mello and I. McCulloch, *Macromolecules*, 2011, **44**, 6649–6652.
- (122) Y.-X. Xu, C.-C. Chueh, H.-L. Yip, F.-Z. Ding, Y.-X. Li, C.-Z. Li, X. Li, W.-C. Chen and A. K.-Y. Jen, *Adv. Mater.*, 2012, **24**, 6356–6361.
- (123) J. J. Intemann, K. Yao, H.-L. Yip, Y.-X. Xu, Y.-X. Li, P.-W. Liang, F.-Z. Ding, X. Li and A. K.-Y. Jen, *Chem. Mater.*, 2013, **25**, 3188–3195.
- (124) Y. Zhang, J. Zou, H.-L. Yip, K.-S. Chen, D. F. Zeigler, Y. Sun and A. K.-Y. Jen, *Chem. Mater.*, 2011, **23**, 2289–2291.
- (125) Y. Gao, C. An, Z. Wang, Y. Sun, Z. Wei, F. Guo, Y. Yang, L. Zhao and Y. Zhang, *Dyes Pigments*, 2018, **154**, 164–171.
- (126) C. L. Chochos, R. Singh, V. G. Gregoriou, M. Kim, A. Katsouras, E. Serpetzoglou, I. Konidakis, E. Stratakis, K. Cho and A. Avgeropoulos, *ACS Appl. Mater. Interfaces*, 2018, **10**, 10236–10245.
- (127) X. Guo, M. Zhang, J. Tan, S. Zhang, L. Huo, W. Hu, Y. Li and J. Hou, *Adv. Mater.*, 2012, **24**, 6536–6541.
- (128) L. Xue, Y. Yang, Z.-G. Zhang, X. Dong, L. Gao, H. Bin, J. Zhang, Y. Yang and Y. Li, *J Mater Chem A*, 2016, **4**, 5810–5816.
- (129) S. Shi, P. Chen, Y. Chen, K. Feng, B. Liu, J. Chen, Q. Liao, B. Tu, J. Luo, M. Su, H. Guo, M. Kim, A. Facchetti and X. Guo, *Adv. Mater.*, 2019, **31**, 1905161.
- (130) X. Wang, H. Luo, Y. Sun, M. Zhang, X. Li, G. Yu, Y. Liu, Y. Li and H. Wang, *J. Polym. Sci. Part Polym. Chem.*, 2012, **50**, 371–377.
- (131) G. You, Q. Zhuang, L. Wang, X. Lin, D. Zou, Z. Lin, H. Zhen, W. Zhuang and Q. Ling, *Adv. Energy Mater.*, 2020, **10**, 1903146.
- (132) C. M. Benavides, P. Murto, C. L. Chochos, V. G. Gregoriou, A. Avgeropoulos, X. Xu, K. Bini, A. Sharma, M. R. Andersson, O. Schmidt, C. J. Brabec, E. Wang and S. F. Tedde, *ACS Appl. Mater. Interfaces*, 2018, **10**, 12937–12946.
- (133) Y. Li, W. K. Tatum, J. W. Onorato, Y. Zhang and C. K. Luscombe, *Macromolecules*, 2018, **51**, 6352–6358.
- (134) Y. Li, W. K. Tatum, J. W. Onorato, S. D. Barajas, Y. Y. Yang and C. K. Luscombe, *Polym Chem*, 2017, **8**, 5185–5193.
- (135) U. Scherf and K. Müllen, *Makromol Chem Rapid Commun*, 1991, 489–497.
- (136) T. W. Bünnagel, B. S. Nehls, F. Galbrecht, K. Schottler, C. J. Kudla, M. Volk, J. Pina, J. S. S. de Melo, H. D. Burrows and U. Scherf, *J. Polym. Sci. Part Polym. Chem.*, 2008, **46**, 7342–7353.
- (137) J. Pina, J. Seixas de Melo, H. D. Burrows, T. W. Bünnagel, D. Dolfen, C. J. Kudla and U. Scherf, *J. Phys. Chem. B*, 2009, **113**, 15928–15936.
- (138) M. Forster, K. O. Annan and U. Scherf, *Macromolecules*, 1999, **32**, 3159–3162.

-
- (139) S. A. Patil, U. Scherf and A. Kadashchuk, *Adv. Funct. Mater.*, 2003, **13**, 609–614.
- (140) K.-J. Kass, M. Forster and U. Scherf, *Angew. Chem. Int. Ed.*, 2016, **55**, 7816–7820.
- (141) B. Wang, M. Forster, E. Preis, H. Wang, Y. Ma and U. Scherf, *J. Polym. Sci. Part Polym. Chem.*, 2009, **47**, 5137–5143.
- (142) D. Milstein and J. K. Stille, *J. Am. Chem. Soc.*, 1978, **100**, 3636–3638.
- (143) C. Cordovilla, C. Bartolomé, J. M. Martínez-Ilarduya and P. Espinet, *ACS Catal.*, 2015, **5**, 3040–3053.
- (144) N. Miyaura and A. Suzuki, *J. Chem. Soc. Chem. Commun.*, 1979, 866.
- (145) A. D. Schlüter, *J. Polym. Sci. Part Polym. Chem.*, 2001, **39**, 1533–1556.
- (146) E. Negishi, *Bull. Chem. Soc. Jpn.*, 2007, **80**, 233–257.
- (147) V. B. Phapale and D. J. Cárdenas, *Chem. Soc. Rev.*, 2009, **38**, 1598.
- (148) K. Tamao, K. Sumitani and M. Kumada, *J. Am. Chem. Soc.*, 1972, **94**, 4374–4376.
- (149) M. M. Heravi, V. Zadsirjan, P. Hajiabbasi and H. Hamidi, *Monatshefte Für Chem. - Chem. Mon.*, 2019, **150**, 535–591.
- (150) N. Snoeij, *Toxicol. Appl. Pharmacol.*, 1985, **81**, 274–286.
- (151) L. A. Estrada, J. J. Deininger, G. D. Kamenov and J. R. Reynolds, *ACS Macro Lett.*, 2013, **2**, 869–873.
- (152) S. Kowalski, S. Allard, K. Zilberberg, T. Riedl and U. Scherf, *Prog. Polym. Sci.*, 2013, **38**, 1805–1814.
- (153) T. Bura, J. T. Blaskovits and M. Leclerc, *J. Am. Chem. Soc.*, 2016, **138**, 10056–10071.
- (154) S.-L. Suraru, J. A. Lee and C. K. Luscombe, *ACS Macro Lett.*, 2016, **5**, 724–729.
- (155) N. S. Gobalasingham and B. C. Thompson, *Prog. Polym. Sci.*, 2018, **83**, 135–201.
- (156) R. M. Pankow and B. C. Thompson, *Polym. Chem.*, 2020, **11**, 630–640.
- (157) J. Zhang, W. Chen, A. J. Rojas, E. V. Jucov, T. V. Timofeeva, T. C. Parker, S. Barlow and S. R. Marder, *J. Am. Chem. Soc.*, 2013, **135**, 16376–16379.
- (158) D. E. Ames and D. Bull, *Tetrahedron*, 1982, **38**, 383–387.
- (159) N. Nakamura, Y. Tajima and K. Sakai, *HETEROCYCLES*, 1982, **17**, 235.
- (160) L. Ackermann, *Chem. Rev.*, 2011, **111**, 1315–1345.
- (161) M. Se'vignon, J. Papillon, E. Schulz and M. Lemaire, *Tetrahedron Lett.*, 1999, **40**, 5873–5876.
- (162) J. Hassan, E. Schulz, C. Gozzi and M. Lemaire, *J. Mol. Catal. Chem.*, 2003, **195**, 125–131.
- (163) T. Jeffery, *Tetrahedron*, 1996, **52**, 10113–10130.
- (164) J.-R. Pouliot, F. Grenier, J. T. Blaskovits, S. Beaupré and M. Leclerc, *Chem. Rev.*, 2016, **116**, 14225–14274.
- (165) M. Wakioka and F. Ozawa, *Asian J. Org. Chem.*, 2018, **7**, 1206–1216.
- (166) Q. Wang, R. Takita, Y. Kikuzaki and F. Ozawa, *J. Am. Chem. Soc.*, 2010, **132**, 11420–11421.

- (167) K. Okamoto, J. Zhang, J. B. Housekeeper, S. R. Marder and C. K. Luscombe, *Macromolecules*, 2013, **46**, 8059–8078.
- (168) M. Lafrance and K. Fagnou, *J. Am. Chem. Soc.*, 2006, **128**, 16496–16497.
- (169) W. Lu, J. Kuwabara and T. Kanbara, *Macromolecules*, 2011, **44**, 1252–1255.
- (170) P. Berrouard, A. Najari, A. Pron, D. Gendron, P.-O. Morin, J.-R. Pouliot, J. Veilleux and M. Leclerc, *Angew. Chem. Int. Ed.*, 2012, **51**, 2068–2071.
- (171) R. Matsidik, H. Komber and M. Sommer, *ACS Macro Lett.*, 2015, **4**, 1346–1350.
- (172) A. E. Rudenko and B. C. Thompson, *Macromolecules*, 2015, **48**, 569–575.
- (173) A. E. Rudenko and B. C. Thompson, *J. Polym. Sci. Part Polym. Chem.*, 2015, **53**, 135–147.
- (174) A. E. Rudenko, C. A. Wiley, J. F. Tannaci and B. C. Thompson, *J. Polym. Sci. Part Polym. Chem.*, 2013, **51**, 2660–2668.
- (175) M. Wakioka, Y. Nakamura, Q. Wang and F. Ozawa, *Organometallics*, 2012, **31**, 4810–4816.
- (176) F. Lombeck, H. Komber, S. I. Gorelsky and M. Sommer, *ACS Macro Lett.*, 2014, **3**, 819–823.
- (177) R. Matsidik, H. Komber, A. Luzio, M. Caironi and M. Sommer, *J. Am. Chem. Soc.*, 2015, **137**, 6705–6711.
- (178) K. Wang, G. Wang and M. Wang, *Macromol. Rapid Commun.*, 2015, **36**, 2162–2170.
- (179) S. Broll, F. Nübling, A. Luzio, D. Lentzas, H. Komber, M. Caironi and M. Sommer, *Macromolecules*, 2015, **48**, 7481–7488.
- (180) A. Hendsbee and Y. Li, *Molecules*, 2018, **23**, 1255.
- (181) Y. Huang and C. K. Luscombe, *Chem. Rec.*, 2019, **19**, 1039–1049.
- (182) J. T. Blaskovits and M. Leclerc, *Macromol. Rapid Commun.*, 2019, **40**, 1800512.
- (183) L. Ye, A. Schmitt, R. M. Pankow and B. C. Thompson, *ACS Macro Lett.*, 2020, **9**, 1446–1451.
- (184) D. R. Stuart and K. Fagnou, *Science*, 2007, **316**, 1172–1175.
- (185) K. Masui, H. Ikegami and A. Mori, *J. Am. Chem. Soc.*, 2004, **126**, 5074–5075.
- (186) C.-Y. He, S. Fan and X. Zhang, *J. Am. Chem. Soc.*, 2010, **132**, 12850–12852.
- (187) X. C. Cambeiro, N. Ahlsten and I. Larrosa, *J. Am. Chem. Soc.*, 2015, **137**, 15636–15639.
- (188) K. Tsuchiya and K. Ogino, *Polym. J.*, 2013, **45**, 281–286.

II. Indacenodithiophene homopolymers via direct arylation: direct polycondensation versus polymer analogous reaction pathways

Desiree Adamczak,^a Hartmut Komber,^a Anna Illy,^a Alberto D. Scaccabarozzi,^c Mario Caironi,^c Michael Sommer^a

^aInstitut für Chemie, Technische Universität Chemnitz, Straße der Nationen 62, 09111 Chemnitz, Germany.

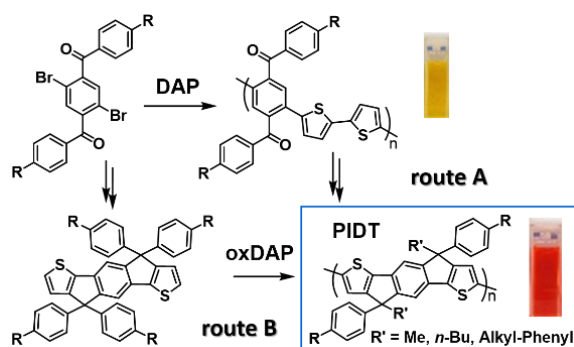
^bLeibniz Institut für Polymerforschung Dresden e. V., Hohe Straße 6, 01069 Dresden, Germany.

^cCenter for Nano Science and Technology @PoliMi, Istituto Italiano di Tecnologia, Via Pascoli 70/3, 20133 Milano, Italy.

published in *Macromolecules*, **2019**, 52 (19), 7251-7259.

Copyright © 2019 American Chemical Society

<https://doi.org/10.1021/acs.macromol.9b01269>



ABSTRACT. Indacenodithiophene (IDT)-based materials are emerging high performance conjugated polymers for use in efficient organic photovoltaics and transistors. However, their preparation generally suffers from long reaction sequences and is often accomplished using disadvantageous Stille couplings. Herein, we present detailed synthesis pathways to IDT homopolymers using C-H activation for all C-C coupling steps. Polyketones are first prepared by direct arylation polycondensation (DAP) in quantitative yield and further cyclized polymer analogously. This protocol is suitable for obtaining structurally well-defined IDT homopolymers, provided that the conditions for cyclization are chosen appropriately and that side reactions are suppressed. Moreover, this polymer analogous pathway gives rise to asymmetric side chain patterns, which allows one to fine-tune physical properties. Alternatively, IDT homopolymers can be obtained *via* oxidative direct arylation polycondensation of IDT monomers (oxDAP), leading to IDT homopolymers with similar properties but at reduced yield. Detailed characterization by NMR, IR, UV-vis and PL spectroscopy, and thermal properties, is used to guide synthesis and to explain varying field-effect transistor hole mobilities in the range of 10^{-6} - 10^{-3} $\text{cm}^2 \text{V}^{-1} \text{s}^{-1}$.

INTRODUCTION

In recent years indacenodithiophene (IDT)-based materials have been investigated extensively.¹⁻³ Both small molecules⁴⁻⁷ and copolymers^{1,8-11} have demonstrated high performance when used as active materials in organic photovoltaic (OPV)¹² devices and organic field-effect transistors (OFETs)¹¹. The ladder-type five membered IDT moiety features desirable and easily tunable properties such as an extended π -conjugated system, an optimal balance of electron density and a quaternary bridging carbon atom that ensures planarity and carries different side groups for solubility and film morphology.^{1,2} This coplanarity and the low energetic disorder of the electron rich fused ring aromatic structure favors π -electron delocalization and charge transport.^{2,8,13-16} The attachment of side groups ensures high solubility for processing OPV^{17,18} and OFET devices^{5,8} from solution. Due to the major success of IDT-based materials, derivatization including backbone extension^{19,20}, different bridging atoms^{21,22} and side chain variation^{23,24} has been carried out.

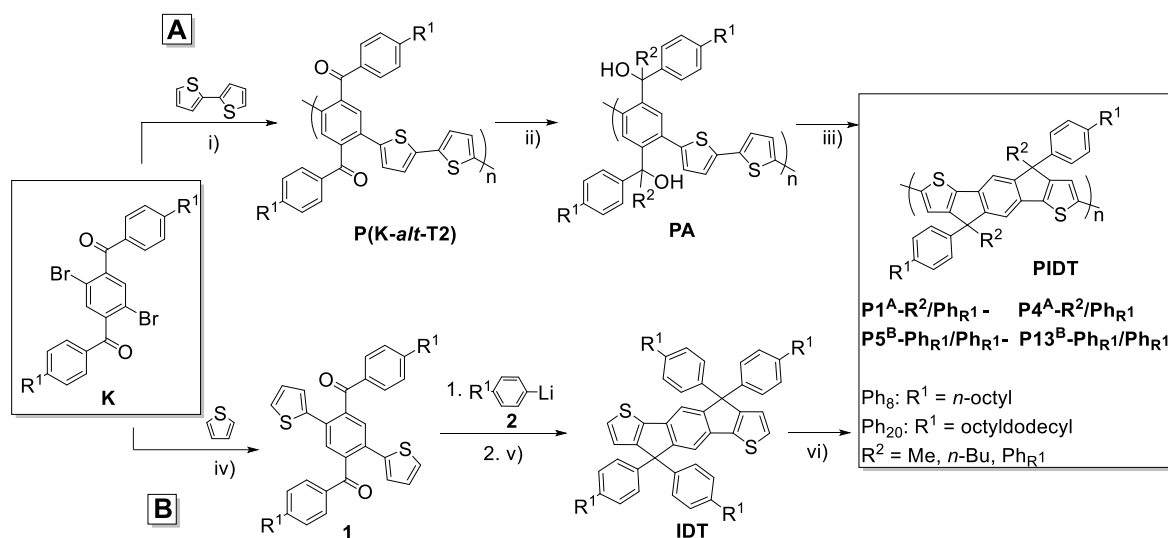
Despite their success in terms of device performance, IDT-based materials generally suffer from tedious synthesis pathways. Several attempts to optimize the synthetic procedure aimed at minimizing and improving the reaction steps of monomer synthesis.²⁵⁻²⁷ The methods of choice involve traditional transition-metal-catalyzed cross couplings such as Stille, Suzuki and

Negishi reactions.^{9,28,29} Despite being commonly established, each of these variants has major disadvantages. For instance, Stille couplings produce toxic reagents and by-products and require additional purification steps. Negishi couplings used for IDT monomer synthesis rely on organometallic reagents of limited stability, and render the already lengthy reaction sequence towards IDT copolymers unnecessarily lengthy. C-H activation, also referred to as direct arylation (DA), is an atom-economically, highly attractive alternative.^{30–32} The usage of simple C-H building blocks as monomers for direct arylation polycondensation (DAP) to furnish conjugated polymers brings about a reduced number of synthetic steps, streamlined protocols and opens up unprecedented possibilities in terms of molecular weight control.^{31,33–37} While initially rather inefficient, recent protocols for high-yielding reactions that can be conducted at low catalyst loadings became available. To date, few IDT monomers have been used in DAP protocols.^{8,25,35} However, IDT monomer synthesis still involves Stille or Negishi cross couplings. Furthermore, side reactions such as homocouplings are possible for IDT monomers used in DAP-based copolymerization.^{8,25,35} Particularly for the case of IDT copolymers, the identification and characterization of generally ubiquitous homocouplings is very challenging due to limited information contained in broad NMR signals.²⁵

Herein, we report on synthetic pathways to IDT-based polymers in which all backbone C-C coupling steps are achieved *via* DA. First, alternating copolymers **P(K-*alt*-T2)** comprising a symmetric, ketone-functionalized phenylene monomer (**K**) and 2,2'-bithiophene (**T2**) are synthesized *via* DAP in quantitative yield. Polymer analogous reductions to the polyalcohol (**PA**) and finally cyclization sequences are optimized and characterized in detail. At the same time, this method gives access to asymmetric substitution patterns at the bridging sp³ carbon of the IDT unit, which may allow for tuning fundamental properties such as glass transition temperature (T_g), solubility as well as interchain interactions in pristine films and binary blends. The characteristics of these IDT polymers are finally compared to analogues made *via* oxidative direct C-H arylation polycondensation (oxDAP) of the IDT monomer.

RESULTS AND DISCUSSION

Material synthesis and characterization. The two synthetic routes towards IDT-based polymers are shown in Scheme II-1. In the nomenclature of the polymers, A and B refer to polymer analogous cyclization and oxDAP, respectively.



Scheme II-1. Synthetic routes towards **PIDT**. Route A: polymer analogous synthesis; Route B: synthesis of **IDT** monomer followed by polymerization via oxDAP. Reaction conditions: (i) Pd_2dba_3 (1 mol%), $P(o\text{-anisyl})_3$ (5 mol%), $PivOH$ (1 eq), K_2CO_3 (3 eq), mesitylene (0.25 M), 100 °C, 72 h; (ii) R^2 -Li (8 eq), toluene ($4 \cdot 10^{-3}$ M), r.t., 3 h; (iii) $BF_3 \cdot OEt_2$ (18 eq), dichloromethane ($4 \cdot 10^{-3}$ M), r.t., 3 h; (iv) PCy_3 Pd G2 (5 mol%), $PivOH$ (1 eq), K_2CO_3 (3 eq), tetrahydrofuran (0.2 M), 100 °C; (v) octane/AcOH (1:1, v/v, 0.02 M), H_2SO_4 , 125 °C, 0.5 h, (vi) $Pd(OAc)_2$ (10 mol%), $Cu(OAc)_2$ (2.1 eq), K_2CO_3 (2.2 eq), DMAc (0.1 M), 110 °C, 72 h, air.

Copolymerization of **K** with 2,2'-bithiophene was first approached using the extraordinarily clean DAP conditions developed by Matsidik *et al.*³⁷ First, polymerizations starting from *n*-octyl-substituted **K** led to polyketones with low solubility unsuitable for polymer analogous reactions. Instead, R^1 = 2-octyldodecyl was used, leading to larger molar mass and reaction yield. Due to the isostructural properties of **K** and 2,6-dibromonaphthalene diimide (NDIBr₂)³⁷, we envisioned transfer of these conditions for the synthesis of **P(K-alt-T2)** to occur without major optimization. However, to get **P(K-alt-T2)** in high yield, optimization of monomer concentration, temperature and catalyst/ligand loading was required, apparently due to a lower reactivity of **K** compared to NDIBr₂ (Table II-1). Under optimized conditions, polyketones with molar masses $M_{n,SEC}$ up to 21 kg mol⁻¹ were obtained quantitatively. Details of ¹H and ¹³C NMR analyses are reported in the Supporting Information (Figure II-S1). The resulting polymers are highly soluble in common solvents as required for polymer analogous reactions. Polymers **P1^A-Me/Ph₂₀**, **P2^A-Bu/Ph₂₀**, **P3^A-Ph₂₀/Ph₂₀** were finally synthesized as described by Scherf *et al.*²⁷ To obtain a clean reaction, the literature protocol had to be modified. Increased concentration and a reduced amount of the corresponding lithium organyls as well as reaction time afford **PIDT P1^A-Me/Ph₂₀**, **P2^A-Bu/Ph₂₀**, **P3^A-Ph₂₀/Ph₂₀** in 60-80% yield. The use of methyl lithium

and *n*-butyl lithium led to an asymmetric substitution pattern in the corresponding homopolymers **P1^A-Me/Ph₂₀** and **P2^A-Bu/Ph₂₀**. Symmetric substitution could be achieved by transforming the synthesized 1-bromo-4-(2-octyldodecyl) benzene into the lithium analogue with *n*-butyl lithium.

Table II-1. Summary of reaction conditions for the syntheses of **P(K-alt-T2)** via direct arylation polycondensation.^a

entry	R ¹	solv	time ^b /h	conc/M	T/°C	Pd ₂ dba ₃ /mol%	P-(<i>o</i> -anisyl) ₃ /mol%	M _n /M _w ^c /kg mol ⁻¹	Đ ^c	yield ^d /%
1	C8	Tol	72	0.5	100	1	-	6/11	1.8	33
2	C8	Tol	14	0.5	100	1	-	6/8	1.3	9
3	C8	Tol	72	0.5	90	1	-	6/9	1.6	52
4	C8	Tol	72	0.25	100	1	-	4/5	1.2	21
5	C8	Tol	72	0.25	90	1	-	7/9	1.3	32
6	C8	Mes	24	0.5	100	1	-	6/8	1.4	34
7	C8	Mes	24	0.25	100	1	-	10/15	1.5	18
8 ^e	C8	Mes	72	0.5	90	1	-	-	-	-
9	C8	Mes	72	0.5	120	1	-	7/11	1.6	34
10	C8	Mes	24	0.5	100	1	5	6/8	1.4	52
11	C8	Mes	72	0.4	100	1	5	6/9	1.4	52
12	C8	Mes	72	0.3	100	1	5	7/8	1.2	48
13	C8	Mes	2	0.25	100	1	5	8/11	1.4	44
14	C8	Mes	72	0.4	90	1	5	7/8	1.3	59
15	C8	Mes	72	0.4	90	5	20	8/10	1.4	30
16	C8C12	Mes	72	0.25	100	1	5	21/36	1.7	91
17	C8C12	Mes	72	0.25	90	1	5	16/26	1.6	99
18	C8C12	Mes	72	0.5	100	1	5	16/18	1.6	97
19	C8C12	Mes	72	0.25	100	1	5	15/19	1.3	77
20 ^{e,f}	C8C12	Mes	72	0.25	100	1	5	-	-	-
21 ^e	C8C12	Mes	72	0.25	100	1	-	-	-	-

^a1 eq PivOH and 3 eq K₂CO₃ were used in all entries. Tol and Mes are toluene and mesitylene, respectively. ^bReduced reaction time in case of gelation. ^cFrom size-exclusion chromatography (SEC) in THF. ^dIsolated yield after Soxhlet extraction. ^eNo chloroform fraction after Soxhlet extraction. ^fSlight excess (5 mol%) of ketone **K-Ph₂₀** was used.

The progress of the post-polymerization sequence was monitored by IR and NMR spectroscopy. The reduction of the carbonyl group in the first reaction step can be well proved by disappearance of the stretching band at 1603 cm^{-1} and 1665 cm^{-1} (Figure II-1). In case of the butyl derivative **P2^A-Bu/Ph₂₀**, the IR spectrum shows unreacted carbonyl groups (Figure II-1b, marked wavenumber range). A possible explanation is the higher reactivity of *n*-BuLi compared to, for example, MeLi, which opens up further reaction possibilities for the former such as reaction with THF or bithiophene end groups. Therefore, the temperature and equivalents of *n*-BuLi were varied. However, neither a decreased temperature nor the use of an excess of *n*-BuLi led to an improvement. All samples of the butyl derivative showed residual carbonyl bands in the IR spectrum and also a significant hypsochromic shift of the absorbance maximum in UV-vis spectra compared to **P1^A-Me/Ph₂₀** and **P3^A-Ph₂₀/Ph₂₀** (Figure II-S2).

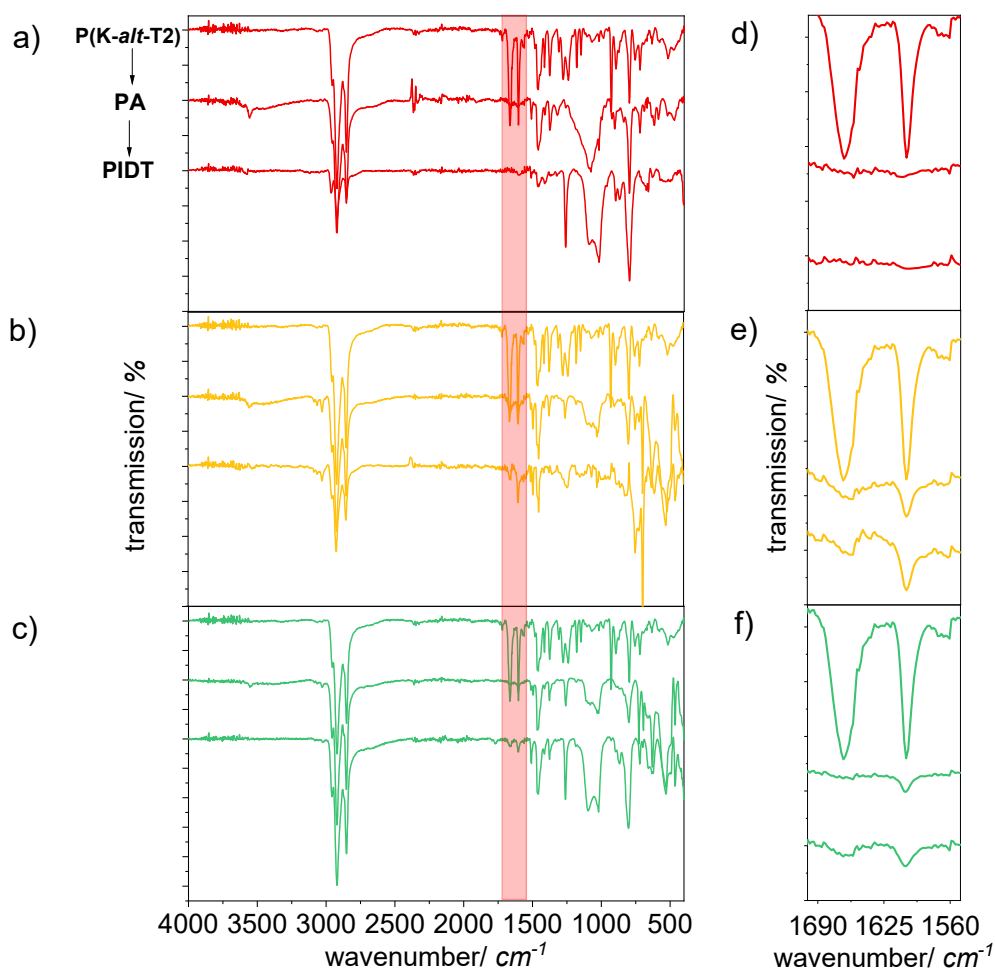


Figure II-1. IR spectra of polymer analogous conversion of **P(K-alt-T2)** to PIDTs **P1^A-Me/Ph₂₀** (a), **P2^A-Bu/Ph₂₀** (b), **P3^A-Ph₂₀/Ph₂₀** (c) including the spectra of the alcohol intermediates (PA). The region of carbonyl bands of the precursor **P(K-alt-T2)** is highlighted and enlarged in (d – f).

The SEC curves of **P1^A-Me/Ph₂₀** and **P2^A-Bu/Ph₂₀** displayed bimodal distributions and a monomodal one for **P3^A-Ph₂₀/Ph₂₀** (Figure II-S3). Bimodal distributions are commonly associated with chain-chain coupling reactions. Interestingly, despite the bimodal distribution of **P1^A-Me/Ph₂₀**, clear indications for defects were not found by other characterization methods. One possibility is oxidative chain-chain coupling of two thiophene chain ends, which may be addressed by endcapping the polyketone with bromobenzene as further described below.

Detailed NMR signal assignments of IDT copolymers are rare in the literature due to the low content of information contained in broad signals of ¹H NMR spectra. To assist in signal assignment and eventually reveal defect structures, NMR spectroscopy was aided by model compounds **8** and **9** (Supporting Information, Figure II-S4 and S5). Cyclization can be well proven by ¹³C NMR spectra, where the signal of the keto group at $\delta = 197$ ppm vanished and the quaternary carbon shows up in the 52 – 64 ppm region depending on R² (Figure II-S5). The different substitution pattern of the quaternary ring carbon (C₈) can be traced by its ¹³C chemical shift (52.7 ppm for Me/alkylphenyl (**8**) vs. 57.1 ppm for *n*-Bu/alkylphenyl (**9**) vs. 62.7 ppm for 4-alkylphenyl/4-alkylphenyl (**IDT-Ph₂₀**)). Very similar chemical shifts were observed for C₈ in **P1^A-Me/Ph₂₀** – **P3^A-Ph₂₀/Ph₂₀** proving successful cyclization (Figure II-2). For **P3^A-Ph₂₀/Ph₂₀** the appearance of a major signal at 63.1 ppm (R² = 4-(2-octyldodecyl)phenyl) and a minor signal at 57.4 ppm (R² = *n*-butyl) points to a side reaction (Figure II-2c). Because the added 4-alkylphenyl lithium was obtained from the bromide and *n*-butyl lithium without further purification, unreacted reactant led to a mixture of 4-octyldodecylphenyl and *n*-butyl substitution in the final cyclized polymer. For **P1^A-Me/Ph₂₀** and **P2^A-Bu/Ph₂₀**, four different substituents at both C₈ result in two diastereomers for the repeat unit as proved by signal splitting for model compounds **8** and **9**. Since both R² can be on the same (*R,R/S,S*-racemate) or different sides (*R,S-meso*-isomer) of the IDT π -plane, they lead to regioirregular backbone structures. Whereas the signals of the aliphatic moieties can be well observed both in the ¹H and ¹³C NMR spectra of the polymers, only **P1^A-Me/Ph₂₀** gives well resolved spectra for the IDT moiety (Figure II-S6a and S7a). The ¹H and ¹³C NMR spectrum fully confirm the desired **PIDT** structure and do not point to structural defects. However, the origin of signal broadening observed for **P2^A-Bu/Ph₂₀** and **P3^A-Ph₂₀/Ph₂₀** with bulkier R² residue is unclear. Possibly, the *n*-butyl and 4-alkylphenyl groups decrease segmental backbone motion whereas side chain motion is less influenced. Because the spin-spin relaxation times (T₂) are sensitive to changes in molecular motions they also influence linewidth ($\Delta\nu_{1/2} \sim 1/T_2$). Thus, a decreasing T₂ value

for the backbone nuclei could cause the line broadening. Apart from the broad signals, the chemical shifts are in accordance with those of **P1^A-Me/Ph₂₀**.

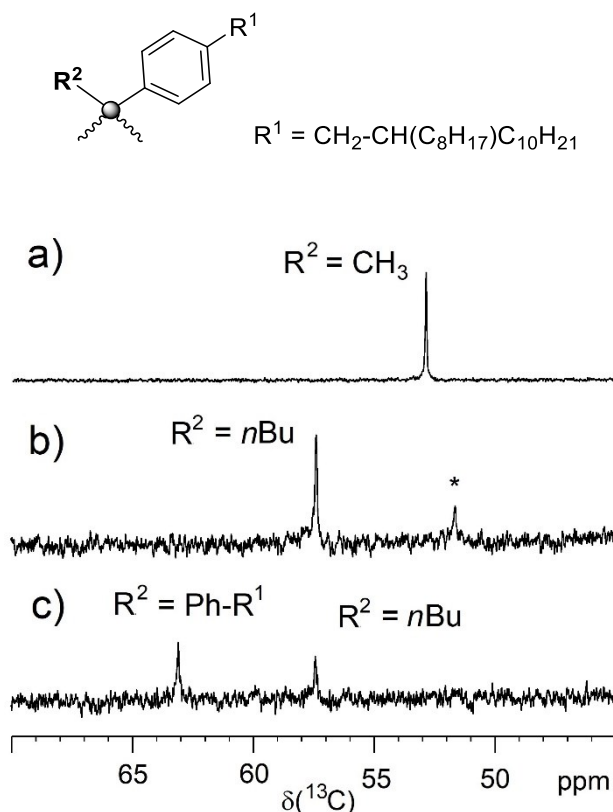


Figure II-2. Region of the quaternary carbon signal of the IDT unit of **PIDT** polymers **P1^A-Me/Ph₂₀** (a), **P2^A-Bu/Ph₂₀** (b) and **P3^A-Ph₂₀/Ph₂₀** (c) in CDCl₃. * marks an impurity.

Optical and thermal properties. The formation of the planar rigid **PIDT** structure can be followed by UV-vis spectroscopy (Figure II-3a). The changes in conformation and of the electronic properties of the polymer backbone lead to major shifts of the absorption maximum. Compared to the polyketones, the polyalcohols (**PA1^A-Me/Ph₂₀**, **PA2^A-Bu/Ph₂₀**, **PA3^A-Ph₂₀/Ph₂₀**) exhibit blue-shifted absorption bands by ~77 nm, which is caused by torsion and eventually by a diminished push-pull character of the backbone. In turn, cyclization increases conjugation and thus leads to a bathochromic effect. A closer look into the optical properties of the synthesized homopolymers exposes significant differences. First discrepancies can already be observed in the optical spectra of the polyalcohols. The absorption bands of **PA2^A-Bu/Ph₂₀** and **PA3^A-Ph₂₀/Ph₂₀** are broadened compared to **PA1^A-Me/Ph₂₀**. This behavior is also reflected in the cyclized polymers. **P1^A-Me/Ph₂₀** shows a structured absorption band with maximum at 515 nm and a well resolved vibronic side band at 544 nm (Figure II-3).

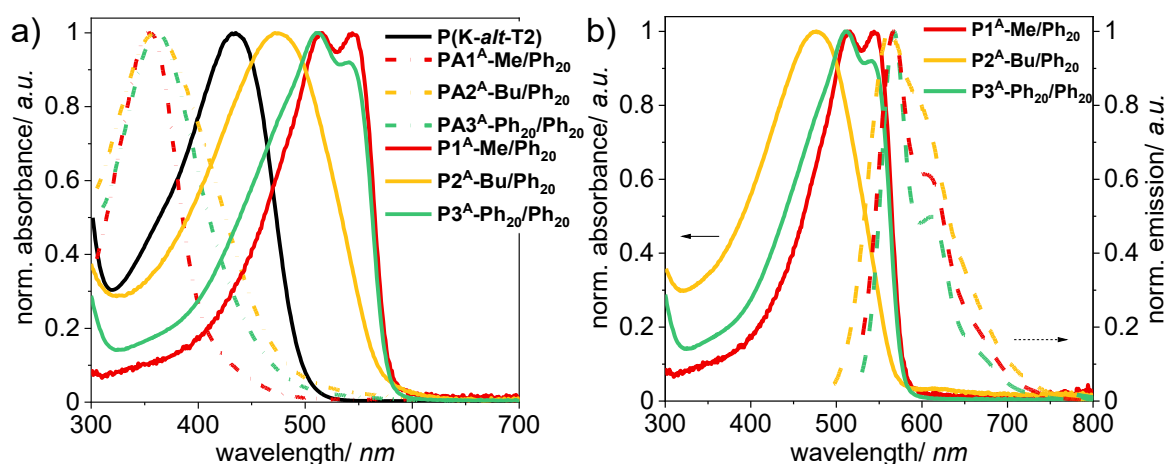


Figure II-3. Reaction control by UV-vis spectroscopy of polymer analogous conversion to **PIDTs** in CHCl_3 solution at r.t (**PA**: crude product after conversion with lithium compound) (a). Absorption and emission spectra of homopolymers in CHCl_3 solution at r.t. (b).

P3^A-Ph₂₀/Ph₂₀ displays a similar shape and absorption maximum with a slightly less distinct shoulder. The resolution of this vibronic structure - caused by the rigid structure of the IDT backbone - can also be seen in the UV-vis spectra of the model compounds **8**, **9** and **IDT-Ph₂₀**. In all cases, the absorption maximum is around 355 nm with a sharp and well resolved side band at around 374 nm (Figure II-S8). In comparison, the band of **P2^A-Bu/Ph₂₀** shows no sign of a side band. However, it is obviously broadened with a less steep absorption edge and a significantly blue-shifted maximum. The emission spectra of the model compounds **8**, **9** and **IDT-Ph₂₀** show a blue-shift of the maximum with increasing size of the second side chain R^2 (Figure II-S8). This effect cannot be observed in the emission spectra of the corresponding homopolymers **P1^A-Me/Ph₂₀**, **P3^A-Ph₂₀/Ph₂₀** and **P2^A-Bu/Ph₂₀** (Figure II-3b). In general, a band with an emission maximum around 565 nm and a shoulder at around 610 nm is visible. The shape of **P2^A-Bu/Ph₂₀** is also broadened and exhibits a bigger Stokes-shift of $\Delta\lambda_{\text{Stokes}} = 87$ nm than **P1^A-Me/Ph₂₀** and **P3^A-Ph₂₀/Ph₂₀** ($\Delta\lambda_{\text{Stokes}} \approx 55$ nm). The anomaly of **P2^A-Bu/Ph₂₀** may be caused by incomplete conversion of the carbonyl groups. A possible side reaction may be lithiation of -T2 end groups of **P(K-alt-T2)** by BuLi followed by an interchain reaction with a carbonyl group. In an attempt to prove the appearance of such defect structures, a model reaction was carried out (Scheme II-S1). The model reaction demonstrates that lithiated T2 is able to attack the carbonyl group of compound **K** leading to model compound **10** (Scheme II-S1). The structure could be verified by NMR spectroscopy (Figure II-S9). Such defects would lead to branching. In an additional control experiment, the polymer precursor **P(K-alt-T2)** was terminated with bromobenzene to eliminate -T2 end groups. The NMR

analysis of **P(K-*alt*-T2)_{term}** confirms the successful termination (Figure II-S10). During the following polymer analogous cyclization leading to **P2_{term}^A-Bu/Ph₂₀**, possible chain-chain coupling should be suppressed. However, characterization by NMR spectroscopy did not reveal significant differences compared to **P2^A-Bu/Ph₂₀** without phenyl termination (Figures II-S11 and S12). UV-vis and IR spectra display the same discrepancy as observed for **P2^A-Bu/Ph₂₀** (Figure II-S13a and S14). Only in the molecular weight distribution of **P2_{term}^A-Bu/Ph₂₀**, a high molecular weight shoulder was no longer seen (Figure II-S13b). From these results we conclude that cyclization by using BuLi is disadvantageous as side reactions, likely branching, are involved. Such side reactions would explain the hypsochromic shift in the UV-vis spectrum and also the lower solubility of **P2^A-Bu/Ph₂₀**. However, also the very electron rich T2 end groups may undergo chain-chain coupling as an additional side reaction, which can simply be detected by SEC but is hard to prove directly by NMR spectroscopy (and not at all by IR and UV-vis spectroscopy). However, such chain-chain coupling will cause quaterthiophene main-chain defects, which pose an electronic alteration to the backbone structure. This aspect will be taken up again when discussing field-effect transistor characterization.

Table II-2. Molecular weights, optical and thermal properties of synthesized polymers.

entry	monomer	R ²	<i>M_n</i> / <i>M_w</i> ^a / kg mol ⁻¹	<i>Đ</i> ^a	<i>λ</i> _{max,abs} ^b / nm	<i>λ</i> _{max,em} ^b / nm	<i>T_g</i> / °C	yield ^c / %
P(K-<i>alt</i>-T2), entry 19	K-Ph ₂₀	-	15/19	1.3	435			99
P1^A-Me/Ph₂₀	K-Ph ₂₀	Me	30/80	2.7	516/544	568/614	59	58
P2^A-Bu/Ph₂₀	K-Ph ₂₀	<i>n</i> -Bu	20/44	2.2	477	564	42	72
P3^A-Ph₂₀/Ph₂₀	K-Ph ₂₀	Ph ₂₀	18/22	2.0	510/541	567/612	65	64
P4^A-Ph₈/Ph₈^d	K-Ph ₈	Ph ₈	5/11	2.3	496	566	-	50
P11^B-Ph₂₀/Ph₂₀	IDT-Ph ₂₀	Ph ₂₀	16/18	1.1	510	568/603	59	4
P13^B-Ph₈/Ph₈	IDT-Ph ₈	Ph ₈	17/22	1.3	514/538	569/611	64	6

^aFrom SEC in THF. ^bIn CHCl₃ solution at r.t. ^cOverall yield starting from monomer **K**. Maxima with the highest intensity in italic type. ^dDue to low molecular weight and small amount of sample material, no further characterization was performed.

Polymers **P1^A-Me/Ph₂₀** and **P2^A-Bu/Ph₂₀** show good thermal stability with degradation temperatures higher than 350 °C and 250 °C, respectively (Figure II-S15). In contrast, polymer **P3^A-Ph₂₀/Ph₂₀** shows two onset temperatures. The first appears at about 100 °C with a weight loss less than 5% and the second is higher than 350 °C with a weight loss of about 15% (Figure II-S15). The thermal properties were also examined by differential scanning

calorimetry (DSC). The **PIDTs** show glass transitions in between 40 – 70 °C (Figure II-S16). Because of the quaternary carbons with asymmetric, bulky substituents ordered packing is more difficult leading to amorphous nature.^{2,19,28,29,38,39} All characteristic data are summarized in Table II-2.

IDT homopolymers via oxidative direct arylation polycondensation and comparison with polymer analogous pathway. In the second approach to IDT-based polymers, the fused monomer **IDT** was synthesized first followed by homopolymerization *via* oxidative direct arylation (oxDAP).^{39–41} As starting material for **IDT** monomer compound **K** was chosen instead of the usually used ester derivative.²⁵ Compound **1** was made *via* DA with thiophene (Scheme II-1b) in 48% yield after the optimization of catalyst/ligand, solvent and concentration. In comparison to route A, the limiting aspect of route B is not solubility but synthesis and purification of monomer **IDT**. Especially purification of **IDT-Ph₂₀** by column chromatography was challenging and accompanied by low yields. Due to the long and branched side chains, the reactivity of intermediates was lower and the final product was obtained as oil. Usage of *n*-octyl resulted in **IDT-Ph₈** being a solid, which facilitated synthesis and purification. The additional possibility of recrystallizing the product after column chromatography led to higher purity as needed for polymerization and yields of up to 53%. Due to only few literature protocols on oxDAP^{40,42,43}, optimization of catalyst loading, atmosphere and oxidant was required (Table II-3). The best results could be achieved with 20 mol% of the Pd catalyst and copper acetate as the oxidant (Table II-3, entry **P8^B-Ph₂₀/Ph₂₀**). Remarkably, no inert gas atmosphere is necessary. Hence, it can be assumed that oxygen from air may act as the co-oxidant. Nevertheless, the molecular weights achieved were low in all cases. Values comparable to route A could only be realized after repeated polymerization of an oligomer fraction under the same conditions (Table II-3, entries **P10^B-Ph₂₀/Ph₂₀/P11^B-Ph₂₀/Ph₂₀/P13^B-Ph₈/Ph₈**, Figure II-S17).

The resulting polymers were further characterized by NMR, IR, UV-vis spectroscopy, photoluminescence, thermogravimetric analysis (TGA) as well as DSC analysis and compared to their polymer analogues from route A. NMR spectra of **P11^B-Ph₂₀/Ph₂₀** are provided in the Supporting Information (Figure II-S6d and Figure II-S18a). As expected the ¹³C-NMR spectrum shows only one signal of the quaternary carbon at 63.0 ppm. In general, the chemical shifts are similar to the polymer analogous synthesized material **P3^A-Ph₂₀/Ph₂₀**. Due to the signal broadening no information about structural defects or end groups could be extracted.

Table II-3. Summary of reaction conditions and molecular weights of **PIDT** via oxDAP.^a

entry	Pd(OAc) ₂ / mol%	oxidant ^a	base ^a	atmosphere	<i>M_n</i> / <i>M_w</i> ^b / kg mol ⁻¹	<i>Đ</i> ^b	yield ^c / %
P5^B-Ph₂₀/Ph₂₀	10	Cu(OAc) ₂	K ₂ CO ₃	argon	6/7	1.2	23 ^e
P6^B-Ph₂₀/Ph₂₀	10	Cu(OAc) ₂	K ₂ CO ₃	air	8/11	1.3	31
P7^B-Ph₂₀/Ph₂₀	10	Ag ₂ CO ₃	K ₂ CO ₃	argon	7/8	1.2	12 ^e
P8^B-Ph₂₀/Ph₂₀	20	Cu(OAc) ₂	K ₂ CO ₃	air	12/15	1.2	39
P9^B-Ph₂₀/Ph₂₀^d	2	Ag ₂ CO ₃	K ₂ CO ₃ / AcOH	argon	-		-
P10^B-Ph₂₀/Ph₂₀^e	10	Cu(OAc) ₂	K ₂ CO ₃	air	24/35	1.5	22
P11^B-Ph₂₀/Ph₂₀^e	20	Cu(OAc) ₂	K ₂ CO ₃	air	16/18	1.1	40
P12^B-Ph₈/Ph₈	10	Cu(OAc) ₂	K ₂ CO ₃	air	16/29	1.8	38
P13^B-Ph₈/Ph₈^e	10	Cu(OAc) ₂	K ₂ CO ₃	air	17/22	1.3	10

^a2.1 eq oxidant, 2.2 eq additives and DMAc as solvent (0.1 M) were used in all entries. ^bFrom SEC in THF. ^cIsolated yield after Soxhlet extraction with acetone, ethyl acetate (EA) and chloroform. ^dOnly acetone-soluble material of low molecular weight (*M_n* ~ 2 kg mol⁻¹). ^ePolymerization of EA soluble fraction of **P6^B-Ph₂₀/Ph₂₀**/**P8^B-Ph₂₀/Ph₂₀** and **P12^B-Ph₈/Ph₈** under same conditions.

The IR spectra display similar characteristics in all cases (Figure II-4). The weak band between 1600 cm⁻¹ and 1700 cm⁻¹ is usually an indication of the appearance of carbonyl groups. In fact, in case of **P3^A-Ph₂₀/Ph₂₀** a C=O stretching band would be a possible explanation. Due to the polymer analogous reaction pathway (route A) the first assumption would be an incomplete ring closure with residual carbonyl groups of the precursor polymer **P(K-*alt*-T2)** being still present. However, the comparison of the IR spectra with those of the monomer **IDT-Ph₂₀** and the polymers **P11^B-Ph₂₀/Ph₂₀** and **P13^B-Ph₈/Ph₈** made *via* route B, reveals the same weak band at 1600 cm⁻¹. As carbonyl groups are not involved here, the weak band between 1600 cm⁻¹ and 1700 cm⁻¹ may alternatively caused by the two bulky aromatic side chains. Aromatic C=C stretching bands show weak signals in this region as well.⁴⁴ Therefore, we assume that in case of **P3^A-Ph₂₀/Ph₂₀** this band can also be attributed to an aromatic C=C stretching and not to C=O stretching by incomplete ring closure. In contrast, the characterization by optical methods shows significant differences (Figure II-5). In case of **P4^A-Ph₈/Ph₈** (*M_n* = 5 kg mol⁻¹) and **P13^B-Ph₈/Ph₈** (*M_n* = 17 kg mol⁻¹) the varied maxima and shapes of the spectra mainly result from different conjugation lengths with the low molecular weight of **P4^A-Ph₈/Ph₈** leading to blue-shifted absorption maximum. In contrast, **P3^A-Ph₂₀/Ph₂₀** (*M_n* = 18 kg mol⁻¹) and **P11^B-Ph₂₀/Ph₂₀** (*M_n* = 16 kg mol⁻¹) display similar optical properties. Nevertheless, **P3^A-Ph₂₀/Ph₂₀** shows a sharper and better resolved absorption as well as emission

than **P11^B-Ph₂₀/Ph₂₀**. The broadened and undefined bands of **P11^B-Ph₂₀/Ph₂₀** may be attributed to impurities caused by tedious monomer purification or structural defects.

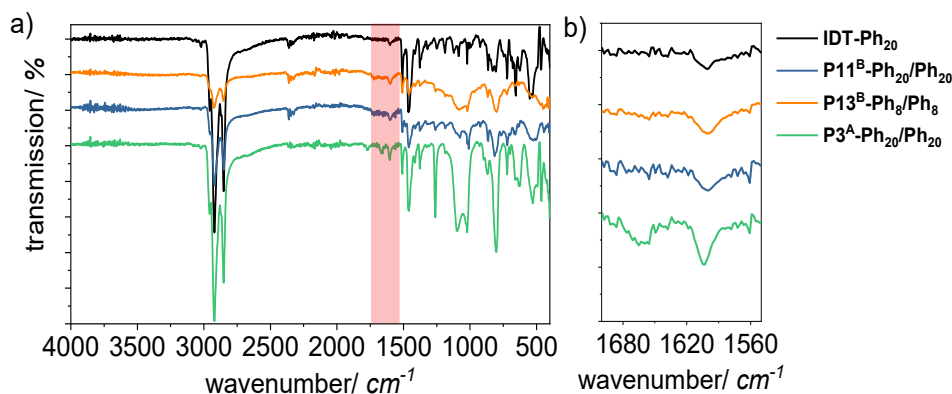


Figure II-4. a) Comparison of IR spectra of PIDTs via route A (**P3^A-Ph₂₀/Ph₂₀**) and route B (**P11^B-Ph₂₀/Ph₂₀**, **P13^B-Ph₈/Ph₈**). b) Enlarged wavenumber range of the red box.

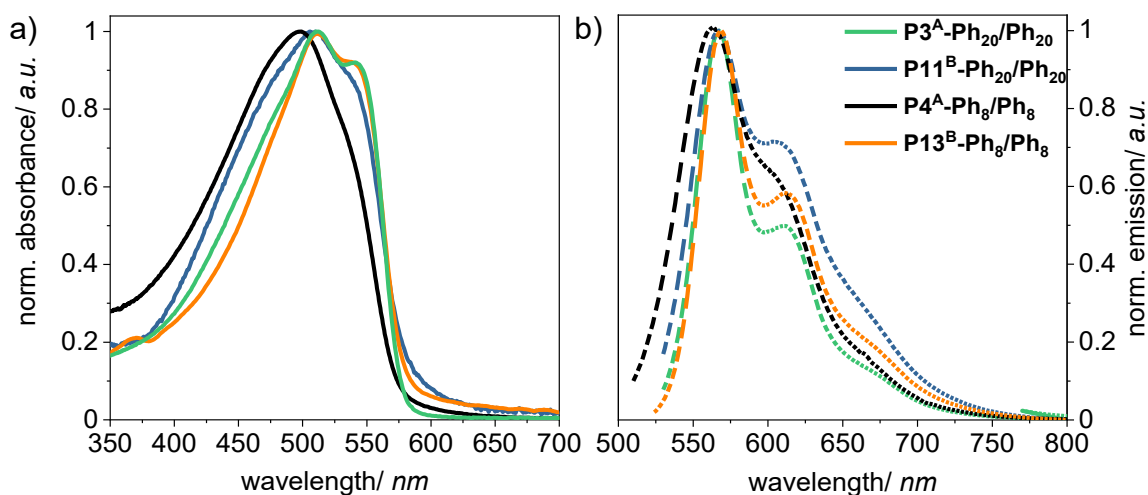


Figure II-5. Comparison of UV-vis (a) and emission spectra (b) of PIDTs via route A (**P3^A-Ph₂₀/Ph₂₀**, **P4^A-Ph₈/Ph₈**) and route B (**P11^B-Ph₂₀/Ph₂₀**, **P13^B-Ph₈/Ph₈**) in CHCl₃ solution at r.t.

This also explains the 100 °C lower degradation temperature of **P11^B-Ph₂₀/Ph₂₀** (Figure II-6). The best thermal stability shows **P13^B-Ph₈/Ph₈** with its 4-octylphenyl substitution pattern. The homopolymers were further investigated by DSC measurements. Glass-transition temperatures of **P11^B-Ph₂₀/Ph₂₀** and **P13^B-Ph₈/Ph₈** can be seen at 59 °C and 64 °C, respectively (Table II-2). As expected for the amorphous morphologies of IDT-based polymers, crystallization and melting temperatures were absent (Figure II-S16). Interestingly, the side-

group mixture of 4-octyldodecylphenyl and *n*-butyl substitution in **P3^A-Ph₂₀/Ph₂₀** has no significant influence on the optical and thermal properties.

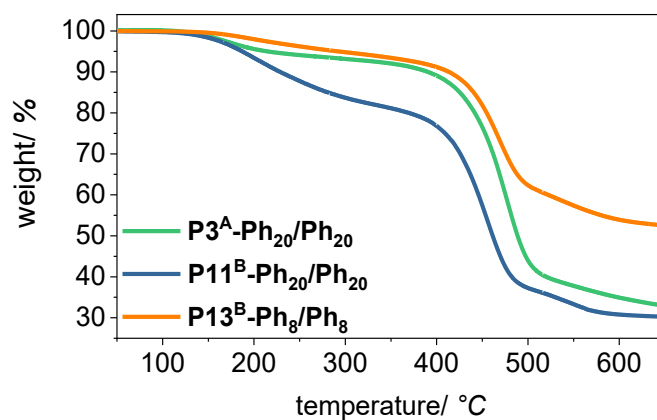


Figure II-6. Comparison of TGA thermograms of PIDTs via route A (**P3^A-Ph₂₀/Ph₂₀**) and route B (**P11^B-Ph₂₀/Ph₂₀**, **P13^B-Ph₈/Ph₈**) in N₂.

To investigate the electronic properties of the IDT copolymers made by different routes, organic field-effect transistors (OFETs) were fabricated. All devices show p-type behavior. **P1^A-Me/Ph₂₀** and **P3^A-Ph₂₀/Ph₂₀** display ideal transfer characteristics with similar source-to-drain currents and field-effect mobilities in the order of 10^{-4} - 10^{-3} cm² V⁻¹ s⁻¹. These two samples exhibit the least structural defects according to IR spectroscopy and show the most structured UV-vis absorption bands. The highest mobility of **P3^A-Ph₂₀/Ph₂₀** may further be rationalized by its monomodal SEC curve indicating the absence of chain-chain couplings. Assuming quaterthiophene main-chain defects as a result of T2 chain end coupling as the reason for the bimodal SEC curves of **P1^A-Me/Ph₂₀** and **P2^A-Bu/Ph₂₀**, this electronic main-chain defect would explain their lower electronic performance and at the same time the superior mobility of **P3^A-Ph₂₀/Ph₂₀**. Clearly, **P2^A-Bu/Ph₂₀** with clear evidence of chain-chain coupling, incomplete cyclization or branching shows only moderate current modulation and poor field-effect mobility. These spectroscopic properties of **P13^B-Ph₈/Ph₈** are comparable to the better defined samples from route A, but hole mobilities are in the 10^{-5} cm² V⁻¹ s⁻¹ range only. The origin of this discrepancy is unclear, especially considering the similar molecular weights of **P3^A-Ph₂₀/Ph₂₀** and **P13^B-Ph₈/Ph₈**. However, most of the difference comes from a much larger threshold voltage, indicating poorer injection at the dielectric-semiconductor interface. A summary of hole mobilities extracted from the saturation regime ($V_d = -60$ V) is reported in Figure II-7.

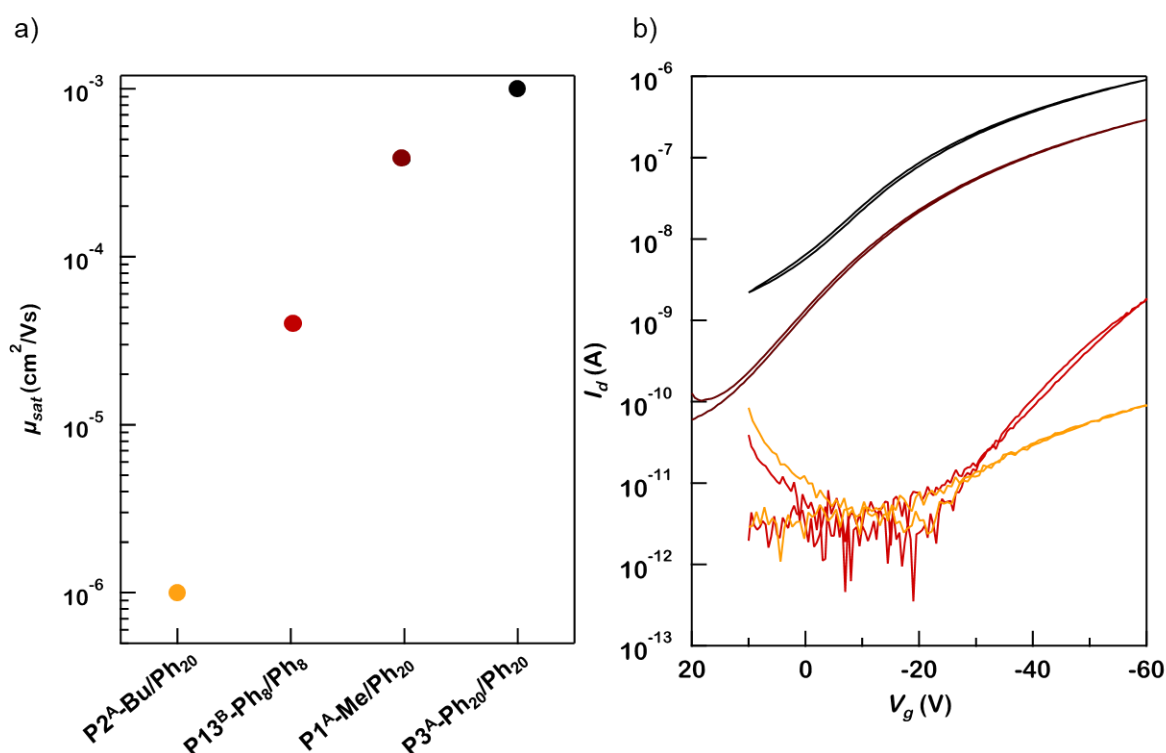


Figure II-7. Field-effect hole mobilities extracted from the saturation regime (a). Representative transfer characteristic curves measured in saturation regime, $V_d = -60$ V (b).

CONCLUSIONS

We introduced and optimized two synthetic ways to IDT-based homopolymers using exclusively C-H activation for C-C bond formation. Pathway A includes direct arylation polycondensation (DAP) for polyketone synthesis followed by reduction to the polyalcohols and cyclization. In pathway B, oxidative direct arylation polycondensation (oxDAP) is used. Using pathway A, polyketones with satisfying molecular weight up to $M_{n,\text{SEC}} = 21 \text{ kg mol}^{-1}$ were obtained in quantitative yield. Only methyl lithium and lithiated phenyl derivatives as reagents for cyclization led to complete conversion and well-defined polymers with asymmetric substitution pattern, while butyl lithium caused side reactions such as chain-chain coupling and/or branching. The ^1H and ^{13}C NMR spectra of IDT homopolymers with methyl groups exhibited significantly sharper signals, making analysis and conclusions more straightforward, despite a concomitant lower solubility. Potentially, pathway A can be transferred to thiophene-acceptor-thiophene comonomers to yield IDT copolymers that are known for their excellent performance in solar cells and field-effect transistor devices. Pathway B involving oxDAP led to IDT homopolymers of similar spectroscopic characteristics but at significantly lower yield. The best charge carrier mobilities up to $10^{-3} \text{ cm}^2 \text{ V}^{-1} \text{ s}^{-1}$ were obtained from IDT homopolymers made by pathway A and showing monomodal SEC curves. Generally, the determination of structural

defects with high precision is most challenging for this class of conjugated polymers, but the herein presented characterization may serve as a starting point for both simplified synthesis protocols as well as yet more detailed and advanced characterization.

EXPERIMENTAL SECTION

Materials. All starting materials were purchased from commercial sources and used without further purification unless otherwise specified. 2,2'-Bithiophene (T2) was obtained from Alfa Aesar (98%) and further purified by eluting through a silica plug with petroleum ether (PE). All reactions were carried out in flame-dried glassware and under dry inert gas atmosphere. The detailed syntheses of compound **K** and model compounds **8** and **9** are shown in Scheme II-S2 and Scheme II-S3 in the Supporting Information (SI). They were prepared as reported.^{45–47}

Monomer syntheses. Compounds **1** and **2** were synthesized as detailed in the SI. Monomer **IDT** was synthesized according to literature procedures.^{25,41}

General route to P(K-alt-T2). Compound **K** (133.7 μmol , 1 eq), 2,2'-bithiophene (22.2 mg, 133.7 μmol , 1 eq), pivalic acid (13.7 mg, 133.7 μmol , 1 eq), potassium carbonate (55.4 mg, 400.9 μmol , 3 eq) were placed in a vial and dissolved in 0.5 mL degassed mesitylene. Then Pd_2dba_3 (1.2 mg, 1 mol%) and $\text{P}(o\text{-anisyl})_3$ (2.4 mg, 5 mol%) were added under argon and stirred for 72 h at 100 °C. After cooling to room temperature, the mixture was diluted with chloroform, precipitated into methanol and purified by Soxhlet extraction with acetone, ethyl acetate and chloroform. The chloroform fraction was filtered through a silica gel plug to afford an orange solid.

General route to IDT homopolymers via route A (P1^A-Me/Ph₂₀, P2^A-Bu/Ph₂₀, P3^A-Ph₂₀/Ph₂₀). To a solution of **P(K-alt-T2)** (entry 19) (50 mg, 49.4 μmol , 1 eq) in 10 mL toluene at room temperature the corresponding lithium compound (395.4 μmol , 8 eq) was added, and after 30 minutes 3 mL THF was added. After stirring for 3 h at room temperature, the reaction mixture was quenched with ethanol and water, extracted with chloroform and dried over magnesium sulfate. The solvent was removed under vacuum and the crude product was immediately dissolved in dry dichloromethane. After the addition of boron trifluoride diethyl etherate (0.1 mL, 130.3 mg, 938.9 μmol , 19 eq) the mixture was stirred for 3 h at room temperature and then quenched with ethanol and water, extracted with chloroform and dried over magnesium sulfate. The crude product was precipitated into methanol and purified by Soxhlet extraction with acetone, ethyl acetate and chloroform. The chloroform fraction was

filtered through a silica gel plug to afford **P1^A-Me/Ph₂₀**, **P2^A-Bu/Ph₂₀**, **P3^A-Ph₂₀/Ph₂₀** as red solid.

General route to IDT homopolymers via route B (P5^B-Ph₂₀/Ph₂₀-P13^B-Ph₈/Ph₈). Compound **IDT** (21.3 μmol, 1 eq), potassium carbonate (6.5 mg, 46.8 μmol, 2.2 eq) and copper(II) acetate (8.1 mg, 44.7 μmol, 2.1 eq) were placed into a vial and dissolved in dry *N,N*-dimethylacetamide. Then Pd(OAc)₂ (0.5 mg, 10 mol%) was added and the mixture was stirred for 72 h at 110 °C under air. After cooling to room temperature, the mixture was diluted with chloroform, precipitated into methanol and purified by Soxhlet extraction with acetone, ethyl acetate and chloroform. The chloroform fraction was filtered through a silica gel plug to afford **P5^B-Ph₂₀/Ph₂₀-P13^B-Ph₈/Ph₈** as red solids.

Supporting Information. Additional data including details of synthesis, measurements as well as characterization of model compounds; additional NMR, SEC, IR, UV-vis and DSC data are provided.

Acknowledgment

The authors acknowledge M. Raisch and S. Schmidt for DSC measurements, J. Streif and D. Stegerer for TGA measurements, and V. Pacheco for initial NMR measurements. Funding from DFG (SO 1213/8-1) is greatly acknowledged. A. S. and M. C. acknowledge the financial support of the European Research Council, European Union's Horizon 2020 Research and Innovation Programme HEROIC under Grant 638059.

REFERENCES

- (1) Li, Y.; Gu, M.; Pan, Z.; Zhang, B.; Yang, X.; Gu, J.; Chen, Y. Indacenodithiophene: A Promising Building Block for High Performance Polymer Solar Cells. *J Mater Chem A* **2017**. <https://doi.org/10.1039/C7TA02562A>.
- (2) McCulloch, I.; Ashraf, R. S.; Biniek, L.; Bronstein, H.; Combe, C.; Donaghey, J. E.; James, D. I.; Nielsen, C. B.; Schroeder, B. C.; Zhang, W. Design of Semiconducting Indacenodithiophene Polymers for High Performance Transistors and Solar Cells. *Acc. Chem. Res.* **2012**, *45* (5), 714–722. <https://doi.org/10.1021/ar200208g>.
- (3) Wadsworth, A.; Moser, M.; Marks, A.; Little, M. S.; Gasparini, N.; Brabec, C. J.; Baran, D.; McCulloch, I. Critical Review of the Molecular Design Progress in Non-Fullerene Electron Acceptors towards Commercially Viable Organic Solar Cells. *Chem. Soc. Rev.* **2019**, *48*, 1596–1625.
- (4) Bai, H.; Cheng, P.; Wang, Y.; Ma, L.; Li, Y.; Zhu, D.; Zhan, X. A Bipolar Small Molecule Based on Indacenodithiophene and Diketopyrrolopyrrole for Solution Processed Organic Solar Cells. *J Mater Chem A* **2014**, *2* (3), 778–784. <https://doi.org/10.1039/C3TA13816J>.
- (5) Liu, D.; Xiao, M.; Du, Z.; Yan, Y.; Han, L.; Roy, V. A. L.; Sun, M.; Zhu, W.; Lee, C. S.; Yang, R. Solution-Processed, Indacenodithiophene-Based, Small-Molecule Organic Field-Effect Transistors and Solar Cells. *J. Mater. Chem. C* **2014**, *2* (36), 7523. <https://doi.org/10.1039/C4TC00721B>.
- (6) Zhu, L.; Gao, W.; Wu, F.; Li, L.; Yang, C. Regulating the Electron Transporting Properties of Indacenodithiophene Derivatives for Perovskite Solar Cells with PCEs up to 19.51%. *J. Mater. Chem. A* **2018**, *6* (37), 18044–18049. <https://doi.org/10.1039/C8TA06730A>.
- (7) Wong, K.-T.; Chao, T.-C.; Chi, L.-C.; Chu, Y.-Y.; Balaiah, A.; Chiu, S.-F.; Liu, Y.-H.; Wang, Y. Syntheses and Structures of Novel Heteroarene-Fused Coplanar π -Conjugated Chromophores. *Org. Lett.* **2006**, *8* (22), 5033–5036. <https://doi.org/10.1021/ol061791y>.
- (8) Li, Y.; Tatum, W. K.; Onorato, J. W.; Barajas, S. D.; Yang, Y. Y.; Luscombe, C. K. An Indacenodithiophene-Based Semiconducting Polymer with High Ductility for Stretchable Organic Electronics. *Polym Chem* **2017**. <https://doi.org/10.1039/C7PY00435D>.
- (9) Xue, L.; Yang, Y.; Zhang, Z.-G.; Dong, X.; Gao, L.; Bin, H.; Zhang, J.; Yang, Y.; Li, Y. Indacenodithienothiophene–Naphthalene Diimide Copolymer as an Acceptor for All-Polymer Solar Cells. *J Mater Chem A* **2016**, *4* (16), 5810–5816. <https://doi.org/10.1039/C6TA01933A>.
- (10) Song, H.; Deng, Y.; Gao, Y.; Jiang, Y.; Tian, H.; Yan, D.; Geng, Y.; Wang, F. Donor–Acceptor Conjugated Polymers Based on Indacenodithiophene Derivative Bridged Diketopyrrolopyrroles: Synthesis and Semiconducting Properties. *Macromolecules* **2017**, *50* (6), 2344–2353. <https://doi.org/10.1021/acs.macromol.6b02781>.

-
- (11) Zhang, X.; Bronstein, H.; Kronemeijer, A. J.; Smith, J.; Kim, Y.; Kline, R. J.; Richter, L. J.; Anthopoulos, T. D.; Sringhaus, H.; Song, K.; et al. Molecular Origin of High Field-Effect Mobility in an Indacenodithiophene–Benzothiadiazole Copolymer. *Nat. Commun.* **2013**, *4*. <https://doi.org/10.1038/ncomms3238>.
- (12) Ma, Y.; Chen, S.-C.; Wang, Z.; Ma, W.; Wang, J.; Yin, Z.; Tang, C.; Cai, D.; Zheng, Q. Indacenodithiophene-Based Wide Bandgap Copolymers for High Performance Single-Junction and Tandem Polymer Solar Cells. *Nano Energy* **2017**, *33*, 313–324. <https://doi.org/10.1016/j.nanoen.2017.01.050>.
- (13) Chochos, C. L.; Katsouras, A.; Gasparini, N.; Koulogiannis, C.; Ameri, T.; Brabec, C. J.; Avgeropoulos, A. Rational Design of High-Performance Wide-Bandgap (≈ 2 eV) Polymer Semiconductors as Electron Donors in Organic Photovoltaics Exhibiting High Open Circuit Voltages (≈ 1 V). *Macromol. Rapid Commun.* **2017**, *38* (2), 1600614. <https://doi.org/10.1002/marc.201600614>.
- (14) Guo, Y.; Li, M.; Zhou, Y.; Song, J.; Bo, Z.; Wang, H. Two-Dimensional Conjugated Polymer Based on Sp^2 -Carbon Bridged Indacenodithiophene for Efficient Polymer Solar Cells. *Macromolecules* **2017**, *50* (20), 7984–7992. <https://doi.org/10.1021/acs.macromol.7b01738>.
- (15) Chen, C.-P.; Chan, S.-H.; Chao, T.-C.; Ting, C.; Ko, B.-T. Low-Bandgap Poly(Thiophene-Phenylene-Thiophene) Derivatives with Broadened Absorption Spectra for Use in High-Performance Bulk-Heterojunction Polymer Solar Cells. *J. Am. Chem. Soc.* **2008**, *130* (38), 12828–12833. <https://doi.org/10.1021/ja801877k>.
- (16) Venkateshvaran, D.; Nikolka, M.; Sadhanala, A.; Lemaire, V.; Zelazny, M.; Kepa, M.; Hurhangee, M.; Kronemeijer, A. J.; Pecunia, V.; Nasrallah, I.; et al. Approaching Disorder-Free Transport in High-Mobility Conjugated Polymers. *Nature* **2014**, *515* (7527), 384–388. <https://doi.org/10.1038/nature13854>.
- (17) Liu, M.; Liu, Z.; Zhang, Y.; Zhao, L. Wide Band Gap Polymer Based on Indacenodithiophene and Acenaphthoquinoline for Efficient Polymer Solar Cells Application. *Polymers* **2017**, *9* (11), 578. <https://doi.org/10.3390/polym9110578>.
- (18) Zhao, W.; Qian, D.; Zhang, S.; Li, S.; Inganäs, O.; Gao, F.; Hou, J. Fullerene-Free Polymer Solar Cells with over 11% Efficiency and Excellent Thermal Stability. *Adv. Mater.* **2016**, *28* (23), 4734–4739. <https://doi.org/10.1002/adma.201600281>.
- (19) Intemann, J. J.; Yao, K.; Li, Y.-X.; Yip, H.-L.; Xu, Y.-X.; Liang, P.-W.; Chueh, C.-C.; Ding, F.-Z.; Yang, X.; Li, X.; et al. Highly Efficient Inverted Organic Solar Cells Through Material and Interfacial Engineering of Indacenodithieno[3,2-*b*]Thiophene-Based Polymers and Devices. *Adv. Funct. Mater.* **2014**, *24* (10), 1465–1473. <https://doi.org/10.1002/adfm.201302426>.
- (20) Song, J.; Li, C.; Ye, L.; Koh, C.; Cai, Y.; Wei, D.; Woo, H. Y.; Sun, Y. Extension of Indacenodithiophene Backbone Conjugation Enables Efficient Asymmetric A–D–A

- Type Non-Fullerene Acceptors. *J. Mater. Chem. A* **2018**, *6* (39), 18847–18852. <https://doi.org/10.1039/C8TA07334A>.
- (21) Donaghey, J. E.; Ashraf, R. S.; Kim, Y.; Huang, Z. G.; Nielsen, C. B.; Zhang, W.; Schroeder, B.; Grenier, C. R. G.; Brown, C. T.; D'Angelo, P.; et al. Pyrroloindacenodithiophene Containing Polymers for Organic Field Effect Transistors and Organic Photovoltaics. *J. Mater. Chem.* **2011**, *21* (46), 18744. <https://doi.org/10.1039/c1jm13428k>.
- (22) Schroeder, B. C.; Huang, Z.; Ashraf, R. S.; Smith, J.; D'Angelo, P.; Watkins, S. E.; Anthopoulos, T. D.; Durrant, J. R.; McCulloch, I. Silaindacenodithiophene-Based Low Band Gap Polymers - The Effect of Fluorine Substitution on Device Performances and Film Morphologies. *Adv. Funct. Mater.* **2012**, *22* (8), 1663–1670. <https://doi.org/10.1002/adfm.201102941>.
- (23) Liu, D.; Sun, L.; Du, Z.; Xiao, M.; Gu, C.; Wang, T.; Wen, S.; Sun, M.; Yang, R. Benzothiadiazole – an Excellent Acceptor for Indacenodithiophene Based Polymer Solar Cells. *RSC Adv.* **2014**, *4* (71), 37934. <https://doi.org/10.1039/C4RA06967F>.
- (24) Liang, C.; Wang, H. Indacenodithiophene-Based D-A Conjugated Polymers for Application in Polymer Solar Cells. *Org. Electron.* **2017**, *50*, 443–457. <https://doi.org/10.1016/j.orgel.2017.06.059>.
- (25) Chen, S.; Lee, K. C.; Zhang, Z.-G.; Kim, D. S.; Li, Y.; Yang, C. An Indacenodithiophene–Quinoxaline Polymer Prepared by Direct Arylation Polymerization for Organic Photovoltaics. *Macromolecules* **2016**, *49* (2), 527–536. <https://doi.org/10.1021/acs.macromol.5b02324>.
- (26) Zhang, Y.; Zou, J.; Yip, H.-L.; Chen, K.-S.; Zeigler, D. F.; Sun, Y.; Jen, A. K.-Y. Indacenodithiophene and Quinoxaline-Based Conjugated Polymers for Highly Efficient Polymer Solar Cells. *Chem. Mater.* **2011**, *23* (9), 2289–2291. <https://doi.org/10.1021/cm200316s>.
- (27) Bünnagel, T. W.; Nehls, B. S.; Galbrecht, F.; Schottler, K.; Kudla, C. J.; Volk, M.; Pina, J.; de Melo, J. S. S.; Burrows, H. D.; Scherf, U. Thiophene-Phenylene/Naphthalene-Based Step-Ladder Copolymers. *J. Polym. Sci. Part Polym. Chem.* **2008**, *46* (22), 7342–7353. <https://doi.org/10.1002/pola.23039>.
- (28) Zhang, W.; Smith, J.; Watkins, S. E.; Gysel, R.; McGehee, M.; Salleo, A.; Kirkpatrick, J.; Ashraf, S.; Anthopoulos, T.; Heeney, M.; et al. Indacenodithiophene Semiconducting Polymers for High-Performance, Air-Stable Transistors. *J. Am. Chem. Soc.* **2010**, *132* (33), 11437–11439. <https://doi.org/10.1021/ja1049324>.
- (29) Wang, X.; Luo, H.; Sun, Y.; Zhang, M.; Li, X.; Yu, G.; Liu, Y.; Li, Y.; Wang, H. Narrow Band Gap D-A Copolymer of Indacenodithiophene and Diketopyrrolopyrrole with Deep HOMO Level: Synthesis and Application in Field-Effect Transistors and Polymer Solar

- Cells. *J. Polym. Sci. Part Polym. Chem.* **2012**, *50* (2), 371–377. <https://doi.org/10.1002/pola.25042>.
- (30) Facchetti, A.; Vaccaro, L.; Marrocchi, A. Semiconducting Polymers Prepared by Direct Arylation Polycondensation. *Angew. Chem. Int. Ed.* **2012**, *51* (15), 3520–3523. <https://doi.org/10.1002/anie.201200199>.
- (31) Kowalski, S.; Allard, S.; Zilberberg, K.; Riedl, T.; Scherf, U. Direct Arylation Polycondensation as Simplified Alternative for the Synthesis of Conjugated (Co)Polymers. *Prog. Polym. Sci.* **2013**, *38* (12), 1805–1814. <https://doi.org/10.1016/j.progpolymsci.2013.04.006>.
- (32) Okamoto, K.; Zhang, J.; Housekeeper, J. B.; Marder, S. R.; Luscombe, C. K. C–H Arylation Reaction: Atom Efficient and Greener Syntheses of π -Conjugated Small Molecules and Macromolecules for Organic Electronic Materials. *Macromolecules* **2013**, *46* (20), 8059–8078. <https://doi.org/10.1021/ma401190r>.
- (33) Wakioka, M.; Ozawa, F. Highly Efficient Catalysts for Direct Arylation Polymerization (DARp). *Asian J. Org. Chem.* **2018**, *7* (7), 1206–1216. <https://doi.org/10.1002/ajoc.201800227>.
- (34) Rudenko, A. E.; Thompson, B. C. Optimization of Direct Arylation Polymerization (DARp) through the Identification and Control of Defects in Polymer Structure. *J. Polym. Sci. Part Polym. Chem.* **2015**, *53* (2), 135–147. <https://doi.org/10.1002/pola.27279>.
- (35) Li, Y.; Tatum, W. K.; Onorato, J. W.; Zhang, Y.; Luscombe, C. K. Low Elastic Modulus and High Charge Mobility of Low-Crystallinity Indacenodithiophene-Based Semiconducting Polymers for Potential Applications in Stretchable Electronics. *Macromolecules* **2018**, *51* (16), 6352–6358. <https://doi.org/10.1021/acs.macromol.8b00898>.
- (36) Pouliot, J.-R.; Grenier, F.; Blaskovits, J. T.; Beaupré, S.; Leclerc, M. Direct (Hetero)Arylation Polymerization: Simplicity for Conjugated Polymer Synthesis. *Chem. Rev.* **2016**, *116*, 14225–14274.
- (37) Matsidik, R.; Komber, H.; Luzio, A.; Caironi, M.; Sommer, M. Defect-Free Naphthalene Diimide Bithiophene Copolymers with Controlled Molar Mass and High Performance via Direct Arylation Polycondensation. *J. Am. Chem. Soc.* **2015**, *137* (20), 6705–6711. <https://doi.org/10.1021/jacs.5b03355>.
- (38) Sun, Y.; Chien, S.-C.; Yip, H.-L.; Chen, K.-S.; Zhang, Y.; Davies, J. A.; Chen, F.-C.; Lin, B.; Jen, A. K.-Y. Improved Thin Film Morphology and Bulk-Heterojunction Solar Cell Performance through Systematic Tuning of the Surface Energy of Conjugated Polymers. *J. Mater. Chem.* **2012**, *22* (12), 5587. <https://doi.org/10.1039/c2jm15517f>.
- (39) Chan, S.-H.; Chen, C.-P.; Chao, T.-C.; Ting, C.; Lin, C.-S.; Ko, B.-T. Synthesis, Characterization, and Photovoltaic Properties of Novel Semiconducting Polymers with

- Thiophene–Phenylene–Thiophene (TPT) as Coplanar Units. *Macromolecules* **2008**, *41* (15), 5519–5526. <https://doi.org/10.1021/ma800494k>.
- (40) Zhang, Q.; Wan, X.; Lu, Y.; Li, Y.; Li, Y.; Li, C.; Wu, H.; Chen, Y. The Synthesis of 5-Alkyl[3,4-c]Thienopyrrole-4,6-Dione-Based Polymers Using a Pd-Catalyzed Oxidative C–H/C–H Homopolymerization Reaction. *Chem Commun* **2014**, *50* (83), 12497–12499. <https://doi.org/10.1039/C4CC06284A>.
- (41) Gao, W.; Zhang, M.; Liu, T.; Ming, R.; An, Q.; Wu, K.; Xie, D.; Luo, Z.; Zhong, C.; Liu, F.; et al. Asymmetrical Ladder-Type Donor-Induced Polar Small Molecule Acceptor to Promote Fill Factors Approaching 77% for High-Performance Nonfullerene Polymer Solar Cells. *Adv. Mater.* **2018**, *30* (26), 1800052. <https://doi.org/10.1002/adma.201800052>.
- (42) Gobalasingham, N. S.; Noh, S.; Thompson, B. C. Palladium-Catalyzed Oxidative Direct Arylation Polymerization (Oxi-DArP) of an Ester-Functionalized Thiophene. *Polym Chem* **2016**, *7* (8), 1623–1631. <https://doi.org/10.1039/C5PY01973G>.
- (43) Gobalasingham, N. S.; Pankow, R. M.; Thompson, B. C. Synthesis of Random Poly(Hexyl Thiophene-3-Carboxylate) Copolymers via Oxidative Direct Arylation Polymerization (Oxi-DArP). *Polym Chem* **2017**, *8* (12), 1963–1971. <https://doi.org/10.1039/C7PY00181A>.
- (44) Socrates, G. *Infrared and Raman Characteristic Group Frequencies: Tables and Charts*, 3. ed., repr. as paperback.; Wiley: Chichester, 2010.
- (45) Yao, Y.; Tour, J. M. Synthesis of Imine-Bridged Phenylene-pyridine Ladder Polymers. Optical Band Gap Widening through Intramolecular Charge Transfer in Planar Polymers. *Macromolecules* **1999**, *32* (8), 2455–2461. <https://doi.org/10.1021/ma981618k>.
- (46) Ishibashi, J. S. A.; Marshall, J. L.; Mazière, A.; Lovinger, G. J.; Li, B.; Zakharov, L. N.; Dargelos, A.; Graciaa, A.; Chrostowska, A.; Liu, S.-Y. Two BN Isosteres of Anthracene: Synthesis and Characterization. *J. Am. Chem. Soc.* **2014**, *136* (43), 15414–15421. <https://doi.org/10.1021/ja508813v>.
- (47) Marshall, J. L.; Uchida, K.; Frederickson, C. K.; Schütt, C.; Zeidell, A. M.; Goetz, K. P.; Finn, T. W.; Jarolimek, K.; Zakharov, L. N.; Risko, C.; et al. Indacenodibenzothiophenes: Synthesis, Optoelectronic Properties and Materials Applications of Molecules with Strong Antiaromatic Character. *Chem Sci* **2016**, *7* (8), 5547–5558. <https://doi.org/10.1039/C6SC00950F>.

SUPPORTING INFORMATION

General measurement and characterization

NMR spectroscopy. NMR spectra were recorded on a Bruker DPX 250 spectrometer (^1H : 250 MHz, ^{13}C : 62.9 MHz), on a Bruker AVANCE 300 spectrometer (^1H : 300 MHz, ^{13}C : 75 MHz) and on a Bruker AVANCE III 500 spectrometer (^1H : 500 MHz, ^{13}C : 125.8 MHz). CDCl_3 (at 30 °C) was used as solvent. The spectra were referenced to the residual solvent peak (CDCl_3 : $\delta(^1\text{H}) = 7.26$ ppm, $\delta(^{13}\text{C}) = 77.0$ ppm). Chemical shifts (δ) are reported in ppm.

Size exclusion chromatography. SEC measurements of all samples were carried out on four SDplus 10^4 \AA 5 \mu m columns with pore sizes ranging from 10^3 to 10^6 \AA (Polymer Standards), connected in series with a RID20A RI detector and a SPD20AV UV detector (Shimadzu) calibrated with polystyrene standards. THF was used as eluent at 40 °C with a flow rate of 1.0 mL min^{-1} .

UV-vis spectroscopy. UV-vis spectra were recorded at 25 °C on a Cary 60 UV-Vis (Agilent Technologies) in chloroform solutions ($c = 0.02 \text{ mg mL}^{-1}$).

Photoluminescence. PL spectra were recorded at 25 °C with a xenon flash lamp and a Czerny Turner monochromator in chloroform solutions ($c = 0.02 \text{ mg mL}^{-1}$).

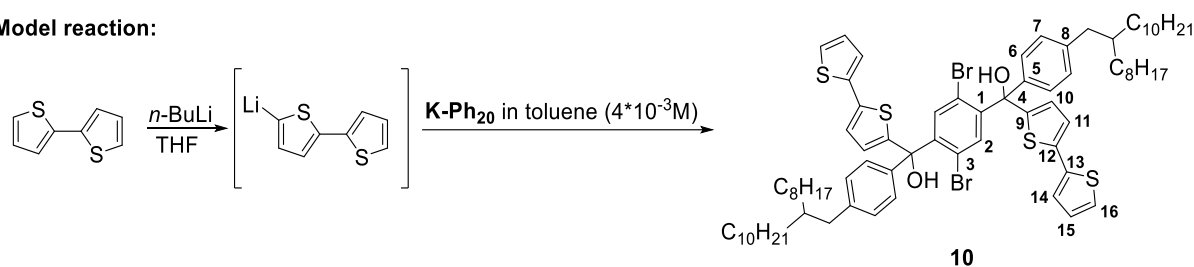
Infrared spectroscopy. IR spectra were obtained at 25 °C on a FTS 165 spectrometer (BIO-RAD) equipped with a Golden Gate single ATR accessory from LOT-Oriel GmbH.

Differential scanning calorimetry. DSC measurements were carried out on a DSC 2500 (TA Instruments) under nitrogen atmosphere. Heating and cooling rates were 20 K min^{-1} . The mass of the samples for each measurement was approximately 2-5 mg.

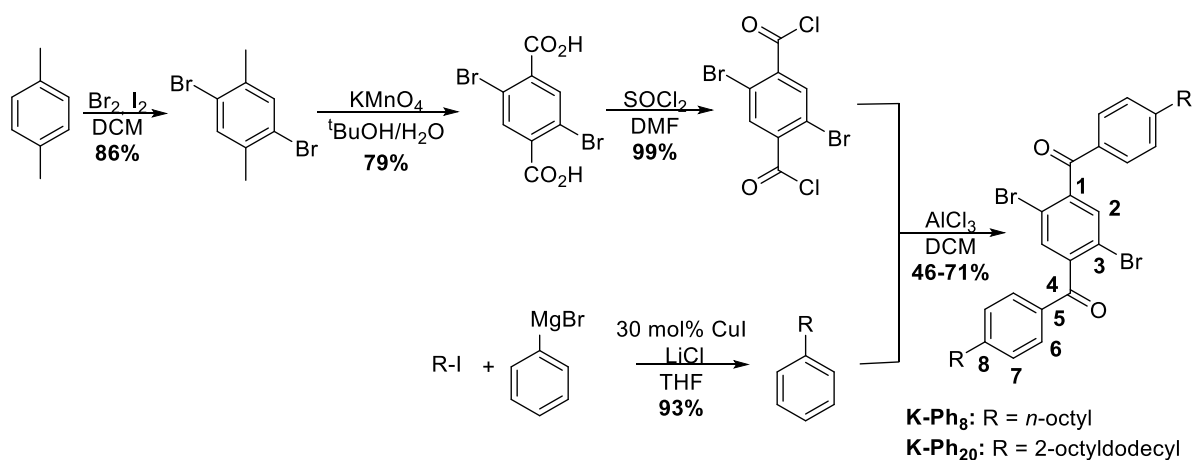
Thermogravimetric analysis. TGA measurements were done on a TGA/DSC3+ from Mettler-Toledo within the temperature range 50 °C to 650 °C at a heating rate of 20 K min^{-1} under N_2 .

Organic field-effect transistors. A top-gate bottom-contact configuration with interdigitated Au source and drain contacts was prepared with a lift-off photolithographic process onto glass substrates and subsequently cleaned in a sonication bath in acetone and isopropanol. Solutions of the IDT copolymers (5 mg mL^{-1} in *o*-dichlorobenzene) were spin-coated at ambient conditions at 2000 rpm for 60 seconds. Following the semiconductor deposition, Cytop was spin-coated on top to obtain a $\sim 600 \text{ nm}$ thick dielectric layer. 40 nm thick Al gate contacts were finally evaporated with a shadow mask and the devices were measured in a nitrogen filled glovebox on a Wentworth Laboratories probe station with an Agilent B1500A semiconductor device analyzer.

Model reaction:

**Scheme II-S1.** Synthesis of model compound **10**.

Synthesis of model compound 10. To a solution of 2, 2'-bithiophene (355.6 mg, 2.14 mmol, 8 eq) in 4 mL tetrahydrofurane was added *n*-butyl lithium (0.7 mL, 1.71 mmol, 2.5 M, 6.4 eq) at -78 °C. The reaction solution was stirred for 1.5 h at -78 °C and warmed to room temperature. Then compound **K-Ph₂₀** (268 mg, 0.27 mmol, 1 eq) in 5 mL toluene was added dropwisely. After stirring for 16 h at room temperature the reaction mixture was quenched with ethanol and water, extracted with chloroform and dried over magnesium sulfate. The solvent was removed under reduced pressure and the crude product was purified by column chromatography (PE:DCM, 1:1) to afford **10** as a solid. ¹H NMR (500 MHz, CDCl₃, δ): 7.24 (s, 2H; 2), 7.23 (d, 7.9 Hz, 4H; 6), 7.20 (d, 5.1 Hz, 2H; 16), 7.16 (d, 3.6 Hz, 2H; 14), 7.15 (d, 7.9 Hz, 4H; 7), 7.02 (d, 3.7 Hz, 2H; 11), 7.00 (dd, 5.1 Hz, 3.6 Hz, 2H; 15), 6.53 (d, 3.7 Hz, 2H; 10), 4.46 (s, 2H; OH), 2.55 (d, 6.9 Hz, 4H; Ar-CH₂), 1.62 (m, 2H; CH), 1.4 – 1.1 (64H; 16 x CH₂ of R¹), 0.87 (t, 6.5 Hz, 12H; 2 x CH₃ of R¹). ¹³C NMR (125 MHz, CDCl₃, δ): 148.3 (9), 145.9 (1), 142.0 (8), 141.2 (5), 138.1 (12), 137.3 (13), 136.9 (2), 129.2 (7), 127.9 (10), 127.8 (15), 127.0 (6), 124.5 (16), 123.8 (14), 122.9 (11), 121.2 (3), 81.0 (4), 40.3 (Ar-CH₂), 39.6 (CH), 33.3, 31.9, 30.0, 29.6, 29.4, 26.6 and 22.7 (CH₂ of R¹), 14.1 (CH₃).

**Scheme II-S2.** Synthesis of keto monomer **K** (2,5-dibromo-1,4-phenylenebis[(4-alkylphenyl)methanone]).

Synthesis of 2,5-dibromo-1,4-phenylenebis[(4-octylphenyl)methanone] (K-Ph₈). To a solution of 2,5-dibromoterephthaloyl dichloride (140 mg, 0.4 mmol, 1 eq) and aluminum chloride (125 mg, 0.9 mmol, 2.4 eq) in 0.5 mL dichloromethane was added dropwisely *n*-octylbenzene (307 mg, 1.6 mmol, 4 eq) in 1 mL dichloromethane at 0 °C. After stirring overnight at room temperature, the mixture was poured onto ice/1 M HCl, extracted with dichloromethane, washed with sat. NaHCO₃ solution and dried over magnesium sulfate. The solvent was removed under reduced pressure and the crude product was recrystallized from *iso*-hexanes to afford **K-Ph₈** as colourless crystals (119 mg, 178 µmol, 46%). ¹H NMR (500 MHz, CDCl₃, δ): 7.76 (d, 8.1 Hz, 4H; 6), 7.58 (s, 2H; 2), 7.32 (d, 8.1 Hz, 4H; 7), 2.70 (t, 7.7 Hz, 4H; α-CH₂), 1.66 (m, 4H; β-CH₂), 1.4-1.2 (20H; 5 x CH₂ of R), 0.89 (t, 6.9 Hz, 6H; CH₃). ¹³C NMR (125 MHz, CDCl₃, δ): 193.4 (4), 150.6 (8), 143.4 (1), 132.9 (5), 132.9 (2), 130.5 (6), 130.0 (7), 118.4 (3), 36.2 (α-CH₂), 31.8, 31.0, 29.4, 29.3, 29.2 and 22.6 (CH₂ of R), 14.1 (CH₃).

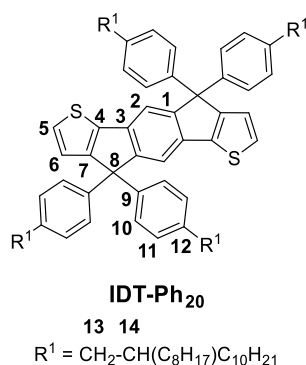
Synthesis of 2,5-dibromo-1,4-phenylenebis[(4-(2-octyldodecyl)phenyl)methanone] (K-Ph₂₀). Preparation similar to **K-Ph₈** The crude product was purified by column chromatography (PE:DCM, 1:1) to afford **K-Ph₂₀** as colourless oil. Yield: 71%. ¹H NMR (300 MHz, CDCl₃, δ): 7.77 (d, 4H), 7.6 (s, 2H), 7.29 (d, 4H), 2.63 (d, 4H), 1.68 (m, 2H), 1.26 (64H), 0.89 (t, 12H). ¹³C NMR (75 MHz, CDCl₃, δ): 193.6, 150.0, 143.5, 133.1, 133.0, 130.5, 129.9, 118.6, 41.1, 39.7, 33.4, 32.1, 30.1, 29.8, 29.7, 29.5, 26.7, 22.8, 14.3.

Synthesis of 2,5-di(thiophen-2-yl)-1,4-phenylenebis[(4-octylphenyl)methanone] (I).

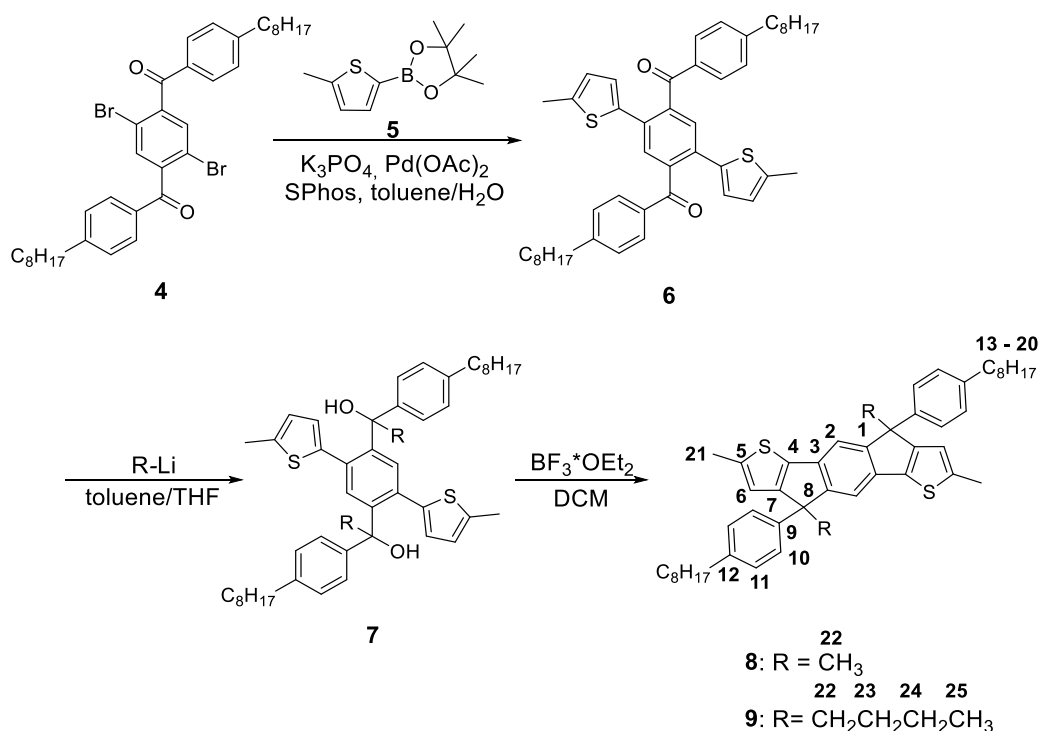
Compound **K-Ph₈** (380 mg, 0.6 mmol, 1 eq), potassium carbonate (236 mg, 1.7 mmol, 3 eq) and pivalic acid (58.1 mg, 0.6 mmol, 1 eq) were weight into a Schlenk tube and dissolved in 6 mL degassed THF. Then degassed thiophene (957 mg, 0.9 mL, 11.4 mmol, 20 eq) and PCy₃ Pd G2 (16.8 mg, 5 mol%) were added. After stirring for 72 h at 100 °C the reaction mixture was allowed to cool to room temperature, filtered and the solvent was removed under reduced pressure. The crude product was recrystallized from *iso*-hexanes to afford **1** as yellow crystals (148 mg, 0.3 mmol, 48%). ¹H NMR (300 MHz, CDCl₃, δ): 7.70 (d, 4H), 7.62 (s, 2H), 7.17 (m, 6H), 7.00 (dd, 2H), 6.85 (dd, 2H), 2.61 (t, 4H), 1.60 (m, 4H), 1.27 (20H), 0.88 (t, 8H). ¹³C NMR (75 MHz, CDCl₃, δ): 197.5, 149.7, 140.5, 140.1, 134.3, 132.0, 130.3, 129.6, 128.6, 128.1, 127.8, 126.9, 36.2, 31.9, 31.0, 29.5, 29.3, 22.8, 14.2.

Synthesis of 1-bromo-4-(2-octyldodecyl) benzene. To a mixture of 2-octyldodecyl iodide (5.77 g, 14.1 mmol, 1 eq), copper(I) iodide (0.81 g, 30 mol%) and lithium chloride (1.20 g, 28.26 mmol, 2 eq) was added dropwisely 45 mL 4-bromophenyl magnesium bromide in dry THF (42.39 mmol, 1 M, 3 eq) at 0 °C. After stirring overnight, the mixture was quenched with 1 M hydrochloride acid, extracted with diethyl ether and dried over magnesium sulfate. The solvent was removed under reduced pressure and the crude product was purified by column chromatography (petroleum ether) to afford the title compound as colourless oil (3.7 g, 8.6 mmol, 61%). ¹H NMR (250 MHz, CDCl₃, δ): 7.37 (d, 2H), 7.00 (d, 2H), 2.47 (d, 2H), 1.58 (m, 1H), 1.25 (32H), 0.88 (t, 6H). ¹³C NMR (63 MHz, CDCl₃, δ): 141.2, 131.4, 131.3, 119.5, 39.4, 33.4, 32.3, 30.3, 30.0, 29.7, 27.3, 26.9, 23.0, 14.4.

Synthesis of compound IDT-Ph₈. To a solution of 1-bromo-4-octylbenzene (119 mg, 444 μmol, 3 eq) in 2 mL THF at -78 °C was added *n*-butyl lithium (0.2 mL, 459 μmol, 2.5 M, 3.1 eq). After stirring at -78 °C for 1 h, compound **1** (100 mg, 148 μmol, 1 eq) in 1 mL THF was added slowly. The reaction mixture was stirred overnight and then quenched with sat. sodium chloride solution, extracted with ethyl acetate and dried over magnesium sulfate. The solvent was removed under reduced pressure and the crude product was dissolved in octane/acetic acid (1:1, v/v). After the addition of sulfuric acid (0.1 mL in 0.5 mL acetic acid) the mixture was stirred under reflux (125 °C) for 30 min. Then the greenish reaction mixture was extracted with dichloromethane, washed with water and dried over magnesium sulfate. The solvent was removed under reduced pressure and the crude product was purified by column chromatography (petroleum ether) to afford **IDT-Ph₈** as yellow crystals (80 mg, 78.5 μmol, 53%). ¹H NMR (250 MHz, CDCl₃, δ): 7.45 (s, 2H), 7.25 (d, 2H), 7.17 (d, 8H) 7.06 (d, 8H), 7.01 (d, 2H), 2.57 (d, 8H), 1.60 (m, 8H), 1.29 (40H), 0.89 (m, 12H). ¹³C NMR (63 MHz, CDCl₃, δ): 155.9, 153.4, 142.1, 141.4, 135.1, 128.3, 127.9, 127.4, 123.2, 117.5, 62.7, 35.6, 31.9, 31.4, 29.5, 29.3, 22.7, 14.2.



Synthesis of compound IDT-Ph₂₀. Preparation similar to **IDT-Ph₈** using 1-bromo-4-(2-octyldodecyl) benzene as starting material. Yield: 15%, yellow oil. ¹H NMR (500 MHz, CDCl₃, δ): 7.43 (s, 2H; 2), 7.23 (d, 4.9 Hz, 2H; 6), 7.14 (d, 8.4 Hz, 8H; 10), 7.00 (10H; 5 and 11), 2.47 (d, 6.9 Hz, 8H; 13), 1.57 (m, 4H; 14), 1.4 – 1.1 (128H; 16 x CH₂ of R¹), 0.87 (t, 6.5 Hz, 24H; 2 x CH₃ of R¹). ¹³C NMR (125 MHz, CDCl₃, δ): 155.9 (7), 153.4 (1), 142.0 (9), 141.2 (4), 140.2 (12), 135.1 (3), 129.0 (11), 127.7 (10), 127.2 (5), 123.2 (6), 117.5 (2), 62.7 (8), 40.2 (13), 39.4 (14), 33.2, 31.9, 30.0, 29.6, 29.4, 26.6 and 22.7 (CH₂ of R¹), 14.1 (CH₃).

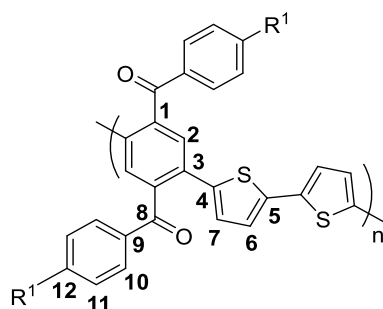


Scheme II-S3. Synthesis of model compounds **8** and **9**.

Synthesis of model compound 8. To a solution of compound **6** (150 mg, 0.21 mmol, 1 eq) in 10 mL toluene at room temperature was added methyl lithium (1.1 mL, 1.71 mmol, 1.6 M, 8 eq) and after 30 minutes 3 mL THF was added. After stirring for 3 h at room temperature the reaction mixture was quenched with ethanol and water, extracted with chloroform and dried over magnesium sulfate. The solvent was removed under reduced pressure and the crude product was dissolved in dichloromethane. After the addition of boron trifluoride diethyl etherate (0.5 mL, 575 mg, 4.05 mmol, 19 eq), the mixture was stirred for 3 h at room temperature and then quenched with ethanol and water, extracted with chloroform and dried over magnesium sulfate. The solvent was removed under reduced pressure and the crude product was purified by column chromatography (PE:DCM, 4:1) to afford **8** as yellow solid (69 mg, 0.1 mmol, 46%). ¹H NMR (500 MHz, CDCl₃, δ): 7.2-7.15 (6H; 2 and 10), 7.06 (d, 8.0 Hz, 4H; 11), 6.56 (m, 2H; 6), 2.55 (t, 7.8 Hz, 4H; 13), 2.49 (d, 2.0 Hz, 6H; 21), 1.83 (s; 22), 1.58 (m, 4H; 14), 1.4 – 1.2 (20H; 15-19), 0.88 (t, 7.0 Hz, 6H; 20). ¹³C NMR (125 MHz, CDCl₃, δ): 157.5 (7), 155.2 (1), 142.4 (5), 141.2 (9), 141.0 (12), 138.4 (4), 134.6 (3), 128.4 (11), 126.1 (10), 119.9 (6), 114.2 (2), 52.7 (8), 35.5 (13), 31.9 (18), 31.4 (14), 29.5 and 29.2 (15,16,17), 24.5 (22), 22.7 (19), 16.3 (21), 14.1 (20). Two signals appear for several positions due to the presence of two diastereomers.

Synthesis of model compound 9. To a solution of compound **6** (150 mg, 0.21 mmol, 1 eq) in 10 mL toluene at room temperature was added *n*-butyl lithium (0.7 mL, 1.71 mmol, 2.5 M, 8 eq) and after 30 minutes 3 mL THF was added. After stirring for 3 h at room temperature the reaction mixture was quenched with ethanol and water, extracted with chloroform and dried over magnesium sulfate. The solvent was removed under reduced pressure and the crude product was dissolved in dichloromethane. After the addition of boron trifluoride diethyl etherate (0.5 mL, 575 mg, 4.05 mmol, 19 eq) the mixture was stirred for 3 h at room temperature and then quenched with ethanol and water, extracted with chloroform and dried over magnesium sulfate. The solvent was removed under reduced pressure and the crude product was purified by column chromatography (PE:DCM, 4:1) to afford **9** as yellow oil (26 mg, 0.1 mmol, 16%). ¹H NMR (500 MHz, CDCl₃, δ): 7.20 and 7.18 (two d, 8.3 Hz, 4H; 10), 7.15 and 7.14 (two s, 2H; 2), 7.07 and 7.05 (two d, 8.3 Hz, 4H; 11), 6.58 (m, 2H; 6), 2.54 (t, 7.8 Hz, 4H; 13), 2.53 (s, 6H; 21), 2.41 and 2.17 (m, 4H; 22), 1.58 (m, 4H; 14), 1.4 – 1.1 (24H; 15-19,24), 0.95 (m, 4H; 23), 0.88 (t, 7.0 Hz, 6H; 20), 0.78 (t, 7.2 Hz, 6H; 25). ¹³C NMR (125 MHz, CDCl₃, δ): 155.2 (7), 153.5 (1), 141.9 (5), 141.0 (9,12), 139.6 (4), 135.1 (3), 128.4 (11), 126.4 (10), 120.8 (6), 114.1 (2), 57.1 (8), 37.8 (22), 35.5 (13), 31.9 (18), 31.3 (14), 29.5

and 29.2 (15,16,17), 26.8 (23), 23.1 (24), 22.7 (19), 16.4 (21), 14.1 (20), 13.9 (25). Two signals appear for several positions due to the presence of two diastereomers.

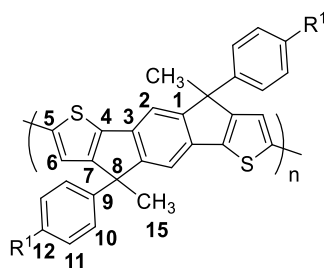


13 14

$R^1 = \text{CH}_2\text{-CH}(\text{C}_8\text{H}_{17})\text{C}_{10}\text{H}_{21}$

P(K-*alt*-T2)

NMR data of **P(K-*alt*-T2)** (entry 19): ^1H NMR (500 MHz, CDCl_3 , δ): 7.67 (d, 8.2 Hz, 4H; 10), 7.53 (s, 2H; 2), 7.11 (d, 8.2 Hz, 4H; 11), 6.83 (d, 3.6 Hz, 2H; 7), 6.78 (d, 3.6 Hz, 2H; 6), 2.52 (d, 4H; 13), 1.58 (m, 4H; 14), 1.4 – 1.1 (64H; 16 x CH_2 of R^1), 0.86 (12H; 2 x CH_3 of R^1). ^{13}C NMR (125 MHz, CDCl_3 , δ): 197.0 (8), 148.9 (12), 140.1 (2), 139.1 (4), 138.2 (5), 134.0 (9), 131.3 (3), 130.0 (10), 129.4 (11), 129.2 (3), 128.7 (7), 124.6 (6), 40.6 (13), 39.4 (14), 33.1, 31.9, 29.9, 29.6, 29.4, 26.6 and 22.7 (CH_2 of R^1), 14.1 (CH_3).



13 14

$R^1 = \text{CH}_2\text{-CH}(\text{C}_8\text{H}_{17})\text{C}_{10}\text{H}_{21}$

P1^A-Me/Ph₂₀

NMR data of **P1^A-Me/Ph₂₀**. ^1H NMR (500 MHz, CDCl_3 , δ): 7.25-7.1 (2 and 10), 7.04 (11), 6.98 (6), 2.47 (13), 1.87 (15), 1.58 (14), 1.4 – 1.0 (16 x CH_2 of R^1), 0.86 (2 x CH_3 of R^1). ^{13}C NMR (125 MHz, CDCl_3 , δ): 158.7 (7), 155.9 (1), 141.5 – 140.0 (5,9,12), 139.5 (4), 134.6 (3), 129.3 (11), 125.9 (10), 117.6 (6), 114.6 (2), 52.9 (8), 40.1 (13), 39.4 (14), 33.1, 31.9, 30.0, 29.6, 29.4, 26.3 and 22.7 (CH_2 of R^1), 24.8 and 24.6 (15), 14.1 (CH_3).

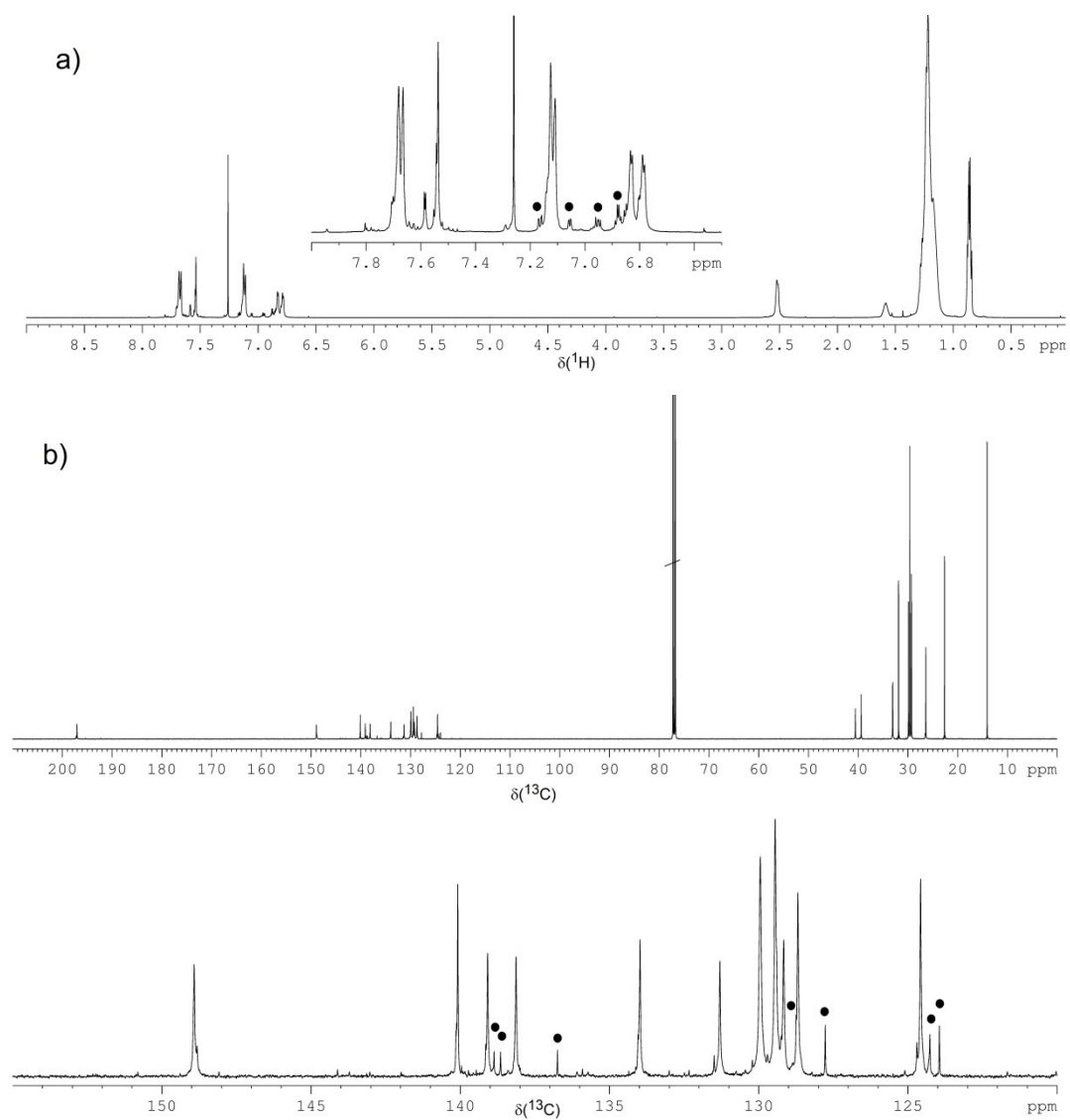


Figure II-S1. ^1H NMR (top) and ^{13}C NMR spectrum (bottom) of **P(K-alt-T2)**, entry 19, in CDCl_3 . The dots mark signals of the $-\text{T2H}$ end group.

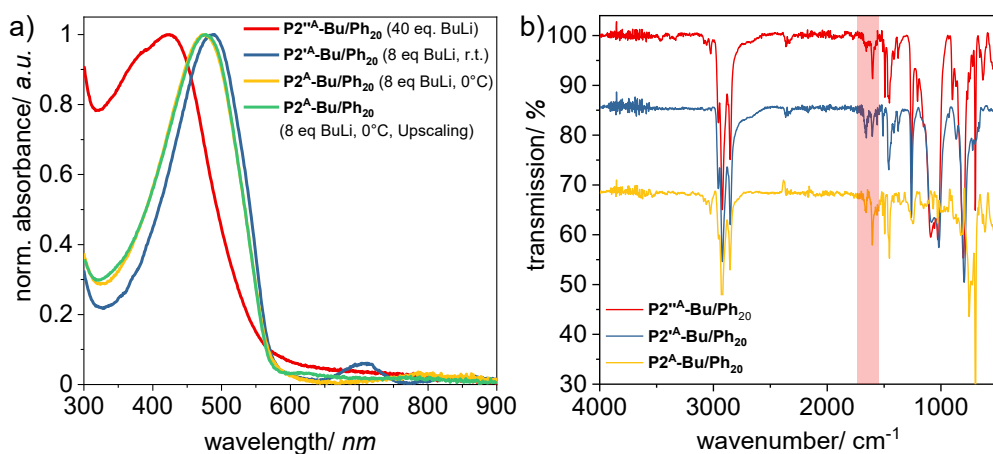


Figure II-S2. UV-vis (a) and IR spectra (b) of butyl derivatives $P2^A-Bu/Ph_{20}$ synthesized under different reaction conditions.

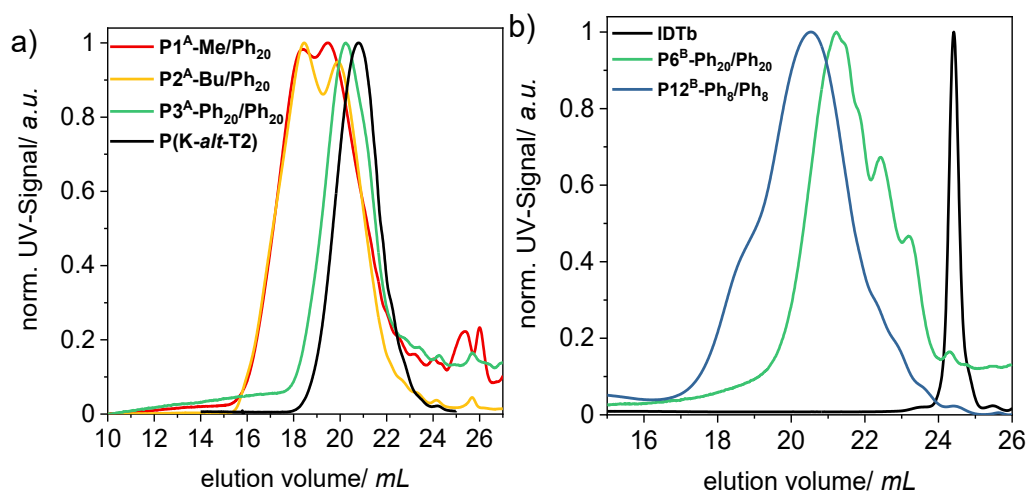


Figure II-S3. SEC curves of $PIDTs$ via route A ($P1^A-Me/Ph_{20}$, $P2^A-Bu/Ph_{20}$, $P3^A-Ph_{20}/Ph_{20}$) (a) and via route B ($P6^B-Ph_{20}/Ph_{20}$, $P12^B-Ph_8/Ph_8$) (b).

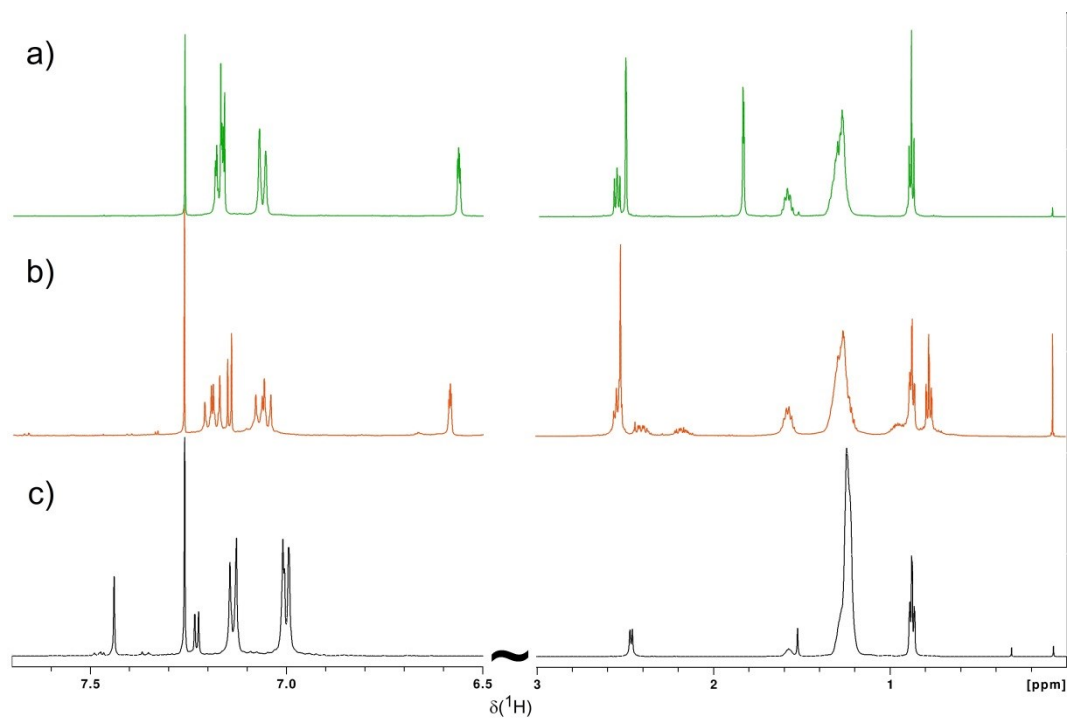


Figure II-S4. ^1H NMR spectra of model compound **8** (a), **9** (b) and monomer **IDT-Ph**₂₀ (c) in CDCl_3 .

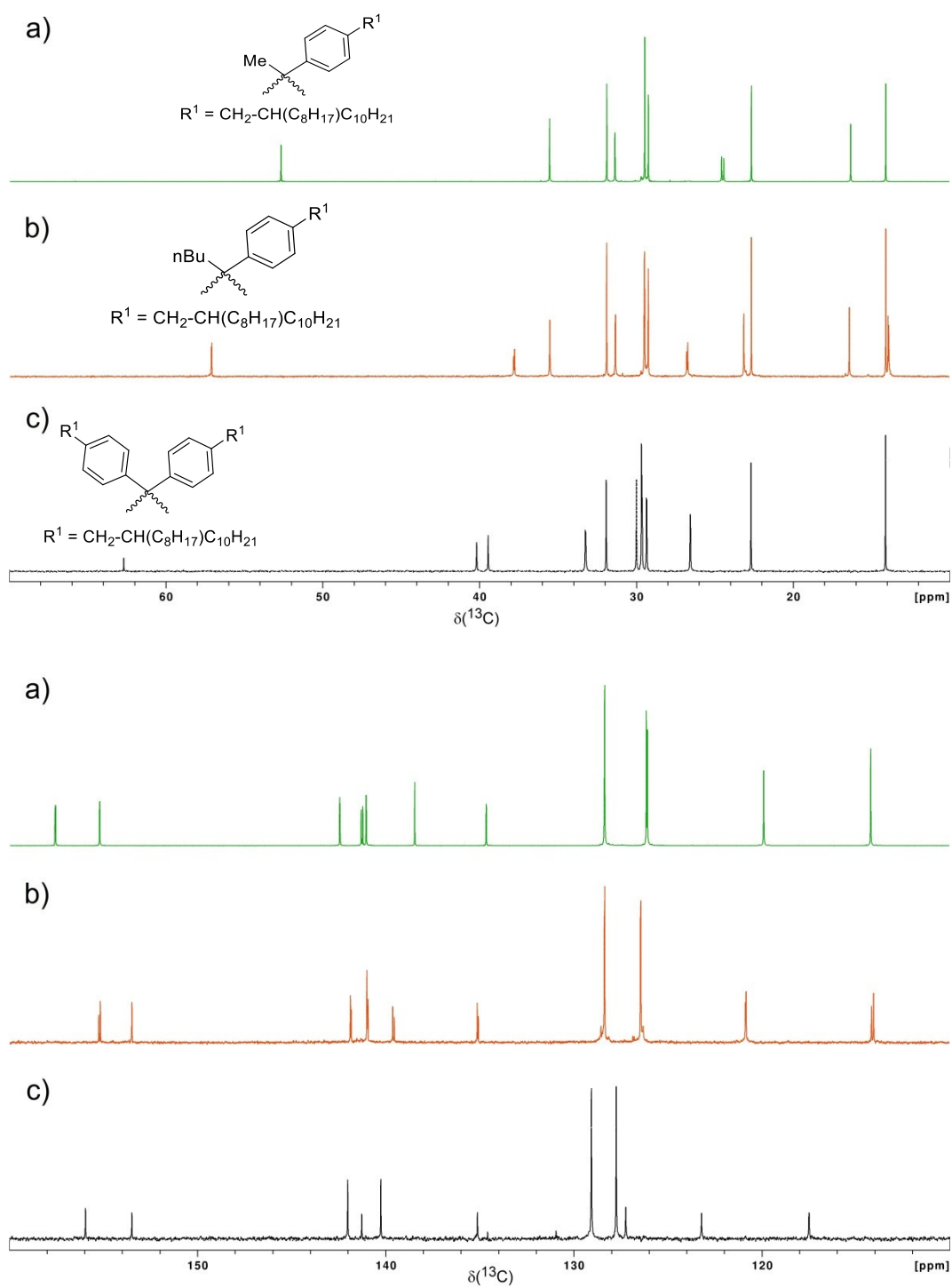


Figure II-S5. ^{13}C NMR spectra (aliphatic (top) and aromatic carbons' region (bottom)) of model compound **8** (a), **9** (b) and monomer **IDT-Ph₂₀** (c) in CDCl_3 .

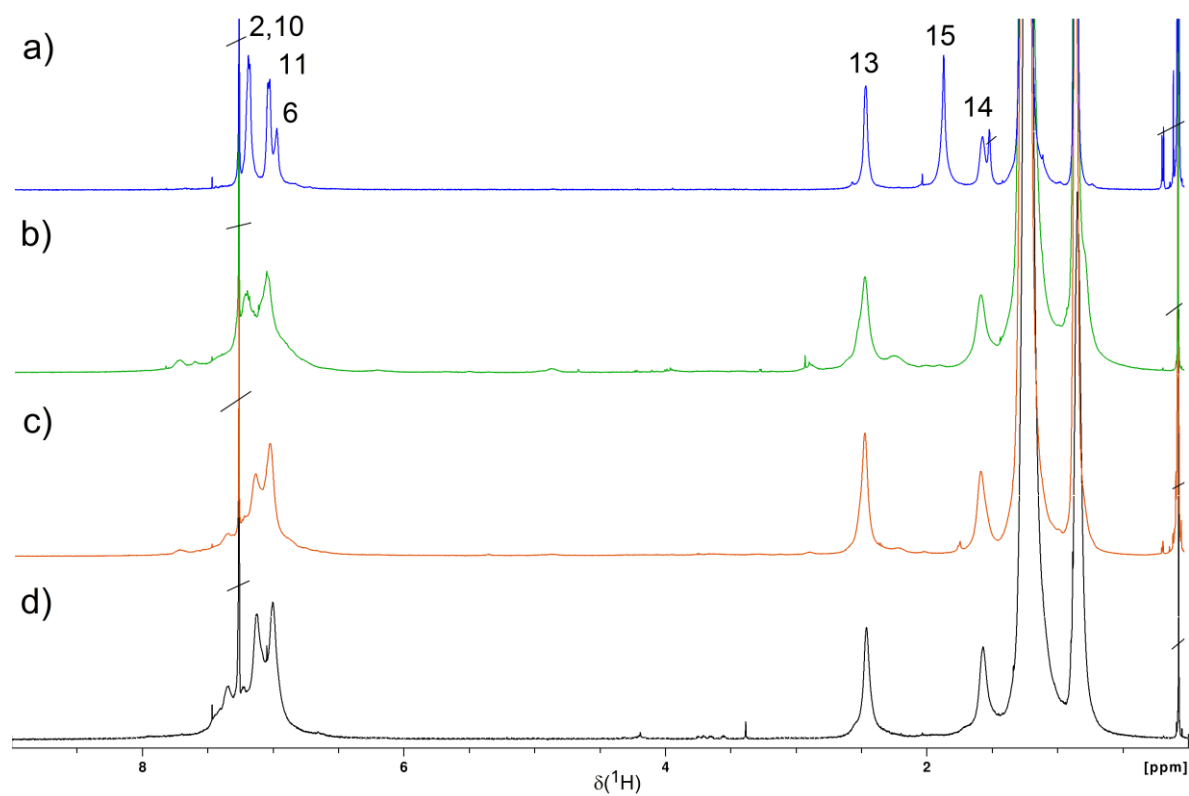


Figure II-S6. ^1H NMR spectra of *PIDT* polymers *P1^A-Me/Ph₂₀* (a), *P2^A-Bu/Ph₂₀* (b), *P3^A-Ph₂₀/Ph₂₀* (c) and *P11^B-Ph₂₀/Ph₂₀* (d) in CDCl_3 .

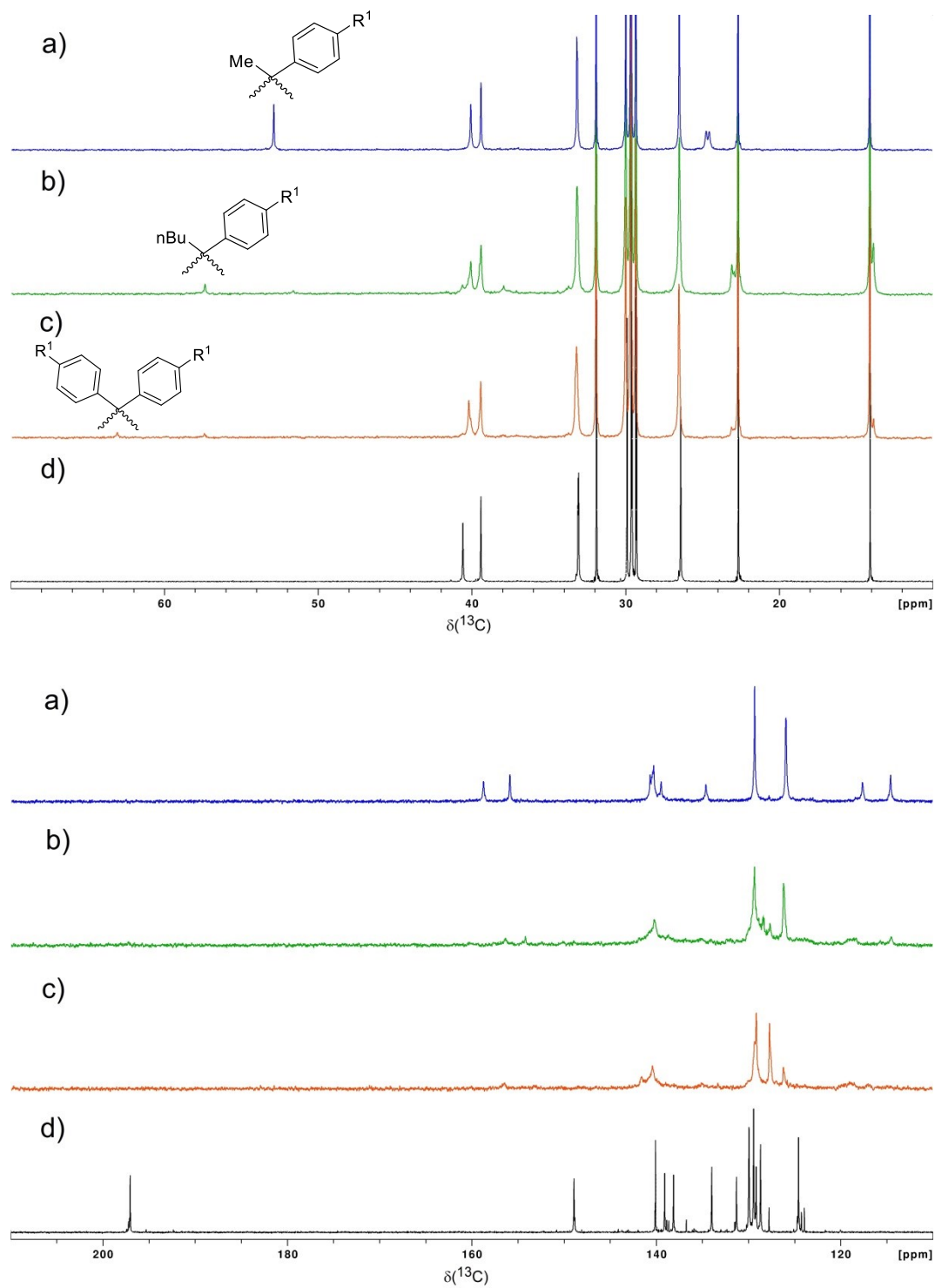


Figure II-S7. ^{13}C NMR spectra (aliphatic (top) and aromatic carbons' region (bottom)) of PIDT polymers $\text{P1}^{\text{A}}\text{-Me/Ph}_{20}$ (a), $\text{P2}^{\text{A}}\text{-Bu/Ph}_{20}$ (b), $\text{P3}^{\text{A}}\text{-Ph}_{20}/\text{Ph}_{20}$ (c) and P(K-alt-T2) , entry 19, (d) in CDCl_3 . $\text{R}^1 = 2\text{-octyldodecyl}$.

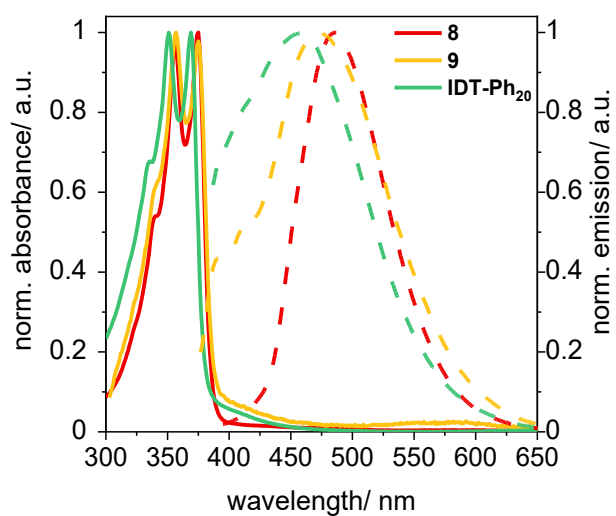


Figure II-S8. UV-vis and emission spectra of model compounds **8**, **9** and monomer **IDT-Ph₂₀**.

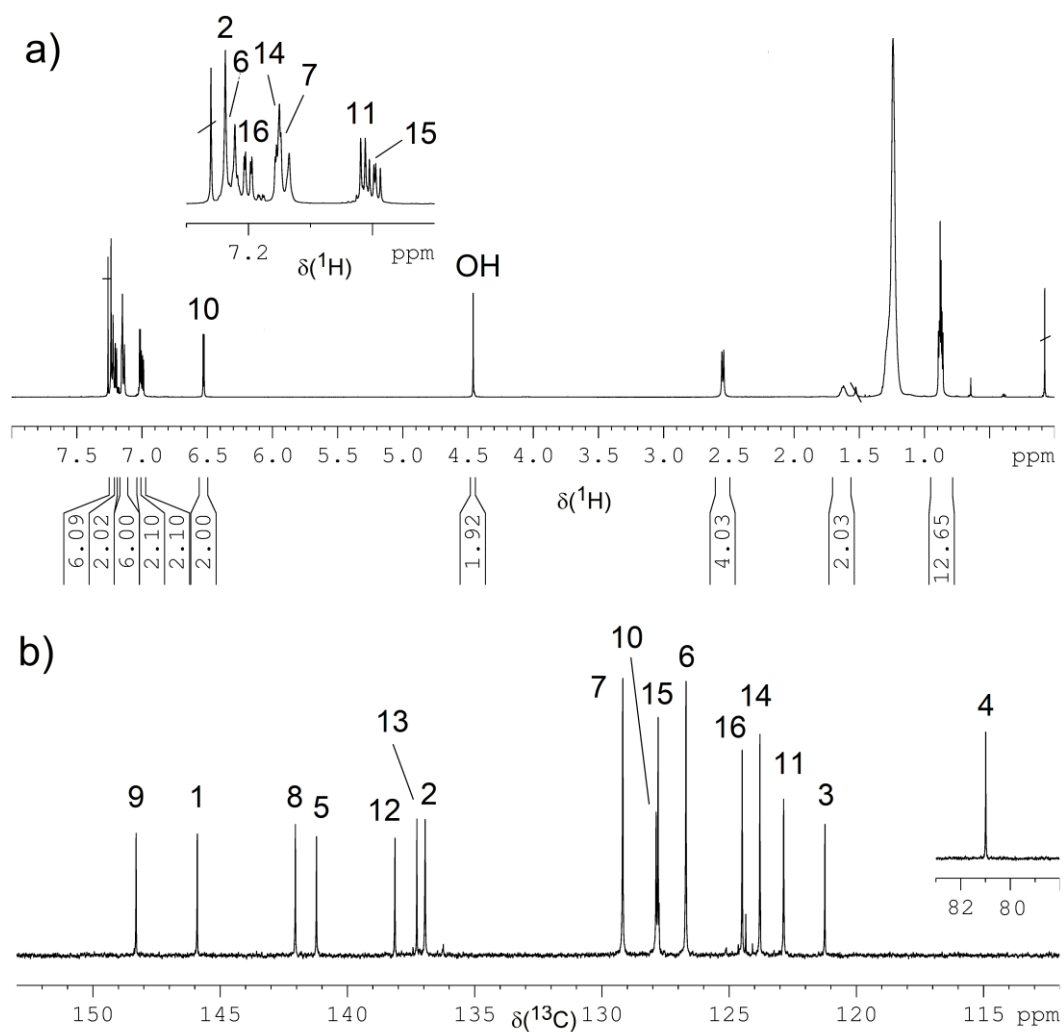


Figure II-S9. ^1H (a) and ^{13}C NMR spectrum (b, regions) of model compound **10** in CDCl_3 .

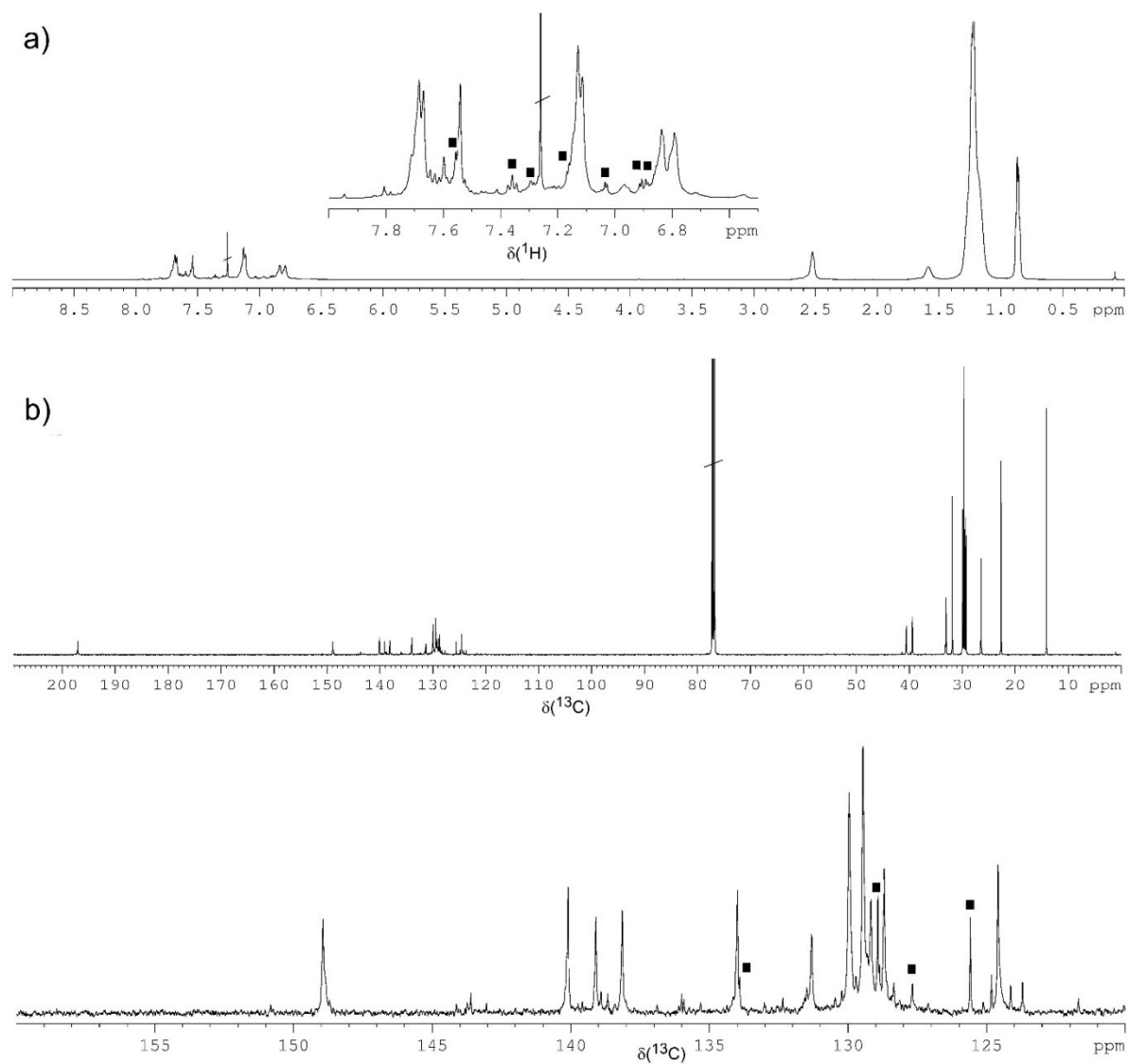


Figure II-S10. ^1H NMR (top) and ^{13}C NMR spectrum (bottom) of $P(K\text{-alt-T2})_{\text{term}}$ in CDCl_3 . The squares mark signals of the seven ^1H NMR signals of the $-\text{T2Ph}$ end group and the four ^{13}C NMR signals of the Ph group, respectively.

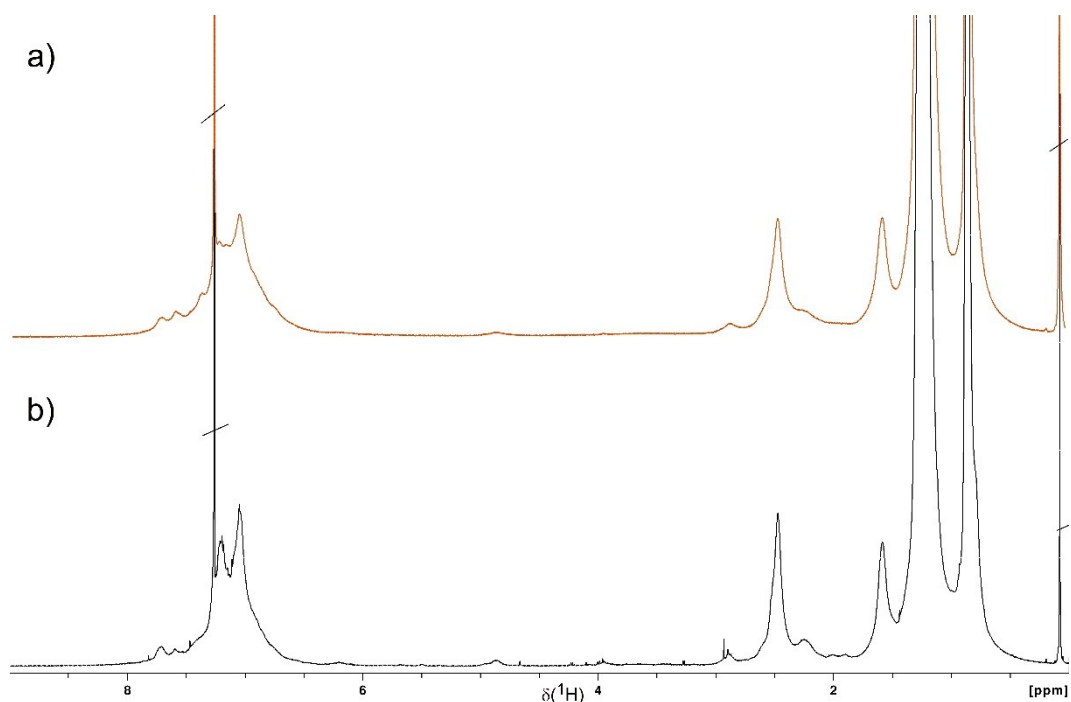


Figure II-S11. ^1H NMR spectra of $\text{P2}^{\text{A-term}}\text{-Bu/Ph}_{20}$ (a) and $\text{P2}^{\text{A}}\text{-Bu/Ph}_{20}$ (b) in CDCl_3 .

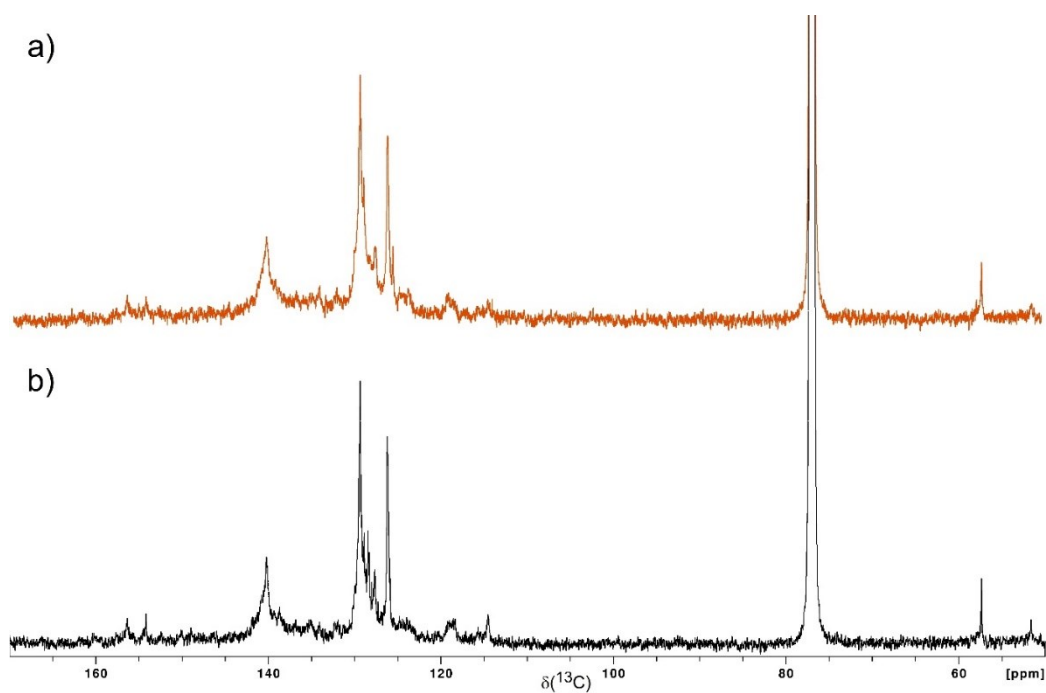


Figure II-S12. ^{13}C NMR spectra (region) of $\text{P2}^{\text{A-term}}\text{-Bu/Ph}_{20}$ (a) and $\text{P2}^{\text{A}}\text{-Bu/Ph}_{20}$ (b) in CDCl_3 .

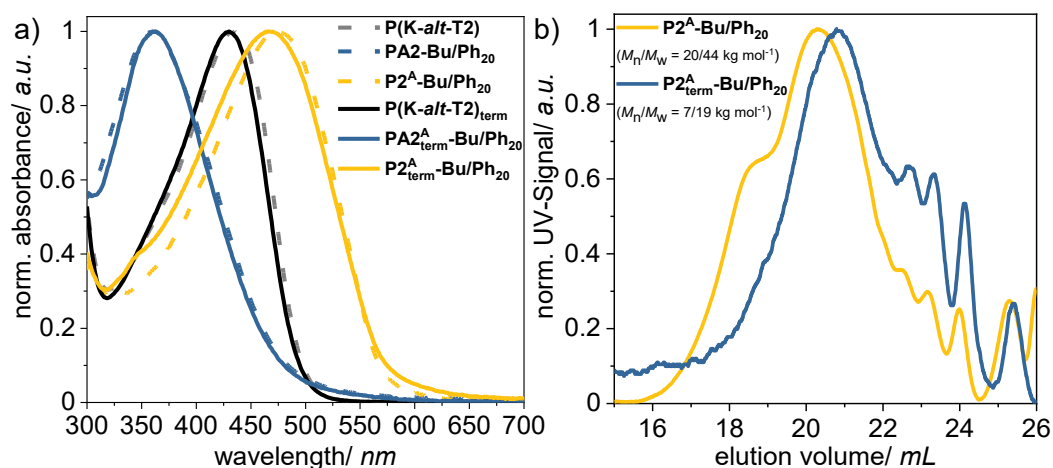


Figure II-S13. a) Comparison of reaction control by UV-vis spectroscopy of polymer analogous cyclization to of $P2^A$ -Bu/Ph₂₀ and $P2^A_{term}$ -Bu/Ph₂₀ in CHCl₃ solution at r.t. b) SEC curves of $P2^A$ -Bu/Ph₂₀ and $P2^A_{term}$ -Bu/Ph₂₀.

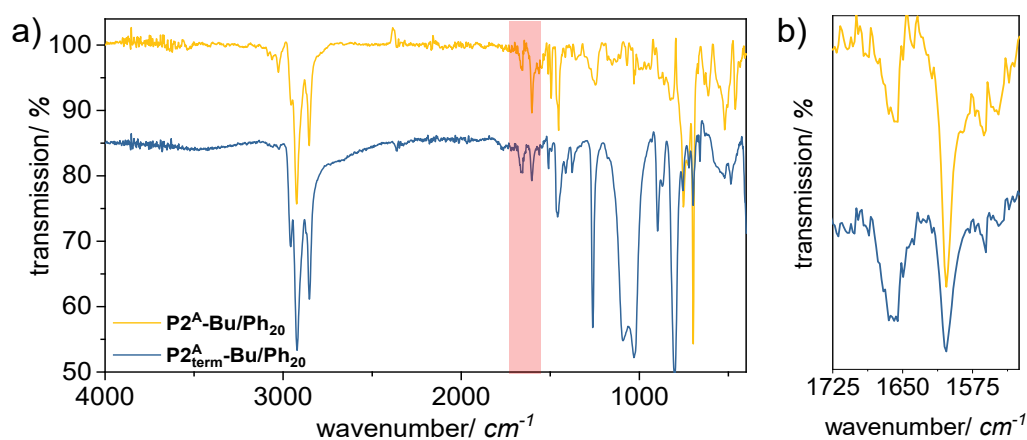


Figure II-S14. a) Comparison of IR spectra of $P2^A$ -Bu/Ph₂₀ and $P2^A_{term}$ -Bu/Ph₂₀ b) shows the enlarged wavenumber range of the red box.

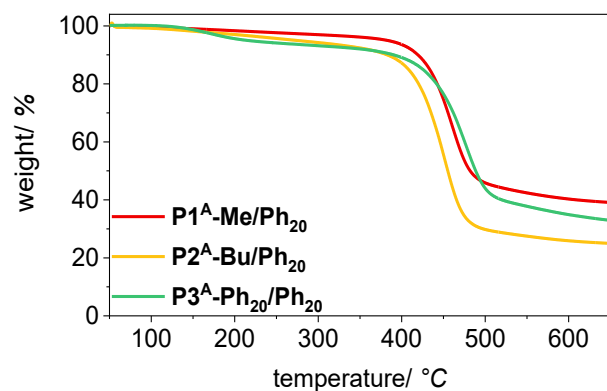


Figure II-S15. Thermograms of *PIDTs* in N_2 .

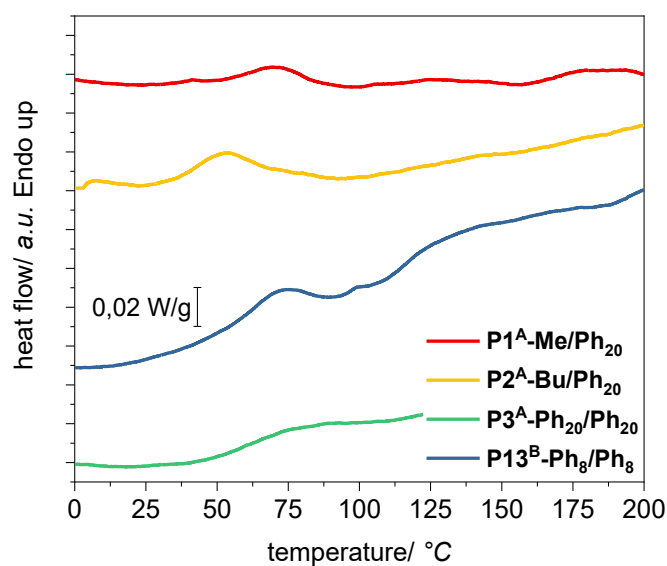


Figure II-S16. DSC curves of *PIDTs* polymers *P1^A-Me/Ph₂₀*, *P2^A-Bu/Ph₂₀*, *P3^A-Ph₂₀/Ph₂₀* and *P13^B-Ph₈/Ph₈*. First heating measured with 20 K min^{-1} .

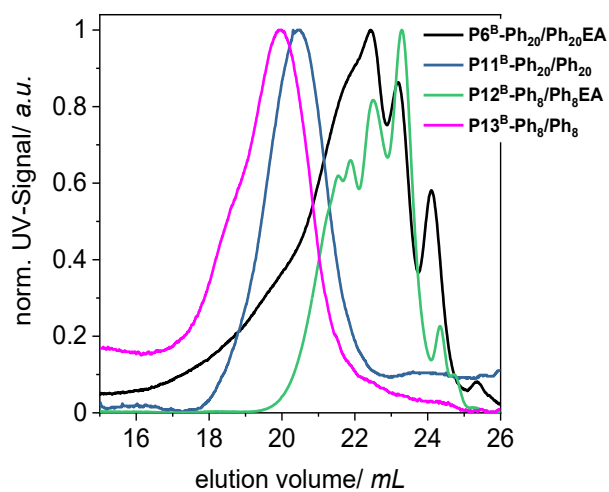


Figure II-S17. SEC curves of $P11^B\text{-Ph}_{20}/\text{Ph}_{20}$ and $P13^B\text{-Ph}_8/\text{Ph}_8$ via oxDAP (ethyl acetate (EA) fractions $P6^B\text{-Ph}_{20}/\text{Ph}_{20}\text{EA}$ and $P12^B\text{-Ph}_8/\text{Ph}_8\text{EA}$ as starting material).

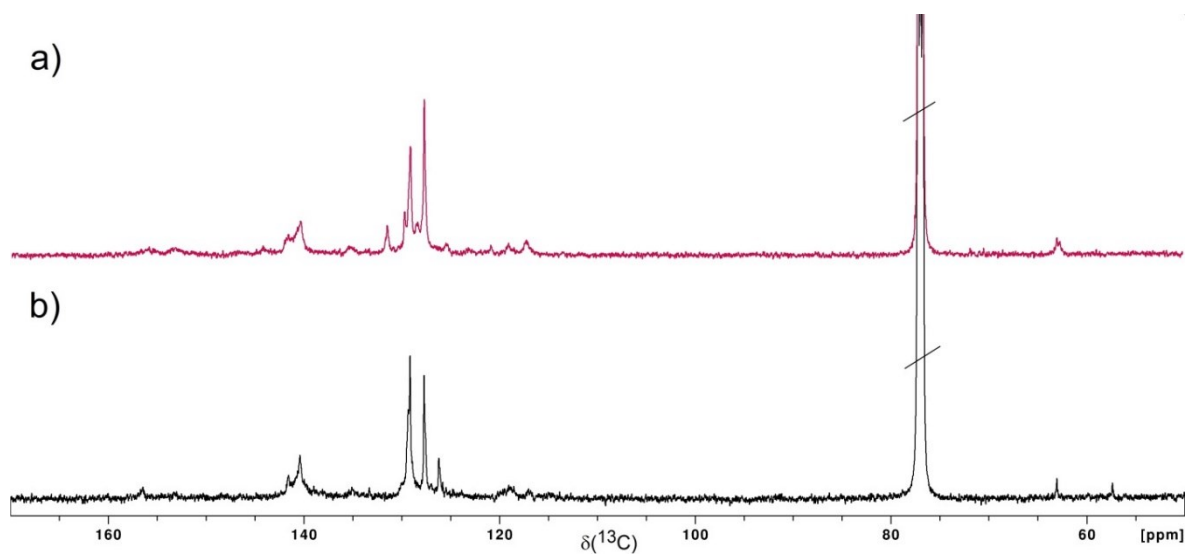


Figure II-S18. ^{13}C NMR spectra (region) of $P11^B\text{-Ph}_{20}/\text{Ph}_{20}$ (a) and $P3^A\text{-Ph}_{20}/\text{Ph}_{20}$ (b) in CDCl_3 .

III. Influence of synthetic pathway, molecular weight and side chains on properties of indacenodithiophene-benzothiadiazole copolymers made by direct arylation polycondensation

Desiree Adamczak,^a Andrea Perinot,^b Hartmut Komber,^c Anna Illy,^a Sandra Hultmark,^d Bianca Passarella,^{b,e} Wen Liang Tan,^f Sebastian Hutsch,^{g,h} David Becker-Koch,ⁱ Charlotte Rapley,^j Alberto D. Scaccabarozzi,^b Martin Heeney,^j Yana Vaynzof,ⁱ Frank Ortmann,^{g,h} Christopher R. McNeill,^f Christian Müller,^d Mario Caironi^b and Michael Sommer^a

^aTechnische Universität Chemnitz Polymerchemie, Straße der Nationen 62, 09111 Chemnitz, Germany.

^bCenter for Nano Science and Technology @PoliMi, Istituto Italiano di Tecnologia, Via Pascoli 70/3, 20133 Milano, Italy.

^cLeibniz-Institut für Polymerforschung Dresden e.V., Hohe Straße 6, 01069 Dresden, Germany.

^dDepartment of Chemistry and Chemical Engineering, Chalmers University of Technology, 412 96 Gothenburg, Sweden.

^eDipartimento di Elettronica, Informazione e Bioingegneria, Politecnico di Milano, 20133, Milan, Italy.

^fDepartment of Materials Science and Engineering, Monash University, Wellington Road, Clayton, Victoria 3800, Australia.

^gDepartment of Chemistry, Technische Universität München, 85748 Garching, Germany.

^hCenter for Advancing Electronics Dresden, Technische Universität Dresden, 01062, Dresden, Germany.

ⁱIntegrated Centre for Applied Physics and Photonic Materials and Centre for Advancing Electronics Dresden (cfaed), Technical University of Dresden, Nöthnitzer Str. 61, Dresden, 01187 Germany.

^jDepartment of Chemistry and Centre for Processable Electronics, Imperial College London, London W12 0BZ, UK.

published in *J. Mater. Chem. C*, **2021**, 9 (13), 4597-4606.

Copyright © 2021 Royal Society of Chemistry

<https://doi.org/10.1039/D1TC00043H>

ABSTRACT. Atom-economic protocols for the synthesis of poly(indacenodithiophene-*alt*-benzothiadiazole) (PIDTBT) are presented in which all C-C coupling steps are achieved by direct arylation. Using two different synthetic pathways, PIDTBT copolymers with different side chains (hexylphenyl, octylphenyl, dodecyl, methyl/2-octyldodecylphenyl, 2-octyldodecylphenyl/2-octyldodecylphenyl) and molecular weight (MW) are prepared. Route A makes use of direct arylation polycondensation (DAP) of indacenodithiophene (IDT) and 4,7-dibromo-2,1,3-benzothiadiazole (BTBr₂) leading to PIDTBT in high yields, with adjustable MW and without indications for structural defects. Route B starts from a polyketone precursor also prepared by DAP following cyclization. While route B allows introduction of asymmetric side chains at the IDT unit, polymer analogous cyclization gives rise to defect formation. The absorption coefficient of PIDTBT with alkylphenyl side chains made by route A increases with MW. Field-effect hole mobilities around $\sim 10^{-2} \text{ cm}^2 \text{ V}^{-1} \text{ s}^{-1}$ are molecular weight-independent, which is ascribed to a largely amorphous thin film morphology. PIDTBT with linear dodecyl side (C12) chains exhibits a bathochromic shift (20 nm), in agreement with theory, and more pronounced vibronic contributions to absorption spectra. In comparison to alkylphenyl side chains, C12 side chains allow for increased order in thin films, a weak melting endotherm and lower energetic disorder, which altogether explain substantially higher field-effect hole mobilities of $\sim 10^{-1} \text{ cm}^2 \text{ V}^{-1} \text{ s}^{-1}$.

INTRODUCTION

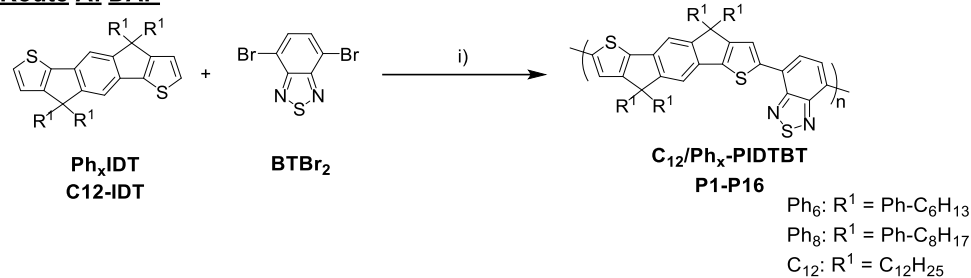
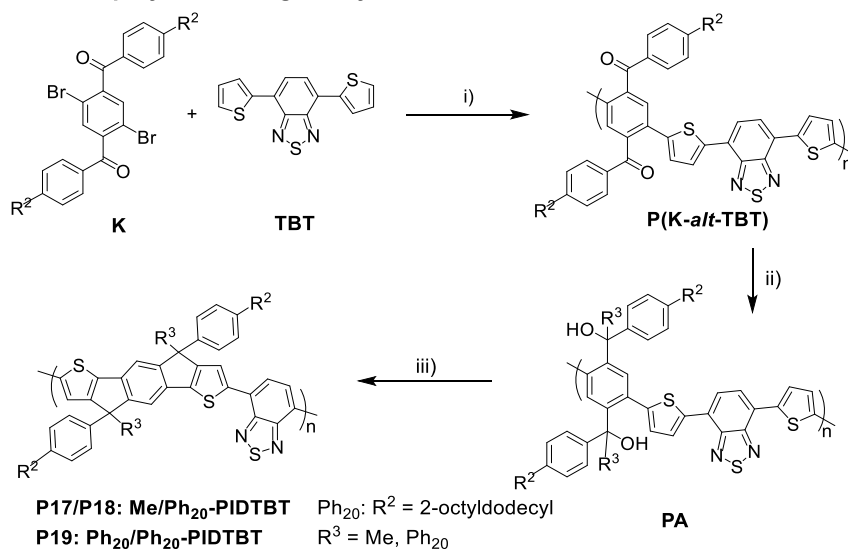
Alternating copolymers of indacenodithiophene (IDT) and benzothiadiazole (BT), PIDTBT, have shown intriguing properties as active materials in organic photovoltaics (OPVs) and organic field-effect transistors (OFETs).¹⁻⁵ Due to the preserved coplanar fused aromatic ring system and thus maximized π -orbital overlap of IDT as well as low energetic disorder of PIDTBT, unique electronic properties have been observed.⁶⁻⁸ In OPV devices, PIDTBT:fullerene (PC₇₁BM) blends achieved power conversion efficiencies (PCE) over 6%.^{9,10} Recently, small molecules based on an IDT-BT core structure were investigated as replacements for fullerene-based acceptors.¹¹⁻¹³ Despite their rigid backbone structure and morphologies lacking long range crystalline order,^{1,14} IDT copolymers are known for their excellent charge transport properties. The combination of IDT and BT units gives rise to a rigid copolymer chain with steep torsion potential, thus favouring charge transport.^{1,3} Alkyl-substituted P(IDT-*alt*-BT) copolymers exhibited low conformational disorder and field-effect mobilities up to $\mu_{\text{sat}} = 10 \text{ cm}^2 \text{ V}^{-1} \text{ s}^{-1}$.^{3,5,15} It is further noted that IDT-based materials with alkyl

side chains are mostly used for transistor applications, while those with alkylphenyl side chains are designed for OPV materials. While the influence of IDT side chains has been investigated for different aliphatic ones,^{2,16} the influence of alkylphenyl side chains on properties of PIDTBT copolymers is less clear. Despite their generally appealing properties, IDT copolymers suffer from tedious reaction pathways.^{17–19} State-of-the-art syntheses involve several steps of traditional transition-metal-catalyzed cross couplings based on Suzuki, Negishi or Stille reactions.^{10,20} To eliminate usage of undesired toxic or unstable reagents as well as byproducts, and to shorten lengthy reaction pathways simultaneously, direct arylation (DA) as an atom-economical method is highly attractive.^{21–23} Direct arylation polycondensation (DAP) is meanwhile the method of choice for naphthalene diimide copolymers^{24–26} and a viable alternative for the preparation of many other donor-acceptor copolymers.^{27–29} Under optimized conditions, control over molecular weight (MW), a low degree of main chain defects and high yields can be achieved. To date, few reports that report IDT copolymers via DAP and that yield moderate molecular weights have emerged.^{30–32} Recently, we reported IDT homopolymers via DAP.³³

Here, we present a comprehensive study on a series of PIDTBT made by different synthetic pathways, with varying aliphatic and alkylphenyl side chains, and different molecular weight. PIDTBT can be made by direct DAP (route A) as well as by polymer analogous cyclization (route B, Scheme III-1). The latter pathway leads to structurally ill-defined products with inferior properties. PIDTBT made by route A with alkylphenyl side chains is molecularly defined, morphology is largely amorphous and field-effect transistor (FET) hole mobilities are independent of molecular weight. In contrast, route A PIDTBT with linear C12 side chains exhibits red-shifted absorption with better defined vibronic structure, increased order in thin films and lower energetic disorder. These findings explain the higher FET hole mobility of PIDTBT with C12 side chains and provide a detailed overview of how side chains influence the properties of PIDTBT.

RESULTS AND DISCUSSION

Synthesis and characterization. The synthetic routes towards PIDTBT are shown in Scheme III-1. All C-C couplings, including monomer synthesis of Ph_xIDT, were achieved via direct arylation. The optimization of IDT monomer synthesis was investigated previously.³³ Monomer K was prepared according to previous reports.^{17,33,34}

Route A: DAP**Route B: polymer analogous cyclization**

Scheme III-1. Two routes for the synthesis of PIDTBT. Reaction conditions: (i) 0.05-0.25 M in mesitylene, Pd_2dba_3 (5 mol%), $P(o\text{-anisyl})_3$ (20 mol%), PivOH (1 eq), K_2CO_3 (3 eq), 80-100 °C, 72 h; (ii) 4×10^{-3} M in toluene, $\text{R}^3\text{-Li}$ (8 eq), room temperature (rt), 3 h; (iii) 4×10^{-3} M in dichloromethane, $\text{BF}_3 \text{OEt}_2$ (18 eq), rt, 3 h.

Copolymerization of Ph_6IDT with 4,7-dibromo-2,1,3-benzothiadiazole (BTBr_2) via DAP yielded $\text{Ph}_6\text{-PIDTBT}$ copolymers with MWs up to $M_{n,\text{SEC}} = 38 \text{ kg mol}^{-1}$. Optimization of MW was carried out considering effects of solvent, temperature, catalyst loading and monomer concentration (Table III-1, entries **P1-P15**). Lowering the reaction temperature led to an increase in MW. Regarding monomer concentration, an optimum was found for 0.1 M. Monomer concentrations smaller than 0.1 M resulted in lower MWs due to slower build-up of chain length and consequently a larger impact of termination reactions (Table III-1, entry **P7**). Concentrations larger than 0.1 M led to early gelation of the reaction mixture (Table III-1, entry **P8**). The use of a different solvent such as chlorobenzene to enhance solubility of the formed polymer chains enabled reactions at higher monomer concentrations and lower catalyst loadings, but did not generate higher MW (Table III-1, entries **P13-P15**). To increase MW further, Ph_8IDT was used in route A. However, despite the better solubility of the monomer higher MWs of the corresponding copolymers were not achieved, eventually due to a lower

monomer purity as a result of more difficult purification. To change MW, a reduction of catalyst loading (Table III-1, **P5**) and variation of reaction temperature (Table III-1, **P9/P10**) can be used. For route A, however, adjustment of MW is best achieved by using optimized conditions of entry **P10** following slightly changed stoichiometry (Table III-1, **P6**). The synthesis of C12-PIDTBT via DAP proceeded smoothly to give **P16** with $M_{n,SEC} = 32 \text{ kg mol}^{-1}$. In comparison to **P10** with Ph_6 side chains, the reaction mixture containing **P16** did not gelate during polymerization.

Table III-1. Reaction conditions for syntheses of PIDTBT made via route A and route B.

	entry	R ¹	R ² /R ³	solv	[M]/ M	T/ °C	cat/ P-ligand mol%	M_n/M_w^a kg mol ⁻¹	\bar{D}^a	yield ^b / %
Route A	P1	Ph ₈		Mes	0.1	100	5/20	21/48	2.3	95
	P2	Ph ₈		DM Ac	0.1	100	5/20	-	-	-
	P3	Ph ₈		Mes	0.1	80	5/20	28/62	2.2	79
	P4	Ph ₈		Mes	0.1	90	5/20	11/18	1.6	62
	P5	Ph ₈		Mes	0.1	100	1/5	18/31	1.7	69
	P6^c	Ph ₈		Mes	0.1	80	5/20	17/38	2.2	75
	P7	Ph ₆		Mes	0.05	100	5/20	15/32	2.2	87
	P8	Ph ₆		Mes	0.25	100	5/20	12/33	2.7	87
	P9^d	Ph ₆		Mes	0.1	100	5/20	18/39	2.1	84
	P10^d	Ph ₆		Mes	0.1	80	5/20	38/130	3.4	92
	P11^{c,d}	Ph ₆		Mes	0.1	80	5/20	24/99	4.1	88
	P12	Ph ₆		Mes	0.1	80	2/-	-	-	-
	P13	Ph ₆		CB	0.1	100	5/20	8/14	1.7	82
	P14	Ph ₆		CB	0.25	100	2/8	19/96	5.2	81
	P15	Ph ₆		CB	0.4	100	5/20	16/78	4.8	87
Route B	P16	C ₁₂ H ₂₅		Mes	0.1	80	5/20	32/55	1.7	74
	P(K-<i>alt</i>-TBT)		Ph ₂₀	Mes	0.25	80	5/20	11/15	1.4	75
	P17^e		Me/Ph ₂₀					21/6.6*10 ^{8f}	3*10 ^{4f}	5
	P18		Me/Ph ₂₀					17/1.5*10 ^{7f}	833 ^f	5
	P19		Ph ₂₀ /Ph ₂₀					18/88	4.9	73

^aFrom SEC in chloroform with PS calibration. ^bIsolated yield after Soxhlet extraction with acetone, ethyl acetate and chloroform. ^cA slight excess of BTBr₂ of 5 mol% was used. ^dGelation after 24 hours. ^eWithout phenyl-termination. ^fBimodal SEC curves with very large M_w and \bar{D} values likely caused by chain-chain coupling as well as aggregation whenever Me/Ph₂₀ side chain patterns were used. Mes and CB are mesitylene and chlorobenzene, respectively.

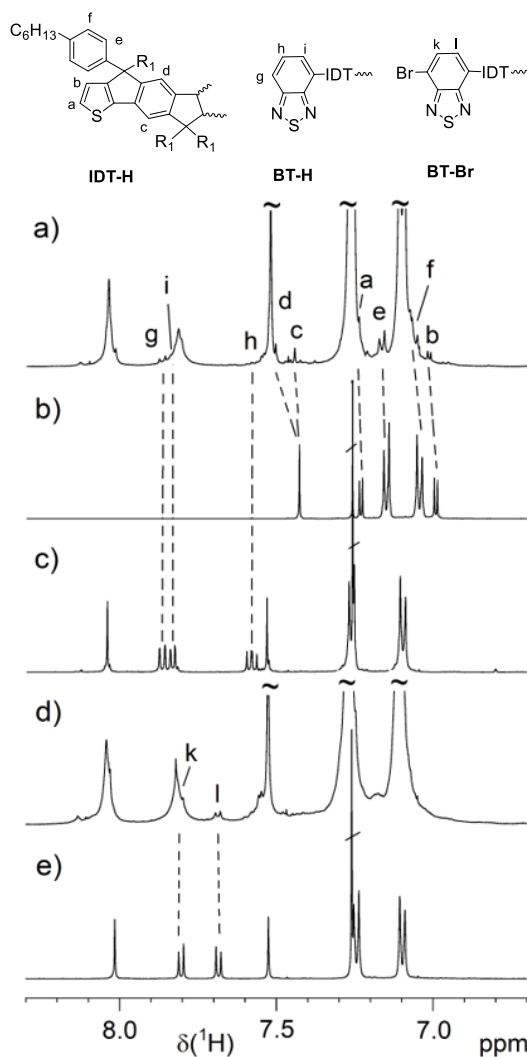
Detected end group structures

Figure III-1. ^1H NMR spectrum (region) of IDT- and H-BT-terminated PIDTBT (a) (**P1**) compared to the spectra of Ph_6IDT monomer (b) and H-BT model compound **2** (c). The spectrum of a Br-BT-terminated PIDTBT (d) (**P6**) is compared with the spectrum of Br-BT model compound **1** (e). $R^1 = \text{Ph}_6$. Solvent: CDCl_3 .

To gain insight into details of the molecular structure of PIDTBT, NMR spectroscopy was used with assignments aided by model compounds. The ^1H and ^{13}C NMR spectra of the PIDTBT copolymers DAP did not show obvious evidence for defects (Figures III-S1–S4). However, it should be noted that defects such as homocouplings³⁵ are generally challenging to detect for IDT copolymers as a result of significant signal broadening and overlap with backbone signals.³³ Because of the low intensity of end group signals, a comparison with spectra of appropriate model compounds is an efficient method to assign these signals in NMR spectra of copolymers (Figure III-1).^{24,25} The Ph_6IDT monomer represents the IDT-H end group, and the two IDT-based model compounds **1** (Br-BTIDTBT-Br) and **2** (H-BTIDTBT-H)

were synthesized to mimic BT-Br and BT-H end groups, respectively (for details see SI). The aromatic region of the ^1H NMR spectra of **P1** and **P6** are depicted in Figure III-1a and d, respectively. Comparison with the monomer Ph₆IDT (Figure III-1b and S5) and model **2** (Figure III-1c and S7) revealed IDT-H and BT-H termination for **P1**. The BT-Br end group (model **1**, Figure III-1e and S6) was not detected. However, BT-Br end groups are contained exclusively in the second copolymer (**P6**), for which a slight excess of BTBr₂ was used. A further difference between **P1** and **P6** is reaction temperature. We assume that the lower temperature used for **P6** (80°C) contributes to the presence of BT-Br end groups by lowering the probability for dehalogenation.

Route B entails the preparation of PIDTBT copolymers via DAP followed by polymer analogous cyclization (Scheme III-1, route B) as described previously.³³ Here, MW is generally strongly limited by solubility of the polyketone precursor **P(K-alt-TBT)**. Even long, branched side chains such as R = 2-octyldodecyl only led to moderate MW of $M_{n,SEC} = 11 \text{ kg mol}^{-1}$. The progress of the polymer analogous reactions was monitored by UV-vis and IR spectroscopy (Figures III-S10 and S11). Additional signals in the NMR spectra (Figure III-S12 and 13) and very broad and bimodal MW distributions of **P17-P19** (Figure III-S14) suggested significant structural defects of unclear nature. Efforts were made to gain further insight. To eliminate possible side reactions associated with thiophene-based end groups during the post-polymerization sequence, **P(K-alt-TBT)** was terminated with bromobenzene.³³ Phenyl termination of **P(K-alt-TBT)** reduced the very large dispersity of the corresponding PIDTBT from 3×10^4 to 833 (compare entries **P17** and **P18** without and with phenyl termination, respectively). Considering that dispersity of **P19** with Ph₂₀/Ph₂₀ side chains is ~ 5 and thus comparably large, yet lower compared to **P17** and **P18**, we conclude that **P17** and **P18** with Me/Ph₂₀ side chains likely show a combination of chain-chain coupling and additional aggregation. These results from NMR spectroscopy and SEC clearly indicated significant defects of unclear nature that are unlikely to be moved entirely. Additionally, UV-vis spectra of PIDTBT made via route B were much different (Figure III-2c and d), and FET hole mobilities were much reduced (see Table III-3 and further discussion below) compared to route A.

Obviously, route A is the method of choice to make well-defined PIDTBT via DAP, and PIDTBT made by route B was only further used and mentioned where helpful for a comprehensive discussion. What remains open at this point is the investigation of homocouplings in PIDTBT made by route A, which cannot be ruled out entirely based on the

herein performed NMR spectroscopic investigations. Even with the homopolymer PIDT as model compound for IDT CH/CH homocoupling being available, the broad signals did not allow for conclusive statements here. Obtaining direct NMR spectroscopic evidence for homocouplings in PIDTBT is therefore very challenging. However, optical data (*vide infra*) suggested well-defined PIDTBT from route A to be formed, which is indirect evidence for the absence of such main chain structural defects.

Selected copolymers were further investigated by UV-vis and photoluminescence (PL) spectroscopy, cyclic voltammetry (CV), density functional theory (DFT) calculations, thermogravimetry (TGA), differential scanning calorimetry (DSC), fast scanning calorimetry (FSC), field-effect mobility measurements, grazing incidence X-ray scattering (GIWAXS) and photothermal deflection spectroscopy (PDS). Important results are compiled in Table III-2 and further discussed in detail in what follows.

Table III-2. Optical and thermal properties of selected PIDTBT copolymers.

entry	R ¹	R ² /R ³	M_n/M_w^a kg mol ⁻¹	$\epsilon_{\text{abs, max}}^b$ (sol) ^b /nm	$\epsilon_{\text{em, max}}^b$ (sol) ^b /nm	$\epsilon_{\text{abs, max}}^c$ (film) ^c /nm	$\epsilon_{\text{abs, max}}^c/10^3$ L mol ⁻¹ cm ⁻¹	$T_d^{c, d}$ °C
Route A	P1	Ph ₈	21/48	<i>645/411</i>	696	-	53	-
	P3	Ph ₈	28/62	<i>644/410</i>	696	<i>651/414</i>	57	427
	P4	Ph ₈	11/18	<i>627/403</i>	695	-	34	-
	P5	Ph ₈	18/31	<i>643/408</i>	696	-	45	-
	P9	Ph ₆	18/39	<i>645/411</i>	697	-	41	449
	P10	Ph ₆	38/138	<i>643/410</i>	698	<i>651/416</i>	57	-
	P16	C ₁₂ H ₂₅	32/55	<i>664/415</i>	715	<i>682/418</i>	56	408
Route B	P17^e	Me/Ph ₂₀	21/6.6*10 ^{8f}	<i>595/394</i>	693		16	-
	P18	Me/Ph ₂₀	17/1.5*10 ^{7f}	<i>596/411</i>	695		-	-
	P19	Ph ₂₀ /Ph ₂₀	18/88	<i>615/410</i>	688		40	371

^aFrom SEC in chloroform with PS calibration. ^bMeasured in chloroform at room temperature; maxima with the highest intensity in italic. ^cMeasurements were carried out on selected samples. ^dDegradation temperature at 5% weight loss. ^eWithout phenyl-termination. ^fBimodal SEC curves, large M_w and D values likely caused by chain-chain coupling as well as aggregation whenever Me/Ph₂₀ side chain patterns were used.

Optical properties. The dependence of MW of PIDTBT with Ph₈ side chains made by Rout A on UV-vis and PL spectra is shown in Figure III-2a and b. With increasing MW a slight bathochromic shift of the absorption maximum and an increase of the molar extinction coefficient $\epsilon_{\text{abs, max}}$ can be observed. This effect can be attributed to an increasing contribution of the vibronic band at longer wavelength, which in turn may be caused by increasing chain

length.³⁶ Notably, the similarity of the spectra in Figure III-2a including a sharp onset at large wavelength is indicative for structurally well-defined copolymers, and thus a robust synthetic DAP protocol. Intensity of PL in solution correlates similarly with MW as found for the molar extinction coefficient. Emission maxima around $\lambda_{\text{em, max}} = 696$ nm are weakly dependent on MW. These almost constant maxima thus result in decreased Stokes shifts for increasing MW (**P3**: $\Delta\lambda = 52$ nm; **P4**: $\Delta\lambda = 68$ nm). Figure III-2c and d illustrates the influence the synthetic method and IDT side chain pattern on absorption. Small differences between the molar extinction coefficients and intensities of emission maxima of **P9** (route A, R = Ph₆) and **P5** (route A, R = Ph₈) likely arise from slightly different molar masses of the repeat unit and MWs. The UV-vis spectra of **P17** and **P19** made via route B are significantly different. The hypsochromically shifted absorption maxima as well as the up to three times smaller molar extinction coefficients suggest disruptions of the π -system due to defects produced during the cyclization step. The emission spectra display the same trends of decreased molar extinction coefficients and hypsochromically shifted spectra thus corroborating this argumentation (Figure III-2d).

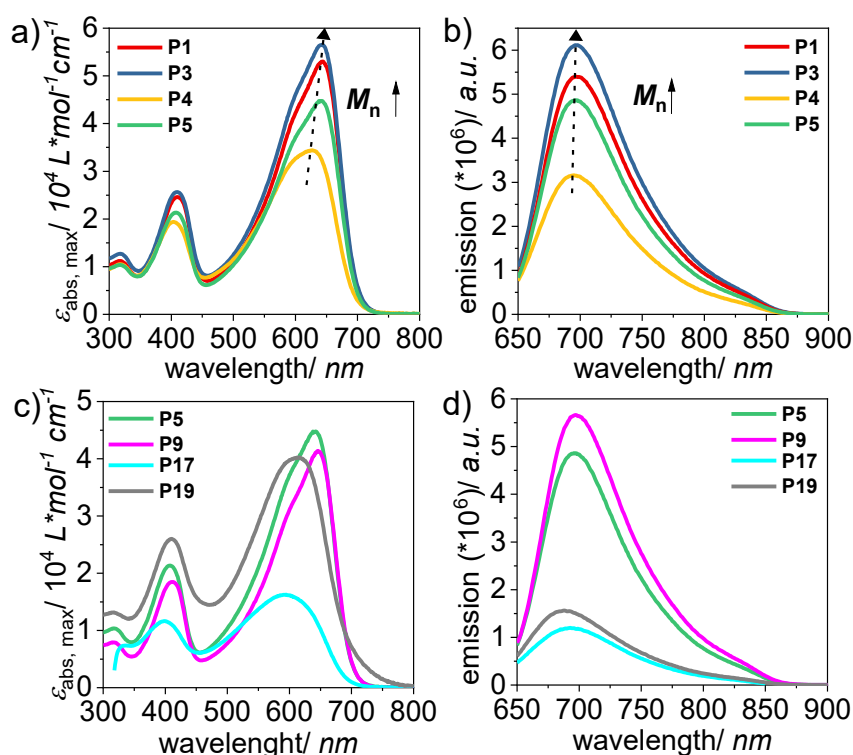


Figure III-2. UV-vis and PL spectra of PIDTBT of different MW (a, b) and of PIDTBT with different side chains (c, d) in chloroform solution. (**P1-P5**: $R^I = \text{Ph}_8$, **P9**: $R^I = \text{Ph}_6$, **P17**: Me/Ph₂₀; **P19**: Ph₂₀/Ph₂₀).

The effect of aromatic *versus* aliphatic side chains on absorption is displayed in Figure III-3. Despite the slightly lower molecular weight of **P16** ($R = C_{12}H_{25}$) compared to **P10** ($R = Ph_6$), the absorption spectrum shows a bathochromic shift of 20 nm with the molar extinction coefficient at maximum wavelength being retained (Figure III-3a). Further differences are a smaller contribution of the vibronic shoulder around 600 nm for **P16**. The film spectrum of **P10** shows a small shift of the absorption maximum ($\Delta\lambda = 8$ nm), suggesting little conformational changes of the chain upon solidification. The thin film absorption spectrum of **P16** displays a shift of $\Delta\lambda = 12$ nm and additionally develops a pronounced shoulder around 630 nm indicative for increased order (Figure III-3b).

The redshifted absorption spectrum of **P16** results in a reduced optical band gap E_g compared to **P10** ($E_g(\mathbf{P16}) = 1.69$ eV; $E_g(\mathbf{P10}) = 1.73$ eV). The difference of the optical band gap is reflected in the HOMO/LUMO energy levels of **P10** and **P16**. Determination of the energy levels were carried out by cyclic voltammetry (Figure III-S15). The electrochemical analyses reveal a slightly higher lying HOMO energy level of **P16**. In film as well as in solution, the energy of the HOMO levels differ by $\Delta HOMO(\text{film}) = 50$ meV and $\Delta HOMO(\text{solution}) = 30$ meV, respectively. However, while the nature of the side chains influences the HOMO energy levels of PIDTBT, the LUMO energy level remains largely unaffected ($\Delta LUMO(\text{film}) = 0$ meV; $\Delta LUMO(\text{solution}) = -1$ meV). The electrochemical properties are summarized in Table III-S1 (see SI).

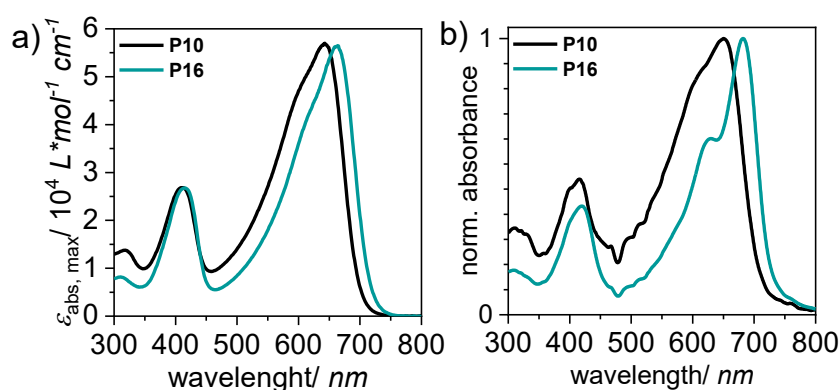


Figure III-3. Comparison of UV-vis spectra in chloroform solution (a) and film (b) of PIDTBT with aromatic (**P10**) and aliphatic (**P16**) side chain pattern via DAP. Films were spin coated (1000 rpm, 60 s) from *o*-DCB solutions (10 mg mL^{-1}).

DFT calculations. To study the reason for the observed shift between the absorption spectra of **P10** and **P16** (ref. Figure III-3), density functional theory (DFT) calculations were performed. First, the structure and energy of the orbitals involved in the optical excitation, which are the highest occupied molecular orbital (HOMO) and the lowest unoccupied

molecular orbital (LUMO), were analysed. The orbitals were calculated with DFT in Gaussian 16³⁷ for a single repeat unit and the complete side chains. More details to the calculations can be found in the methods section (see SI). The resulting orbitals and corresponding Kohn-Sham energies are presented in Figure III-4. The LUMOs are shown in the top of Figure III-4. LUMOs primarily localize at the BT units, while the IDT units receive much less orbital weight and the side chains essentially none. As a result, the different side chains of **P10** and **P16** have a minor impact on the orbital energy of the LUMO and the Kohn-Sham energies differ by only $E_{\text{P16}}^{\text{LUMO}} - E_{\text{P10}}^{\text{LUMO}} = -5 \text{ meV}$. In contrast, the HOMOs delocalize over the full backbone (bottom of Figure III-4) and expand over the alkyl chain of **P16** and phenyl group of **P10**, as shown in the insets of Figure III-4. Therefore, the side chains do affect the HOMO energies and the resulting Kohn-Sham energies differ by $E_{\text{P16}}^{\text{HOMO}} - E_{\text{P10}}^{\text{HOMO}} = 36 \text{ meV}$. As a result, the HOMO of **P16** is shifted to higher energies, while the LUMO is nearly unaffected. This decreases the single-particle gap and causes a redshift in the excitation energy. To analyze this in more detail, the first excitation energy of each structure is calculated with time-dependent DFT (TD-DFT) for an enlarged polymer backbone in solution for which we use a polymer model of three repeat units. To make the calculations computational feasible, the side chains are cut-off after the first alkyl segment, since the frontier orbitals do not significantly delocalize beyond these as shown in Figure III-4.

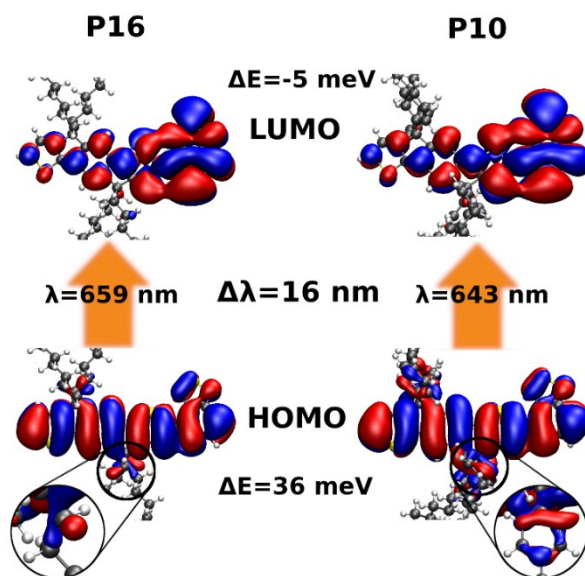


Figure III-4. Frontier orbitals and excitation energies of **P16** (left) and **P10** (right). The LUMOs (top) primarily localize at the BT units. Energy differences ΔE are based on Kohn-Sham orbital energies. The HOMOs (bottom) delocalize over the full backbone and the side chains (inset). The wavelengths λ of the low-energy excitations of **P16** and **P10** obtained from TD-DFT differ by about $\Delta\lambda = 16 \text{ nm}$ (centre).

The chloroform solution used in the experiment is modelled by the polarizable continuum model as implemented in Gaussian 16.³⁷ More details on the simulation parameters can be found in the methods section (see SI). The TD-DFT simulations yield excitation energies of $\epsilon_{P16} = 2.329$ eV (532 nm) and $\epsilon_{P10} = 2.376$ eV (522 nm). However, the excitation energies calculated with TD-DFT usually show a systematic overestimation in the range of $\Delta\epsilon^{\text{TD-DFT}} = 300\text{--}600$ meV.^{38,39} Here, we apply a shift of $\Delta\epsilon^{\text{sim-exp}} = 448$ meV that yields corrected excitation energies of $\epsilon_{P16} = 1.882$ eV (659 nm) and $\epsilon_{P10} = 1.928$ eV (643 nm), which are shown in the centre of Figure III-4. More important than the absolute position of the excitation energy, the TD-DFT simulations reveal a redshift of the excitation energy of **P16** by $\Delta\epsilon^{\text{sim}} = 16$ nm similar to the experimental observation of $\Delta\epsilon^{\text{exp}} = 20$ nm. We therefore find that the deeper and slightly more delocalized HOMO on the alkylphenyl side chains causes the observed shift. Conformation and coplanarity of the IDT is not affected by the different side chains.

Thermal properties. All polymers possess good thermal stability with degradation temperatures (5% weight loss) T_d between 370–450 °C (Table III-2, Figure III-S16). DSC second heating thermograms reveal a shallow exotherm around 90 °C (Figure III-S17), which we explain with reorganization at temperatures exceeding the glass transition temperature T_g . We note that all investigated copolymers show similar DSC traces and appear to undergo such a process in a similar temperature range, as expected for polymers with an $M_n > 10$ kg mol⁻¹ for which the T_g becomes less dependent on chain length.⁴⁰ Only for **P16** with C12 side chains, a T_g of 96 °C can be determined (Figure III-S17 and S18).⁴¹ **P16** also shows two weak transitions that are ascribed to melting ($T_m = 213$ °C, $\Delta H_m = 1.5$ J g⁻¹) and crystallization ($T_c = 168$ °C, $\Delta H_c = 3.7$ J g⁻¹). The weak crystallinity of **P16** is in accordance to the observations of vibronic structure seen in thin film UV-vis spectra and indicates improved intermolecular packing enabled by the more flexible aliphatic side chains compared to Ph₆-substituted PIDTBT, for which conventional DSC thermograms did not show signs of crystallization.

Due to the difficulty for all polymers to extract T_g values from conventional DSC, we additionally carried out physical ageing experiments to investigate T_g values in more detail. We chose to focus on **P19** because we expected this material to display a high degree of disorder, and hence a prominent T_g , due to the presence of main chain defects (cf. discussion above). The same type of experiment was inconclusive for samples made *via* route A (not shown). We used fast scanning calorimetry (FSC) to anneal **P19** for 30 min at T_{anneal} ranging from 30 to 140 °C, followed by rapid heating at 4000 K s⁻¹ from -50 to 300 °C (Figure III-5a), which follows a

protocol that has been used for other conjugated polymers.^{42,43} A distinct endothermic overshoot can be discerned for each T_{anneal} with a clear minimum in enthalpy ΔH at $T_{\text{anneal}} = 80^\circ\text{C}$ (Figure III-5b). We identify two temperature regimes below and above 80°C , which we assign to enthalpy relaxation of the mobile amorphous fraction (MAF) and rigid amorphous fraction (RAF), respectively. We extrapolate an upper limit of the T_g of 88°C , which is in agreement with the exotherms observed with conventional DSC (Figures III-S17). The same type of experiment was performed on C12-PIDTBT **P16** to investigate the influence of the side chains on the relaxation kinetics of the polymer backbone and hence the T_g of the polymer.⁴⁰ FSC measurements reveal a slightly higher T_g of 98°C (Figure III-5c). The rather small difference in T_g between **P16** and **P19** is remarkable considering the very different nature of side chains in the two polymers. The larger side chains of **P19** (52 carbons) compared to **P16** (24 carbons) are expected to decrease T_g of the former,⁴⁴ but this effect may be partially compensated by the phenyl rings that are part of the side chains of Ph₂₀, which cause an increase at a constant number of carbons.^{40,45}

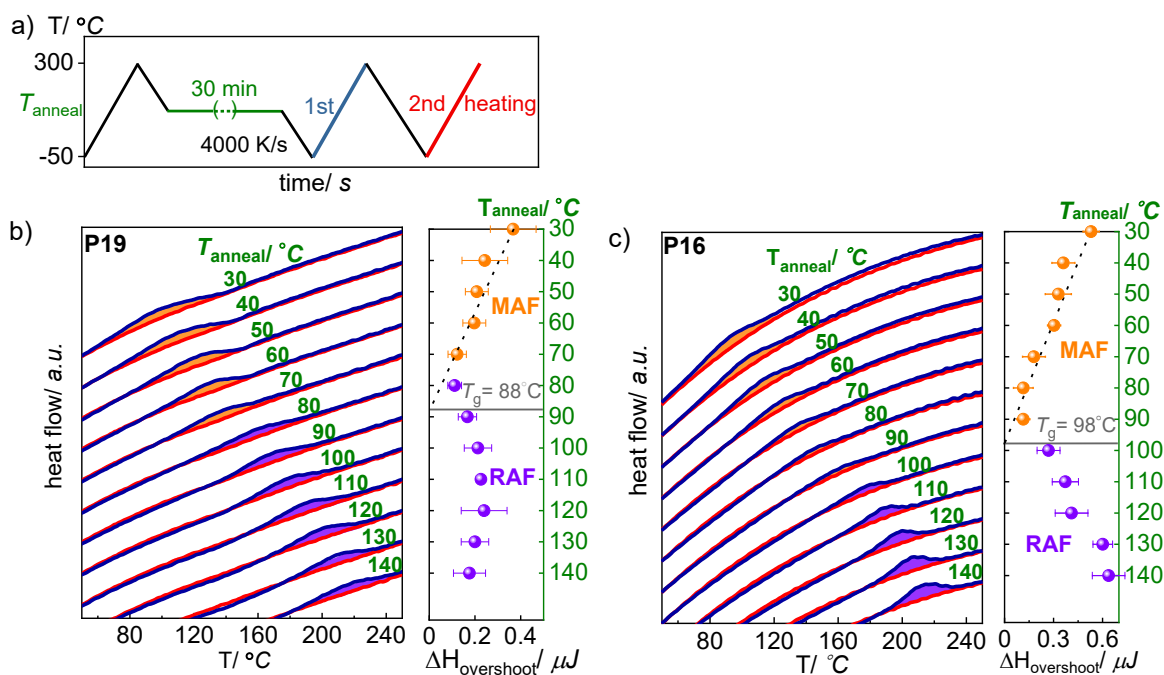


Figure III-5. (a) Protocol used for FSC measurements comprising a heating scan after physical ageing for 30 min at annealing temperature T_{anneal} (blue) and a second reference heating scan from -50 to 300°C (red); FSC heating thermograms of (b) **P19** and (c) **P16**, after ageing (blue) and corresponding reference scans (red) as well as the enthalpy of the endothermic overshoot ΔH as a function of T_{anneal} ; the dashed line represents the extrapolation of the upper limit of the T_g .

Electrical properties. The charge transport properties of the polymers thin films were investigated with field-effect transistors, using a standard top-gate bottom-contact configuration characterized by a channel length of 20 μm (Figure III-S19–S22). The extracted values for the apparent charge mobility in the saturation regime ($V_d = V_g = -60\text{ V}$) are summarized in Table III-3. The hole mobilities of the polymers *via* route A are in the range of $\mu_{\text{sat}} = 0.02\text{--}0.04\text{ cm}^2\text{ V}^{-1}\text{ s}^{-1}$, in line with values reported for polymer analogues made by Stille coupling.^{9,10} Reducing the channel length to 5 μm leads to a slight improvement of mobility in a similar manner for all investigated copolymers, up to $\mu_{\text{sat}} = 0.05\text{ cm}^2\text{ V}^{-1}\text{ s}^{-1}$. We tentatively attribute the channel length dependence to lateral-field enhancement of charge transport and/or injection.⁴⁶ In general, the measured values of PIDTBT with alkylphenyl side chains are one order of magnitude lower than C12-substituted PIDTBT **P16** (Figure III-S21). This effect may be caused by the steric hindrance of the rigid phenyl rings that reduce intermolecular stacking of backbones and thus a contribution from interchain transport. Unlike alkyl-substituted PIDTBT where longer alkyl chains as well as higher MW lead to improved μ_{sat} by up to one order of magnitude (R = octyl, $\mu_{\text{sat}} = 0.15\text{ cm}^2\text{ V}^{-1}\text{ s}^{-1}$; R = hexyldecyl, $\mu_{\text{sat}} = 1.2\text{ cm}^2\text{ V}^{-1}\text{ s}^{-1}$)², alkylphenyl-substituted PIDTBT neither exhibits a MW nor a side chain length dependence (Figure III-S19 and S20). PIDTBT **P17–P19** made by route B exhibits decreased transport performance with mobilities smaller by two to three orders of magnitude that obviously result from defective backbones (Figure III-S22).

Table III-3. OFET characteristics of selected PIDTBT copolymers.

entry	R ¹	R ² /R ³	on/off ratio	$\mu_{\text{sat}}/\text{cm}^2\text{ V}^{-1}\text{ s}^{-1}$
P1	Ph ₈		$\sim 10^6$	$3.9 \cdot 10^{-2}$
P3	Ph ₈		$\sim 10^6$	$3.8 \cdot 10^{-2}$
P5	Ph ₈		$\sim 10^5$	$2.2 \cdot 10^{-2}$
P9	Ph ₆		$\sim 10^5$	$4.0 \cdot 10^{-2}$
P10	Ph ₆		$\sim 10^5$	$3.5 \cdot 10^{-2}$
P16	C ₁₂ H ₂₅		$\sim 10^6$	$3 \cdot 10^{-1}$
P17		Me/Ph ₂₀	$\sim 10^1$	$1 \cdot 10^{-4}$
P18		Me/Ph ₂₀	$\sim 10^2$	$1.2 \cdot 10^{-6}$
P19		Ph ₂₀ /Ph ₂₀	$\sim 10^1$	$7.4 \cdot 10^{-5}$

To gain further insight into the differences in device performance, photothermal deflection spectroscopy (PDS) was carried out (Figure III-S23). The Urbach energy U_E which can be extracted from the PDS measurements is related to energetic disorder in the material. **P16** with the highest mobility exhibits a lower Urbach energy and slightly less sub-band gap states than the alkylphenyl-substituted **P10** ($U_E(\mathbf{P16}) = 36$ meV; $U_E(\mathbf{P10}) = 49$ meV). This trend indicates larger energetic disorder of **P10** which is in agreement with its lower mobility.

GIWAXS measurements. The impact of the side chain architecture on morphology was analyzed by grazing incidence wide angle X-ray scattering (GIWAXS) measurements. The films were prepared using the same conditions as for OFETs. The results are represented in Figure III-6.

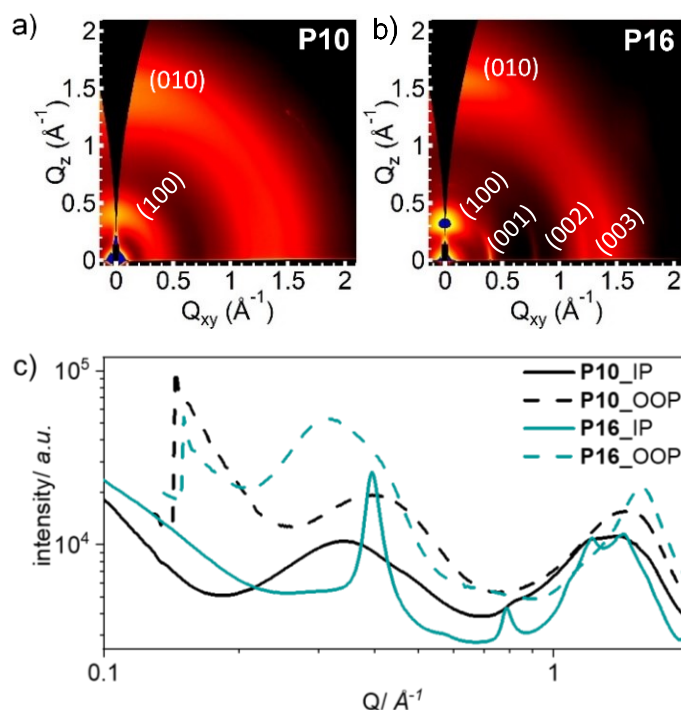


Figure III-6. 2D GIWAXS images of **P10** (a) and **P16** (b) polymer films and comparison of in-plane (IP) and out-of-plane (OOP) diffraction patterns (c).

The alkylphenyl-substituted PIDTBT **P10** film shows broader peaks compared to the alkyl-substituted **P16** indicating a less ordered stacking and is in agreement with the previous observations from optical, thermal and charge transport characterization. The GIWAXS pattern of **P16** is consistent with previous measurements of alkyl-substituted PIDTBT,^{1,3} with a prominent (010) (π -stacking) peak located in the out-of-plane direction $Q_z = 1.57 \text{ \AA}^{-1}$ corresponding to a π - π stacking of 4.0 \AA . There are also a series of sharp in-plane reflections observed for **P16** which are indexed to backbone reflections with the (001) peak appearing at

$Q_{XY} = 0.395 \text{ \AA}^{-1}$ corresponding to a d -spacing of 15.9 \AA . There is also a diffuse peak at $Q_Z \sim 0.3 \text{ \AA}^{-1}$ in the out-of-plane direction. The indexing of this peak is uncertain; it is reminiscent of a lamellar stacking peak, but its appearance along Q_Z is inconsistent with the otherwise face-on texture of **P16**. This peak could be associated with a disordered, edge-on population³ or reflect a more complicated unit cell. In contrast to **P16**, **P10** shows an absence of backbone reflections, with a broader (010) peak. The broad ring at $Q = 1.4 \text{ \AA}^{-1}$ – which is reflective of amorphous chains – is also more prominent in **P10** compared to **P16**. Overall, the scattering data indicating increased order for **P16** with aliphatic side chains is in full accordance with DSC, UV-vis spectroscopy and PDS, and provides an explanation for the observed charge transport behavior in this series of polymers.

CONCLUSIONS

We have presented two synthetic pathways towards PIDTBT copolymers using direct arylation for all C-C coupling steps. Route A relies on a classical DAP approach in which preformed monomers undergo polycondensation to give well-defined PIDTBT. Route B proceeds *via* a polyketone precursor also made *via* DAP following polymer analogous cyclization. The comprehensive investigation of PIDTBT prepared by these different routes, with different molecular weights as well as different side chains revealed that i) route A is superior compared to route B in terms of structural defects, ii) optical properties of PIDTBT made *via* route A are strongly influenced by molecular weight, iii) PIDTBT with alkylphenyl side chains exhibits MW-independent field-effect hole mobilities in the range of $10^{-2} \text{ cm}^2 \text{ V}^{-1} \text{ s}^{-1}$ due to a mostly amorphous structure and iv) PIDTBT with aliphatic C12 side chains and made *via* route A shows increased order, lower energetic disorder and accordingly higher field-effect hole mobilities on the order of $10^{-1} \text{ cm}^2 \text{ V}^{-1} \text{ s}^{-1}$. Thus, the presence or absence of phenyl rings in the side chains of PIDTBT has drastic consequences for packing, which is relevant for both transistor performance^{3,16,47} as well as stability of blends with IDT-based components used for non-fullerene solar cells.⁴⁸

Regarding a more comprehensive analysis of defects in PIDTBT made *via* route B, and neither proven nor unproven homocouplings in PIDTBT made *via* route A, further model compounds as well as significantly extended spectroscopic investigations will be required to make finale statements. A full homocoupling analysis of PIDTBT is generally much more challenging compared to other copolymers due to broad signals in ^1H NMR spectra. Unless irregularities between different samples show up, such study does not appear rewarding, and there is also no reason to assume their presence at this point.

EXPERIMENTAL

Instrumentation and methods. Detailed information about instrumentation, experimental procedures and theoretical calculations are described in the Supporting Information (SI).

Materials. All starting materials were purchased from commercial sources and used without further purification unless otherwise specified. All reactions were carried out in flame dried glassware and under dry inert gas atmosphere. Compounds Ph_xIDT , **K** and **TBT** were synthesized according to published protocols.^{17,33,49} Detailed ^1H and ^{13}C NMR analyses of the precursor polymer **P(K-*alt*-TBT)** are reported in the SI (Figure III-S8 and S9).

Synthetic procedures.

Representative procedure for synthesis of PIDTBT via DAP (P1). Ph_8IDT (54.2 mg, 53 μmol , 1 eq), 4,7-dibromo-2,1,3-benzothiadiazole (15.6 mg, 53 μmol , 1 eq), pivalic acid (5.3 mg, 53 μmol , 1 eq) and potassium carbonate (22.0 mg, 158 μmol , 3 eq) were placed in a vial and dissolved in 0.53 mL degassed mesitylene. Then Pd_2dba_3 (2.4 mg, 5 mol%) and $\text{P}(o\text{-anisyl})_3$ (3.8 mg, 20 mol%) were added under argon and stirred for 72 h at 100 °C. After cooling to room temperature, the mixture was diluted with chloroform, precipitated into methanol and purified by Soxhlet extraction with acetone, ethyl acetate and chloroform. The chloroform fraction was filtered through a silica gel plug and dried overnight in a vacuum oven at 50 °C to afford a dark blue solid. Yield: 58.4 mg (95%).

*Synthesis of P(K-*alt*-TBT).* Compound **K** (738 mg, 0.74 mmol, 1 eq), 4,7-di(thiophene-2-yl)-2,1,3-benzothiadiazole (221 mg, 0.74 mmol, 1 eq), pivalic acid (75.2 mg, 0.74 mmol, 1 eq) and potassium carbonate (305 mg, 2.21 mmol, 3 eq) were placed in a vial and dissolved in 2.9 mL degassed mesitylene. Then Pd_2dba_3 (33.7 mg, 5 mol%) and $\text{P}(o\text{-anisyl})_3$ (51.9 mg, 20 mol%) were added under argon and the whole was stirred for 72 h at 90 °C. Then 4.5 mL degassed bromobenzene was added under argon and stirred for another 24 h at 90 °C. After cooling to room temperature, the mixture was diluted with chloroform, precipitated into methanol and purified by Soxhlet extraction with acetone, ethyl acetate and chloroform. The chloroform fraction was filtered through a silica gel plug to afford a red solid. Yield: 638 mg (75%).

General procedure to Me/Ph₂₀-PIDTBT (P17, P18) and Ph₂₀/Ph₂₀-PIDTBT (P19). To a solution of **P(K-*alt*-TBT)** (200 mg, 0.17 mmol, 1 eq) in 40 mL toluene at room temperature the corresponding lithium compound (1.40 mmol, 8 eq) was added and after 30 minutes 5 mL THF was added. After stirring for 3 h at room temperature, the reaction mixture was quenched with ethanol and water, extracted with chloroform and dried over magnesium sulfate. The solvent was removed under vacuum and the crude product was immediately dissolved in dry

chloroform. After the addition of boron trifluoride diethyl etherate (0.42 mL, 471 mg, 3.22 mmol, 18 eq) the mixture was stirred for 3 h at room temperature and then quenched with ethanol and water, extracted with chloroform and dried over magnesium sulfate. The crude product was precipitated into methanol and purified by Soxhlet extraction with acetone, ethyl acetate and chloroform. The chloroform fraction was filtered through a silica gel plug to afford the title compounds as dark blue solid.

Me/Ph₂₀-PIDTBT. Yield: 10 mg (5%).

Ph₂₀/Ph₂₀-PIDTBT. Yield: 233 mg (73%).

Supporting Information (SI): Experimental details, general measurements and characterization; additional NMR, SEC, IR, UV-vis, TGA and DSC data are provided.

Acknowledgements

The authors thank M. Raisch for initial DSC measurements and D. Stegerer for TGA measurements. M. S. thanks the DFG (project SO 1213/8-2) for funding. A.P., A.S., B.P. and M.C. acknowledge funding from the European Research Council (ERC) under the European Union's Horizon 2020 research and innovation programme "HEROIC", Grant Agreement 638059. This work has been partially carried out at Polifab, the micro- and nanotechnology center of the Politecnico di Milano. S.H. and C.M. acknowledge funding from the Knut and Alice Wallenberg Foundation through the project "Mastering Morphology for Solution-borne Electronics". This work was performed in part at the SAXS/WAXS beamline⁵⁰ at the Australian Synchrotron, part of ANSTO. We thank Jaime Martín for insightful discussions. F.O. would like to thank the DFG for funding through projects OR 349/1 and OR 349/3 and the Zentrum für Informationsdienste und Hochleistungsrechnen of TU Dresden for grants of computing time.

REFERENCES

- (1) W. Zhang, J. Smith, S. E. Watkins, R. Gysel, M. McGehee, A. Salleo, J. Kirkpatrick, S. Ashraf, T. Anthopoulos, M. Heeney and I. McCulloch, *J. Am. Chem. Soc.*, 2010, **132**, 11437–11439.
- (2) H. Bronstein, D. S. Leem, R. Hamilton, P. Woebkenberg, S. King, W. Zhang, R. S. Ashraf, M. Heeney, T. D. Anthopoulos, J. de Mello and I. McCulloch, *Macromolecules*, 2011, **44**, 6649–6652.
- (3) X. Zhang, H. Bronstein, A. J. Kronemeijer, J. Smith, Y. Kim, R. J. Kline, L. J. Richter, T. D. Anthopoulos, H. Sirringhaus, K. Song, M. Heeney, W. Zhang, I. McCulloch and D. M. DeLongchamp, *Nat. Commun.*, 2013, **4**, 2238.
- (4) R. S. Ashraf, B. C. Schroeder, H. A. Bronstein, Z. Huang, S. Thomas, R. J. Kline, C. J. Brabec, P. Rannou, T. D. Anthopoulos, J. R. Durrant and I. McCulloch, *Adv. Mater.*, 2013, **25**, 2029–2034.
- (5) D. Venkateshvaran, M. Nikolka, A. Sadhanala, V. Lemaire, M. Zelazny, M. Kepa, M. Hurhangee, A. J. Kronemeijer, V. Pecunia, I. Nasrallah, I. Romanov, K. Broch, I. McCulloch, D. Emin, Y. Olivier, J. Cornil, D. Beljonne and H. Sirringhaus, *Nature*, 2014, **515**, 384–388.
- (6) I. McCulloch, R. S. Ashraf, L. Biniek, H. Bronstein, C. Combe, J. E. Donaghey, D. I. James, C. B. Nielsen, B. C. Schroeder and W. Zhang, *Acc. Chem. Res.*, 2012, **45**, 714–722.
- (7) Y. Li, M. Gu, Z. Pan, B. Zhang, X. Yang, J. Gu and Y. Chen, *J Mater Chem A*, 2017, **5**, 10798–10814.
- (8) C. Liang and H. Wang, *Org. Electron.*, 2017, **50**, 443–457.
- (9) C.-P. Chen, S.-H. Chan, T.-C. Chao, C. Ting and B.-T. Ko, *J. Am. Chem. Soc.*, 2008, **130**, 12828–12833.
- (10) K.-S. Chen, Y. Zhang, H.-L. Yip, Y. Sun, J. A. Davies, C. Ting, C.-P. Chen and A. K.-Y. Jen, *Org. Electron.*, 2011, **12**, 794–801.
- (11) A. Wadsworth, M. Moser, A. Marks, M. S. Little, N. Gasparini, C. J. Brabec, D. Baran and I. McCulloch, *Chem. Soc. Rev.*, 2019, **48**, 1596–1625.
- (12) G. Zhang, J. Zhao, P. C. Y. Chow, K. Jiang, J. Zhang, Z. Zhu, J. Zhang, F. Huang and H. Yan, *Chem. Rev.*, 2018, **118**, 3447–3507.
- (13) C. Yan, S. Barlow, Z. Wang, H. Yan, A. K.-Y. Jen, S. R. Marder and X. Zhan, *Nat. Rev. Mater.*, 2018, **3**, 18003.
- (14) M. Nikolka, K. Broch, J. Armitage, D. Hanifi, P. J. Nowack, D. Venkateshvaran, A. Sadhanala, J. Saska, M. Mascal, S.-H. Jung, J. Lee, I. McCulloch, A. Salleo and H. Sirringhaus, *Nat. Commun.*, 2019, **10**, 2122.

-
- (15) Z. A. Lampion, K. J. Barth, H. Lee, E. Gann, S. Engmann, H. Chen, M. Guthold, I. McCulloch, J. E. Anthony, L. J. Richter, D. M. DeLongchamp and O. D. Jurchescu, *Nat. Commun.*, 2018, **9**, 5130.
- (16) A. Wadsworth, H. Chen, K. J. Thorley, C. Cendra, M. Nikolka, H. Bristow, M. Moser, A. Salleo, T. D. Anthopoulos, H. Sirringhaus and I. McCulloch, *J. Am. Chem. Soc.*, 2020, **142**, 652–664.
- (17) W. Gao, M. Zhang, T. Liu, R. Ming, Q. An, K. Wu, D. Xie, Z. Luo, C. Zhong, F. Liu, F. Zhang, H. Yan and C. Yang, *Adv. Mater.*, 2018, **30**, 1800052.
- (18) T. W. Bünnagel, B. S. Nehls, F. Galbrecht, K. Schottler, C. J. Kudla, M. Volk, J. Pina, J. S. S. de Melo, H. D. Burrows and U. Scherf, *J. Polym. Sci. Part Polym. Chem.*, 2008, **46**, 7342–7353.
- (19) Y. Ma, Q. Zheng, Z. Yin, D. Cai, S.-C. Chen and C. Tang, *Macromolecules*, 2013, **46**, 4813–4821.
- (20) Y.-C. Chen, C.-Y. Yu, Y.-L. Fan, L.-I. Hung, C.-P. Chen and C. Ting, *Chem. Commun.*, 2010, **46**, 6503.
- (21) A. S. Dudnik, T. J. Aldrich, N. D. Eastham, R. P. H. Chang, A. Facchetti and T. J. Marks, *J. Am. Chem. Soc.*, 2016, **138**, 15699–15709.
- (22) S. Holliday, Y. Li and C. K. Luscombe, *Prog. Polym. Sci.*, 2017, **70**, 34–51.
- (23) P.-O. Morin, T. Bura and M. Leclerc, *Mater Horiz*, 2016, **3**, 11–20.
- (24) R. Matsidik, H. Komber, A. Luzio, M. Caironi and M. Sommer, *J. Am. Chem. Soc.*, 2015, **137**, 6705–6711.
- (25) R. Matsidik, H. Komber and M. Sommer, *ACS Macro Lett.*, 2015, **4**, 1346–1350.
- (26) F. Nübling, H. Komber and M. Sommer, *Macromolecules*, 2017, **50**, 1909–1918.
- (27) A. E. Rudenko and B. C. Thompson, *J. Polym. Sci. Part Polym. Chem.*, 2015, **53**, 135–147.
- (28) M. Wakioka and F. Ozawa, *Asian J. Org. Chem.*, 2018, **7**, 1206–1216.
- (29) J.-R. Pouliot, F. Grenier, J. T. Blaskovits, S. Beaupré and M. Leclerc, *Chem. Rev.*, 2016, **116**, 14225–14274.
- (30) S. Chen, K. C. Lee, Z.-G. Zhang, D. S. Kim, Y. Li and C. Yang, *Macromolecules*, 2016, **49**, 527–536.
- (31) Y. Li, W. K. Tatum, J. W. Onorato, S. D. Barajas, Y. Y. Yang and C. K. Luscombe, *Polym Chem*, 2017, **8**, 5185–5193.
- (32) Y. Li, W. K. Tatum, J. W. Onorato, Y. Zhang and C. K. Luscombe, *Macromolecules*, 2018, **51**, 6352–6358.
- (33) D. Adamczak, H. Komber, A. Illy, A. D. Scaccabarozzi, M. Caironi and M. Sommer, *Macromolecules*, 2019, **52**, 7251–7259.
- (34) Y. Yao and J. M. Tour, *Macromolecules*, 1999, **32**, 2455–2461.

- (35) F. Lombeck, H. Komber, S. I. Gorelsky and M. Sommer, *ACS Macro Lett.*, 2014, **3**, 819–823.
- (36) M. S. Vezie, S. Few, I. Meager, G. Pieridou, B. Dörfling, R. S. Ashraf, A. R. Goñi, H. Bronstein, I. McCulloch, S. C. Hayes, M. Campoy-Quiles and J. Nelson, *Nat. Mater.*, 2016, **15**, 746–753.
- (37) M. J. Frisch et al., *Gaussian 16 Rev. C.01*, Wallingford, CT, 2016.
- (38) K. S. Schellhammer, T.-Y. Li, O. Zeika, C. Körner, K. Leo, F. Ortman and G. Cuniberti, *Chem. Mater.*, 2017, **29**, 5525–5536.
- (39) S. Chibani, B. Le Guennic, A. Charaf-Eddin, O. Maury, C. Andraud and D. Jacquemin, *J. Chem. Theory Comput.*, 2012, **8**, 3303–3313.
- (40) C. Müller, *Chem. Mater.*, 2015, **27**, 2740–2754.
- (41) M. Xiao, A. Sadhanala, M. Abdi-Jalebi, T. H. Thomas, X. Ren, T. Zhang, H. Chen, R. L. Carey, Q. Wang, S. P. Senanayak, C. Jellett, A. Onwubiko, M. Moser, H. Liao, W. Yue, I. McCulloch, M. Nikolka and H. Sirringhaus, *Adv. Funct. Mater.*, 2020, 2007359.
- (42) J. Martín, N. Stingelin and D. Cangialosi, *J. Phys. Chem. Lett.*, 2018, **9**, 990–995.
- (43) L. Yu, D. Qian, S. Marina, F. A. A. Nugroho, A. Sharma, S. Hultmark, A. I. Hofmann, R. Kroon, J. Benduhn, D.-M. Smilgies, K. Vandewal, M. R. Andersson, C. Langhammer, J. Martín, F. Gao and C. Müller, *ACS Appl. Mater. Interfaces*, 2019, **11**, 21766–21774.
- (44) R. Xie, A. R. Weisen, Y. Lee, M. A. Aplan, A. M. Fenton, A. E. Masucci, F. Kempe, M. Sommer, C. W. Pester, R. H. Colby and E. D. Gomez, *Nat. Commun.*, 2020, **11**, 893.
- (45) F. Kempe, F. Riehle, H. Komber, R. Matsidik, M. Walter and M. Sommer, *Polym. Chem.*, 2020, **11**, 6928–6934.
- (46) L. Wang, D. Fine, D. Basu and A. Dodabalapur, *J. Appl. Phys.*, 2007, **101**, 054515.
- (47) M. Nikolka, M. Hurhangee, A. Sadhanala, H. Chen, I. McCulloch and H. Sirringhaus, *Adv. Electron. Mater.*, 2018, **4**, 1700410.
- (48) S. Hultmark, S. H. K. Paleti, A. Harillo, S. Marina, F. A. A. Nugroho, Y. Liu, L. K. E. Ericsson, R. Li, J. Martín, J. Bergqvist, C. Langhammer, F. Zhang, L. Yu, M. Campoy-Quiles, E. Moons, D. Baran and C. Müller, *Adv. Funct. Mater.*, 2020, **30**, 2005462.
- (49) F. Lombeck, H. Komber, A. Sepe, R. H. Friend and M. Sommer, *Macromolecules*, 2015, **48**, 7851–7860.
- (50) N. M. Kirby, S. T. Mudie, A. M. Hawley, D. J. Cookson, H. D. T. Mertens, N. Cowieson and V. Samardzic-Boban, *J. Appl. Crystallogr.*, 2013, **46**, 1670–1680.

SUPPORTING INFORMATION

General measurement and characterization

NMR spectroscopy. NMR spectra were recorded on a Bruker AVANCE III 500 spectrometer (^1H : 500.1 MHz, ^{13}C : 125.8 MHz) at 30 °C. CDCl_3 was used as solvent. The spectra were referenced to the residual solvent peak ($\delta(^1\text{H}) = 7.26$ ppm, $\delta(^{13}\text{C}) = 77.0$ ppm). 2D NMR spectra were recorded to support signal assignment.

SEC measurements. Molecular weights were measured on a Shimadzu system comprising a 5 μm precolumn and three SDplus columns with pore sizes ranging from 10^2 to 10^4 Å (Polymer Standards), connected in series with a RID-20A RI detector and a SPD-M20A photodiode array UV-vis detector (Shimadzu) calibrated with polystyrene standards. CHCl_3 was used as eluent at 40 °C with a flow rate of 1.0 mL min^{-1} .

UV-vis spectroscopy. UV-vis spectra were recorded at 25 °C on a Cary 60 UV-vis (Agilent Technologies) in chloroform solutions ($c = 0.02 \text{ mg mL}^{-1}$). Extinction coefficients ϵ were calculated using the Beer-Lambert law: $\epsilon = \frac{A}{c \cdot d}$; where A is the absorptivity, d is the optical path length (1 cm) and c is the concentration in mol L^{-1} . Conversion of the concentration into mol L^{-1} was done using the molecular weight of the corresponding repeating unit.

Photoluminescence. PL spectra were recorded at 25 °C with a xenon flash lamp and a Czerny Turner monochromator in chloroform solutions ($c = 0.02 \text{ mg mL}^{-1}$).

IR spectroscopy. IR spectra were obtained at 25 °C on a FTS 165 spectrometer (BIO-RAD) equipped with a Golden Gate single ATR accessory from LOT-Oriel GmbH.

DFT calculations. The frontier orbitals of **P10** and **P16** have been analyzed for a single chain segment of the respective polymer in gas phase. The chain segments were structurally optimized before calculating the orbital energies. The DFT calculations have been performed with the M06-2X hybrid functional¹ and cc-pVTZ basis set² within the Gaussian 16 program suite.³ The given orbital energies were the respective Kohn-Sham energies and the orbitals were visualized using the VMD software.⁴ The excitation wavelengths λ for **P10** and **P16** have been calculated with time-dependent DFT. To this end, the polymer was modelled *via* three chain segments. The side chains were cut after the first alkyl segment to keep the computational load manageable. The calculations were performed in Gaussian 16³ using the M06-2X hybrid functional and 6-311G** basis set.^{5,6} The experimental solution of chloroform was modelled using the polarizable continuum model^{7,8} as implemented in Gaussian. The chosen solvent was chloroform ($\epsilon = 4.7$).

Cyclic voltammetry. CV measurements were performed at room temperature using a PalmSens4 potentiostat with NBu₄PF₆ (0.1 M) as electrolyte under argon with a scan rate of 50 mV s⁻¹. Films were spin coated (1000 rpm, 60 s) onto ITO substrates as working electrode and measured in dry acetonitrile. A platinum wire was used as counter electrode and a silver wire as reference. The CV curves were plotted against the oxidation potential of ferrocene. CV measurements in solution were done at room temperature in a 0.1 M NBu₄PF₆ *o*-DCB solution using a glassy carbon working electrode.

TGA measurements. TGA measurements were done on a TGA/DSC3+ from Mettler-Toledo within the temperature range 50 °C to 650 °C at a heating rate of 10 K min⁻¹ under N₂.

DSC measurements. DSC measurements were carried out on a DSC 2500 (TA Instruments) under nitrogen atmosphere. Heating and cooling rates were 20 K min⁻¹. The mass of the samples for each measurement was approximately 2-5 mg.

FSC measurements. FSC measurements were done with a Mettler Toledo Flash DSC 1 equipped with an intracooler and nitrogen purge. A thin film was spin-coated from a 5 g L⁻¹ chlorobenzene solution directly on the backside of the FSC chip. The sample was first heated by 4000 K s⁻¹ to 300 °C to delete the thermal history and was then aged at different temperatures (30-140 °C) for 30 minutes.

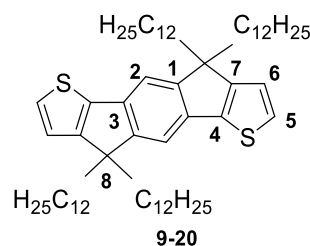
OFET preparation. The samples were fabricated in nitrogen atmosphere. Gold contacts (30 nm) were fabricated on Low alkali 1737F Corning glass substrates using conventional photolithography and thermal evaporation, yielding transistor channels with a length $L = 20\ \mu\text{m}$ and a width $W = 2\ \text{mm}$. The semiconducting polymer was dissolved in *o*-dichlorobenzene at a concentration of 5 mg mL⁻¹, and deposited *via* off-centered spin-coating at 1000 rpm for 60 s. After deposition, the residual solvent was removed *via* vacuum-drying. Then a layer of CYTOP was deposited *via* spin coating at 4000 rpm for 90 s, yielding a 550 nm-thick dielectric layer, and the residual solvent was removed *via* vacuum drying. Finally, a 40 nm-thick aluminum layer was deposited on the channel area by thermal evaporation through a shadow mask, in order to realize the gate electrodes. The devices were then annealed at 100 °C in ambient for 2 h. The samples were measured in nitrogen atmosphere using an Agilent B1500A Semiconductor Parameter Analyzer.

GIWAXS. Grazing-incidence wide-angle X-ray scattering (GIWAXS) measurements were performed at the SAXS/WAXS beamline at the Australian Synchrotron. Measurements were performed in vacuum, with an in-vacuum PILATUS 2M detector (Dectris) placed ~ 0.63 cm downstream from the sample. A photon energy of 15.2 keV was used, with the sample to

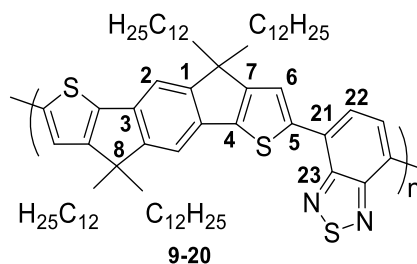
detector distance calibrated using a silver behenate standard. Further details of data analysis can be found in previous work.⁹

PDS. The polymer samples were dissolved in *o*-dichlorobenzene at a concentration of 10 mg mL⁻¹, and deposited on a glass substrate *via* off-centered spin-coating at 1000 rpm for 60 s. The sample film was placed into a sample holder filled with Fluorinert™ FC-770 (3 M). The PDS setup uses a 150W Xenon short-arc lamp (Ushio) which provides light for a monochromator (Oriel Cornerstone, 16 nm FWHM) to achieve a chopped, tunable, monochromatic pump beam. The heat caused through absorption of the pump light in the film changes the refractive index of the Fluorinert™. This change is detected by deflecting a diode laser (Thorlabs) whose displacement is measured by a position sensitive detector (Thorlabs PDP90A). The magnitude of the deflection is determined by a lock-in amplifier (Amatec SR 7230) and directly correlated to the absorption of the film.

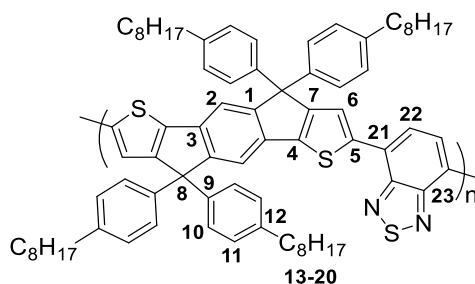
EXPERIMENTAL SECTION



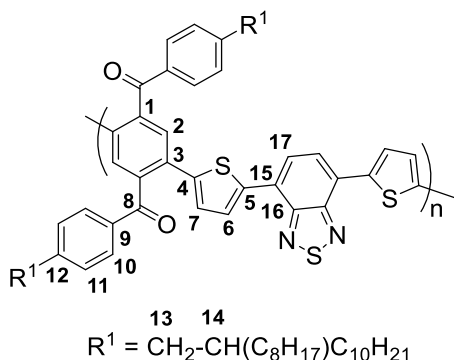
NMR data of **C12-IDT**. ¹H NMR (500 MHz, CDCl₃): δ 7.27 (s, 2H; 2), 7.25 (d, 4.8 Hz, 2H; 5), 6.96 (d, 4.8 Hz, 2H; 6), 1.97 and 1.84 (2 x m, 8H; 9), 1.3-1.05 (72H; 11-19), 0.88 (t, 7.6 Hz, 12H; 20), 0.84 ppm (m, 8H; 10). ¹³C NMR (125 MHz, CDCl₃): δ 155.1 (7), 153.2 (1), 141.7 (4), 135.6 (3), 126.1 (5), 121.7 (6), 113.1 (2), 53.7 (8), 39.1 (9), 31.9 (18), 30.0 (11), 29.6-29.3 (12-17), 24.2 (10), 22.7 (19), 14.1 ppm (20).



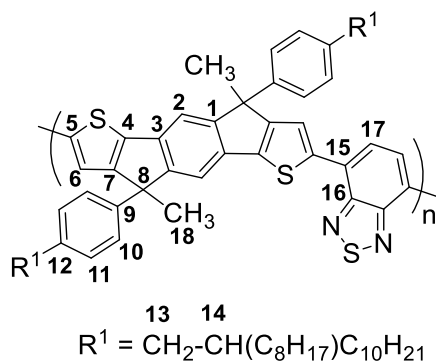
NMR data of **C12-PIDTBT (P16)**. ¹H NMR (500 MHz, CDCl₃): δ 8.11 (6), 7.93 (22), 7.42 (2), 2.12 and 1.98 (9), 1.4-0.9 (10-19), 0.83 ppm (20). ¹³C NMR (125 MHz, CDCl₃): δ 156.4 (7), 153.7 (1), 152.7 (23), 143.6 (4), 141.4 (5), 136.2 (3), 126.2 (21), 124.6 (22), 122.0 (6), 113.5 (2), 54.3 (8), 39.2 (9), 31.9 (18), 30.1 (11), 30.0-29.2 (12-17), 24.3 (10), 22.7 (19), 14.1 ppm (20).



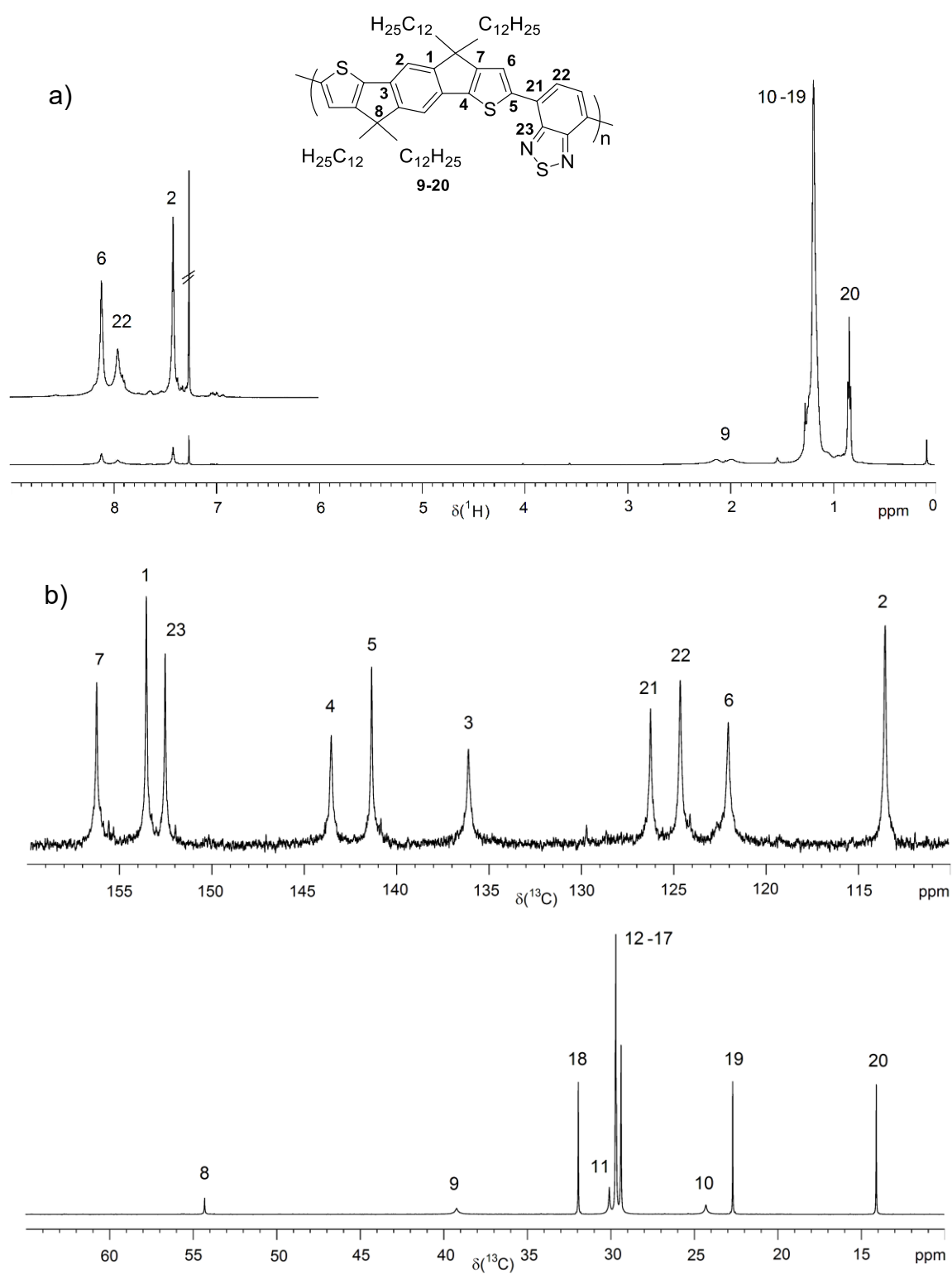
NMR data of **PIDTBT**. ¹H NMR (500 MHz, CDCl₃): δ 8.05 (6), 7.82 (22), 7.53 (2), 7.28 (10), 7.11 (11), 2.59 (13), 1.61 (14), 1.4-1.1 (15-19), 0.87 ppm (20). ¹³C NMR (125 MHz, CDCl₃): δ 156.8 (7), 153.8 (1), 152.4 (23), 143.3 (4), 142.2 (5), 141.8 (9), 141.5 (12), 135.5 (3), 128.4 (11), 128.0 (10), 126.1 (21), 124.7 (22), 123.1 (6), 117.7 (2), 63.2 (8), 35.6 (13), 31.9 (18), 31.4 (14), 30.0-29.2 (15-17), 22.7 (19), 14.1 ppm (20).



NMR data of **P(K-alt-TBT)**. ^1H NMR (500 MHz, CDCl_3): δ 7.85 (d, 3.4 Hz, 2H; 6), 7.78 (s, 2H; 2), 7.77 (d, 8.0 Hz, 4H; 10), 7.70 (s, 2H; 17), 7.15 (d, 8.0 Hz, 4H; 11), 7.10 (d, 3.4 Hz, 2H; 7), 2.50 (d, 4H; 13), 1.56 (m, 4H; 14), 1.4 – 1.1 (64H; 16 x CH_2 of R^1), 0.86 ppm (12H; 2 x CH_3 of R^1). ^{13}C NMR (125 MHz, CDCl_3): δ 197.2 (8), 152.3 (16), 148.8 (12), 141.5 (4), 140.5 (5), 140.3 (1), 134.2 (9), 131.7 (3), 130.0 (10), 129.5 (11), 129.4 (2), 129.0 (7), 128.2 (6), 125.5 (15), 125.3 (17), 40.6 (13), 39.4 (14), 33.0, 31.9, 29.9, 29.5, 29.3, 29.2, 26.4 and 22.6 (CH_2 of R^1), 14.1 ppm (CH_3).



NMR data of **P17**. ^1H NMR (500 MHz, CDCl_3): δ 8.00 (6), 7.84 (17), 7.39 (2), 7.28 (10), 7.08 (11), 2.48 (13), 2.00 (18), 1.61 (14), 1.4-1.1 (CH_2), 0.87 ppm (CH_3). ^{13}C NMR (125 MHz, CDCl_3): δ 159.1 (7), 156.4 (1), 152.5 (16), 142.3 (5), 140.4 (4, 9, 12), 135.2 (3), 129.3 (11), 126.5-124 (10, 15, 17), 122.0 (6), 115.2 (2), 53.0 (8), 40.1 (13), 39.4 (14), 33.2, 31.9, 31-29, 26.5 (all CH_2), 24.8 (18), 22.7 (CH_2), 14.1 ppm (CH_3).



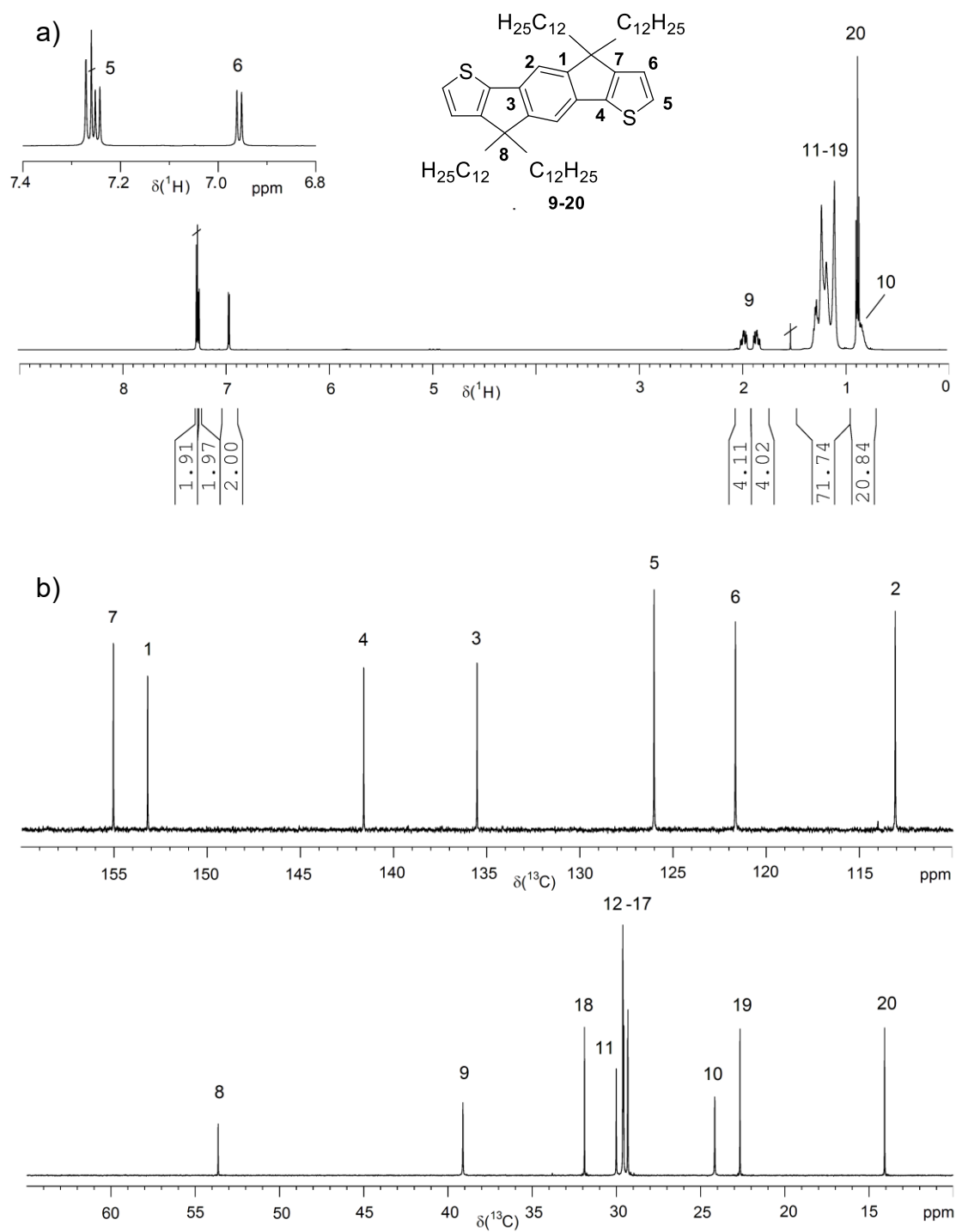
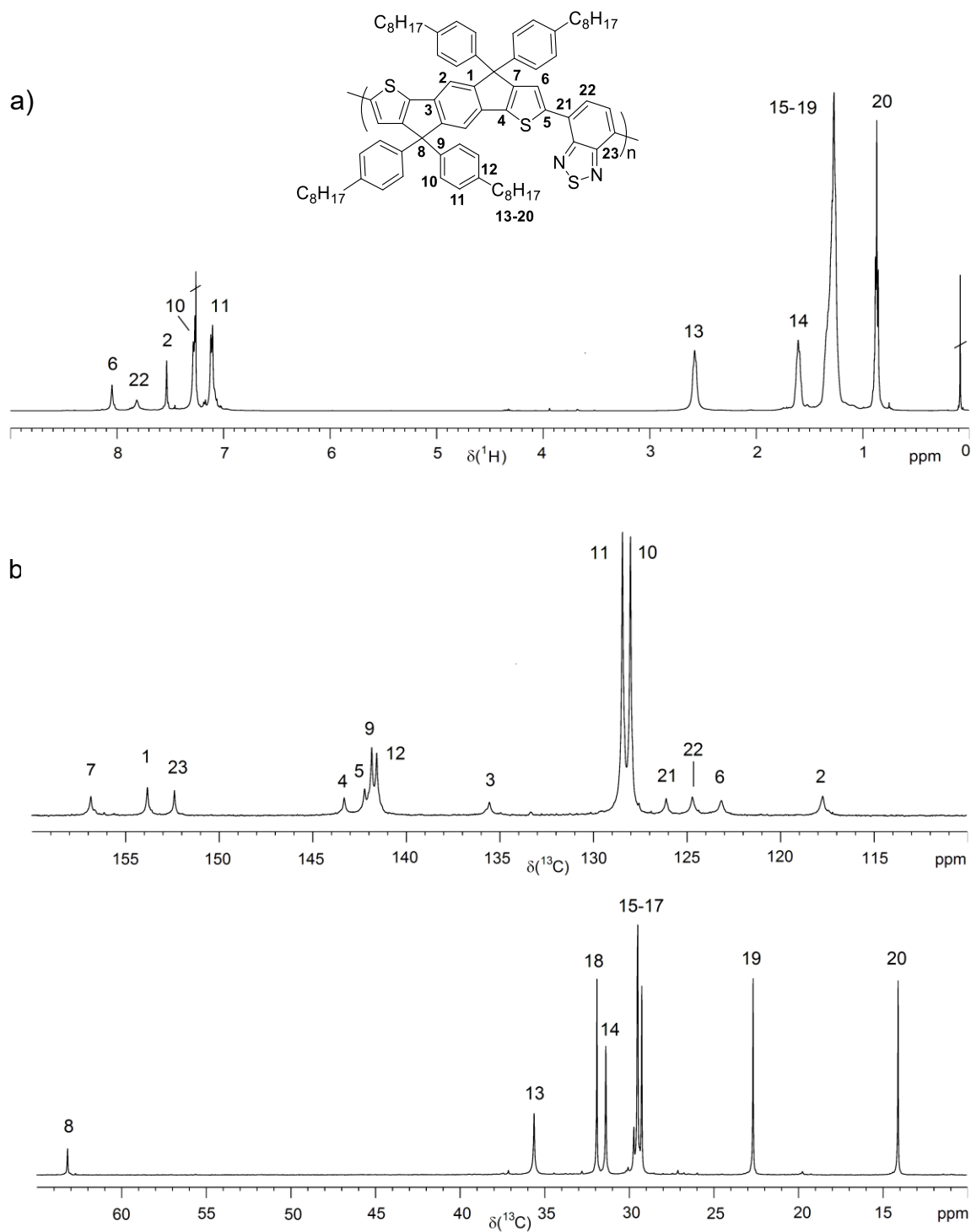


Figure III-S2. ^1H (a) and ^{13}C NMR spectrum (b) of **C12-IDT** (solvent: CDCl_3).



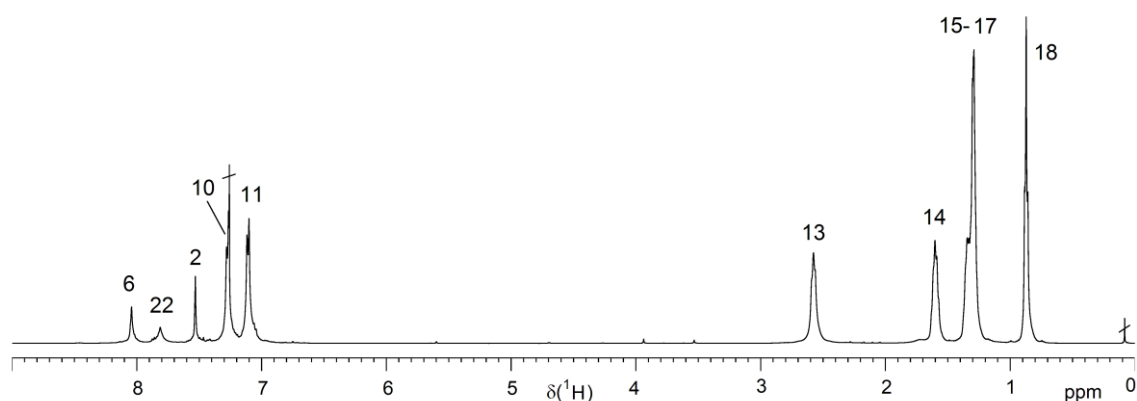
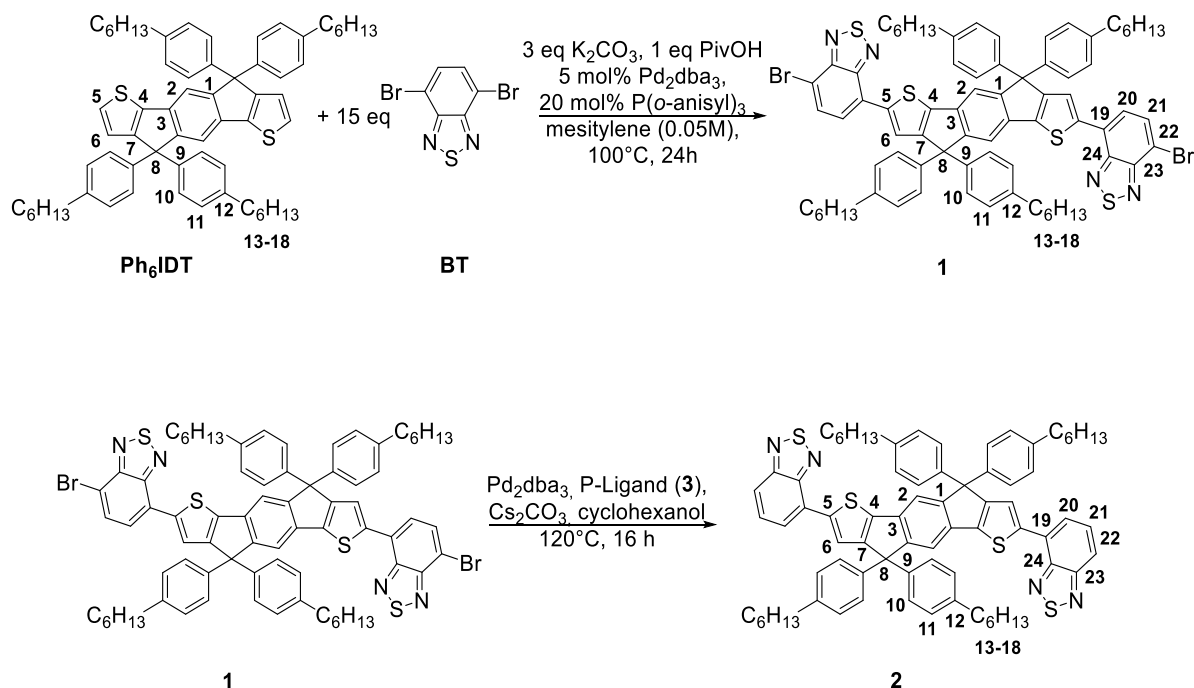


Figure III-S4. ^1H NMR spectrum of **Ph₆-PIDTBT** (entry **P9**; solvent: CDCl_3). The numbering corresponds to the formula of PIDTBT except for the C_6 alkyl chain with 13 – 18.

Synthesis of Ph₆IDT. To a solution of 1-bromo-4-hexylbenzene (400 mg, 1.65 mmol, 3 eq) in 3 mL THF at $-78\text{ }^\circ\text{C}$ was added *n*-butyl lithium (0.7 mL, 1.77 mmol, 2.5 M, 3.2 eq). After stirring at $-78\text{ }^\circ\text{C}$ for 1 h, 2,5-di(thiophen-2-yl)-1,4-phenylenebis[(4-hexylphenyl)methanone] (342 mg, 0.55 mmol, 1 eq) in 4 mL THF was added slowly. The reaction mixture was stirred overnight and then quenched with sat. sodium chloride solution, extracted with ethyl acetate and dried over magnesium sulfate. The solvent was removed under vacuum. Under inert gas atmosphere the crude product was dissolved in 6 mL dry dichloromethane and $\text{BF}_3\cdot\text{OEt}_2$ (1.4 mg, 1.3 mL, 9.9 mmol, 18 eq) was added. After stirring for 2 h at room temperature the reaction mixture was quenched with ethanol and water, extracted with chloroform and dried over magnesium sulfate. The solvent was removed under vacuum and the crude product was recrystallized from petroleum ether to afford **Ph₆IDT** as off-white solid (210 mg, 0.23 mmol, 42%). ^1H NMR (500 MHz, CDCl_3): δ 7.43 (s, 2H; 2), 7.23 (d, 4.8 Hz, 2H; 5), 7.15 (d, 8.2 Hz, 8H; 10), 7.05 (d, 8.2 Hz, 8H; 11), 6.99 (d, 4.8 Hz, 2H; 6), 2.55 (t, 7.7 Hz, 8H; 13), 1.58 (m, 8H; 14), 1.4–1.2 (24H; 15–17), 0.88 ppm (t, 7.6 Hz, 12H; 18). ^{13}C NMR (125 MHz, CDCl_3): δ 155.9 (7), 153.4 (1), 142.1 (9), 141.3 (12), 141.2 (4), 135.1 (3), 128.3 (11), 127.9 (10), 127.3 (5), 123.1 (6), 117.5 (2), 62.7 (8), 35.6 (13), 31.7 (16), 31.3 (14), 29.1 (15), 22.6 (17), 14.1 ppm (18).



Scheme III-S1. Synthesis of model compounds **1** and **2**.

Synthesis of model compound 1. Compound **Ph₆IDT** (200 mg, 0.2 mmol, 1 eq), 4,7-dibromo-2,1,3-benzothiadiazole (972 mg, 3.3 mmol, 15 eq), potassium carbonate (91.4 mg, 0.7 mmol, 3 eq) and pivalic acid (22.5 mg, 0.2 mmol, 1 eq) were weight into a Schlenk tube and dissolved in 4.4 mL degassed mesitylene. Then Pd₂dba₃ (10.1 mg, 5 mol%) and P(*o*-anisyl)₃ (15.5 mg, 20 mol%) were added. After stirring for 24 h at 100 °C the reaction mixture was allowed to cool to room temperature, diluted with petroleum ether, filtered and the solvent was removed under vacuum. The crude product was purified by column chromatography (petroleum ether:dichloromethane, 1:1) to afford **1** as dark red crystals (75 mg, 56 μmol, 26%). ¹H NMR (500 MHz, CDCl₃): δ 8.00 (s, 2H; 6), 7.77 (d, 7.7 Hz, 2H; 21), 7.62 (d, 7.7 Hz, 2H; 20), 7.54 (s, 2H; 2), 7.26 (d, 7.9 Hz, 8H; 10), 7.11 (d, 7.9 Hz, 8H; 11), 2.57 (t, 7.7 Hz, 8H; 13), 1.60 (m, 8H; 14), 1.4-1.2 (24H; 15-17), 0.87 ppm (t, 7.6 Hz, 12H; 18). ¹³C NMR (125 MHz, CDCl₃): δ 156.8 (7), 153.7 (1, 23), 151.4 (24), 143.8 (4), 141.7 (9, 12), 141.1 (5), 135.5 (3), 132.2 (21), 128.5 (11), 127.9 (10), 127.4 (19), 124.5 (20), 123.5 (6), 117.9 (2), 111.6 (22), 63.2 (8), 35.6 (13), 31.7 (16), 31.3 (14), 29.1 (15), 22.6 (17), 14.0 ppm (18).

*Synthesis of model compound 2.*¹⁰ Compound **1** (29 mg, 21.8 μmol , 1 eq), caesium carbonate (17 mg, 52.3 μmol , 2.4 eq) were weight into a Schlenk tube and dissolved in 27 μL degassed cyclohexanol. Then Pd_2dba_3 (0.2 mg, 1 mol%) and tris(2,4-di-*tert*-butylphenyl) phosphite (**3**) (0.6 mg, 4 mol%) were added and stirred for 16 h at 120 $^\circ\text{C}$. After cooling to room temperature the reaction mixture was extracted with dichloromethane, washed with water and dried over magnesium sulfate. The solvent was removed under vacuum to afford **2** as red solid (21 mg, 17.9 μmol , 82%). ^1H NMR (500 MHz, CDCl_3): δ 8.04 (s, 2H; 6), 7.87 (d, 8.7 Hz, 2H; 22), 7.83 (d, 7.1 Hz, 2H; 20), 7.58 (dd, 8.7 Hz, 7.1 Hz, 2H; 21), 7.53 (s, 2H; 2), 7.26 (d, 8.4 Hz, 8H; 10), 7.10 (d, 8.4 Hz, 8H; 11), 2.57 (t, 7.7 Hz, 8H; 13), 1.60 (m, 8H; 14), 1.4-1.2 (24H; 15-17), 0.86 ppm (t, 7.6 Hz, 12H; 18). ^{13}C NMR (125 MHz, CDCl_3): δ 156.6 (7), 155.6 (23), 153.7 (1), 151.9 (24), 143.3 (4), 141.8 (5, 9), 141.6 (12), 135.5 (3), 132.2 (21), 129.6 (21), 128.4 (11), 128.2 (19), 128.0 (10), 124.4 (20), 123.6 (6), 119.6 (22), 117.8 (2), 63.2 (8), 35.6 (13), 31.7 (16), 31.3 (14), 29.1 (15), 22.6 (17), 14.1 ppm (18).

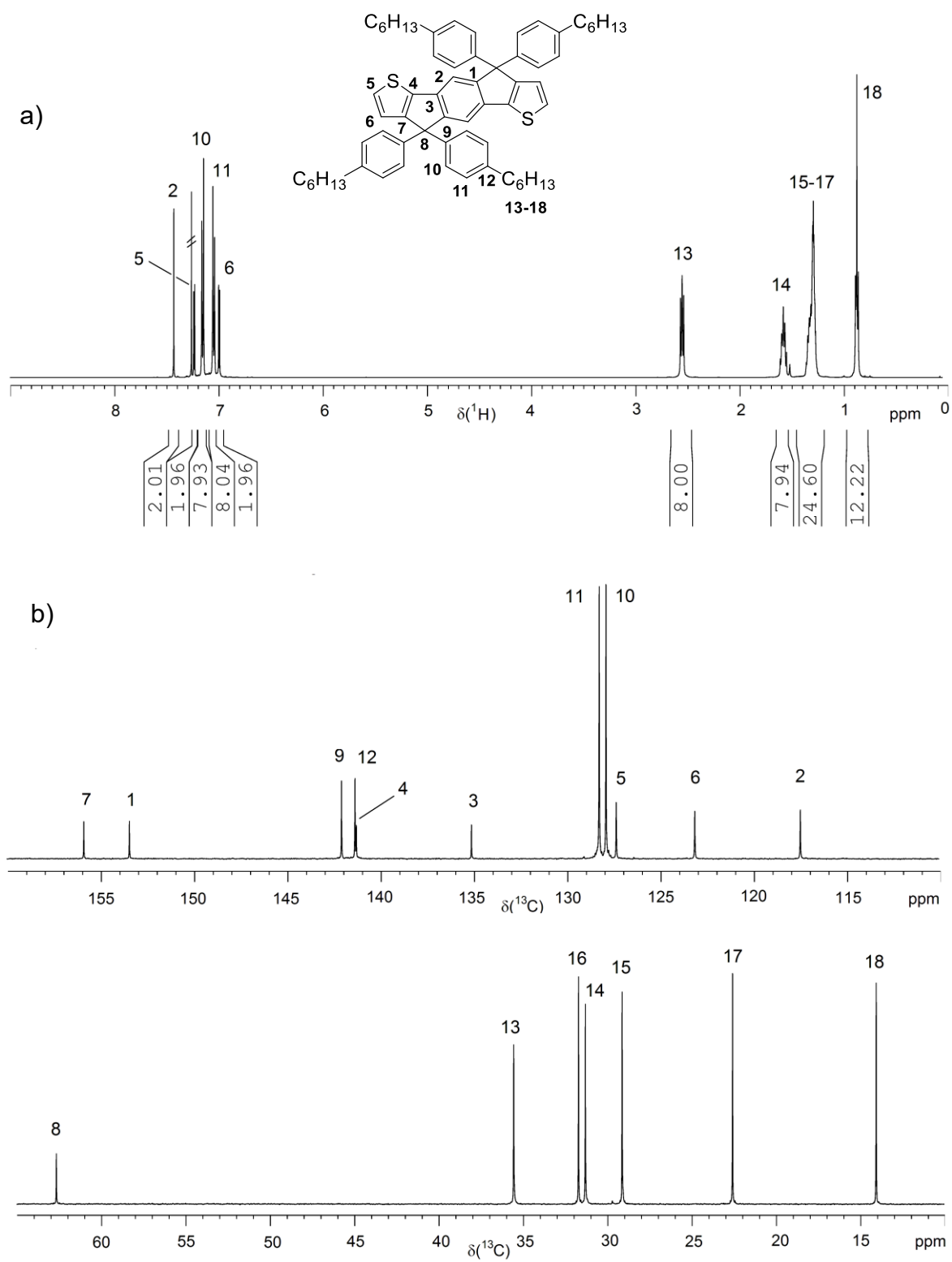


Figure III-S5. ^1H (a) and ^{13}C NMR spectrum (b) of **Ph₆IDT** (solvent: CDCl_3).

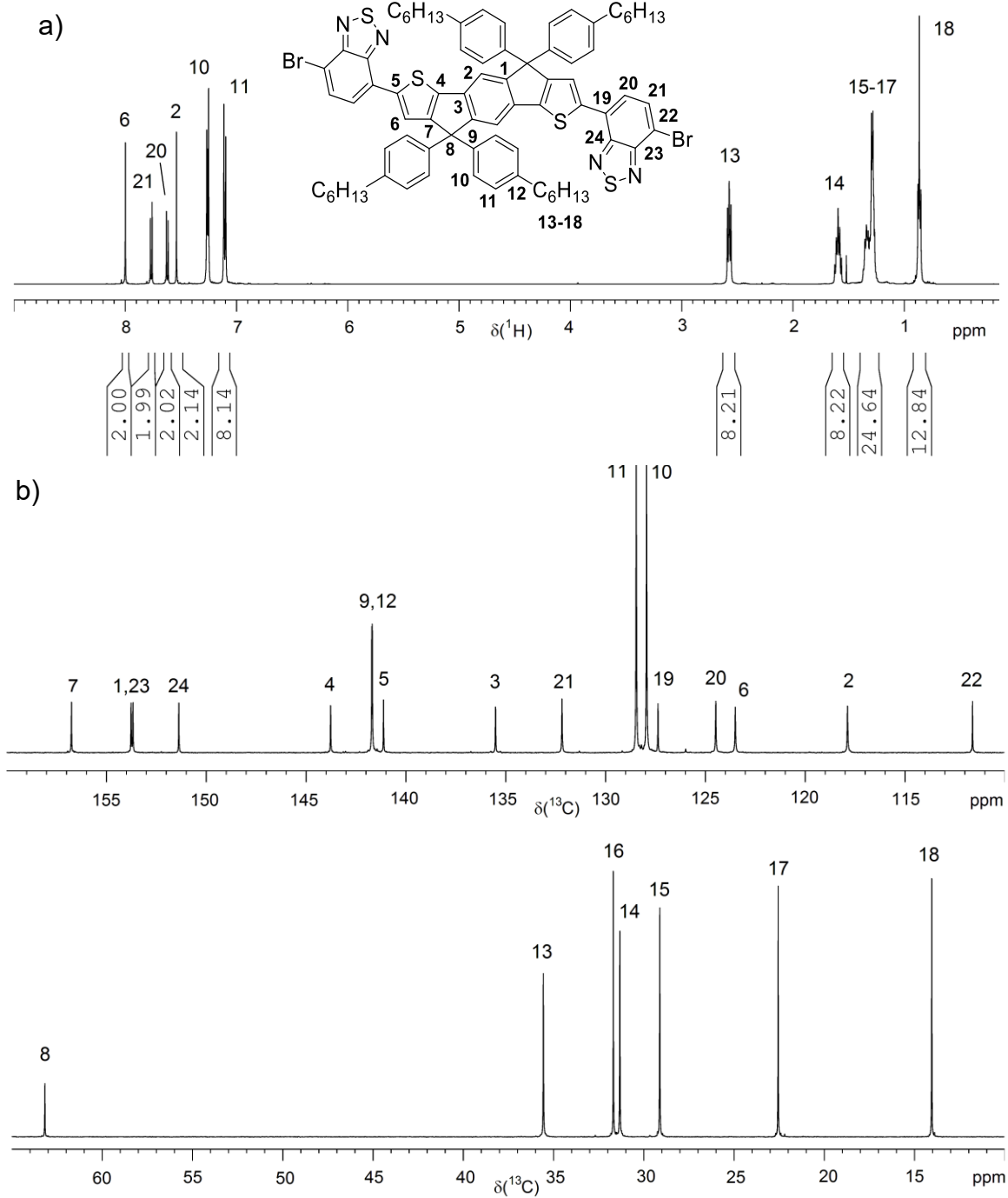


Figure III-S6. ^1H (a) and ^{13}C NMR spectrum (b) of compound **1** – BT-Br end group model (solvent: CDCl_3).

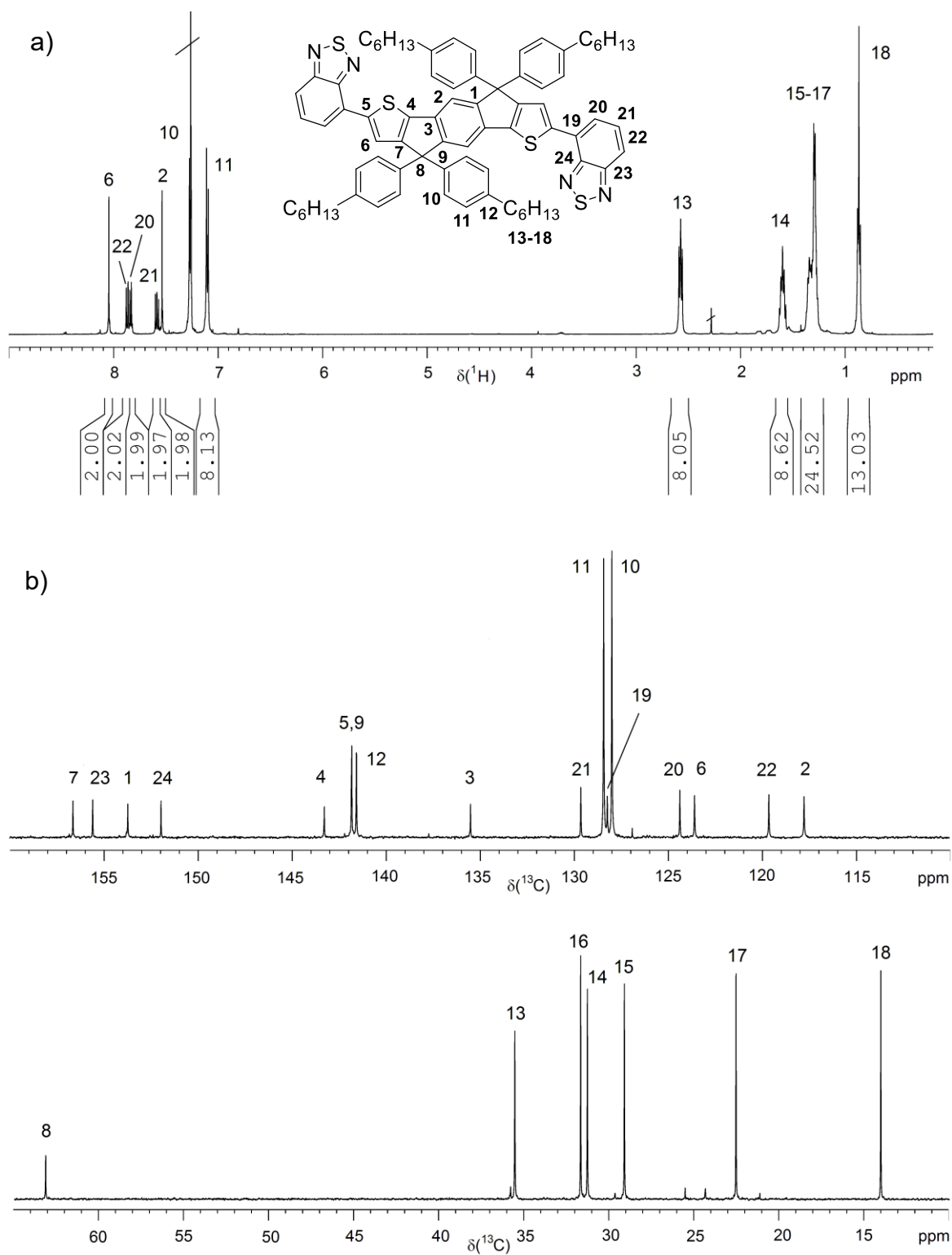


Figure III-S7. ^1H (a) and ^{13}C NMR spectrum (b) of compound 2 – BT-H end group model (solvent: CDCl_3).

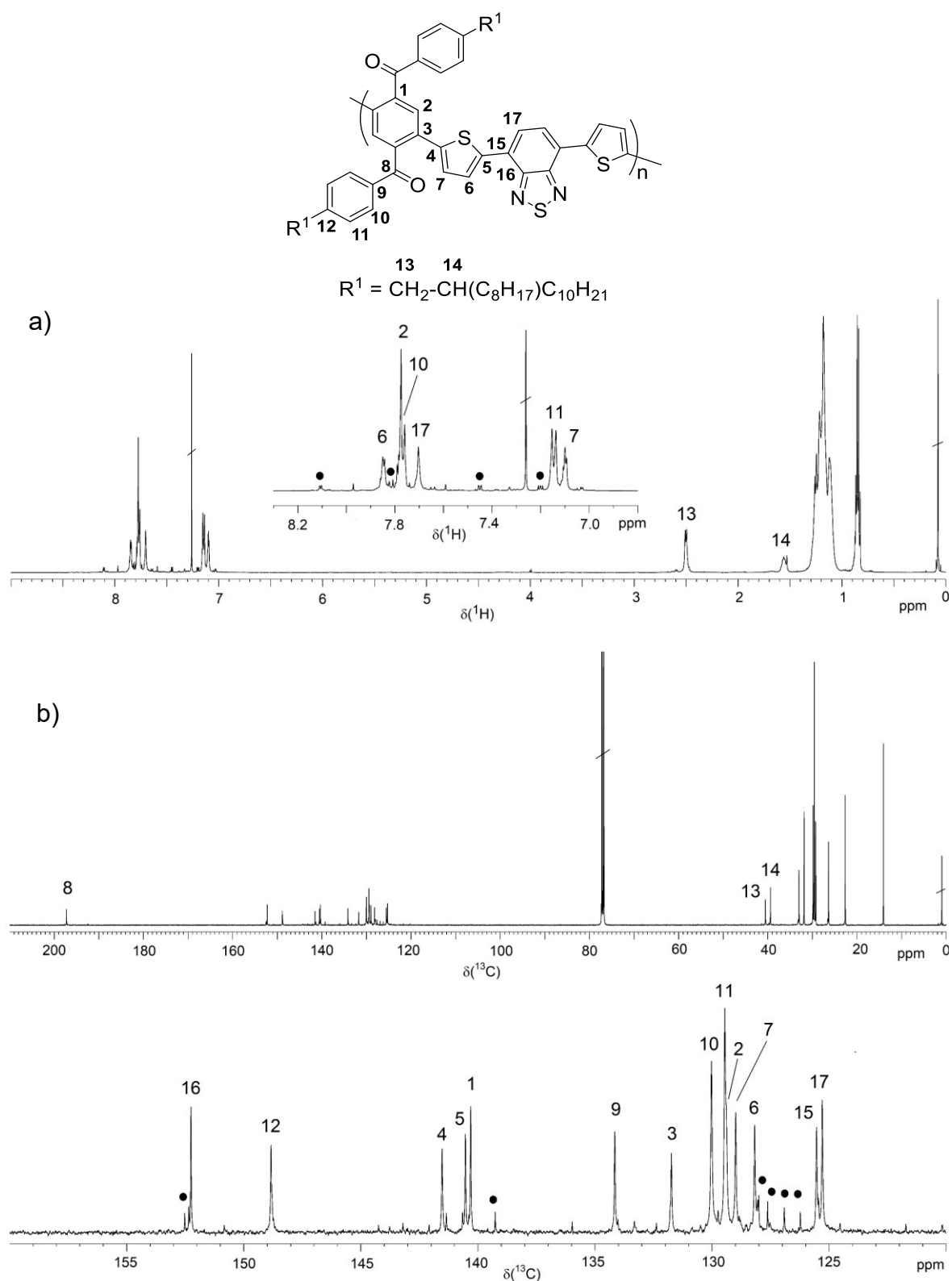


Figure III-S8. ^1H (a) and ^{13}C NMR spectrum (b) of *P(K-alt-TBT)*. The dots mark signals of the *-TBT-H* end group (solvent: CDCl_3).

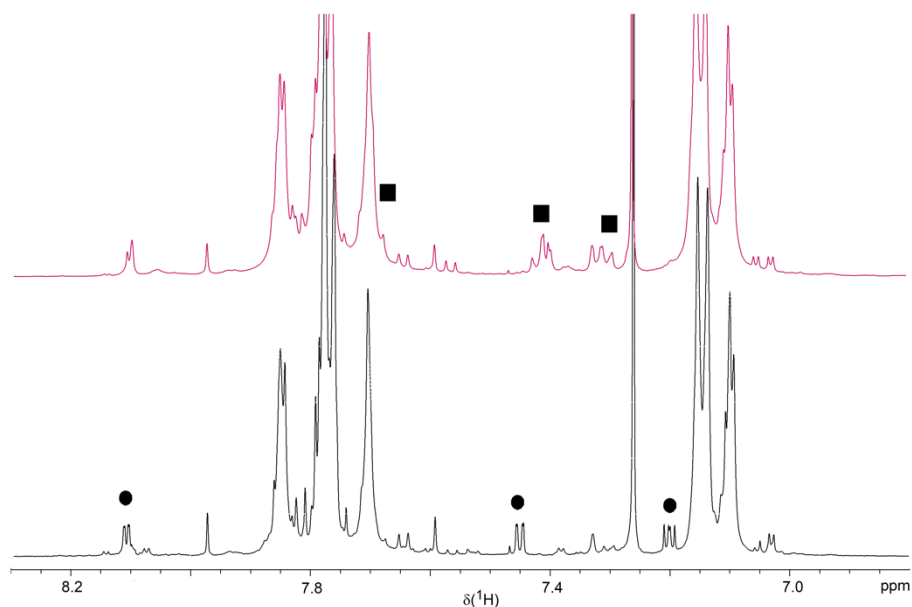


Figure III-S9. ^1H NMR spectrum (region) of **P(K-alt-TBT)** before (bottom) and after phenyl end capping (top). The dots mark signals of the $-\text{TBT-H}$ end group and the squares the phenyl signals of the formed $-\text{TBT-Ph}$ end group. The $-\text{TBT-H}$ signals are disappeared (solvent: CDCl_3).

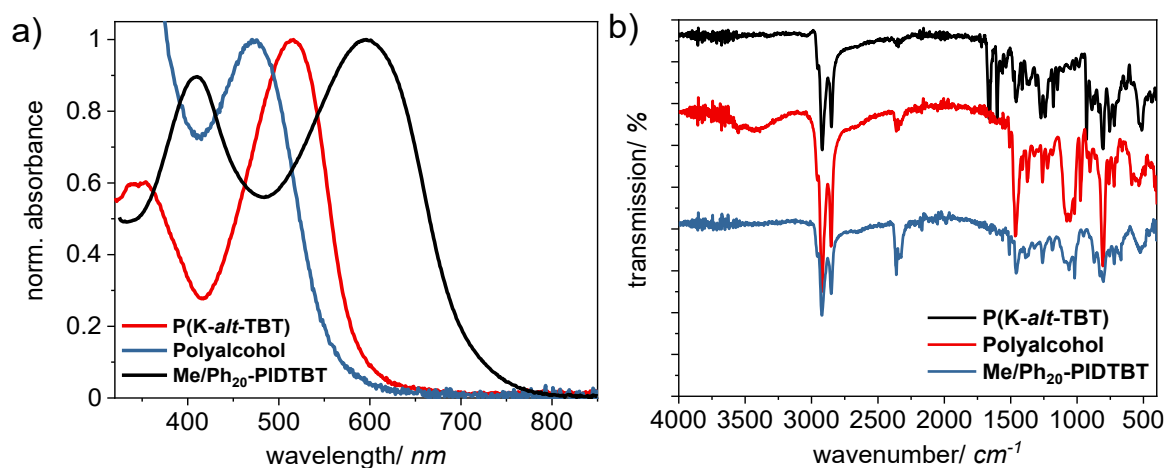


Figure III-S10. Reaction control of **Me/Ph₂₀-PIDTBT (P18)** via route B by UV-vis (a) and IR (b) spectroscopy.

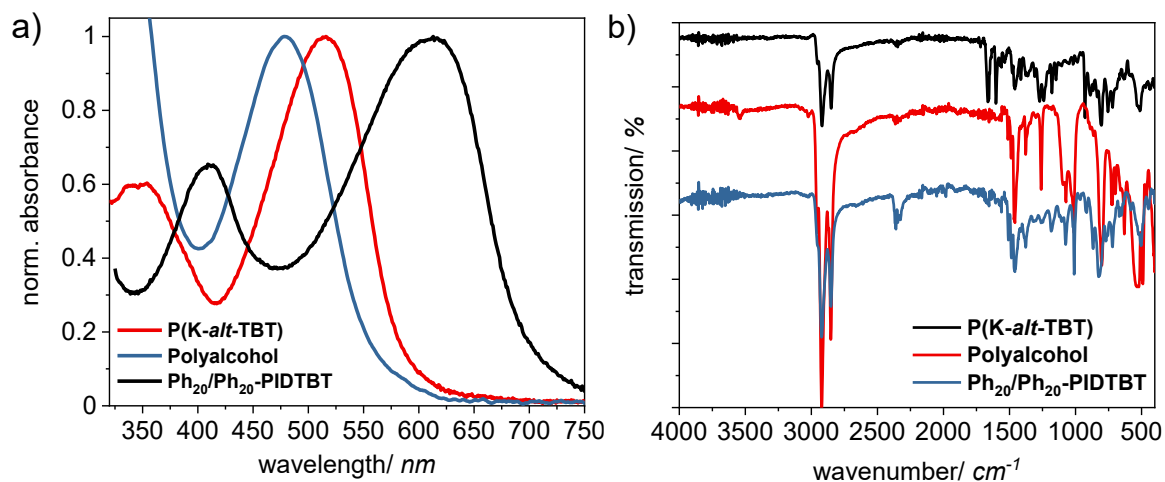


Figure III-S11. Reaction control of Ph₂₀/Ph₂₀-PIDTBT (**P19**) via route B by UV-vis (a) and IR (b) spectroscopy.

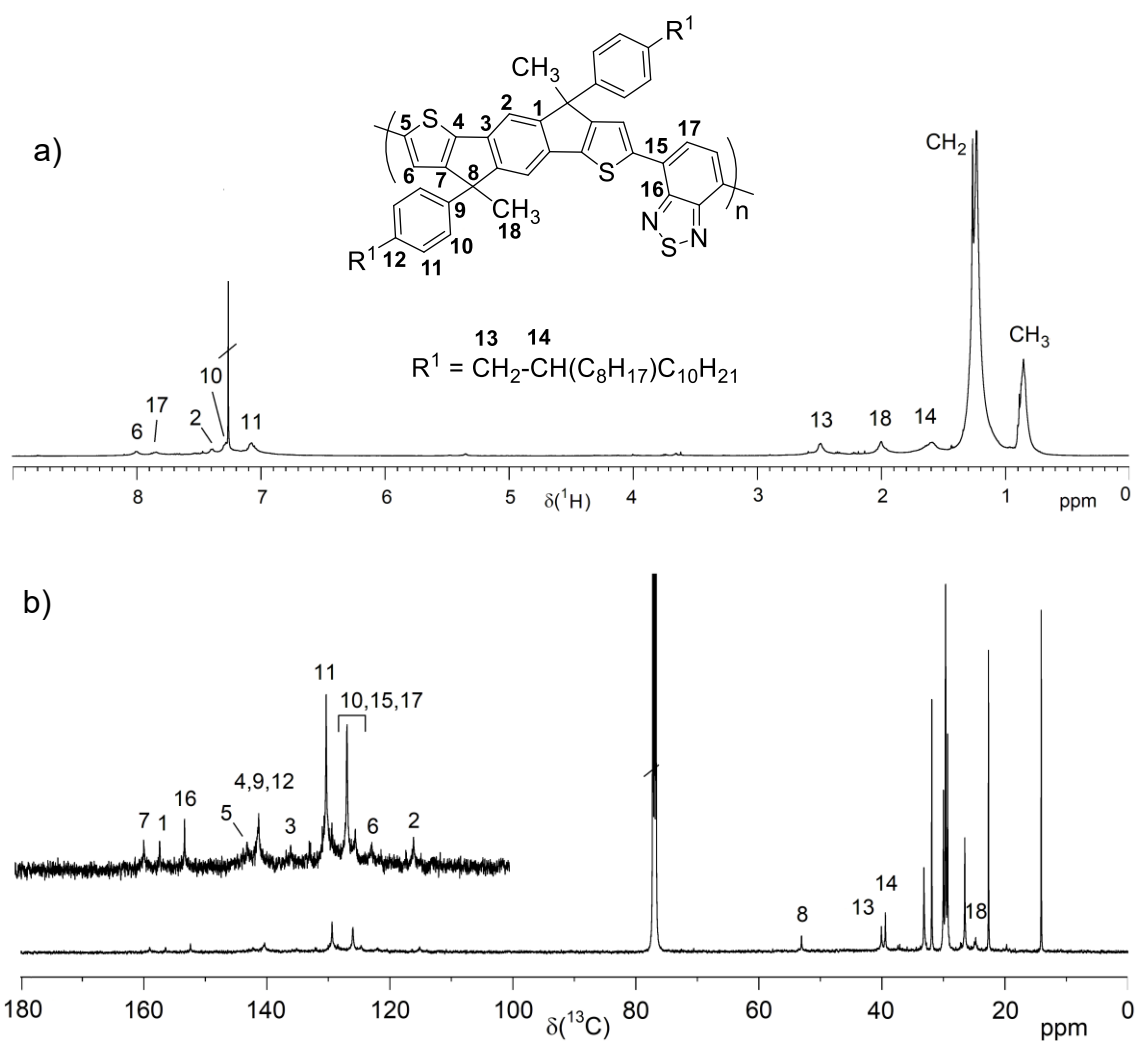


Figure III-S12. ¹H (a) and ¹³C NMR spectrum (b) of **P17** (solvent: CDCl₃).

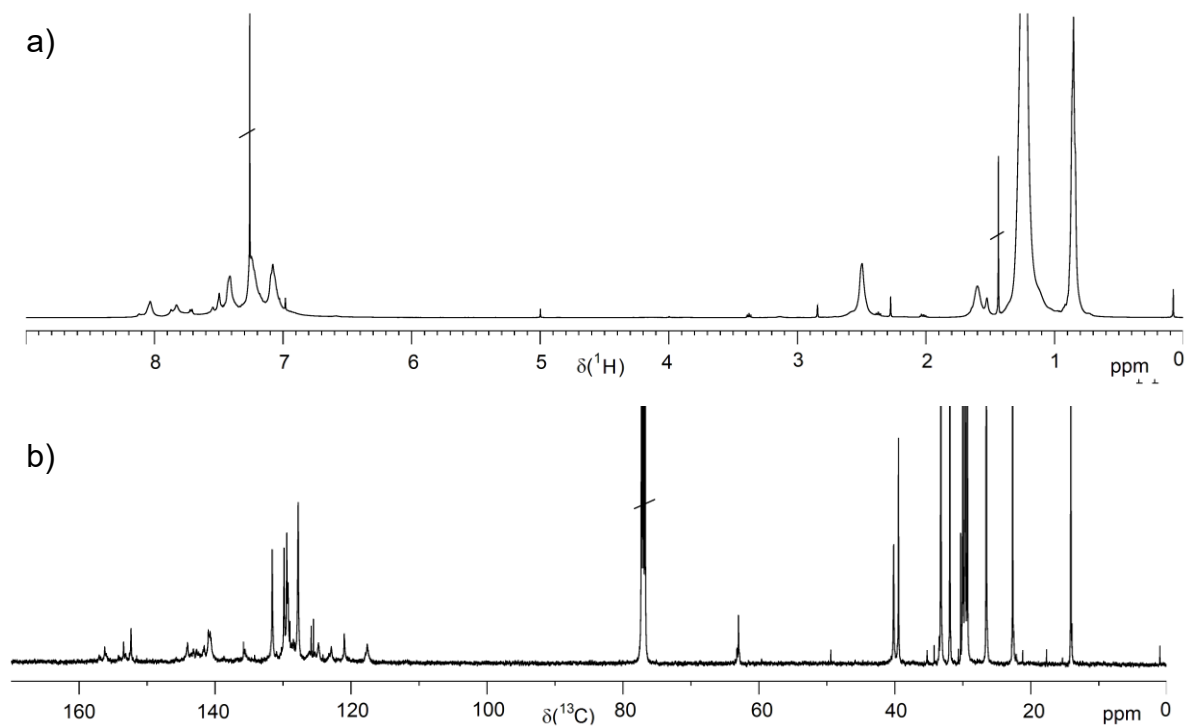


Figure III-S13. ^1H (a) and ^{13}C NMR spectrum (b) of **P19** from polymer analogous synthesis (solvent: CDCl_3).

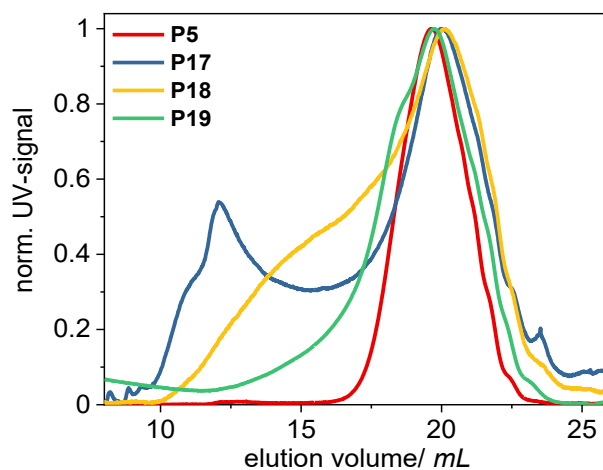


Figure III-S14. Comparison of SEC curves of PIDTBT via route A (**P5**) and via route B (**P17-P19**).

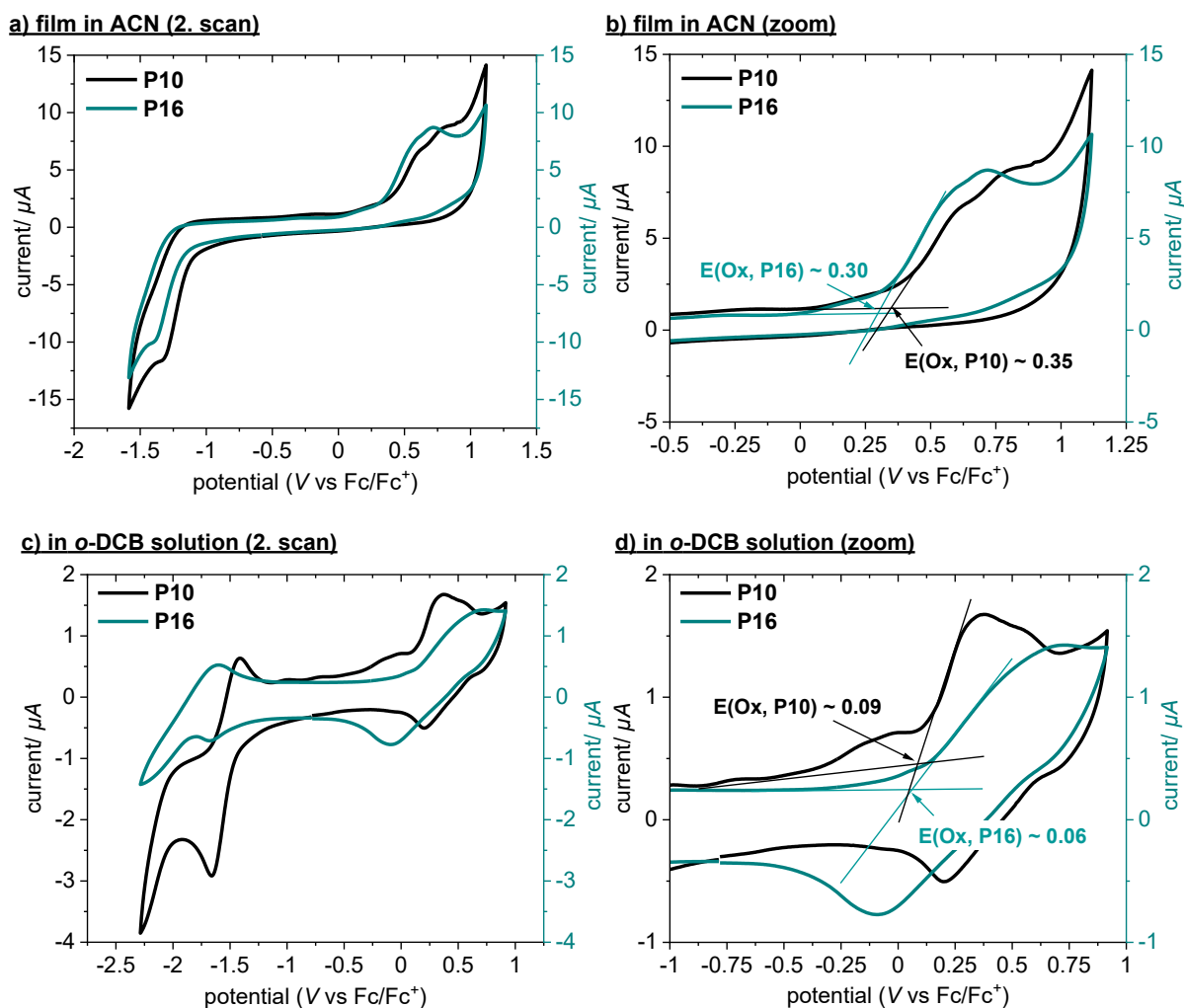


Figure III-S15. Cyclic voltammograms of **P10** and **P16** as film deposited on an ITO substrate in a 0.1 M NBu_4PF_6 acetonitrile solution (a, b) and in a 0.1 M NBu_4PF_6 o-DCB solution (c, d) at a scan rate of 50 mV s^{-1} . b) and d) show the enlarged region of oxidation onsets.

Table III-S1. Summary of electrochemical properties.

		E(Ox)	$\lambda_{\text{abs}}^{\text{onset}} / \text{nm}$	E_g / eV	HOMO ^b / eV	LUMO ^b / eV	$\Delta\text{HOMO} (\text{CV}) / \text{meV}$	$\Delta\text{LUMO} (\text{CV}) / \text{meV}$
film ^a	P10	0.35	715	1.73	-5.15	-3.46	50	0
	P16	0.30	733	1.69	-5.10	-3.46		
solution	P10	0.09	707	1.76	-4.89	-3.13	30	-1
	P16	0.06	721	1.72	-4.86	-3.14		

^aFilms were spin coated on ITO substrate (1000 rpm, 60 s). ^bCalculated as followed $E(\text{HOMO}) = E(\text{Ox}) + 4.8 \text{ eV}$ and $E(\text{LUMO}) = E(\text{HOMO}) + E_g$. $E^{1/2}(\text{Fc}/\text{Fc}^+) = 0.58 \text{ eV}$ in ACN and 0.79 eV in o-DCB, respectively.

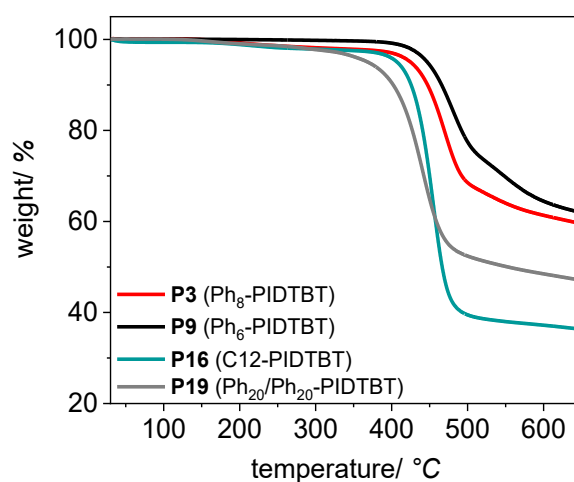


Figure III-S16. TGA thermograms of PIDTBT in N_2 .

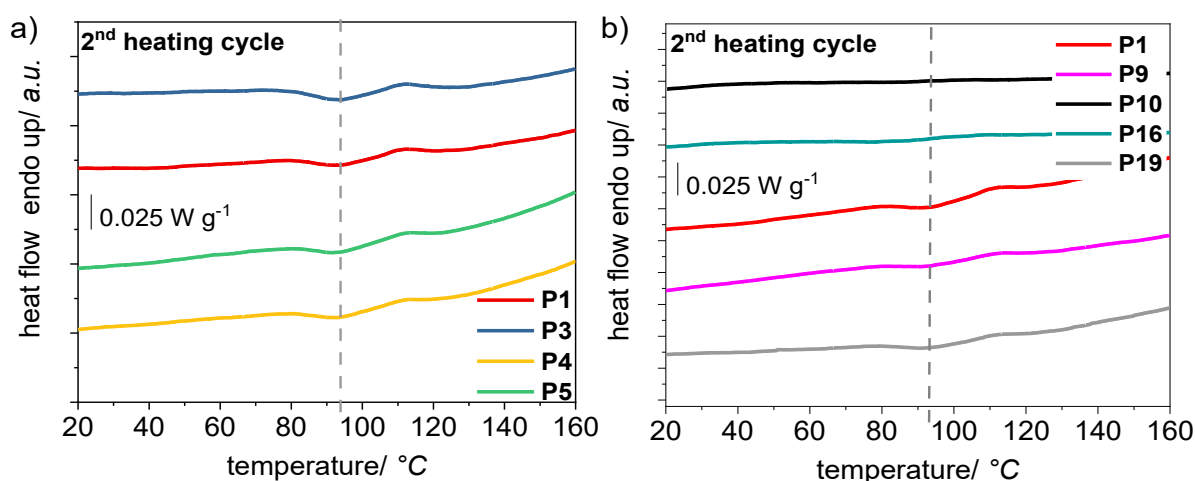


Figure III-S17. DSC curves of PIDTBT via DAP (route A) in dependence on molecular weight (a) and in dependence on side chain pattern and synthetic method. **P1** ($R = Ph_8$), **P9**, **P10** ($R = Ph_6$) and **P16** ($R = C_{12}H_{25}$) were made via DAP (route A); **P19** ($R = Ph_{20}/Ph_{20}$) via route B. Measured under N_2 with 20 K min^{-1} .

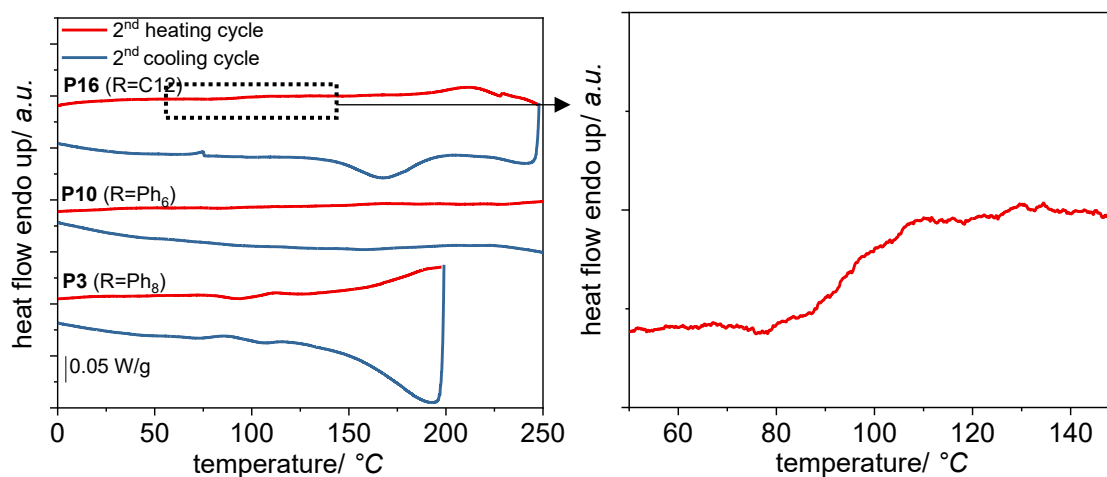


Figure III-S18. Comparison of DSC curves of PIDTBT with alkylphenyl (**P3**, **P10**) and aliphatic (**P16**) side chains on IDT unit. Measured under N_2 with 20 K min^{-1}

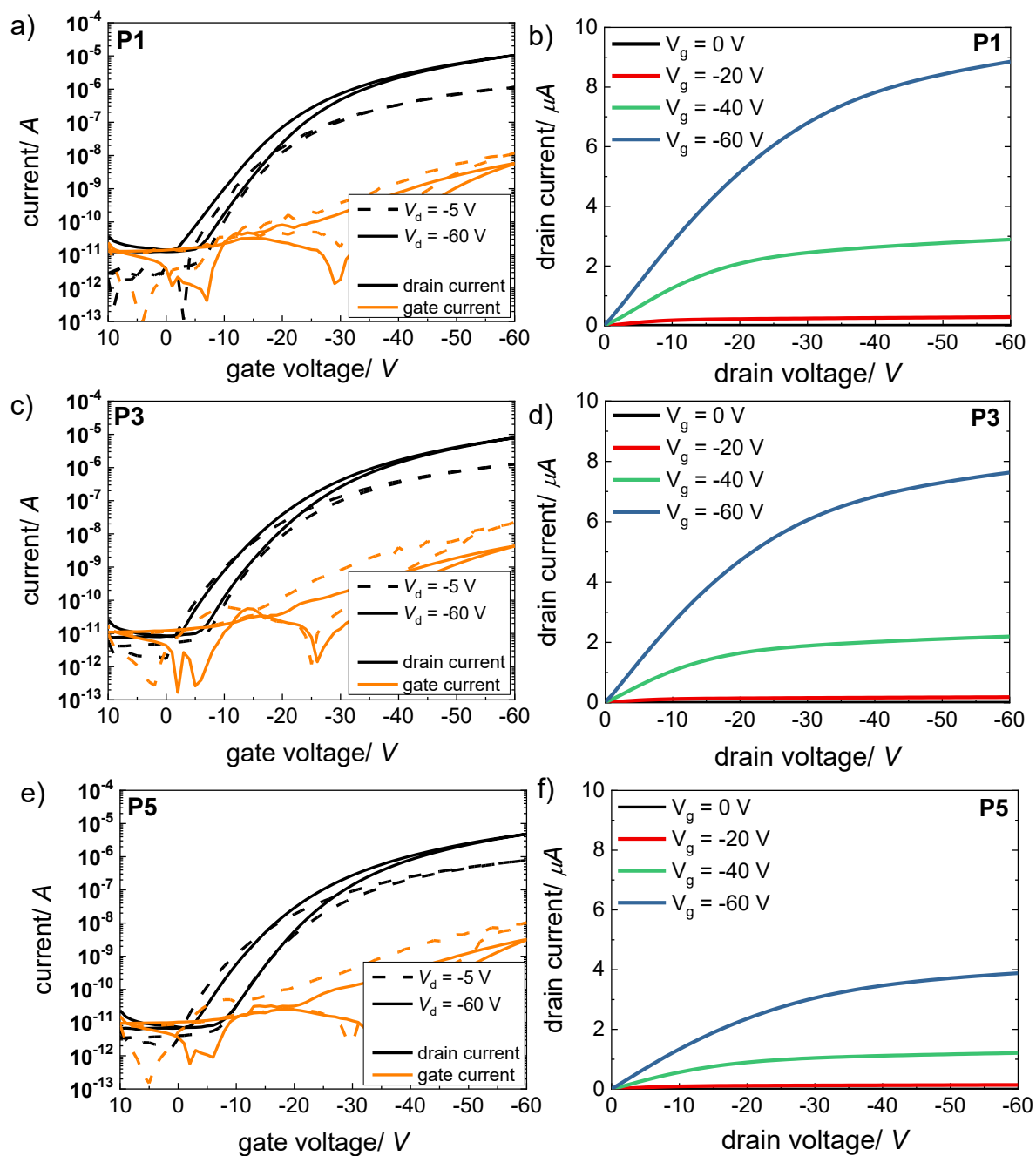


Figure III-S19. Transfer and output curves for the realized OFETs based on a-b) **P1**, c-d) **P3**, e-f) **P5**.

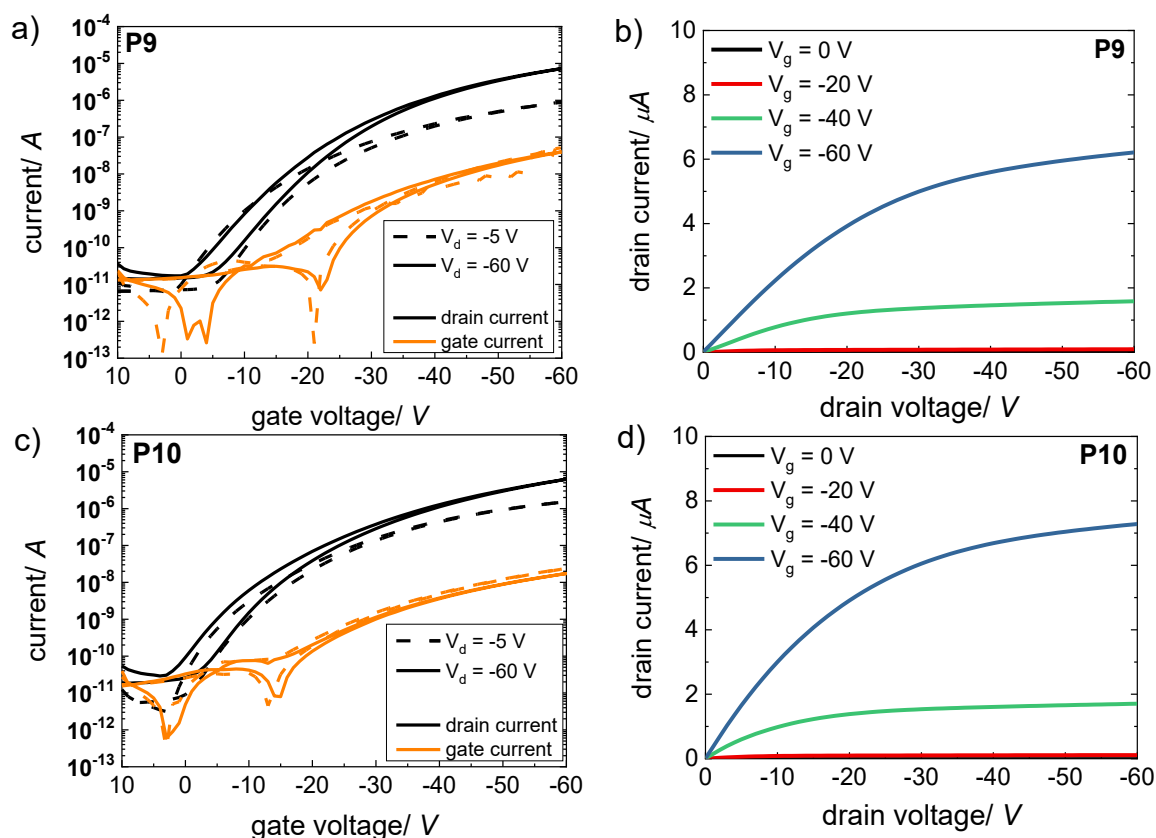


Figure III-S20. Transfer and output curves for the realized OFETs based on a-b) P9, c-d) P10.

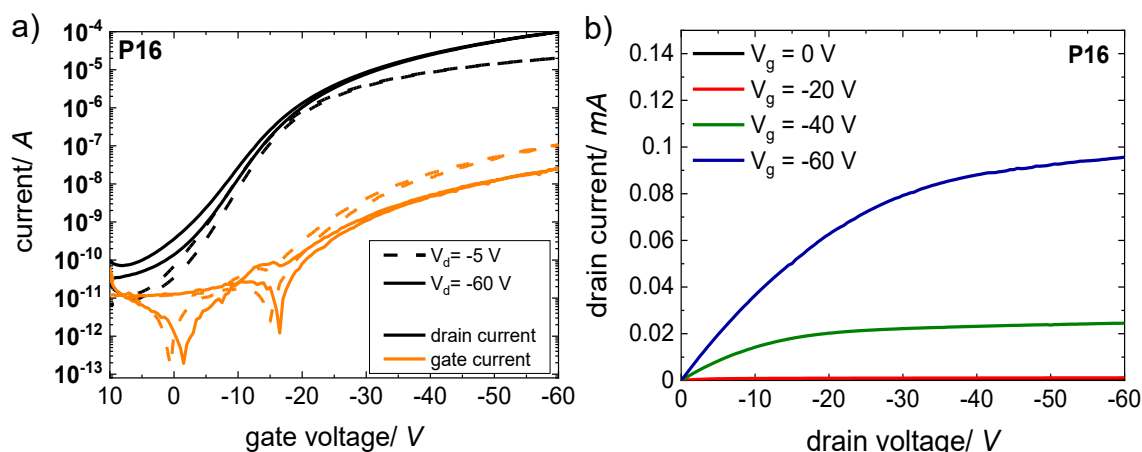


Figure III-S21. Transfer (a) and output (b) curve for the realized OFETs based on P16.

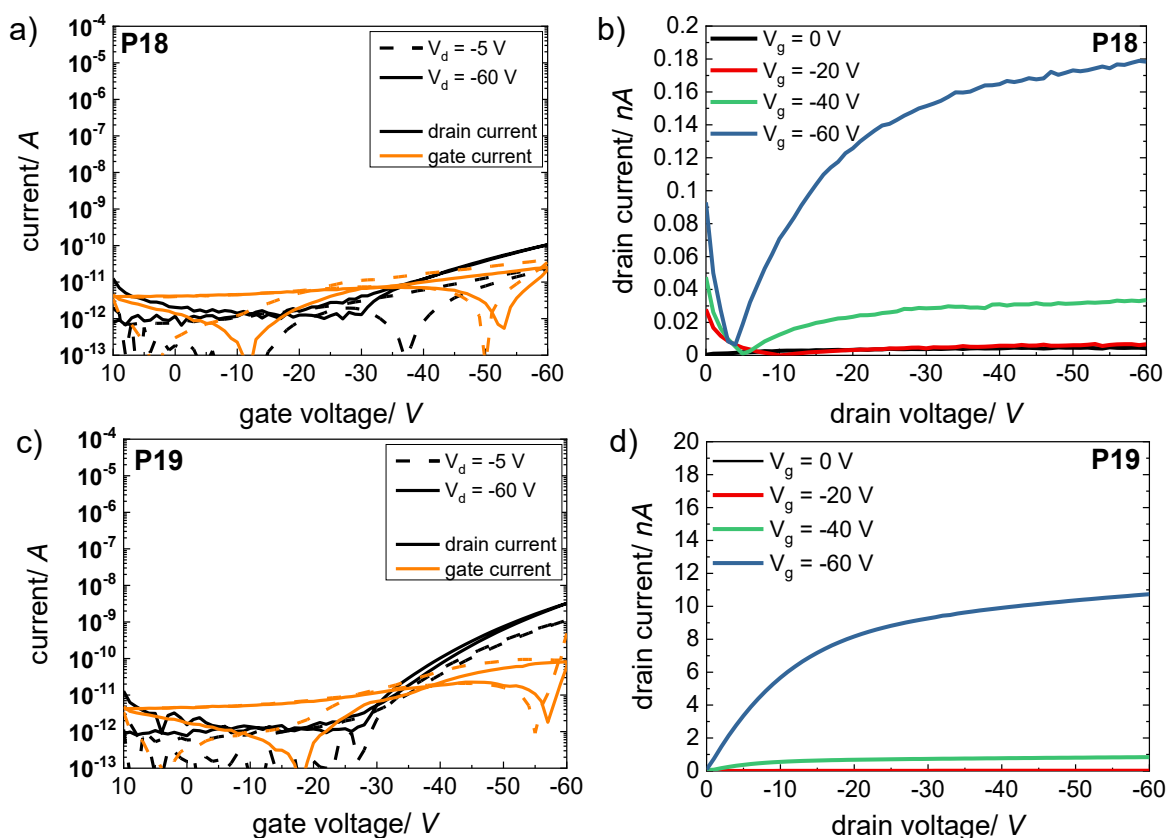


Figure III-S22. Transfer and output curves for the realized OFETs based on a-b) P18, c-d) P19.

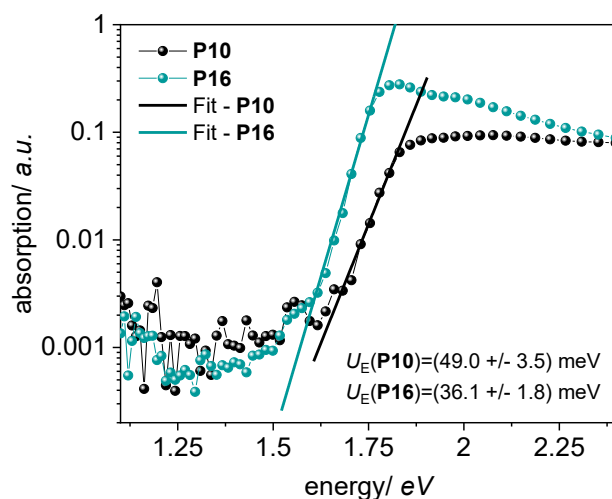


Figure III-S23. Absorption of $\text{Ph}_6\text{-PIDTBT}$ (P10) and $\text{C}_{12}\text{-PIDTBT}$ (P16) films; measured by photothermal deflection spectroscopy. The solid line displays the exponential fit for extraction of the Urbach energies U_E .

REFERENCES

- (1) Y. Zhao and D. G. Truhlar, The M06 suite of density functionals for main group thermochemistry, thermochemical kinetics, noncovalent interactions, excited states, and transition elements: two new functionals and systematic testing of four M06-class functionals and 12 other functionals, *Theor. Chem. Acc.*, 2008, **120**, 215–241.
- (2) R. A. Kendall, T. H. Dunning and R. J. Harrison, Electron affinities of the first-row atoms revisited. Systematic basis sets and wave functions, *J. Chem. Phys.*, 1992, **96**, 6796–6806.
- (3) M. J. Frisch et al., *Gaussian 16 Rev. C.01*, Wallingford, CT, 2016.
- (4) W. Humphrey, A. Dalke and K. Schulten, VMD: Visual molecular dynamics, *J. Mol. Graph.*, 1996, **14**, 33–38.
- (5) R. Krishnan, J. S. Binkley, R. Seeger and J. A. Pople, Self-consistent molecular orbital methods. XX. A basis set for correlated wave functions, *J. Chem. Phys.*, 1980, **72**, 650–654.
- (6) A. D. McLean and G. S. Chandler, Contracted Gaussian basis sets for molecular calculations. I. Second row atoms, $Z = 11-18$, *J. Chem. Phys.*, 1980, **72**, 5639–5648.
- (7) J. Tomasi, B. Mennucci and R. Cammi, Quantum Mechanical Continuum Solvation Models, *Chem. Rev.*, 2005, **105**, 2999–3094.
- (8) S. Miertuš, E. Scrocco and J. Tomasi, Electrostatic interaction of a solute with a continuum. A direct utilization of AB initio molecular potentials for the prevision of solvent effects, *Chem. Phys.*, 1981, **55**, 117–129.
- (9) E. Gann, M. Caironi, Y.-Y. Noh, Y.-H. Kim and C. R. McNeill, Diffractive X-ray Waveguiding Reveals Orthogonal Crystalline Stratification in Conjugated Polymer Thin Films, *Macromolecules*, 2018, **51**, 2979–2987.
- (10) J. Moon and S. Lee, Palladium catalyzed-dehalogenation of aryl chlorides and bromides using phosphite ligands, *J. Organomet. Chem.*, 2009, **694**, 473–477.

IV. Temperature-dependent morphology-electron mobility correlations of naphthalene diimide-indacenodithiophene copolymers prepared via direct arylation polymerization

Desiree Adamczak,^a Bianca Passarella,^{b,c} Hartmut Komber,^d David Becker-Koch,^e Oleksandr Dolynchuk,^f Simon B. Schmidt,^a Yana Vaynzof,^e Mario Caironi^b and Michael Sommer^a

^aTechnische Universität Chemnitz Polymerchemie, Straße der Nationen 62, 09111 Chemnitz, Germany.

^bCenter for Nano Science and Technology @PoliMi, Istituto Italiano di Tecnologia, Via Pascoli 70/3, 20133 Milano, Italy.

^cDipartimento di Elettronica, Informazione e Bioingegneria, Politecnico di Milano, 20133, Milan, Italy.

^dLeibniz-Institut für Polymerforschung Dresden e.V. Hohe Straße 6, 01069 Dresden, Germany.

^eIntegrated Centre for Applied Physics and Photonic Materials and Centre for Advancing Electronics Dresden (cfaed), Technische Universität Dresden, Nöthnitzer Str. 61, Dresden, 01187 Germany.

^fExperimental Polymer Physics, Martin Luther University Halle-Wittenberg, Halle 06120, Germany.

Submitted

ABSTRACT. A series of defect-free n-type copolymers poly(naphthalene diimide-*alt*-indacenodithiophene) P(NDI-IDT) comprising alternating naphthalene diimide (NDI) and indacenodithiophene (IDT) units is prepared using atom-economic direct arylation polycondensation (DAP). Copolymers with varying molecular weights up to $M_{n,SEC} = 113 \text{ kg mol}^{-1}$ are obtained in high yield and used to investigate optical, thermal and electrical properties as a function of chain length. Two weak endotherms are seen in differential scanning calorimetry experiments at 68 °C and 180 – 220 °C, depending on molecular weight, which are ascribed to side chain and main chain melting, respectively. Thin-film morphologies are weakly crystalline for annealing temperatures below main chain melting, with organic field-effect (OFET) mobilities being on the order of $10^{-3} \text{ cm}^2 \text{ V}^{-1} \text{ s}^{-1}$. Under these conditions very low Urbach energies between 27 and 30 meV are found. However, thermal annealing above main chain melting results in amorphous morphologies with hypsochromically shifted optical spectra, increased Urbach energies and complete loss of mobility. In comparison to the well-investigated bithiophene analogue P(NDIT2), P(NDI-IDT) thin films are far less crystalline than P(NDIT2) ones. This is ascribed to the additional bulky hexylphenyl side chains in P(NDI-IDT) that hamper main chain ordering and aggregate formation and thus, interchain charge hopping. As a result, field-effect electron mobilities are limited to $\sim 10^{-3} \text{ cm}^2 \text{ V}^{-1} \text{ s}^{-1}$ and mostly independent of chain length.

INTRODUCTION

Conjugated polymers are useful materials for high-performance organic electronic devices^{1–3} such as organic solar cells (OSCs)^{4,5} or organic field-effect transistors (OFETs).^{4,6} Especially donor-acceptor copolymers have emerged as modular systems due to versatile tailoring of their structural and electronic properties by proper selection of donor and acceptor blocks.^{7–9} In the last decade, one focus has been the development of new n-type polymers for OSCs and OFETs.^{10–14} Many of these n-type conjugated polymers are based on naphthalene diimide (NDI), perylene diimide (PDI) or bithiophene imide (BTI).^{10,15–17} A prominent and well-known representative is the naphthalene diimide bithiophene copolymer P(NDIT2), which exhibits excellent optical and electrical properties.^{16,18,19} Thus, it has been widely employed in all-polymer solar cells (all-PSCs) yielding power conversion efficiencies (PCEs) up to 10%.^{20–22} Moreover, derivatization of P(NDIT2) as lead structure upon variation of the NDI monomer,^{23–25} the donor monomer,^{15,16,26,27} or the side chains^{28–31} has been subject of many reports. While performance of n-type polymers is catching up in the fields of organic photovoltaics

(OPVs),^{10,32,33} progress in other domains such as organic thermoelectrics and energy storage systems still lag behind those of p-type materials.^{34,35} The replacement of bithiophene with the fused donor indacenodithiophene (IDT) has opened up further possibilities for n-type copolymers.^{28,36–38} IDT building blocks are highly rigid and coplanar and can be easily modified by, for example, side chain variation and backbone extension.^{39–41} Thereby, polymers such as PIDTBT were designed with low degree of energetic disorder leading to superior charge transport properties.^{39,42–44} Copolymerisation of IDT with NDI yields low band gap copolymers with n-type transistor characteristics and typical dual band absorption in the red and blue region of visible light. First fabrications of all-PSC devices in combination with common donor materials such as J51,³⁶ PBDB-T³⁸ and PBZ-C6²⁸ has led to PCEs of > 5%. Another possible application are flexible n-channel organic phototransistors (OTPRs) which can be used in skin therapy systems yielding mobilities in the range from 10^{-5} to 10^{-4} cm²V⁻¹s⁻¹.³⁷

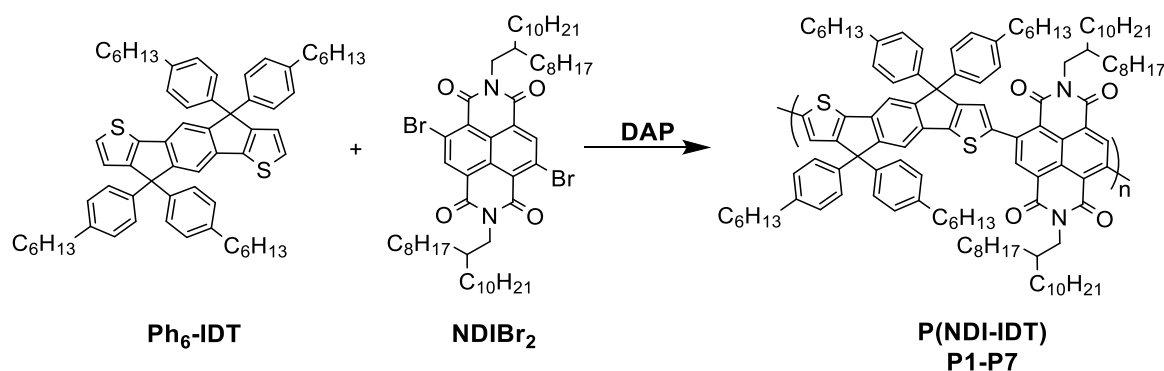
Next to the choice of building blocks, control over molecular weight (MW) and defects is key to optimizing performance and achieving reproducibility. Syntheses of copolymers based on NDI and/or IDT mostly make use of Stille polycondensation,^{36–38} with several well-known drawbacks.^{45–50} The use of direct arylation polycondensation (DAP) is not only more atom-economic, cost-efficient and faster as less reaction steps are involved,^{47,51,52} but also ideally suited for virtually all combinations of NDIBr₂ and thiophene-based comonomers.^{21,26,53–54} Thus, DAP has been successfully applied to the synthesis of defect-free NDI-based copolymers.^{26,53,54} However, there are few reports on IDT-based copolymers using DAP protocols yielding moderate MWs, in which a detailed defect analysis is missing.^{28,56–58} Recently, we reported synthesis of well-defined IDT homo- and copolymers *via* DAP.^{59,60} To date, the rare studies on NDI-IDT based copolymers mainly focus on their application in the field of organic photovoltaics. However, in order to optimize the performance of the material it is essential to understand its structure-property relationships. The influence of MW, end groups, processing solvents and post-temperature treatments are important factors that govern morphology and need to be optimized to understand the performance of new materials for organic electronics.

Herein, we present a detailed study of the synthesis, the characterization and the effect of annealing temperature on the morphology and optoelectronic properties of P(NDI-IDT) made by DAP. Polymerization of *n*-hexylphenyl-substituted IDT with NDIBr₂ yields defect-free P(NDI-IDT) in high yields and varying molecular weights up to $M_{n,SEC} = 113$ kg mol⁻¹. The polymers show a broad CT band around 728 nm with a band gap of 1.5 eV. While in solution

the CT band is highly affected by MW, thin film absorption is mostly dependent on thermal annealing. For annealing below main chain melting, P(NDI-IDT) thin films show weakly crystalline behavior and very low Urbach energies below 30 meV. However, field-effect mobilities are at a moderate level on the order of $10^{-3} \text{ cm}^2 \text{ V}^{-1} \text{ s}^{-1}$. Upon thermal annealing above main chain melting, thin film morphologies become amorphous resulting in blue-shifted absorption, significantly enhanced Urbach energies and loss of mobilities. Compared to P(NDIT2), thin films show much weaker crystallinity and lower field-effect mobilities, which is caused by the additional bulky hexylphenyl side chains in P(NDI-IDT) hindering molecular order of the polymer main chain.

RESULTS AND DISCUSSION

Synthesis and characterization. Copolymerization of *n*-hexylphenyl-substituted indaceno-dithiophene (Ph₆-IDT) and 2,6-dibromonaphthalene diimide with 2-octyldodecyl side chains (NDIBr₂) via DAP yielded P(NDI-IDT) copolymers with high molar masses $M_{n,SEC}$ up to 113 kg mol^{-1} (Scheme IV-1, Table IV-1).



Scheme IV-1. Synthesis of P(NDI-IDT) via direct arylation polycondensation.

Table IV-1. Reaction conditions of P(NDI-IDT).^a

entry	solvent	[IDT]/M	T/°C	cat/P-Ligand mol%	M_n/M_w^b kg mol ⁻¹	\bar{D}^b	yield ^c /%
P1	mesitylene	0.1	100	5/20	18/25	1.4	60
P2	mesitylene	0.25	100	5/20	43/86	2.0	91
P3	toluene	0.25	100	2/-	61/113	1.9	85
P4	mesitylene	0.1	100	2/-	103/516	5.0	79
P5	mesitylene	0.25	100	2/-	76/188	2.5	90
P6	mesitylene	0.25	80	2/-	113/295	2.6	90
P7	mesitylene	0.5	100	2/-	64/140	2.2	86

^aNDIBr₂ (1 eq.), Ph₆-IDT (1 eq.), PivOH (1 eq.) and K₂CO₃ (3 eq.) were used in all entries. ^bFrom size-exclusion chromatography (SEC) in CHCl₃. ^cIsolated yield after Soxhlet extraction with acetone, ethyl acetate and chloroform.

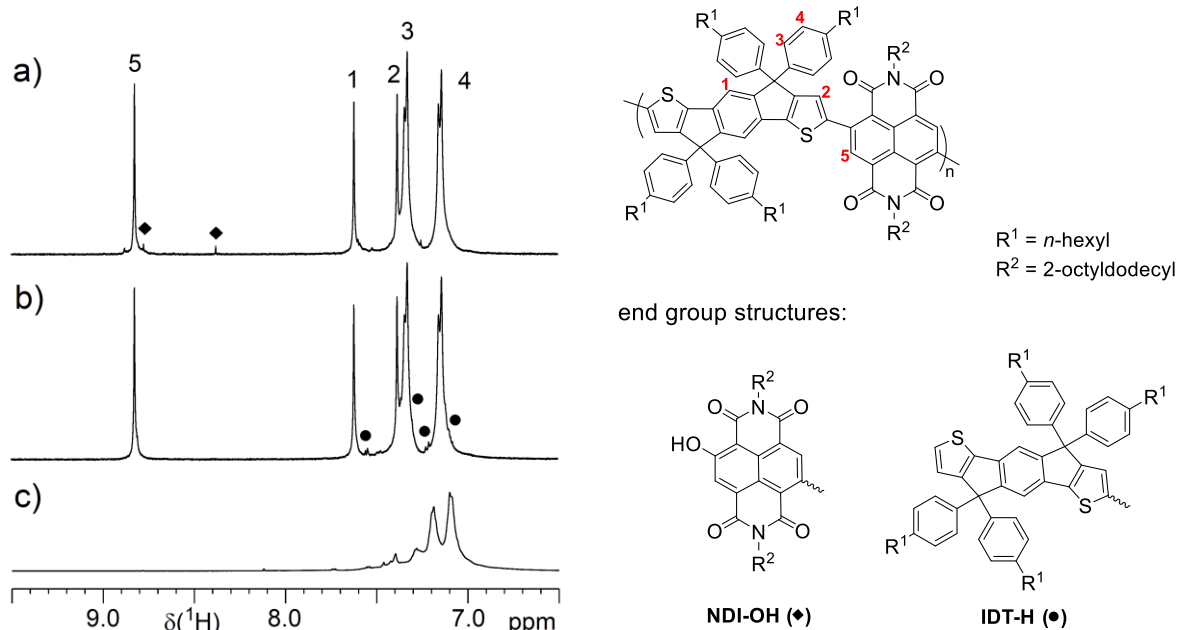


Figure IV-1. ^1H NMR spectra of **P7** (a), **P6** (b). ^1H NMR spectrum of model compound **Ph₈-PIDT** (c). Squares and dots mark signals of the $-\text{NDI-OH}$ and the $-\text{IDT-H}$ end groups, respectively.

These rather high values were achieved as a result of appropriately chosen reaction conditions as well as high solubility, which in turn is caused by side chains being present at both comonomers. Control over molecular weight could be achieved by regulation of reaction temperature and monomer concentration. A reduction of either one of them led to an increase of the molar mass (entries **P4-P6**). Interestingly, all polymerizations were stopped following gelation of the mixture after a few hours, indicating rapid build-up of MW. The sole exception is entry **P1**, where the low concentration and higher catalyst loading in combination with the addition of a phosphine-ligand favors nucleophilic substitution of NDI-Br chain ends by pivalate, leading to NDI-OH end groups after hydrolysis and accordingly low molar masses.^{18,26,53} High temperature ^1H NMR measurements at 120 °C in $\text{C}_2\text{D}_2\text{Cl}_4$ allow to prove this end group by a characteristic signal⁵³ at 8.38 ppm for the proton *ortho* to the OH group (Figure IV-1a). Without the usage of the P-ligand the polymers contain predominantly $-\text{IDT-H}$ end groups (Figure IV-1b, Figure IV-S2). **Ph₈-PIDT** is a model compound for IDT-IDT homocouplings. The signals from the phenyl rings do not overlap with P(NDI-IDT) signals and their appearance in the P(NDI-IDT) spectrum should indicate such defects. Fortunately, the ^1H NMR signals of the P(NDI-IDT) backbone are well separated, but apart from end group signals, additional signals that indicate structural defects are absent. Detailed ^1H and ^{13}C NMR analyses are provided in the Supporting Information (Figure IV-S1-S4, SI).

Optoelectronic and thermal properties. The UV-vis spectra of P(NDI-IDT) in dependence of molecular weight are shown in Figure IV-2a and b. In chloroform solutions, the polymers are characterized by a pronounced $\pi-\pi^*$ band at 395 nm and a broad charge transfer (CT) band at 728 nm with an absorption edge at 818 nm and a slight vibronic shoulder around 650 nm. Neither molecular weight nor the nature of the end groups influence the shape of the absorption spectra. In contrast, the molar extinction coefficients are strongly dependent on molecular weight (Table IV-2).⁶¹

Table IV-2. Summary of optical and thermal properties of selected samples.

entry	M_n/M_w^a kg mol ⁻¹	$\lambda_{\text{abs,max}}^b$ / nm	$\epsilon_{\text{abs,max}}^b/10^3$ L mol ⁻¹ cm ⁻¹	T_{m1}^c / °C	T_{m2}^c / °C	T_c^c / °C	ΔH_{m2}^c / J g ⁻¹	ΔH_c^c / J g ⁻¹
P1	18/25	394/726	21	68	183	178	4.03	4.58
P2	43/86	395/731	27	65	202	191	1.90	1.76
P3	61/113	395/728	29	66	207	196	0.79	0.72
P4	103/516	394/726	56	69	213	201	0.64	0.84

^aFrom SEC in CHCl₃. ^bMeasured in chloroform at room temperature; molar extinction coefficient was calculated from maximum wavelength of the low-energy band (see non-italic values). ^cDSC measured with 20 K min⁻¹ under N₂.

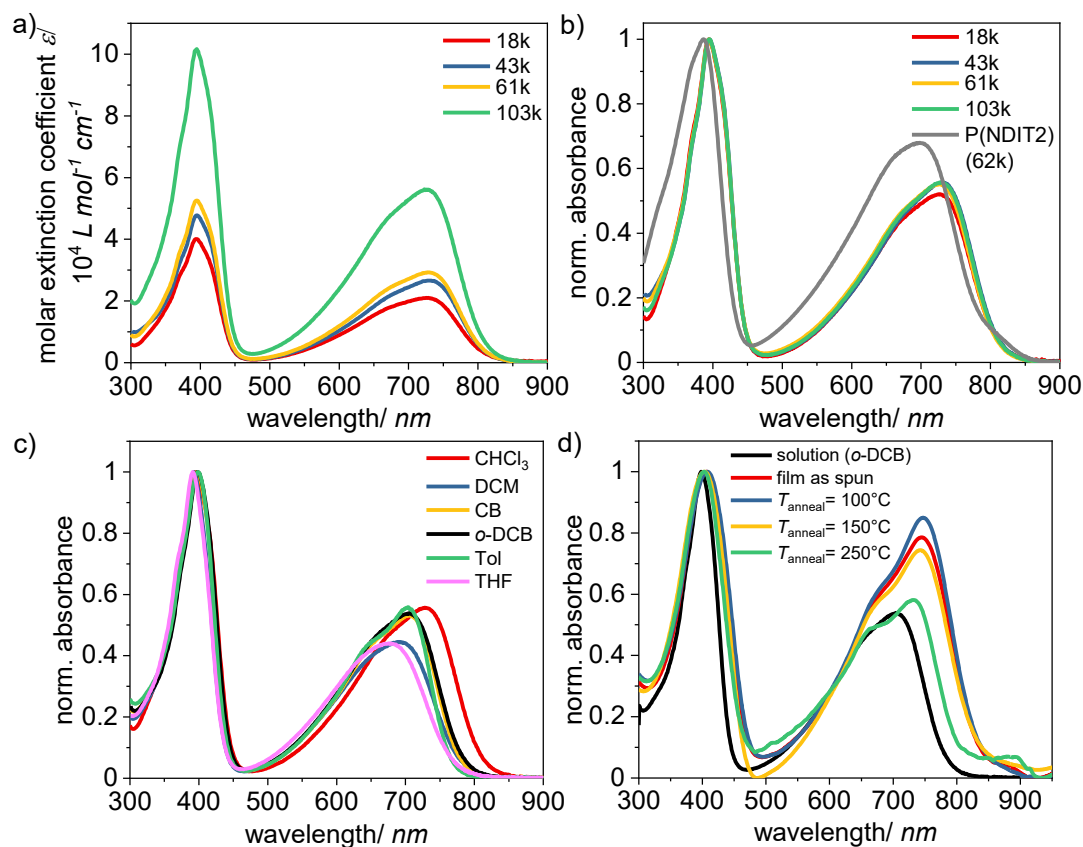


Figure IV-2. Molar extinction coefficient (a) and normalized UV-vis (b) spectra of P(NDI-IDT) of different MW (g mol⁻¹) in chloroform solution at room temperature. Solvent dependent (c) and film (d) UV-vis spectra of **P3** ($M_n = 61$ kg mol⁻¹).

Compared to P(NDIT2), the absorption maximum of the low energy band exhibits a bathochromic shift of 35 nm (Figure IV-2b), that can be attributed to the stronger donor strength of the IDT building block compared to bithiophene. However, the relative intensity of the CT band is lower, pointing to a reduced electronic interaction between NDI and IDT.^{23,26} To investigate the optical properties in more detail we chose polymer **P3** with a medium molar mass of $\sim 60 \text{ kg mol}^{-1}$ (Figure IV-2c and d). The solvent has a moderate impact on absorbance. The vibronic shoulder of the CT band is most pronounced in the non-polar solvent toluene. In polar solvents such as tetrahydrofuran (THF) and dichloromethane (DCM) the CT band is slightly blueshifted (Figure IV-2c). High-temperature UV-vis spectra do not show significantly altered spectra (Figure IV-S6). All these results are consistent with highly soluble copolymers that feature weak aggregation in solution. This is different to the optical behavior of P(NDIT2) and is caused by the additional side chains of P(NDI-IDT) located at IDT.⁶² Thin film absorption and the influence of the annealing temperature is displayed in Figure IV-2d. As spun films show spectra qualitatively similar to those of toluene solutions but with bathochromic shifts of around 40 nm. The spectral shift and the increased intensity of the CT band is attributed to conformational changes/planarization of the polymer backbone as well as chain-chain interactions during film formation. Thermal annealing below main chain melting (cf Figure IV-4) at temperatures of 100-150 °C slightly changes CT band intensity. Annealing at 250 °C, which is above T_{m2} , however, reduces CT band intensity as well as causes a hypsochromic shift of 16 nm. Additionally, a new band with low intensity and of unknown nature around 850 nm appears. The onset of the absorption band is used to determine the optical bandgap of **P1-P4**. The spectra reveal an optical bandgap for P(NDI-IDT) of 1.57 eV in solution and a slightly smaller band gap of 1.50 eV in film. The electrical band gaps extracted from cyclic voltammetry (CV), are about 1.85 eV in film and 1.69 eV in solution, respectively (Figure IV-3, Table IV-3).

Table IV-3. Summary of electrochemical properties.

	$\lambda_{abs}^{onset}/$ nm	$E_{g,opt}^c/$ eV	$E_{g,el}/$ eV	E(Ox)/ V	E(Red)/ V	$E^{1/2}(\text{Red})/$ V	HOMO ^d / eV	LUMO ^d / eV
film^a	824	1.50	1.85	0.76	-1.09	-1.10	-5.56	-3.71
solution^b	789	1.57	1.69	0.53	-1.12	-1.17	-5.32	-3.63

^aFilms were spin coated on ITO substrate (1000 rpm, 60 s) from *o*-DCB solutions. ^bIn *o*-DCB solution at r.t. ^cDetermined from absorption onset. ^dCalculated as followed $E(\text{HOMO}) = [E(\text{Ox}) + 4.8] \text{ eV}$ and $E(\text{LUMO}) = [-E^{1/2}(\text{Red}) - 4.8] \text{ eV}$.

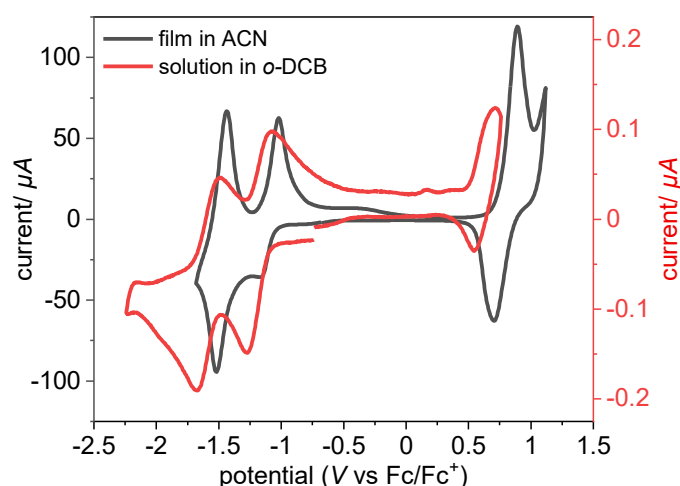


Figure IV-3. Cyclic voltammograms of P(NDI-IDT) as film deposited on an ITO substrate in a 0.1 M NBu_4PF_6 acetonitrile solution (black) and in a 0.1 M NBu_4PF_6 o-DCB solution (red) at a scan rate of 50 mV s^{-1} .

Compared to CV measurements in solution with a calculated HOMO of -5.32 eV , the determination from film CV results in a lower lying HOMO energy level of -5.56 eV (Table IV-3, Figure IV-3). However, the reduction onset $E(\text{Red})$ in solution and film are similar yielding comparable LUMO energy levels of -3.63 eV and -3.71 eV , respectively. The calculated LUMOs are slightly less negative than the reported values for P(NDIT2)^{23,26,38} and reflect the stronger donor strength of IDT in comparison with bithiophene.

P(NDI-IDT) shows excellent thermal stability with a degradation temperature greater than 440°C (Figure IV-S7). The thermal properties were further investigated by differential scanning calorimetry (DSC) as a function of molecular weight (Table IV-2, Figure IV-S8). **P1-P4** exhibit weakly semicrystalline behavior seen by two broad and weak endothermic transitions around $T_{\text{m1}} = 68^\circ\text{C}$ and $T_{\text{m2}} = 178 - 223^\circ\text{C}$ depending on molecular weight. Both transitions are most distinct in **P1** with lowest MW (Figure IV-4a). The transition at T_{m1} around 68°C vanishes in the second heating cycle and reappears in the first heating after the sample was stored at room temperature for several weeks. In analogy to P3HT,⁶³ we hypothesize that the first melting point T_{m1} arises from side chain melting and the second one T_{m2} from main chain melting (Figure IV-4b). Apparently the rather high density of side chains of P(NDI-IDT) allows for some ordering, and thus, for the appearance of an endothermic peak in the DSC traces, which is not seen with P(NDIT2). The mixed structure of side chains and their rather random orientation may cause slow crystallization over a time scale much larger than that of the DSC experiment.

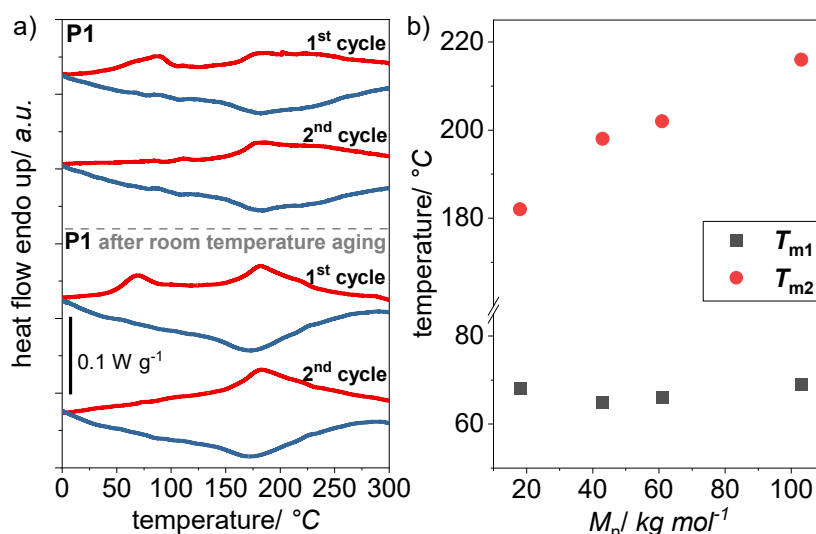


Figure IV-4. DSC curves of **P1** ($M_n = 18 \text{ kg mol}^{-1}$). First and second cycles were measured under N_2 with 10 K min^{-1} before and with 20 K min^{-1} after room temperature aging (a); Side chain T_{m1} and main chain T_{m2} melting transitions in dependence of MW (b).

Charge transport properties. Organic field-effect transistor (OFET) devices with a top-gate bottom-contact configuration were fabricated to investigate the electron transport properties of P(NDI-IDT). The devices show n-channel behavior and were optimized by screening the solvent for spin coating, annealing temperature, contact engineering and channel length (Figure IV-5 and Figure IV-S9 and S10). While the solvent seems to have a minor influence on the transfer characteristic curves, the annealing temperature has a greater impact (Figure IV-5a and b). Annealing of the devices at moderate temperatures, up to 150°C , is necessary to enhance performance, but is deleterious for annealing temperatures that approach T_{m2} (Figure IV-5b, Table IV-4). The charge mobilities of the optimized OFET devices in the saturation regime ($V_d = 40 \text{ V}$) are in the order of $10^{-3} \text{ cm}^2 \text{ V}^{-1} \text{ s}^{-1}$ (Table IV-5). The reduction of the channel length from 20 to $5 \mu\text{m}$ resulted in a correct scaling of currents, suggesting that contact resistance is not a limiting factor for the estimated field-effect mobility. The current as well as electron mobility increases with increasing molecular weight up to $M_n = 61 \text{ kg mol}^{-1}$ and afterwards slightly decreases for the highest MW sample **P4** (Figure IV-5c and d). Overall, MW dependence of mobility is rather limited. In general, electron mobilities are up to three orders of magnitude lower than the reported values for P(NDIT2).²⁶

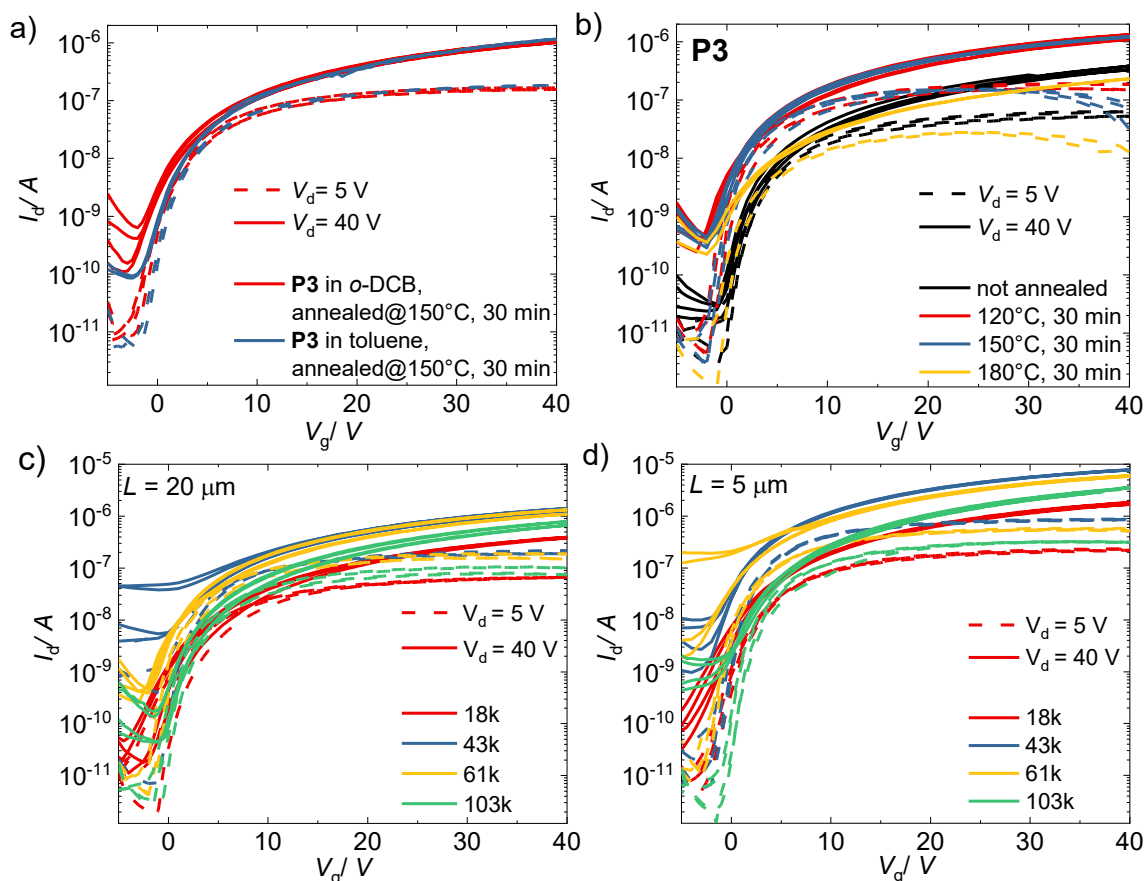


Figure IV-5. Optimization of OFET devices. Effect of solvent for spin coating (a) and annealing temperature for **P3** (b). Transfer curves of optimized devices as a function of MW (g mol^{-1}) and channel length (c,d).

Table IV-4. OFET data of **P3** devices at different annealing temperatures.^a

$T_{\text{anneal}}/^{\circ}\text{C}$	V_{th}^b/V	on/off ratio	$\mu_{\text{sat}}^c/\text{cm}^2 \text{V}^{-1} \text{s}^{-1}$
not annealed	2.8	$\sim 10^3$	$1.5 \cdot 10^{-3}$
120	1.9	$\sim 10^4$	$3.9 \cdot 10^{-3}$
150	1.7	$\sim 10^4$	$4.2 \cdot 10^{-3}$
180	2.5	$\sim 10^3$	$5.3 \cdot 10^{-4}$
250 ^d	-	-	-

^aDevices with $L = 20 \mu\text{m}$ were used in all entries. ^bCalculated at $V_d = 5 \text{ V}$ in linear scale. ^cCalculated at $V_d = 40 \text{ V}$. ^dNo mobilities could be extracted due to noise in the measurements.

Table IV-5. OFET characteristics of optimized devices ($T_{\text{anneal}} = 150^{\circ}\text{C}$) in dependence of MW.^a

entry	M_n/M_w kg mol^{-1}	V_{th}^b/V	on/off ratio ^c	$\mu_{\text{sat}}^d/\text{cm}^2 \text{V}^{-1} \text{s}^{-1}$
P1	18/25	1.8	$\sim 10^3$	$1.1 \cdot 10^{-3}$
P2	43/86	2.8	$\sim 10^2$	$4.4 \cdot 10^{-3}$
P3	61/113	1.9	$\sim 10^3$	$3.9 \cdot 10^{-3}$
P4	103/516	3.4	$\sim 10^4$	$1.7 \cdot 10^{-3}$

^aDevices with $L = 20 \mu\text{m}$ were used in all entries. ^bCalculated at $V_d = 5 \text{ V}$ in linear scale. ^cValues are similar for $V_d = 5 \text{ V}$ and $V_d = 40 \text{ V}$. ^dCalculated at $V_d = 40 \text{ V}$.

In order to better understand the OFET behavior as a function of the annealing temperature, we carried out photothermal deflection spectroscopy (PDS) on thin films of **P3** and P(NDIT2) as reference. This sensitive technique provides insight into the electronic order of polymers. Thereby, the bandgap edge absorption of polymer films is measured to extract the so-called Urbach energy U_E . The Urbach energy is known to be related to the degree of energetic disorder of the material and hence, can be associated with the charge transport properties.^{41,42,64,65} The thin films were prepared analogously to the OFET fabrication process. P(NDI-IDT) **P3** exhibits a sharp sub-band gap absorption and an extracted Urbach energy of $U_E = (29.3 \pm 0.9)$ meV ($T_{\text{anneal}} = 120$ °C). The value is comparable to P(NDIT2) with an extracted Urbach energy of $U_E = (30.6 \pm 0.9)$ meV (Figure IV-6, Table IV-6).

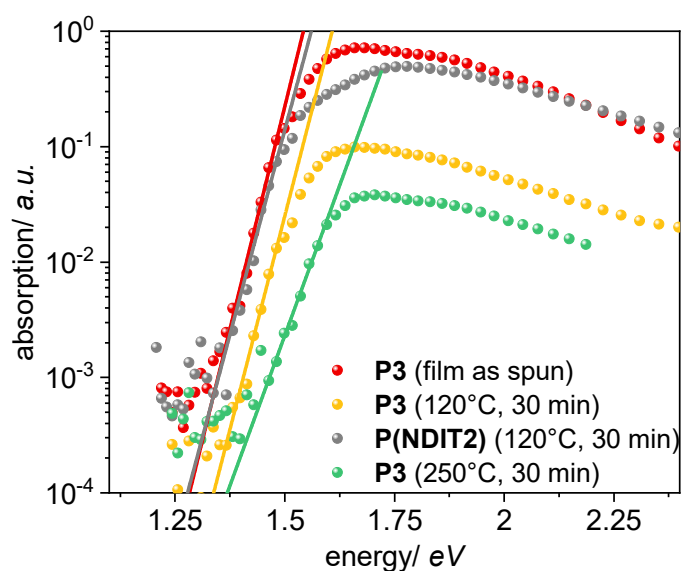


Figure IV-6. Comparison between the absorption of **P3** ($M_n = 61 \text{ kg mol}^{-1}$) and P(NDIT2) ($M_n = 62 \text{ kg mol}^{-1}$) thin films in dependence of the annealing temperature; measured by photothermal deflection spectroscopy. The solid line displays the corresponding exponential fits for extraction of the Urbach energy U_E . Films were spin-coated (1000 rpm, 60 s) from *o*-DCB solutions.

Table IV-6. Urbach energy of **P3** and P(NDIT2) in dependence of annealing temperature.

entry	$T_{\text{anneal}}^a / ^\circ\text{C}$	U_E / meV
P3	not annealed	28.2 ± 1.0
P3	120	29.3 ± 0.9
P3	250	41.7 ± 2.9
P(NDIT2)	120	30.6 ± 2.0

^aFilms were spin-coated (1000 rpm, 60 s) from *o*-DCB solutions and annealed at the given temperature for 30 min under argon.

Further experiments, in which the influence of annealing temperature on the energetic disorder were investigated, show that annealing at temperature higher than 150 °C is detrimental for the energetic order of the material (Table IV-6). Interestingly, the lowest Urbach energy (28.2 ± 1.0 meV) could be extracted from the absorption of the **P3** as spun thin film, which is one of the lowest reported values for conjugated polymers (Figure IV-6).^{42,66} These observations clearly show that U_E alone cannot grasp the complexity of charge transport process in a polymer thin film. While U_E can help to understand the relation between thin film morphology and energetic order of optically probed states, the accessibility of such states along the channel of a transistors through an efficient percolative path is a requirement for high carrier mobility. The presence of bulky hexylphenyl side chains at the IDT unit, hindering solution aggregation, as well as crystallization and overall interconnectivity in thin films, can have a drastic effect on interchain transport. The latter plays a dominant role in the case of highly localized states, as typical of NDI-based copolymers, where intrachain transport is not effective.^{67,68}

GIWAXS measurements. To gain further information about the molecular packing of P(NDI-IDT), grazing incidence wide-angle X-ray scattering (GIWAXS) measurements were performed on thin films of **P3**. The films were prepared using the conditions for the best OFET device with $T_{\text{anneal}} = 120$ °C (below main chain melting) and, in comparison, for annealing above main chain melting at $T_{\text{anneal}} = 250$ °C. The results are illustrated in Figure IV-7a-d. The sample annealed at 120 °C shows a low degree order suggesting a liquid crystalline organization rather than crystalline. The observed (100) and (200) peaks at $q = 0.334$ Å⁻¹ and $q = 0.668$ Å⁻¹ allowed determining the interchain d_{100} -spacing along the side chain direction being 18.81 Å. The azimuthal distribution of the (100) peak clearly indicates a preferential edge-on orientation (Figure IV-7a and b). Furthermore, the 2D GIWAXS image and the 1D scattering curves extracted from it along meridian and equator do not show any prominent π - π stacking peaks (Figure IV-7a and b). Such observation confirms the drastic effect of the molecular structure on the π - π stacking disorder, introducing energetic barriers to interchain transport of electrons through the films. Upon annealing at 250 °C (Figure IV-7c and d) the material evidences a solely edge-on orientation and a significantly reduced molecular ordering, as the area below the (100) peak decreased by about 20 times (see SI, Figure IV-S11), with a slightly decreased d_{100} -spacing. The dependence of the annealing temperature on the molecular ordering complies with the previously discussed reduction of the CT absorption band and can partly explain the diminished mobilities for annealing above 150 °C.

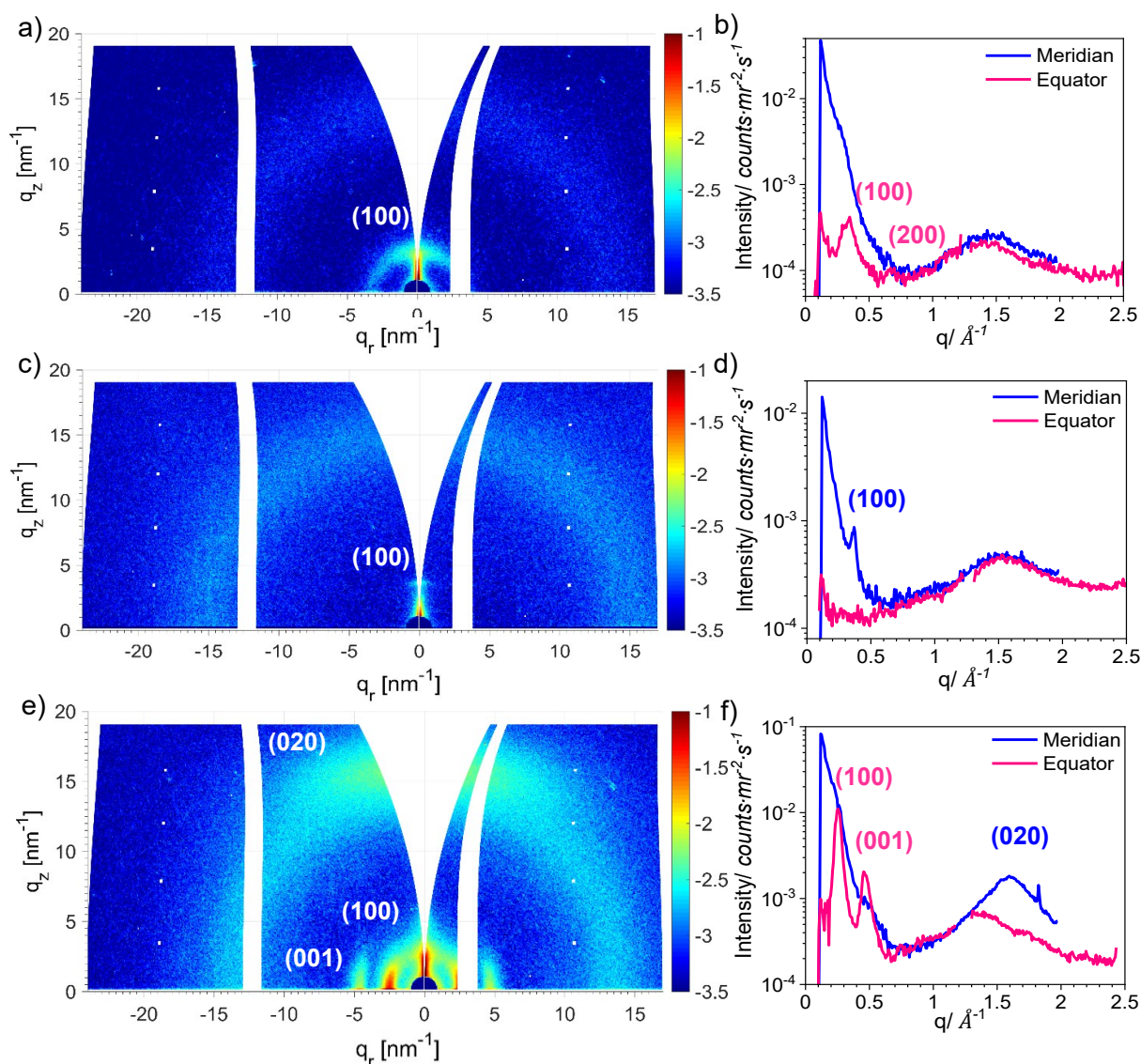


Figure IV-7. GIWAXS patterns and 1D GIWAXS profiles of **P3** thin films annealed at 120 °C (a,b) and at 250 °C (c,d) as well as of P(NDIT2) thin film annealed at 120 °C (e,f).

In order to investigate the difference of ordering between P(NDI-IDT) and P(NDIT2), the GIWAXS measurements of a P(NDIT2) film annealed at 120 °C were carried out (Figure IV-7e and f). In contrast to the edge-on orientation of P(NDI-IDT), P(NDIT2) exhibits a predominant face-on orientation. In addition, a (020) diffraction peak corresponding to the π - π stacking distance of 3.94 Å can be monitored suggesting a higher crystalline order than that in P(NDI-IDT).

CONCLUSIONS

We have presented a robust and atom-economic friendly protocol for highly soluble alternating copolymers made from naphthalene diimide (NDI) and indacenodithiophene (IDT) *via* direct arylation polycondensation. Detailed molecular characterizations indicate that P(NDI-IDT) is defect-free. Molecular weights (MWs) up to $M_{n,SEC} = 113 \text{ kg mol}^{-1}$ can be tuned by an appropriate adjustment of reaction conditions. The optical properties are almost independent of solvent, temperature as well as end groups and show a low degree of aggregation. While molar extinction coefficients and thermal properties are highly dependent on MW, absorption onset and maximum of the charge transfer band are not affected by MW. DSC shows two weak and broad endothermic transitions which are ascribed to side chain and main chain melting. Optimization of the OFET devices reveal that annealing is important to boost performances but it is deleterious at temperatures above 150 °C, which is in accordance with the optical behavior of the thin films. Electron mobilities are moderate and mostly independent of MW for as spun films and entirely vanish for thermal annealing above main chain melting. Urbach energies are very low for as spun films but rather higher after thermal annealing above main chain melting. GIWAXS reveals a very weakly crystalline morphology of films after spin coating and an almost entirely amorphous morphology after thermal annealing above main chain melting. Taken together, low Urbach energies as well as a semicrystalline morphology with chain-chain contacts is required for efficient charge transport. The latter is not possible in P(NDI-IDT) films, as the additional and bulky hexylphenyl side chains do not allow for significant solution aggregation and crystallization in thin films. These results emphasize the importance of interchain transport for high carrier mobility, especially if intrachain transport alone is not efficient as is the case with P(NDIT2).

EXPERIMENTAL

Materials and methods. All starting materials were purchased from commercial sources and used without further purification unless otherwise specified. All reactions were carried out in flame dried glassware and under dry inert gas atmosphere. Compounds Ph₆IDT, NDIBr₂ and the model compound Ph₈-PIDT were synthesized according to published protocols.^{59,60,69}

Detailed information about instrumentation and experimental procedures are described in the Supporting Information (SI). SEC curves of the samples **P1-P7** are shown in Figure IV-S5.

Synthetic procedures.

General synthetic procedure for synthesis of P(NDI-IDT) via DAP (P6). Ph₆IDT (141.1 mg, 155.5 μ mol, 1 eq), NDIBr₂ (153.2 mg, 155.5 μ mol, 1 eq), pivalic acid (15.9 mg, 155.5 μ mol, 1 eq) and potassium carbonate (64.5 mg, 466.6 μ mol, 3 eq) were placed in a vial and dissolved in 0.62 mL degassed mesitylene. Then Pd₂dba₃ (2.8 mg, 2 mol%) were added under argon and stirred for 48 h at 80 °C. After cooling to room temperature, the mixture was diluted with chloroform, precipitated into methanol and purified by Soxhlet extraction with acetone, ethyl acetate and chloroform. The chloroform fraction was filtered through a silica gel plug and dried overnight in a vacuum oven at 50 °C to afford a dark green solid. Yield: 243 mg (90%).

Supporting Information (SI): General measurements and characterization; additional NMR, SEC, TGA, DSC and GIWAXS data.

Acknowledgements

The authors thank M. Raisch and R. Hertel for DSC measurements and D. Stegerer for TGA measurements. O.D. acknowledges financial support from the European Union (EFRE). Y. V. thanks the Fulbright Commission for support (Fulbright-Cottrell Award 2018).

The OFETs fabrication of this work was partially carried out at Polifab, the micro- and nanotechnology center of the Politecnico di Milano.

REFERENCES

- (1) Y. J. Wang and G. Yu, *J. Polym. Sci. Part B Polym. Phys.*, 2019, **57**, 1557–1558.
- (2) J. de Mello, J. Anthony and S. Lee, *ChemPhysChem*, 2015, **16**, 1099–1100.
- (3) R. M. Pankow and B. C. Thompson, *Polymer*, 2020, **207**, 122874.
- (4) A. Facchetti, *Chem. Mater.*, 2011, **23**, 733–758.
- (5) S. Holliday, Y. Li and C. K. Luscombe, *Prog. Polym. Sci.*, 2017, **70**, 34–51.
- (6) M. Kim, S. U. Ryu, S. A. Park, K. Choi, T. Kim, D. Chung and T. Park, *Adv. Funct. Mater.*, 2019, 1904545.
- (7) S. E. Root, S. Savagatrup, A. D. Printz, D. Rodriguez and D. J. Lipomi, *Chem. Rev.*, 2017, **117**, 6467–6499.
- (8) Y. Huang, D. L. Elder, A. L. Kwiram, S. A. Jenekhe, A. K. Y. Jen, L. R. Dalton and C. K. Luscombe, *Adv. Mater.*, 2019, 1904239.
- (9) M. Goel, C. D. Heinrich, G. Krauss and M. Thelakkat, *Macromol. Rapid Commun.*, 2019, **40**, 1800915.
- (10) Z. Genene, W. Mammo, E. Wang and M. R. Andersson, *Adv. Mater.*, 2019, **31**, 1807275.
- (11) A. F. Paterson, S. Singh, K. J. Fallon, T. Hodsdon, Y. Han, B. C. Schroeder, H. Bronstein, M. Heeney, I. McCulloch and T. D. Anthopoulos, *Adv. Mater.*, 2018, **30**, 1801079.
- (12) H. Sun, X. Guo and A. Facchetti, *Chem*, 2020, **6**, 1310–1326.
- (13) K.-J. Baeg, M. Caironi and Y.-Y. Noh, *Adv. Mater.*, 2013, **25**, 4210–4244.
- (14) T. L. D. Tam and J. Xu, *J. Mater. Chem. A*, 2021, **9**, 5149–5163.
- (15) N. Zhou and A. Facchetti, *Mater. Today*, 2018, **21**, 377–390.
- (16) M. Sommer, *J Mater Chem C*, 2014, **2**, 3088–3098.
- (17) X. Guo, A. Facchetti and T. J. Marks, *Chem. Rev.*, 2014, **114**, 8943–9021.
- (18) R. Matsidik, A. Luzio, S. Hameury, H. Komber, C. R. McNeill, M. Caironi and M. Sommer, *J. Mater. Chem. C*, 2016, **4**, 10371–10380.
- (19) H. Yan, Z. Chen, Y. Zheng, C. Newman, J. R. Quinn, F. Dötz, M. Kastler and A. Facchetti, *Nature*, 2009, **457**, 679–686.
- (20) B. Fan, L. Ying, P. Zhu, F. Pan, F. Liu, J. Chen, F. Huang and Y. Cao, *Adv. Mater.*, 2017, **29**, 1703906.
- (21) K. D. Deshmukh, R. Matsidik, S. K. K. Prasad, N. Chandrasekaran, A. Welford, L. A. Connal, A. C. Y. Liu, E. Gann, L. Thomsen, D. Kabra, J. M. Hodgkiss, M. Sommer and C. R. McNeill, *ACS Appl. Mater. Interfaces*, 2018, **10**, 955–969.
- (22) N. Zhou, A. S. Dudnik, T. I. N. G. Li, E. F. Manley, T. J. Aldrich, P. Guo, H.-C. Liao, Z. Chen, L. X. Chen, R. P. H. Chang, A. Facchetti, M. Olvera de la Cruz and T. J. Marks, *J. Am. Chem. Soc.*, 2016, **138**, 1240–1251.

-
- (23) Y. Shin, A. Welford, H. Komber, R. Matsidik, T. Thurn-Albrecht, C. R. McNeill and M. Sommer, *Macromolecules*, 2018, **51**, 984–991.
- (24) E. Zhou, M. Nakano, S. Izawa, J. Cong, I. Osaka, K. Takimiya and K. Tajima, *ACS Macro Lett.*, 2014, **3**, 872–875.
- (25) S. B. Schmidt, M. Hönig, Y. Shin, M. Cassinelli, A. Perinot, M. Caironi, X. Jiao, C. R. McNeill, D. Fazzi, T. Biskup and M. Sommer, *ACS Appl. Polym. Mater.*, 2020, **2**, 1954–1963.
- (26) R. Matsidik, M. Giorgio, A. Luzio, M. Caironi, H. Komber and M. Sommer, *Eur. J. Org. Chem.*, 2018, **2018**, 6121–6126.
- (27) J. W. Jung, J. W. Jo, C.-C. Chueh, F. Liu, W. H. Jo, T. P. Russell and A. K.-Y. Jen, *Adv. Mater.*, 2015, **27**, 3310–3317.
- (28) B. Zhu, L. Guo, P. Deng and S. Liu, *J. Mater. Chem. C*, 2021, **9**, 2198–2204.
- (29) D. Kiefer, A. Giovannitti, H. Sun, T. Biskup, A. Hofmann, M. Koopmans, C. Cendra, S. Weber, L. J. Anton Koster, E. Olsson, J. Rivnay, S. Fabiano, I. McCulloch and C. Müller, *ACS Energy Lett.*, 2018, **3**, 278–285.
- (30) Y. Shin, H. Komber, D. Caiola, M. Cassinelli, H. Sun, D. Stegerer, M. Schreiter, K. Horatz, F. Lissel, X. Jiao, C. R. McNeill, S. Cimò, C. Bertarelli, S. Fabiano, M. Caironi and M. Sommer, *Macromolecules*, 2020, **53**, 5158–5168.
- (31) H. You, D. Kim, H.-H. Cho, C. Lee, S. Chong, N. Y. Ahn, M. Seo, J. Kim, F. S. Kim and B. J. Kim, *Adv. Funct. Mater.*, 2018, **28**, 1803613.
- (32) A. Wadsworth, M. Moser, A. Marks, M. S. Little, N. Gasparini, C. J. Brabec, D. Baran and I. McCulloch, *Chem. Soc. Rev.*, 2019, **48**, 1596–1625.
- (33) K. Feng, J. Huang, X. Zhang, Z. Wu, S. Shi, L. Thomsen, Y. Tian, H. Y. Woo, C. R. McNeill and X. Guo, *Adv. Mater.*, 2020, **32**, 2001476.
- (34) H. Jia and T. Lei, *J. Mater. Chem. C*, 2019, **7**, 12809–12821.
- (35) Y. Lu, J.-Y. Wang and J. Pei, *Chem. Mater.*, 2019, **31**, 6412–6423.
- (36) L. Xue, Y. Yang, Z.-G. Zhang, X. Dong, L. Gao, H. Bin, J. Zhang, Y. Yang and Y. Li, *J Mater Chem A*, 2016, **4**, 5810–5816.
- (37) S. Lee, C. Lee, H. Kim and Y. Kim, *J. Mater. Chem. C*, 2020, **8**, 15778–15787.
- (38) S. Shi, P. Chen, Y. Chen, K. Feng, B. Liu, J. Chen, Q. Liao, B. Tu, J. Luo, M. Su, H. Guo, M. Kim, A. Facchetti and X. Guo, *Adv. Mater.*, 2019, **31**, 1905161.
- (39) Y. Li, M. Gu, Z. Pan, B. Zhang, X. Yang, J. Gu and Y. Chen, *J Mater Chem A*, 2017, **5**, 10798–10814.
- (40) C. Liang and H. Wang, *Org. Electron.*, 2017, **50**, 443–457.
- (41) A. Wadsworth, H. Chen, K. J. Thorley, C. Cendra, M. Nikolka, H. Bristow, M. Moser, A. Salleo, T. D. Anthopoulos, H. Sirringhaus and I. McCulloch, *J. Am. Chem. Soc.*, 2020, **142**, 652–664.

- (42) D. Venkateshvaran, M. Nikolka, A. Sadhanala, V. Lemaire, M. Zelazny, M. Kepa, M. Hurhangee, A. J. Kronemeijer, V. Pecunia, I. Nasrallah, I. Romanov, K. Broch, I. McCulloch, D. Emin, Y. Olivier, J. Cornil, D. Beljonne and H. Sirringhaus, *Nature*, 2014, **515**, 384–388.
- (43) I. McCulloch, R. S. Ashraf, L. Biniek, H. Bronstein, C. Combe, J. E. Donaghey, D. I. James, C. B. Nielsen, B. C. Schroeder and W. Zhang, *Acc. Chem. Res.*, 2012, **45**, 714–722.
- (44) X. Zhang, H. Bronstein, A. J. Kronemeijer, J. Smith, Y. Kim, R. J. Kline, L. J. Richter, T. D. Anthopoulos, H. Sirringhaus, K. Song, M. Heeney, W. Zhang, I. McCulloch and D. M. DeLongchamp, *Nat. Commun.*, 2013, **4**, 2238.
- (45) C. Cordovilla, C. Bartolomé, J. M. Martínez-Ilarduya and P. Espinet, *ACS Catal.*, 2015, **5**, 3040–3053.
- (46) L. A. Estrada, J. J. Deininger, G. D. Kamenov and J. R. Reynolds, *ACS Macro Lett.*, 2013, **2**, 869–873.
- (47) N. S. Gobalasingham and B. C. Thompson, *Prog. Polym. Sci.*, 2018, **83**, 135–201.
- (48) N. Snoeij, *Toxicol. Appl. Pharmacol.*, 1985, **81**, 274–286.
- (49) D. J. Burke and D. J. Lipomi, *Energy Environ. Sci.*, 2013, **6**, 2053.
- (50) T. M. Pappenfus, F. Almyahi, N. A. Cooling, E. W. Culver, S. C. Rasmussen and P. C. Dastoor, *Macromol. Chem. Phys.*, 2018, **219**, 1800272.
- (51) S.-L. Suraru, J. A. Lee and C. K. Luscombe, *ACS Macro Lett.*, 2016, **5**, 724–729.
- (52) J.-R. Pouliot, F. Grenier, J. T. Blaskovits, S. Beaupré and M. Leclerc, *Chem. Rev.*, 2016, **116**, 14225–14274.
- (53) R. Matsidik, H. Komber, A. Luzio, M. Caironi and M. Sommer, *J. Am. Chem. Soc.*, 2015, **137**, 6705–6711.
- (54) R. Matsidik, H. Komber and M. Sommer, *ACS Macro Lett.*, 2015, **4**, 1346–1350.
- (55) Y. Shin, M. Massetti, H. Komber, T. Biskup, D. Nava, G. Lanzani, M. Caironi and M. Sommer, *Adv. Electron. Mater.*, 2018, **4**, 1700581.
- (56) S. Chen, K. C. Lee, Z.-G. Zhang, D. S. Kim, Y. Li and C. Yang, *Macromolecules*, 2016, **49**, 527–536.
- (57) Y. Li, W. K. Tatum, J. W. Onorato, S. D. Barajas, Y. Y. Yang and C. K. Luscombe, *Polym Chem*, 2017, **8**, 5185–5193.
- (58) Y. Li, W. K. Tatum, J. W. Onorato, Y. Zhang and C. K. Luscombe, *Macromolecules*, 2018, **51**, 6352–6358.
- (59) D. Adamczak, H. Komber, A. Illy, A. D. Scaccabarozzi, M. Caironi and M. Sommer, *Macromolecules*, 2019, **52**, 7251–7259.
- (60) D. Adamczak, A. Perinot, H. Komber, A. Illy, S. Hultmark, B. Passarella, W. L. Tan, S. Hutsch, D. Becker-Koch, C. Rapley, A. D. Scaccabarozzi, M. Heeney, Y. Vaynzof,

- F. Ortmann, C. R. McNeill, C. Müller, M. Caironi and M. Sommer, *J. Mater. Chem. C*, 2021, **9**, 4597–4606.
- (61) M. S. Vezie, S. Few, I. Meager, G. Pieridou, B. Dörling, R. S. Ashraf, A. R. Goñi, H. Bronstein, I. McCulloch, S. C. Hayes, M. Campoy-Quiles and J. Nelson, *Nat. Mater.*, 2016, **15**, 746–753.
- (62) R. Steyrlleuthner, M. Schubert, I. Howard, B. Klaumünzer, K. Schilling, Z. Chen, P. Saalfrank, F. Laquai, A. Facchetti and D. Neher, *J. Am. Chem. Soc.*, 2012, **134**, 18303–18317.
- (63) Z. Wu, A. Petzold, T. Henze, T. Thurn-Albrecht, R. H. Lohwasser, M. Sommer and M. Thelakkat, *Macromolecules*, 2010, **43**, 4646–4653.
- (64) A. J. Kronemeijer, V. Pecunia, D. Venkateshvaran, M. Nikolka, A. Sadhanala, J. Moriarty, M. Szumilo and H. Sirringhaus, *Adv. Mater.*, 2014, **26**, 728–733.
- (65) H. Chen, A. Wadsworth, C. Ma, A. Nanni, W. Zhang, M. Nikolka, A. M. T. Luci, L. M. A. Perdigão, K. J. Thorley, C. Cendra, B. Larson, G. Rumbles, T. D. Anthopoulos, A. Salleo, G. Costantini, H. Sirringhaus and I. McCulloch, *J. Am. Chem. Soc.*, 2019, **141**, 18806–18813.
- (66) T. H. Thomas, D. J. Harkin, A. J. Gillett, V. Lemaure, M. Nikolka, A. Sadhanala, J. M. Richter, J. Armitage, H. Chen, I. McCulloch, S. M. Menke, Y. Olivier, D. Beljonne and H. Sirringhaus, *Nat. Commun.*, 2019, **10**, 2614.
- (67) R. Noriega, J. Rivnay, K. Vandewal, F. P. V. Koch, N. Stingelin, P. Smith, M. F. Toney and A. Salleo, *Nat. Mater.*, 2013, **12**, 1038–1044.
- (68) A. Onwubiko, W. Yue, C. Jellett, M. Xiao, H.-Y. Chen, M. K. Ravva, D. A. Hanifi, A.-C. Knall, B. Purushothaman, M. Nikolka, J.-C. Flores, A. Salleo, J.-L. Bredas, H. Sirringhaus, P. Hayoz and I. McCulloch, *Nat. Commun.*, 2018, **9**, 416.
- (69) X. Guo and M. D. Watson, *Org. Lett.*, 2008, **10**, 5333–5336.

SUPPORTING INFORMATION

General measurement and characterization

NMR spectroscopy. NMR spectra were recorded on a Bruker AVANCE III 500 spectrometer (^1H : 500.1 MHz, ^{13}C : 125.8 MHz). CDCl_3 (at 30 °C) and $\text{C}_2\text{D}_2\text{Cl}_4$ (at 120 °C) were used as solvents. The spectra were referenced to the residual solvent peak (CDCl_3 : $\delta(^1\text{H}) = 7.26$ ppm, $\delta(^{13}\text{C}) = 77.0$ ppm; $\text{C}_2\text{D}_2\text{Cl}_4$: $\delta(^1\text{H}) = 5.98$ ppm). 2D NMR spectra were recorded to support signal assignment.

SEC measurements. Molecular weights were measured on a Shimadzu system comprising a 5 μm precolumn and three SDplus columns with pore sizes ranging from 10^2 to 10^4 Å (Polymer Standards), connected in series with a RID-20A RI detector and a SPD-M20A photodiode array UV-vis detector (Shimadzu) calibrated with polystyrene standards. CHCl_3 was used as eluent at 40 °C with a flow rate of 1.0 mL min^{-1} .

UV-vis spectroscopy. UV-vis spectra were recorded at 25 °C on a Cary 60 UV-vis (Agilent Technologies) in chloroform solutions ($c = 0.02 \text{ mg mL}^{-1}$). Extinction coefficients ε were calculated using the Beer-Lambert law: $\varepsilon = \frac{A}{c \cdot d}$; where A is the absorptivity, d is the optical path length (1 cm) and c is the concentration in mol L^{-1} . Conversion of the concentration into mol L^{-1} was done using the molecular weight of the repeating unit. Thin film absorption was recorded on the Flame-S UV-vis-spectrometer from Ocean Optics, controlled by the OceanView 1.5.2 software. The films were spin coated (1000 rpm, 60 s) from *o*-DCB solutions.

Cyclic voltammetry. CV measurements were performed at room temperature using a PalmSens4 potentiostat with NBu_4PF_6 (0.1 M) as electrolyte under argon with a scan rate of 50 mV s^{-1} . Films were spin coated (1000 rpm, 60 s) onto ITO substrates as working electrode and measured in dry acetonitrile. A platinum wire was used as counter electrode and a silver wire as reference. The CV curves were plotted against the oxidation potential of ferrocene. CV measurements in solution were done at room temperature in a 0.1 M NBu_4PF_6 *o*-DCB solution using a glassy carbon working electrode.

TGA measurements. TGA measurements were done on a TGA/DSC3+ from Mettler-Toledo within the temperature range 50 °C to 650 °C at a heating rate of 10 K min^{-1} under N_2 .

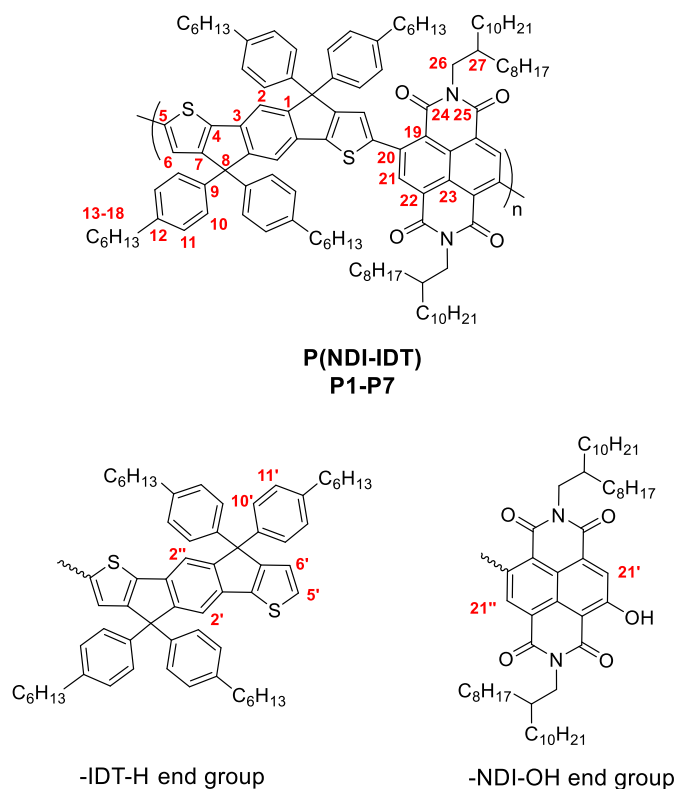
DSC measurements. DSC measurements were carried out on a DSC 2500 (TA Instruments) under nitrogen atmosphere. Heating and cooling rates were 20 K min^{-1} . The mass of the samples for each measurement was approximately 2-5 mg.

OFET preparation. The samples were fabricated in nitrogen atmosphere. Gold contacts (30 nm) were fabricated on Low alkali 1737F Corning glass substrates using conventional photolithography and thermal evaporation, yielding transistor channels with a length $L = 20\ \mu\text{m}$ and a width $W = 2\ \text{mm}$. The semiconducting polymers were dissolved in *o*-dichlorobenzene or toluene at a concentration of $10\ \text{mg mL}^{-1}$, and deposited *via* spin-coating at 1000 rpm for 30 s in nitrogen atmosphere. After deposition, the residual solvent was removed *via* vacuum-drying in the case of toluene or annealed at $100\ ^\circ\text{C}$ for 30 min in nitrogen in the case of *o*-DCB. Then, a layer of Poly(methyl methacrylate) (PMMA) was deposited *via* spin coating at 1300 rpm for 60 s, yielding a 500 nm-thick dielectric layer, and the residual solvent was removed *via* vacuum drying. Finally, a 40 nm-thick aluminum layer was deposited on the channel area by thermal evaporation through a shadow mask, in order to realize the gate electrodes. The devices were then annealed at different temperatures for 30 min in nitrogen atmosphere. The samples were measured in nitrogen atmosphere using an Agilent B1500A Semiconductor Parameter Analyzer.

PDS. The polymer samples were dissolved in *o*-dichlorobenzene at a concentration of $10\ \text{mg mL}^{-1}$ and deposited on a glass substrate *via* off-centered spin-coating at 1000 rpm for 60 s. The sample film was placed into a sample holder filled with Fluorinert™ FC-770 (3 M). The PDS setup uses a 150 W Xenon short-arc lamp (Ushio) which provides light for a monochromator (Oriel Cornerstone, 16 nm FWHM) to achieve a chopped, tunable, monochromatic pump beam. The heat caused through absorption of the pump light in the film changes the refractive index of the Fluorinert™. This change is detected by deflecting a diode laser (Thorlabs) whose displacement is measured by a position sensitive detector (Thorlabs PDP90A). The magnitude of the deflection is determined by a lock-in amplifier (Amatec SR 7230) and directly correlated to the absorption of the film.

GIWAXS. The GIWAXS experiments were performed using a SAXSLAB laboratory setup (Retro-F) (Copenhagen, Denmark) equipped with an AXO microfocus X-ray source (Dresden, Germany) and an AXO multilayer X-ray optics (ASTIX) as a monochromator for Cu-K α radiation ($\lambda = 0.15418\ \text{nm}$). A DECTRIS PILATUS3 R 300 K detector (Daettwil, Switzerland) was used to record the 2D WAXS patterns. The measurements were performed in reflection geometry in vacuum at room temperature and at the angle of incidence of 0.16° being above the critical angles of the polymers, the sample to detector distance was around 89 mm. The detector images were converted into the reciprocal space maps of scattering patterns with two components, q_z and q_r , being perpendicular and parallel to the sample surface, respectively. On

account of the special geometry of measurements, a certain area of the reciprocal space along the q_z axis was not accessible and appeared as a blank arc. Two additional blank vertical strips arose at the positions where two of three adjacent parts of the detector meet, and were inactive regions of the detector.



^1H NMR (500 MHz, CDCl_3): δ 8.75 (21), 7.54 (2), 7.27 (6,10), 7.10 (11), 4.09 (v br, 26), 2.58 (13), 1.98 (27), 1.61 (14), 1.4-1.1 (CH_2), 0.95-0.8 (CH_3). End groups: *NDI-OH* -12.9 (OH), 8.70 (21'), 8.35 (21'), *IDT-H* - 7.48 (2', 2''), 7.27 (6'), 7.16 (10'), 7.06 (11'), 7.02 ppm (5').

^1H NMR (500 MHz, $\text{C}_2\text{D}_2\text{Cl}_4$, 120°C): δ 8.82 (21), 7.62 (2), 7.28 (6), 7.33 (10), 7.15 (11), 4.15 (v br, 26), 2.65 (13), 2.07 (27), 1.69 (14), 1.5-1.2 (CH_2), 1.0-0.8 (CH_3). End groups: *NDI-OH* -12.8 (OH), 8.77 (21''), 8.38 (21'), *IDT-H* - 7.55 (2', 2''), 7.37 (6'), 7.22 (10'), 7.11 (11'), 7.08 ppm (5').

^{13}C NMR (125 MHz, CDCl_3): δ 162.2 (24,25), 156.4 (7), 153.7 (1), 144.9 (4), 142.9 (20), 141.6 (9,12), 139.9 (5), 136.3 (21), 135.7 (3), 128.4 (11), 128.0 (10), 127.6 (23), 125.7 (6), 125.1 (22), 122.5 (19), 118.0 (2), 63.2 (8), 45.2 (26), 36.5 (27), 35.6 (13), 31.9, 31.8, 31.4, 30.1, 29.6, 29.3, 29.2, 26.6, 22.6 (all CH_2), 14.1 ppm (CH_3).

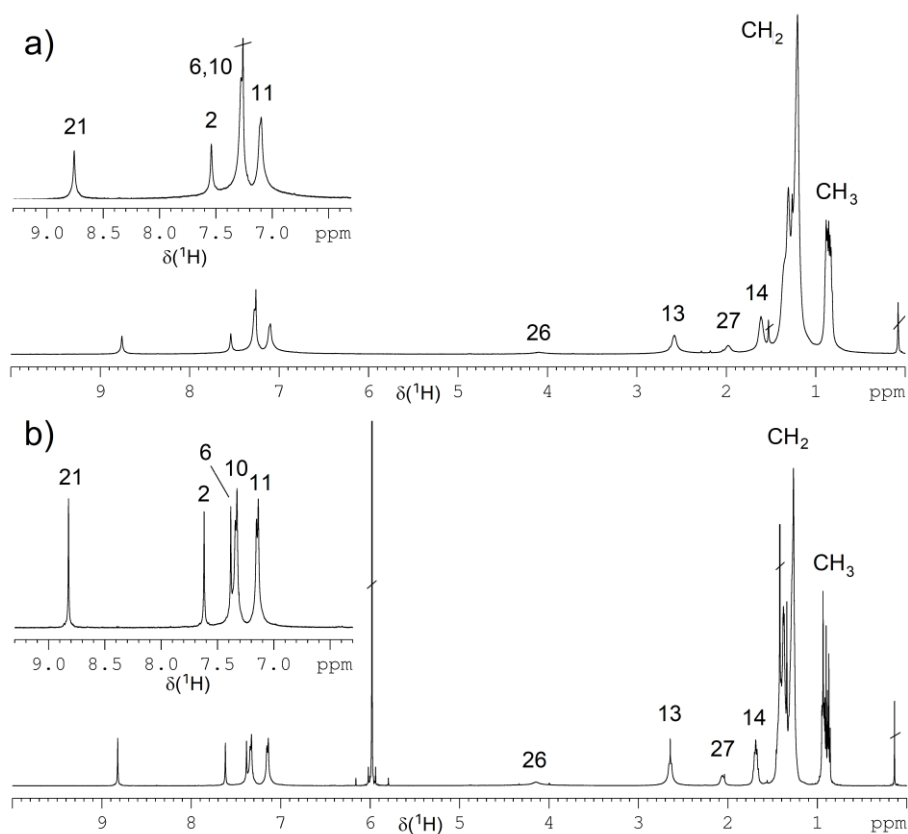


Figure IV-S1. ^1H NMR spectrum of **P4** in CDCl_3 at 30°C (a) and in $\text{C}_2\text{D}_2\text{Cl}_4$ at 120°C (b).

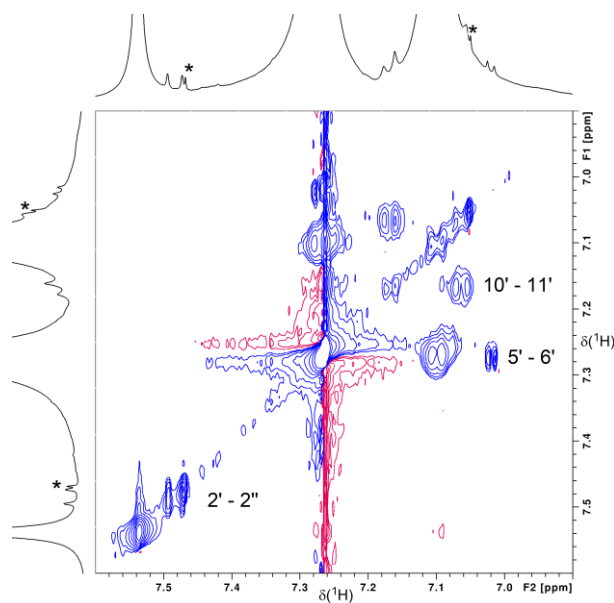


Figure IV-S2. TOCSY spectrum of **P5** in CDCl_3 with assigned correlations between IDT-H end group signals. * marks ^{13}C satellite signals of CHCl_3 .

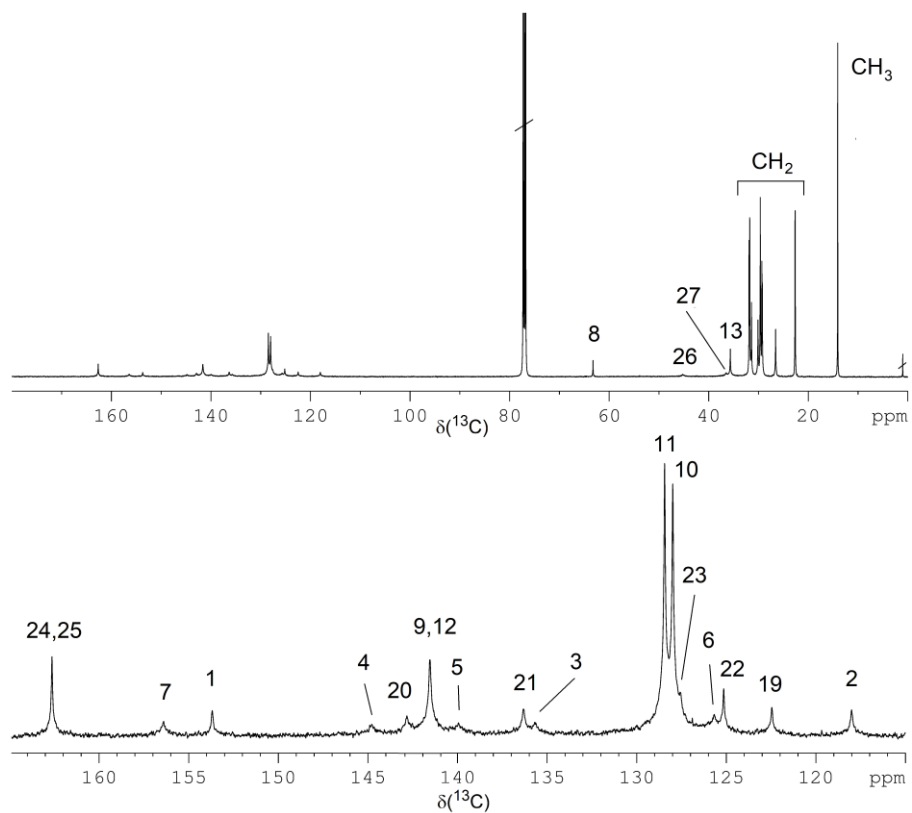


Figure IV-S3. ^{13}C NMR spectrum of **P4** in CDCl_3 .

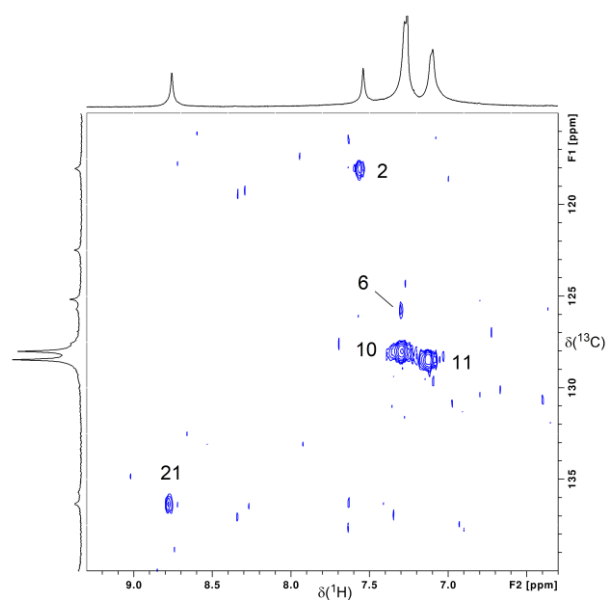


Figure IV-S4. HSQC spectrum (region) of **P4** in CDCl_3 .

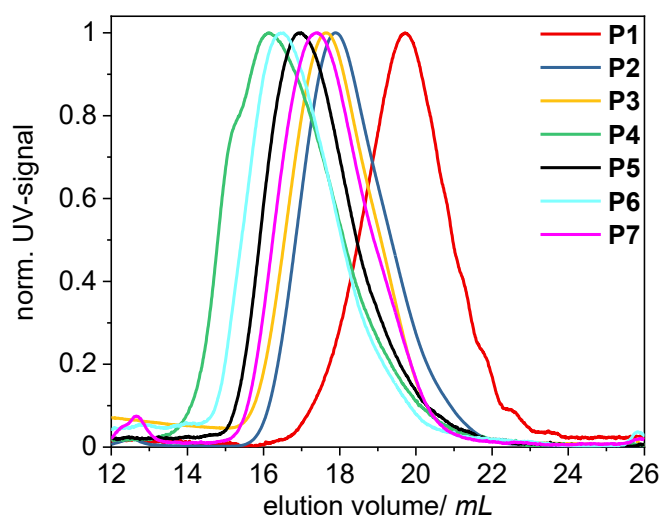


Figure IV-S5. SEC curves of P(NDI-IDT) samples in chloroform.

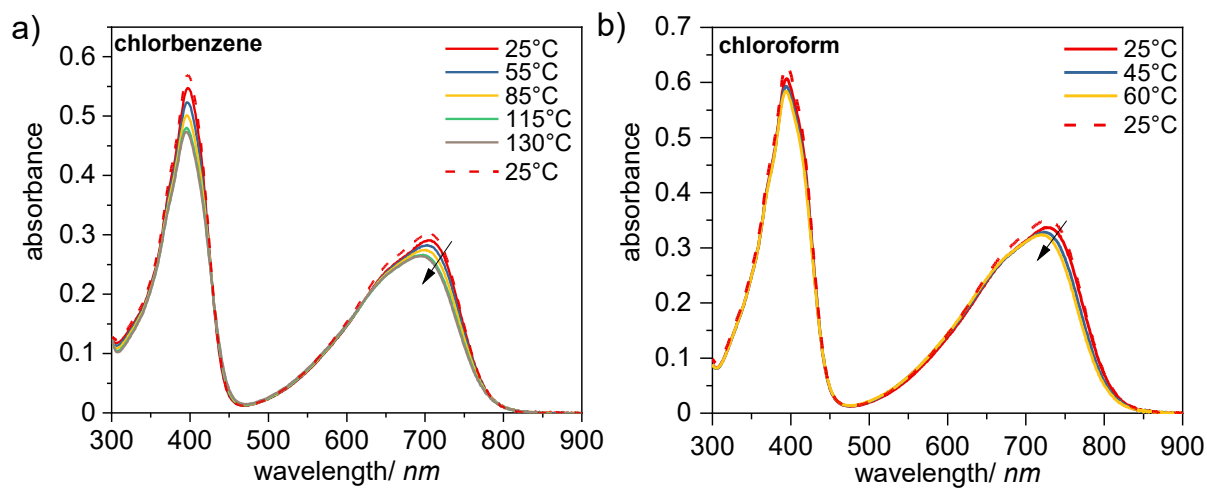


Figure IV-S6. High temperature UV-vis spectra in chlorobenzene (a) and chloroform (b) of P3.

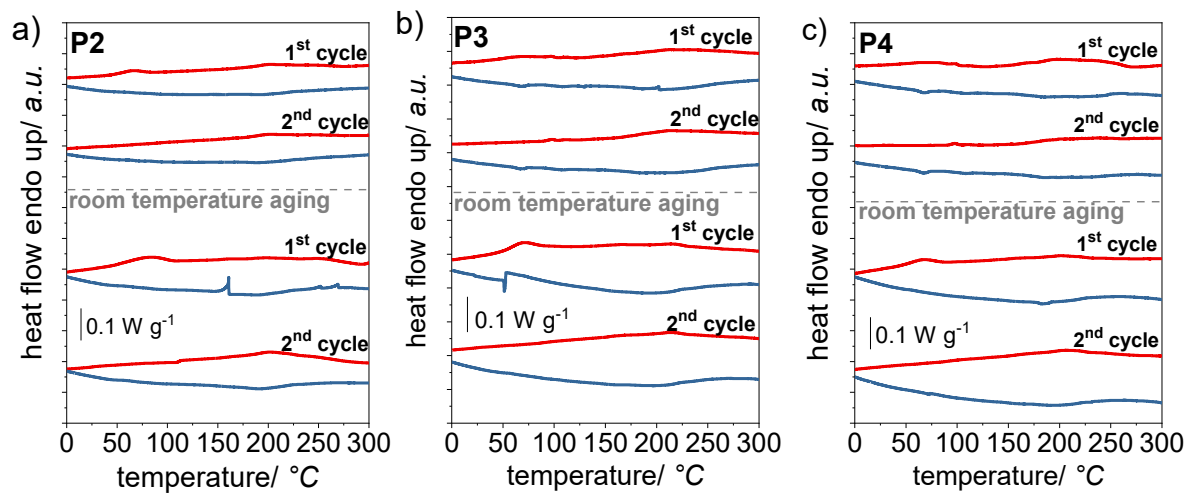


Figure IV-S7. DSC curves of P(NDI-IDT) for $M_n = 43 \text{ kg mol}^{-1}$ (a), $M_n = 61 \text{ kg mol}^{-1}$ (b) and $M_n = 103 \text{ kg mol}^{-1}$ (c). First and second cycles were measured under N_2 with 10 K min^{-1} before and with 20 K min^{-1} after room temperature aging.

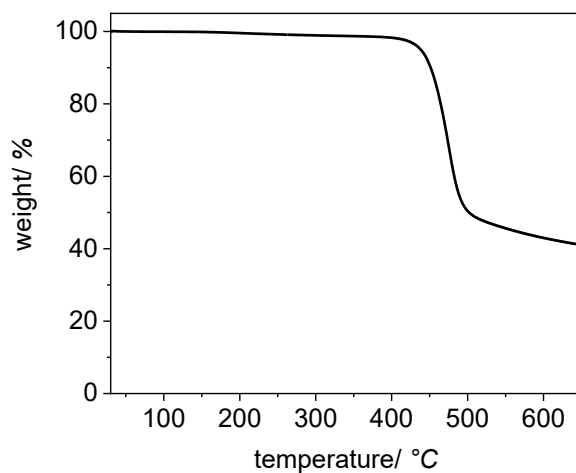


Figure IV-S8. Thermograms of P(NDI-IDT) in N_2 .

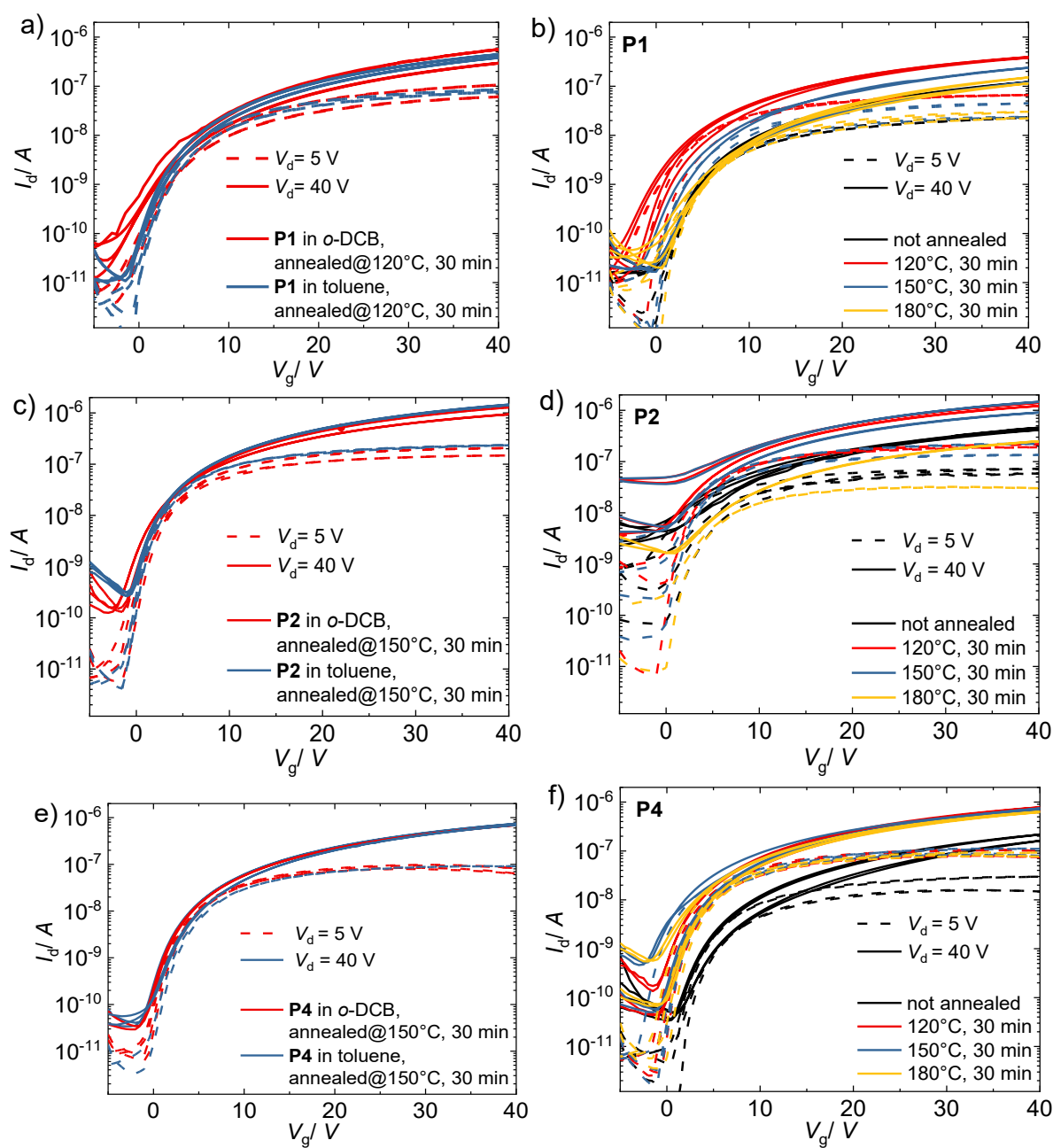


Figure IV-S9. Influence of the solvent (a, c, e) and annealing temperature (b, d, f) on the transfer curves of OFET devices with **P1**, **P2** and **P4**.

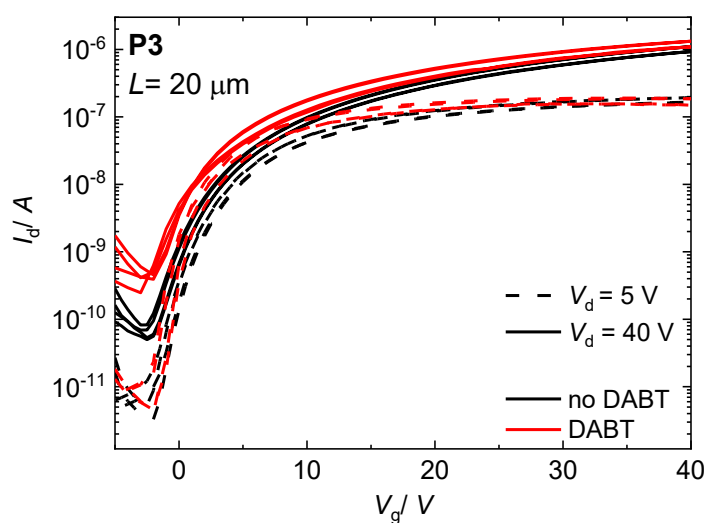


Figure IV-S10. Comparison of the transfer curves of **P3** between OFETs with and without SAM.

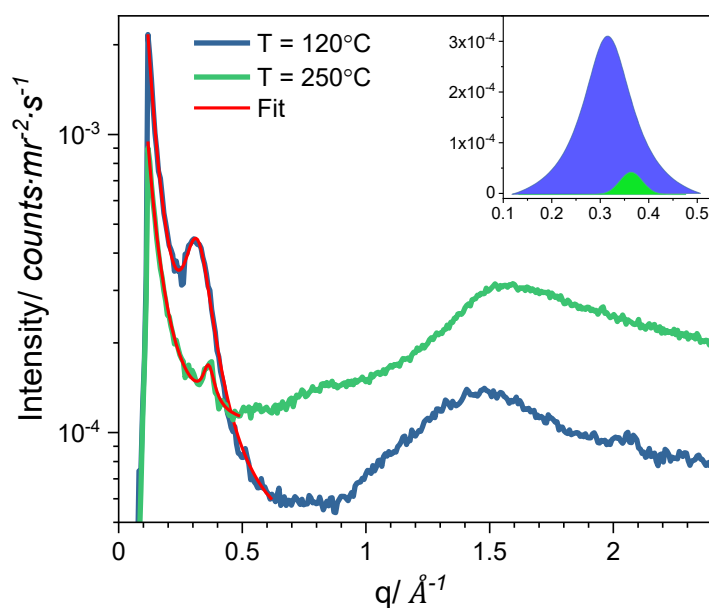
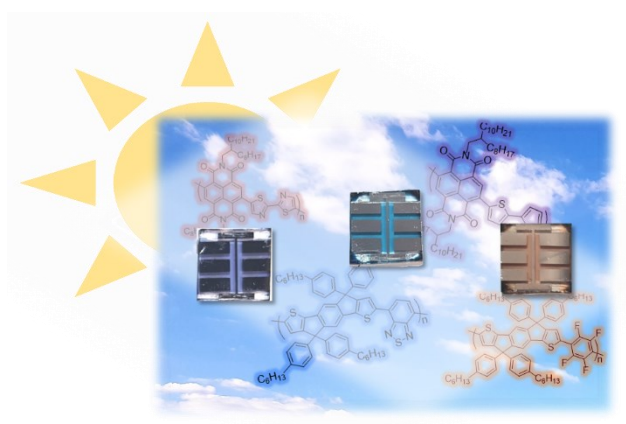


Figure IV-S11. 1D scattering curves of **P3** annealed at 120 °C (green line) and at 250 °C (blue line). The scattering curves were extracted by a complete azimuthal integration of the 2D GIWAXS patterns in Figure IV-7a and 7c, respectively. The red lines are fitting of the experimental scattering curves. The background scattering was fitted using a power law dependence of intensity on the scattering vector q : $I_{\text{background}} = I_0 \cdot q^{-n}$. Fitting of the scattering signals was used to find the area A below the (100) peaks, which resulted in $A = 6.96 \cdot 10^{-5}$ for **P3** annealed at 120 °C and $A = 3.8 \cdot 10^{-6}$ for **P3** annealed at 250 °C. The corresponding fitted Lorentzian peaks of the (100) crystal reflections are shown in the Figure inset. As the area below the diffraction peaks is proportional to the degree of crystallinity of the samples, it is evident that annealing at 250 °C entailed a dramatic decrease in the sample crystallinity.

V. Indacenodithiophene-based copolymers for application in all-polymer solar cells



INTRODUCTION

In the last decades all-polymer solar cells (all-PSCs) have attracted a high interest to replace silicon-based devices due to their major advantages such as flexibility, lightweight, long-term stability, semi-transparent characteristics and the potential for large-scale roll-to-roll processing. Their performances have been significantly improved and power conversion efficiencies (PCE) over 14% in single-junction solar cells could be achieved.¹⁻³ Compared to polymer/fullerene devices all-PSCs possess superior mechanical endurance as well as facile tunability of chemical structures and energy levels. However, achieving of an ideal blend film morphology is a major challenge of all-PSCs due to the low entropic contribution by the two polymer donor and polymer acceptor chains that energetically disfavors mixing. An interconnected network of appropriately phase separated D-A domain sizes is critical in order to obtain high performance devices.^{1,2,4-6} Several strategies such as thermal annealing, optimization of the processing solvent and molecular weights were employed to control the morphology of the polymer blend.⁵⁻⁹ Many state-of-the-art all-PSCs contain poly{[*N,N'*-bis(2-octyldodecyl)naphthalene-1,4,5,8-bis(dicarboximide)-2,6-diyl]-*alt*-5,5'-(2,2'-bithiophene)} (PNDIT2; N2200) as acceptor component due to their facile synthesis, high electron mobilities and good thermal and oxidative stability.^{2,10,11} Blended with common commercial donor materials such as PBDB-T all-PSCs with PCEs above 10% could be fabricated.^{2,7,10,12-14} Nevertheless, they still lack behind solar cells based on small molecule acceptors (SMAs). SMAs profit from their high absorption coefficients and excellent thermal, chemical as well as photo-stability.^{15,16} A common class of SMAs is based on the highly coplanar indacenodithiophene building blocks due to their high absorption coefficients, improved charge carrier mobilities, reduced reorganization energy and facile structural modification.^{17,15,18-20} As a result of their excellent properties, IDT is also a widely used moiety in push-pull copolymers.^{17,19,20} One prominent representative is poly(indacenodithiophene-*alt*-benzothiadiazole) (PIDTBT) which shows great performance in optoelectronic devices.²¹⁻²⁴ However, most IDT-based solar cells are blended with fullerene acceptors obtaining PCEs over 6%.^{19,22-28} Fullerene as acceptor material has several drawbacks such as a weak light absorption in the visible spectral region, limited ability of chemical modifications, low mechanical, thermal and photo-stability as well as high synthetic costs.^{4,15,29} To date, there are only a few reports in which IDT-based copolymers are incorporated in all-PSCs yielding PCEs of up to 8%.^{30,31}

In this chapter, all-PSCs comprised of IDT-based and NDI-based copolymers were fabricated. The donor materials poly(indacenodithiophene-*alt*-benzothiadiazole) (**PIDTBT**)

and poly(indacenodithiophene-*alt*-tetrafluorobenzene) (**PIDTF4**) show complementary absorption as well as appropriate energy levels with the well-known acceptor poly(naphthalene diimide-*alt*-bithiophene) (**PNDIT2**). As third system **PIDTBT** was blended with poly(naphthalene diimide-*alt*-bithiazole) (**PNDIBTz**). All devices exhibit a relatively high V_{oc} but moderate values of J_{sc} . While devices containing **PIDTBT:PNDIT2** and **PIDTBT:PNDIBTz** blends showed similar output characteristics, cells with a **PIDTF4:PNDIT2** blend showed inferior performance. Due to the higher absorption of the **PIDTBT:PNDIT2** blend in near infrared region compared to **PIDTBT:PNDIBTz**, optimization were carried out on the devices composed of **PIDTBT** and **PNDIT2**. The effects of D:A weight ratio, processing solvent, blend concentrations and finally molecular weight (MW) variation on the device performance were investigated and discussed in the following section.

RESULTS AND DISCUSSION

The molecular structures of the active materials are shown in Figure V-1. Poly(indacenodithiophene-*alt*-benzothiadiazole) (**PIDTBT**) as well as poly(indacenodithiophene-*alt*-tetrafluorobenzene) (**PIDTF4**) were chosen as donor component and the well-known poly(naphthalene diimide-*alt*-bithiophene) (**PNDIT2**) as well as poly(naphthalene diimide-*alt*-bithiazole) (**PNDIBTz**) as acceptor components.

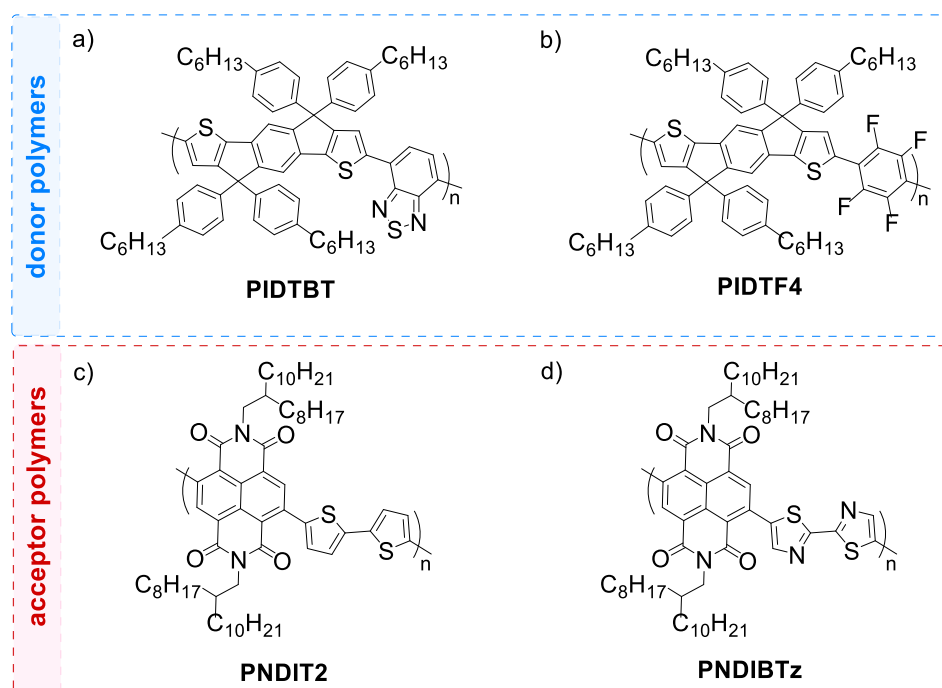


Figure V-1. Chemical structures of donor polymers **PIDTBT** (a) and **PIDTF4** (b) as well as acceptor polymers **PNDIT2** (c) and **PNDIBTz** (d).

All polymers were synthesized by atom-economic direct arylation polycondensation (DAP). **PNDIT2**, **PNDIBTz** and **PIDTBT** were synthesized according to literature protocols.^{32–35} Details, a synthetic description and NMR analysis (Figure V-S1 and S2) of **PIDTF4** are provided in the Experimental Section. Molecular weights were determined by size exclusion chromatography (SEC) (see Figure V-S3, Experimental Section). M_n s of the donor polymers are around 17 kg mol⁻¹ and of the acceptors polymers **PNDIT2** and **PNDIBTz** are $M_n = 62$ kg mol⁻¹ and $M_n = 39$ kg mol⁻¹.

The optoelectronic properties of the materials are summarized in Table V-1. The energy levels of the donor polymers were obtained from cyclic voltammetry in thin film (see Figure V-S4, Experimental Section) and HOMO/LUMO values of the acceptor polymers were taken from literature^{31,33} (Table V-1).

Table V-1. Key properties of the active materials.

		M_n/M_w^a kg mol ⁻¹	$\lambda_{\max, \text{abs}}(\text{sol})^b$ nm	$\varepsilon_{\text{abs}}(\text{sol})^c/10^3$ L mol ⁻¹ cm ⁻¹	E_g^d eV	HOMO ^e eV	LUMO ^e eV
Donor	PIDTBT	17/37	410/643	57	1.74	-5.19	-3.45
	PIDTF4	16/28	509	73	2.16	-5.16	-3.00
Acceptor	PNDIT2	62/379	386/698	28	1.54	-5.79 ^f	-3.78 ^f
	PNDIBTz	39/99	370/542	22	2.1	-5.89 ^f	-3.83 ^f

^aFrom SEC in CHCl₃. ^bMeasured in chloroform at room temperature. ^cMolar extinction coefficient was calculated from maximum wavelength of the low-energy band (see italic values). ^dDetermined from absorption onset. ^eCalculated as followed E(HOMO) = E(Ox) + 4.8 eV and E(LUMO) = E(HOMO) + E_g ; films were spin coated on ITO substrate (1000 rpm, 60 s). ^fTaken from literature.^{31,33}

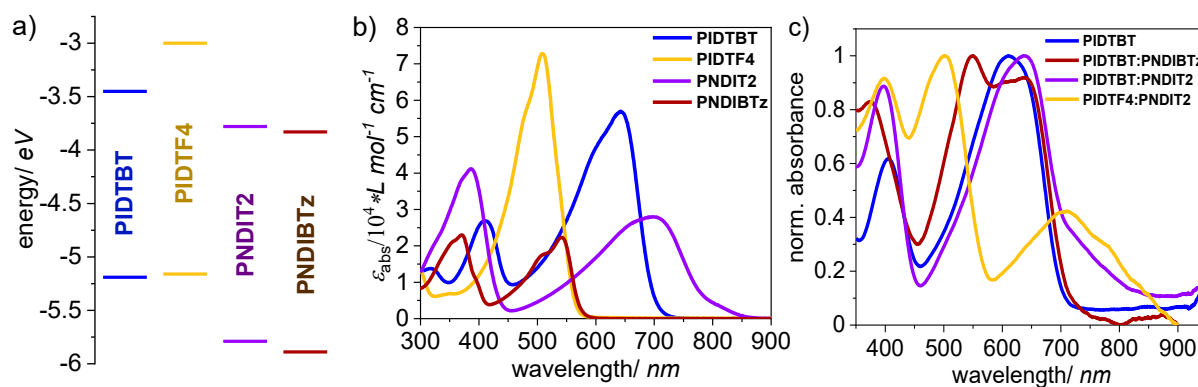


Figure V-2. Schematic energy levels (a) and absorption spectra in chloroform solution at room temperature (b) of the active materials. Normalized absorption of the blend films (c).

A schematic overview of the energy level alignment is displayed in Figure V-2a. In all cases, the LUMO-LUMO and HOMO-HOMO offsets between the p-type and n-type materials are greater than 0.3 eV, which is essential for efficient charge transport.^{2,4,29,36} In addition to appropriate energy level alignment, a complementary absorption of the donor and acceptor polymer is beneficial to enlarge the light harvesting of the active layer.^{2,14} From the absorption spectra (Figure V-2b), three suitable blend combinations arise – namely **PIDTBT:PNDIT2**, **PIDTBT:PNDIBTz** and **PIDTF4:PNDIT2**. The p-type polymers **PIDTBT** and **PIDTF4** exhibit strong absorption in the range of 500-700 nm and 400-550 nm, respectively, amending the weak absorption in the visible region of the acceptor polymer **PNDIT2**. As a result, films blended with **PNDIT2** absorb light from visible into the near infrared region (Figure V-2c). Due to the blueshifted charge transfer band, **PNDIBTz** can be blended with **PIDTBT** as matching donor material. The blend system shows a strong absorption from around 400-700 nm (Figure V-2c). Except **PNDIT2** with a relatively low optical band gap E_g of 1.54 eV, the materials possess medium to wide optical bandgaps ranging from 1.74 eV (**PIDTBT**) to 2.1 eV (**PIDTF4**, **PNDIBTz**) expecting solar cells with high open-circuit voltages V_{oc} .^{2,36}

To investigate photovoltaic performance of the three blend systems, solar cells with a conventional architecture of indium tin oxide (ITO)/poly(3,4-ethylenedioxythiophene):poly(styrenesulfonate) (PEDOT:PSS)/active layer (D:A, 1:1)/Ca/Al were fabricated (Figure V-3a). The active layer with a 1:1 D/A weight ratio was spin coated from a 20 mg L⁻¹ chlorobenzene solution. Details of device fabrication and characterization of the solar cells are described in the Experimental Section. The current density (J)-voltage (V) curves are shown in Figure V-3b and the output characteristics are presented in Table V-2.

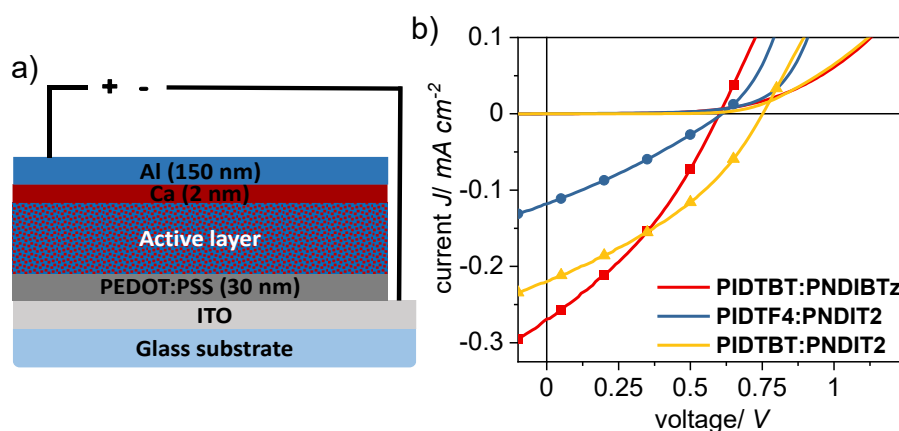


Figure V-3. Conventional device configuration (a) and current density-voltage curves of the three blend systems. Solid lines represent dark measurements; lines with symbols were recorded under illumination.

Table V-2. Summary of photovoltaic properties of the three different blend systems.^a

active layer	$M_n(D): M_n(A)/$ kg mol^{-1}	D:A	V_{oc}^b/V	$J_{sc}^b/\text{mA cm}^{-2}$	FF ^b /%	PCE ^b /%
PIDTBT:PNDIBTz	17:39	1:1	0.60	0.27	33	0.1
PIDTF4:PNDIT2	16:62	1:1	0.61	0.12	30	0
PIDTBT:PNDIT2	17:62	1:1	0.75	0.22	35	0.1

^aIn all cases chlorobenzene was used as processing solvent. The active layers were spin coated (1000 rpm, 60 s) from a 20 mg mL⁻¹ blend solution followed by annealing at 150 °C for 10 minutes.

^bAveraged values of maximum five cells.

The prepared solar cells with **PIDTF4:PNDIT2** as active layer showed no photovoltaic activity and therefore, the system was not further investigated. Devices consisting of **PIDTBT:PNDIBTz** and **PIDTBT:PNDIT2** blend, respectively, showed similar photovoltaic properties. While the blend with **PNDIBTz** exhibits a slightly higher J_{sc} , values for V_{oc} as well as fill factor (FF) are lower compared to the blend containing **PNDIT2** as acceptor. In the following the **PIDTBT:PNDIT2** system was chosen to further optimize all-polymer solar cells.

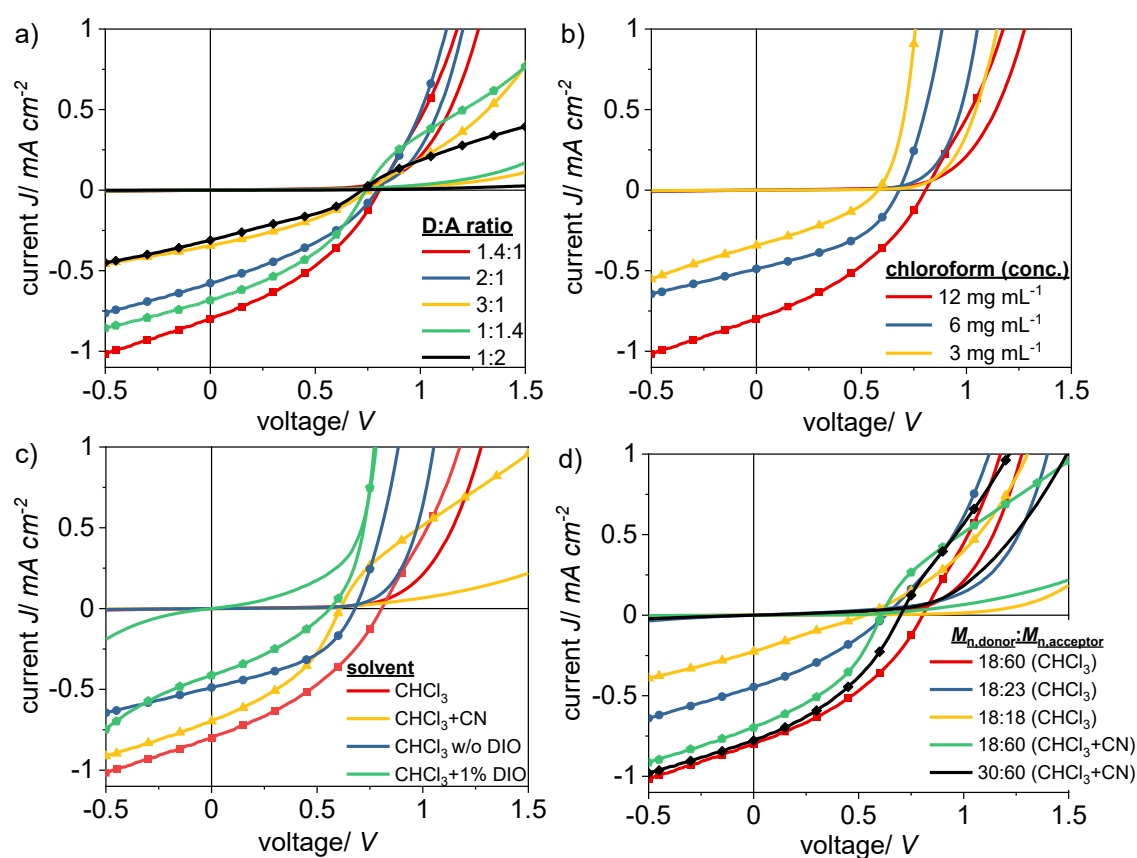


Figure V-4. Current density-voltage curves of solar cells optimized by D:A weight ratio (a), blend concentration (b), addition of solvent additives (c) and molecular weight variation (d). Solid lines represent dark measurements; lines with symbols were recorded under illumination.

Table V-3. Summary of output characteristics of the devices prepared under various fabrication conditions.^a

entry	D:A	solvent	$c_{\text{blend}}/\text{mg mL}^{-1}$	spin coating parameters	V_{oc}^b/V	$J_{\text{sc}}^b/\text{mA cm}^{-2}$	$\text{FF}^b/\%$	$\text{PCE}^b/\%$
1	1.4:1	CHCl ₃	12	1000 rpm, 60s	0.81	0.62	35	0.16
2	2:1	CHCl ₃	12	1000 rpm, 60s	0.81	0.46	36	0.1
3	3:1	CHCl ₃	12	1000 rpm, 60s	0.76	0.31	32	0.08
4	1:1.4	CHCl ₃	12	1000 rpm, 60s	0.67	0.73	34	0.15
5	1:2	CHCl ₃	12	1000 rpm, 60s	0.72	0.31	34	0.1
6	1.4:1	CHCl ₃	6	1000 rpm, 60s	0.68	0.48	43	0.1
7	1.4:1	CHCl ₃	3	1000 rpm, 60s	0.57	0.34	33	0.1
8	1.4:1	CHCl ₃ +DIO (1%, v/v)	6	1000 rpm, 60s	0.56	0.41	33	0.1
9	1.4:1	CHCl ₃ /CN (99:1, v/v)	12	1000 rpm, 60s	0.76	0.38	35	0.1
10	1.4:1	CHCl ₃ /CN (99:1,v/v)	12	2000 rpm, 60s	0.61	0.70	39	0.2

^aIn all cases the molecular weight of the donor and acceptor is 17 kg mol^{-1} and 62 kg mol^{-1} , respectively. The active layer was annealed at 120°C for 10 minutes. CHCl₃, DIO and CN is chloroform, 1,8-diiodooctane and 1-chloronaphthalene, respectively. ^bAveraged values of maximum five cells.

The devices were systematically optimized by (i) variation of the D:A weight ratio, (ii) the concentration of the blend solution, (iii) addition of solvent additives and lastly (iv) by variation of the donor and acceptor molecular weights. The corresponding J - V curves are displayed in Figure V-4. The results are summarized in Table V-3 as well as Table V-4 and discussed in detail below.

First, a screening for an optimum D:A weight ratio was carried out (Figure V-4a, Table V-3, entries **1-5**). The active layer was spin coated on the PEDOT:PSS layer from a 12 mg mL^{-1} chloroform solution and annealed for 10 minutes at 120°C . With increasing D:A weight ratio from 1.4:1 to 3:1 values of V_{oc} , J_{sc} as well as FF are dropping. The maximum power conversion efficiency (PCE) of 0.2% could be achieved at a 1.4:1 D/A weight ratio (Table V-3, entry **1**). Interestingly, using a higher content of the acceptor material at a D:A ratio of 1:1.4 (Table V-3, entry **4**) lead to a slightly higher J_{sc} , while both V_{oc} and FF decrease. Further decrease of the D:A ratio results in a significantly drop of solely J_{sc} .

In the following a D:A ratio of 1.4:1 was chosen and in the next step influence of the active layer thickness on solar cell performance was investigated. To adjust the thickness of the active layer, blend solutions at 12, 6 and 3 mg mL⁻¹ in chloroform were prepared (Table V-3, entries **1**, **6**, **7**). Lowering the concentration led to a substantial decrease of both, J_{sc} and V_{oc} (Figure V-4b). Hence, thicker films seem to be beneficial for the performance of the devices. Nevertheless, the performance efficiencies of the **PIDTBT:PNDIT2** based cells remain under 1% due to very low short-circuit currents. This may be caused by an unfavourable blend film morphology. The use of solvent additives such as 1,8-diiodooctane (DIO) can be employed to effectively tune the film forming process.³⁷ DIO (1%, v/v) was added into the active layer solution prior to the spin-coating process (Table V-3, entry **8**). However, the addition of DIO has no significant effect on J_{sc} (Figure V-4c) and, hence, no boost in the performance could be observed. Another strategy to influence the film morphology is the addition of a co-solvent. For instance, 1-chloronaphthalene can prevent preaggregation of the acceptor polymer **PNDIT2** optimizing film morphology.^{38–43} The addition of a co-solvent leads to a significant drop of J_{sc} (Table V-3, entry **1** vs. **9**). Interestingly, after doubling the rotation speed the performances could be slightly improved (Table V-3, entry **10**). While a drop in V_{oc} can be observed, both J_{sc} and FF could be enhanced up to 0.7 mA cm⁻² and 39%, respectively.

In a last attempt to boost the performance of the solar cell devices the molecular weights of both **PIDTBT** donor polymer and **PNDIT2** acceptor polymer were varied. Molecular weight of the materials has a great influence on intrachain and interchain interactions and, hence, the degree of phase separation.^{9,44–46} The results of the molecular weight variation are presented in Table V-4 and the corresponding J - V curves are shown in Figure V-4d.

Table V-4. Molecular weight dependency of photovoltaic parameters.^a

	entry	$M_n(D):M_n(A)$ kg mol ⁻¹	D:A	solvent	$c_{blend}/$ mg mL ⁻¹	$V_{oc}^b/$ V	$J_{sc}^b/$ mA cm ⁻²	FF ^{b/} %	PCE ^{b/} %
PIDTBT:PNDIT2	1	17:62	1.4:1	CHCl ₃	12	0.81	0.62	35	0.16
	11	17:23	1.4:1	CHCl ₃	12	0.63	0.67	32	0.1
	12	17:18	1.4:1	CHCl ₃	12	0.54	0.23	24	0
	10	17:62	1.4:1	CHCl ₃ /CN (99:1, v/v)	12	0.61	0.70	39	0.2
	13	30:60	1.4:1	CHCl ₃ /CN (99:1, v/v)	12	0.70	0.78	37	0.2

^aIn all cases the active layer was spin coated at 2000 rpm, 60 s and annealed at 120 °C for 10 minutes. CHCl₃ and CN is chloroform and 1-chloronaphthalene, respectively. ^bAveraged values of maximum five cells.

In the first set of experiments, MW of the acceptor polymer was changed while MW of the donor remained constant at 17 kg mol⁻¹ (Table V-4, entries **1**, **11**, **12**). A reduction of the acceptor MW from 62 kg mol⁻¹ to 23 kg mol⁻¹ leads to a decrease of V_{oc} and FF. However, a constant value of J_{sc} was observed that could be attributed to a lower degree of aggregation of **PNDIT2** resulting in a higher miscibility with the donor polymer and a more balanced charge transport.⁴⁵ Further reduction to 18 kg mol⁻¹ drastically reduced J_{sc} and hence, no photovoltaic performance of the device was monitored; probably, due to a coarse phase separation and a poorly connected polymer network.⁹ In a final experiment the molecular weight of the **PIDTBT** donor polymer was enhanced to 30 kg mol⁻¹ (Table V-4, entry **13**). It was proven that increasing MW for both donor and acceptor polymer could improve the blend film morphology obtaining smaller polymer domain sizes as well as larger D-A polymer-polymer interfaces. Hence, higher J_{sc} s could be achieved.^{9,45} The outcome characteristics of entry **13** demonstrate a slightly improved J_{sc} and V_{oc} compared to the device prepared with a lower MW sample (Table V-4, entry **10**).

For one of the best performing cell photoluminescence (PL) and external quantum efficiency (EQE) were recorded. The PL emission of the pristine **PIDTBT** film is displayed in Figure V-5a. In blend films the PL emission of the donor polymer at 713 nm is quenched by less than 70% when blended with **PNDIT2** and less than 60% when blended with **PNDIBTz**. The moderate PL quenching efficiency points to inefficient charge transfer due to a large phase separation.^{46,47} This is also reflected in the EQE measurement (Figure V-5b). The device shows a low photoresponse from 280 to 830 nm with a maximum EQE value of 17% at 630 nm.

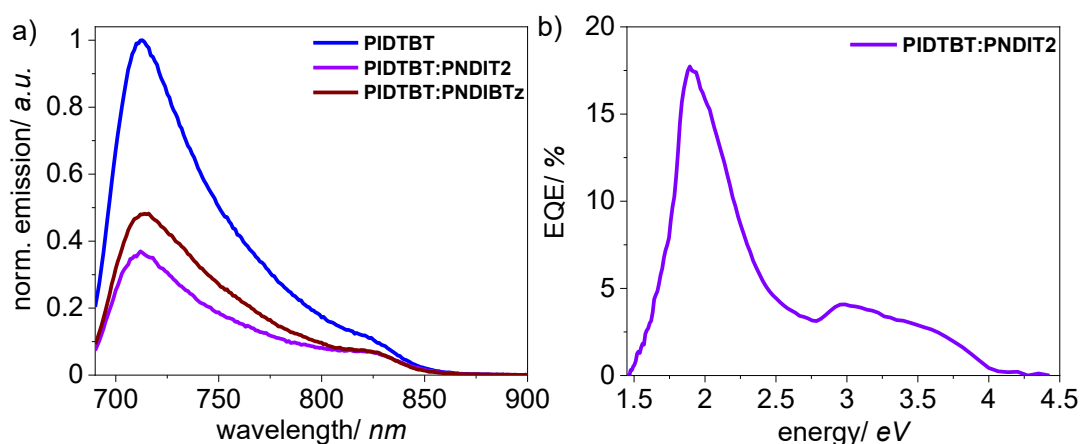


Figure V-5. Photoluminescence quenching of the optimized blend films (a); external quantum efficiency (EQE) spectrum (b) of the best device (entry **1**).

EXPERIMENTAL SECTION

Materials. The acceptor materials (**PNDIT2**, **PNDIBTz**) were synthesized in our research group according to literature procedures.^{32,33} **PIDTBT** was synthesized according to published protocols described in chapter III.³⁵

*Synthetic procedure of **PIDTF4**.* IDT (94.6 mg, 104.3 μmol , 1 eq), F4Br₂ (32.1 mg, 104.3 μmol , 1 eq), pivalic acid (10.6 mg, 104.3 μmol , 1 eq) and potassium carbonate (43.2 mg, 312.8 μmol , 3 eq) were placed in a vial and dissolved in 0.4 mL degassed mesitylene. Then Pd₂dba₃ (4.8 mg, 5 mol%) and P(*o*-anisyl)₃ (7.3 mg, 20 mol%) were added under argon atmosphere. The reaction mixture was stirred at 80 °C. After 24 h, a second portion of Pd₂dba₃ (4.8 mg, 5 mol%) and P(*o*-anisyl)₃ (7.3 mg, 20 mol%) were added and stirred for another 48 h at 80 °C. After cooling to room temperature, the mixture was diluted with chloroform, precipitated into methanol and purified by Soxhlet extraction with acetone, ethyl acetate and chloroform. The chloroform fraction was filtered through a silica gel plug and dried overnight in a vacuum oven at 50 °C to afford a orange solid. Yield: 53.0 mg (48%).

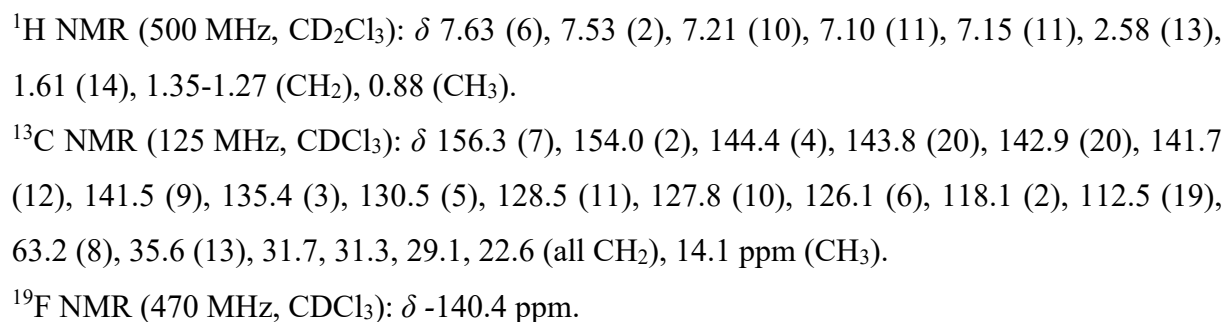
Fabrication and characterization of solar cells. The all-polymer solar cells were constructed with a conventional structure: glass/ITO/PEDOT:PSS/active layer/Ca/Al. At first the indium tin oxide (ITO) coated glass substrates were cleaned sequentially by sonicating in detergent, de-ionized water, acetone, and isopropyl alcohol, followed by blowdrying under nitrogen stream and exposing under oxygen plasma for 5-10 min. Subsequently, a filtered aqueous solution of poly(3,4-ethylenedioxy-thiophene)–poly(styrenesulfonate) (PEDOT:PSS; Heraeus-CleviosTM) was spin coated (3000 rpm, 60 s) onto the ITO surface and then baked at 150 °C for 30 min in ambient to form a 30 nm thick PEDOT:PSS thin film. After transferring into a nitrogen-filled glovebox, the substrates were annealed a second time at 150 °C for 10 min. In the next step the active layer was spin coated from the corresponding blend solutions onto the PEDOT:PSS layer and annealed at 120 °C for 10 min. All blend solutions were prepared previously and stirred at least 24 h at room temperature before use. Finally, a 2 nm calcium layer as well as a 150 nm aluminum layer were sequentially deposited under high vacuum ($<5.0 \times 10^{-5}$ Pa). The active area of each sample was 4.0 mm². The current–voltage characteristics were measured using a Keithley 236 source under illumination of an AM1.5G solar simulator with an intensity of 100 mW cm⁻². The EQE measurements were performed using Bentham TM300 monochromator and a Si reference photodiode.

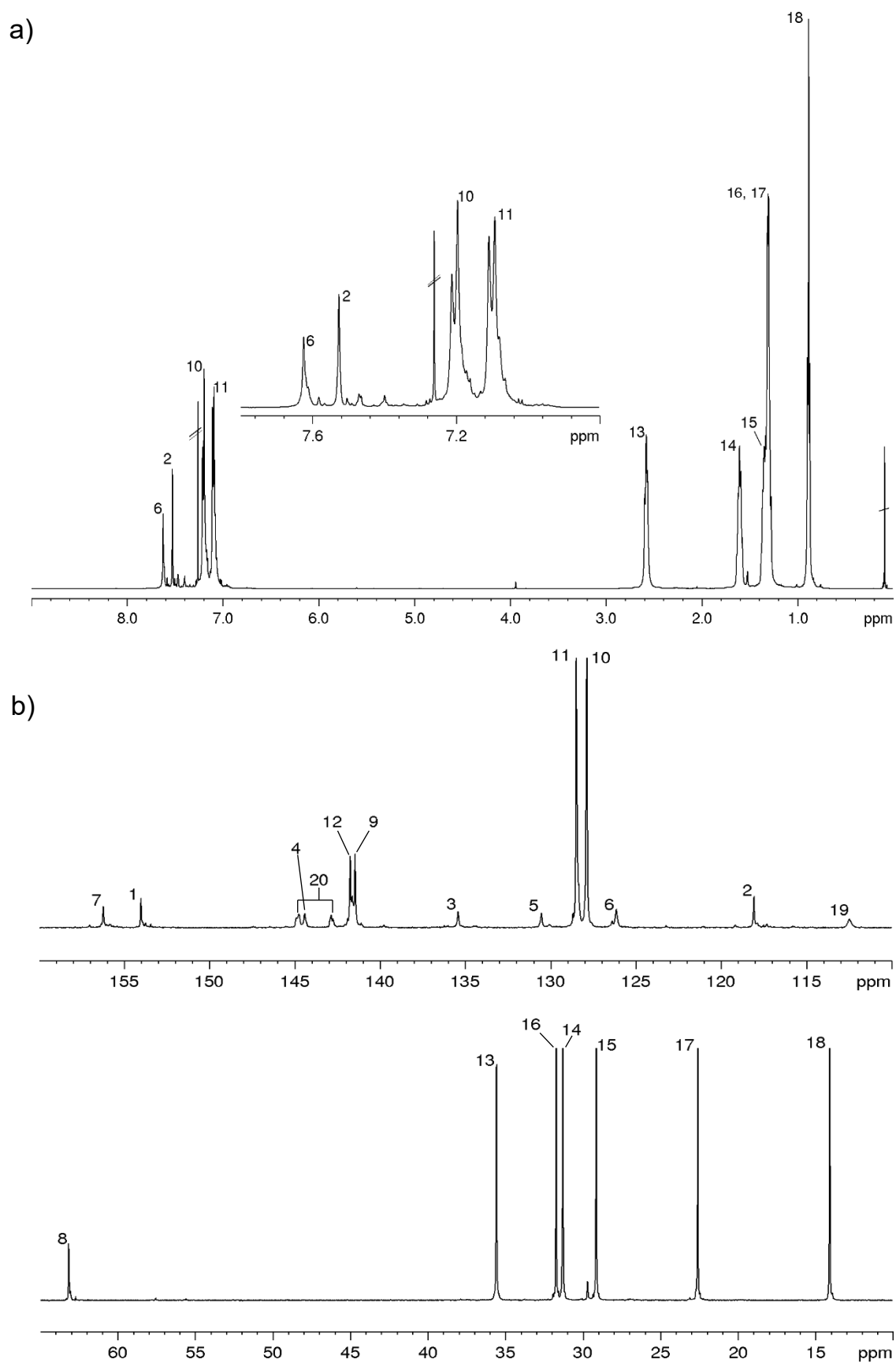
Molecular weights were measured on a Shimadzu system comprising a 5 μm precolumn and

The optical characterisation of solutions was carried out on a Shimadzu UV-1800 series UV-vis-spectrometer, controlled by the UVProbe 2.30 software. The samples were measured in quartz cuvettes with chloroform as a solvent. Thin film absorption of the blends were recorded on the Flame-S UV-Vis-spectrometer from Ocean Optics, controlled by the OceanView 1.5.2 software. The films were spin coated (1000 rpm, 60 s) from a 12 mg mL⁻¹ chloroform solution and annealed at 120 °C for 10 minutes under argon.

NMR spectra of PIDTF4 were recorded on a Bruker AVANCE III 500 spectrometer (^1H : 500.1 MHz, ^{13}C : 125.8 MHz, ^{19}F : 470.5 MHz) at 30 °C. CDCl_3 was used as solvent. The spectra were referenced to the residual solvent peak ($\delta(^1\text{H}) = 7.26$ ppm, $\delta(^{13}\text{C}) = 77.0$ ppm).

NMR data of PIDTF4





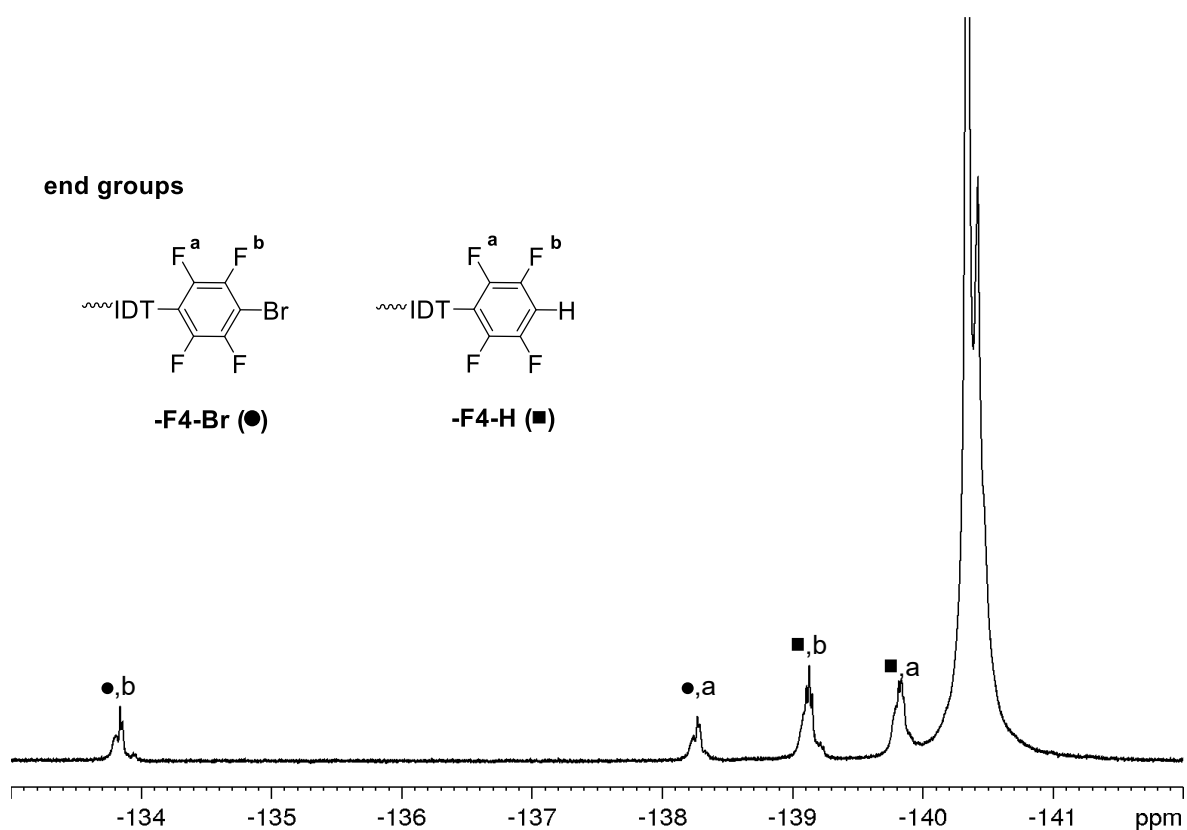


Figure V-S2. ^{19}F NMR spectrum of PIDTF4 (solvent: CDCl_3). The dots and squares mark signals of -F4-Br and F4-H end groups, respectively.

SEC data of active materials

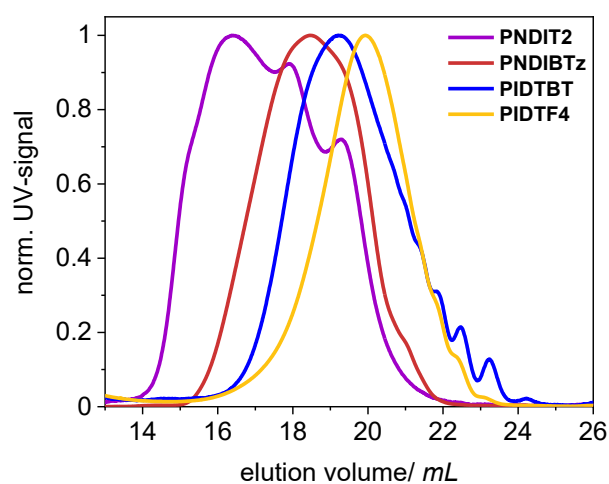


Figure V-S3. SEC curves of donor and acceptor polymers.

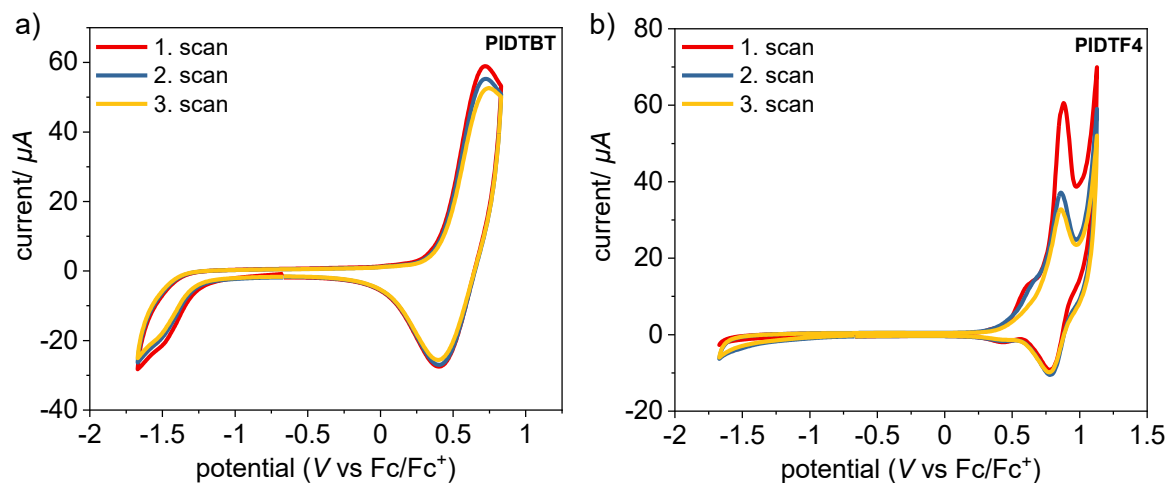
CV measurements of donor materials

Figure V-S4. Cyclic voltammograms of **PIDTBT** (a) and **PIDTF4** (b) as film deposited on an ITO substrate in a 0.1 M NBu_4PF_6 acetonitrile solution at a scan rate of 50 mV s^{-1} .

CONCLUSION AND OUTLOOK

To the best of my knowledge, IDT-based copolymers were employed as donor component in all-PSCs for the first time. **PIDTBT** was blended with **PNDIT2** and **PNDIBTz**. Both fabricated devices showed in the first batch similar short-circuit current densities J_{sc} and efficiencies. However, due to the slightly lower LUMO energy level of the **PNDIBTz** acceptor the corresponding solar cell exhibited a slightly lower V_{oc} and additionally, a decreased PL quenching efficiency compared to the **PIDTBT:PNDIT2** cell. In addition, the **PIDTBT:PNDIT2** blend showed a broader absorption range into the NIR region. In general, all-PSCs exhibited relatively high V_{oc} up to 0.81 V but very low J_{sc} s below 1 mA cm^{-2} . Even after optimization of the all-PSCs using **PIDTBT:PNDIT2** as active layer the currents remained under 1 mA cm^{-2} . Hence, the devices afforded PCEs smaller than 1%. One of the best performing cell could be obtained by using a 1.4:1 D:A ratio and a mixture of chloroform/1-chloronaphthalene as processing solvent. Moreover, it was shown that higher blend concentrations seem to be beneficial for the device performance. Under optimized conditions a PCE of 0.2% could be achieved. The results point to an unfavourable blend film morphology such as a coarse phase separation which is also reflected in the decent PL quenching efficiency of 63% proving inefficient charge transfer. In order to gain more information about the blend film morphology atomic force microscopy (AFM) measurements should be carried out. The film forming properties of the blend might be further tuned by decreasing the chloroform/1-chloronaphthalene ratio and increasing the blend concentration to achieve thicker films. Further

parameters that were not investigated in this study but can have an immense effect on the morphology of the active layer are the processing conditions such as thermal annealing, solvent annealing, controlled solvent evaporation and solvent vapor annealing.^{48–51} For instance, the performance of PIDTBT:PC₇₁BM cells could be enhanced by 12% by treatment with solvent vapor annealing.²³

Another attempt to enhance the PSC performance could be made by modifying the organic/electrode interface. Employing an amine-functionalized perylene-diimide derivative such as PDINO as cathode interlayer can significantly raise J_{sc} by improving the collection of electrons.^{52,53}

REFERENCES

- (1) G. Wang, F. S. Melkonyan, A. Facchetti and T. J. Marks, *Angew. Chem. Int. Ed.*, 2019, **58**, 4129–4142.
- (2) Z. Genene, W. Mammo, E. Wang and M. R. Andersson, *Adv. Mater.*, 2019, **31**, 1807275.
- (3) T. Jia, J. Zhang, W. Zhong, Y. Liang, K. Zhang, S. Dong, L. Ying, F. Liu, X. Wang, F. Huang and Y. Cao, *Nano Energy*, 2020, **72**, 104718.
- (4) H. Kang, W. Lee, J. Oh, T. Kim, C. Lee and B. J. Kim, *Acc. Chem. Res.*, 2016, **49**, 2424–2434.
- (5) C. Lee, Y. Li, W. Lee, Y. Lee, J. Choi, T. Kim, C. Wang, E. D. Gomez, H. Y. Woo and B. J. Kim, *Macromolecules*, 2016, **49**, 5051–5058.
- (6) C. R. McNeill, *Energy Environ. Sci.*, 2012, **5**, 5653.
- (7) Z. Li, L. Ying, P. Zhu, W. Zhong, N. Li, F. Liu, F. Huang and Y. Cao, *Energy Environ. Sci.*, 2019, **12**, 157–163.
- (8) B. Xie, K. Zhang, Z. Hu, H. Fang, B. Lin, Q. Yin, B. He, S. Dong, L. Ying, W. Ma, F. Huang, H. Yan and Y. Cao, *Sol. RRL*, 2020, **4**, 1900385.
- (9) N. Zhou, A. S. Dudnik, T. I. N. G. Li, E. F. Manley, T. J. Aldrich, P. Guo, H.-C. Liao, Z. Chen, L. X. Chen, R. P. H. Chang, A. Facchetti, M. Olvera de la Cruz and T. J. Marks, *J. Am. Chem. Soc.*, 2016, **138**, 1240–1251.
- (10) N. Zhou and A. Facchetti, *Mater. Today*, 2018, **21**, 377–390.
- (11) M. Sommer, *J Mater Chem C*, 2014, **2**, 3088–3098.
- (12) B. Fan, W. Zhong, L. Ying, D. Zhang, M. Li, Y. Lin, R. Xia, F. Liu, H.-L. Yip, N. Li, Y. Ma, C. J. Brabec, F. Huang and Y. Cao, *Nat. Commun.*, 2019, **10**, 4100.
- (13) B. Fan, L. Ying, P. Zhu, F. Pan, F. Liu, J. Chen, F. Huang and Y. Cao, *Adv. Mater.*, 2017, **29**, 1703906.
- (14) L. Gao, Z.-G. Zhang, L. Xue, J. Min, J. Zhang, Z. Wei and Y. Li, *Adv. Mater.*, 2016, **28**, 1884–1890.
- (15) G. Zhang, J. Zhao, P. C. Y. Chow, K. Jiang, J. Zhang, Z. Zhu, J. Zhang, F. Huang and H. Yan, *Chem. Rev.*, 2018, **118**, 3447–3507.
- (16) P. Cheng, G. Li, X. Zhan and Y. Yang, *Nat. Photonics*, 2018, **12**, 131–142.
- (17) I. McCulloch, R. S. Ashraf, L. Biniek, H. Bronstein, C. Combe, J. E. Donaghey, D. I. James, C. B. Nielsen, B. C. Schroeder and W. Zhang, *Acc. Chem. Res.*, 2012, **45**, 714–722.
- (18) C. Cui, *Front. Chem.*, 2018, **6**, 404.
- (19) Y. Li, M. Gu, Z. Pan, B. Zhang, X. Yang, J. Gu and Y. Chen, *J Mater Chem A*, 2017, **5**, 10798–10814.
- (20) C. Liang and H. Wang, *Org. Electron.*, 2017, **50**, 443–457.

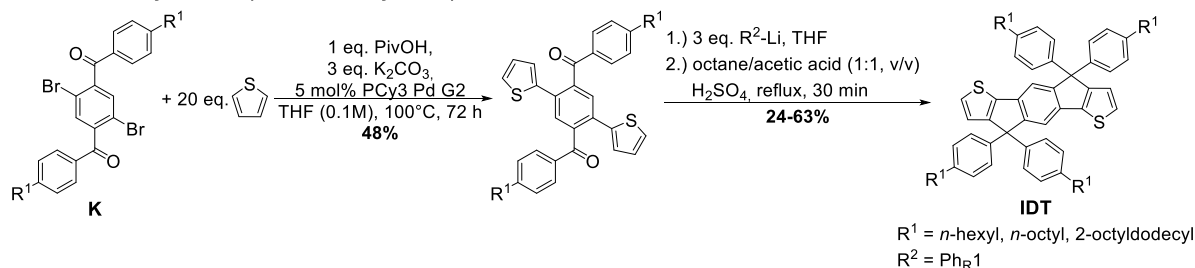
-
- (21) A. Wadsworth, H. Chen, K. J. Thorley, C. Cendra, M. Nikolka, H. Bristow, M. Moser, A. Salleo, T. D. Anthopoulos, H. Sirringhaus and I. McCulloch, *J. Am. Chem. Soc.*, 2020, **142**, 652–664.
- (22) H. Bronstein, D. S. Leem, R. Hamilton, P. Woebkenberg, S. King, W. Zhang, R. S. Ashraf, M. Heeney, T. D. Anthopoulos, J. de Mello and I. McCulloch, *Macromolecules*, 2011, **44**, 6649–6652.
- (23) Y.-C. Chen, C.-Y. Yu, Y.-L. Fan, L.-I. Hung, C.-P. Chen and C. Ting, *Chem. Commun.*, 2010, **46**, 6503.
- (24) K.-S. Chen, Y. Zhang, H.-L. Yip, Y. Sun, J. A. Davies, C. Ting, C.-P. Chen and A. K.-Y. Jen, *Org. Electron.*, 2011, **12**, 794–801.
- (25) P.-C. Yang, J.-Y. Sun, S.-Y. Ma, Y.-M. Shen, Y.-H. Lin, C.-P. Chen and C.-F. Lin, *Sol. Energy Mater. Sol. Cells*, 2012, **98**, 351–356.
- (26) Y.-X. Xu, C.-C. Chueh, H.-L. Yip, F.-Z. Ding, Y.-X. Li, C.-Z. Li, X. Li, W.-C. Chen and A. K.-Y. Jen, *Adv. Mater.*, 2012, **24**, 6356–6361.
- (27) C.-P. Chen, S.-H. Chan, T.-C. Chao, C. Ting and B.-T. Ko, *J. Am. Chem. Soc.*, 2008, **130**, 12828–12833.
- (28) Y. Zhang, S.-C. Chien, K.-S. Chen, H.-L. Yip, Y. Sun, J. A. Davies, F.-C. Chen and A. K.-Y. Jen, *Chem. Commun.*, 2011, **47**, 11026.
- (29) C. Lee, S. Lee, G.-U. Kim, W. Lee and B. J. Kim, *Chem. Rev.*, 2019, **119**, 8028–8086.
- (30) L. Xue, Y. Yang, Z.-G. Zhang, X. Dong, L. Gao, H. Bin, J. Zhang, Y. Yang and Y. Li, *J. Mater. Chem. A*, 2016, **4**, 5810–5816.
- (31) S. Shi, P. Chen, Y. Chen, K. Feng, B. Liu, J. Chen, Q. Liao, B. Tu, J. Luo, M. Su, H. Guo, M. Kim, A. Facchetti and X. Guo, *Adv. Mater.*, 2019, **31**, 1905161.
- (32) R. Matsidik, H. Komber, A. Luzio, M. Caironi and M. Sommer, *J. Am. Chem. Soc.*, 2015, **137**, 6705–6711.
- (33) R. Matsidik, M. Giorgio, A. Luzio, M. Caironi, H. Komber and M. Sommer, *Eur. J. Org. Chem.*, 2018, **2018**, 6121–6126.
- (34) D. Adamczak, H. Komber, A. Illy, A. D. Scaccabarozzi, M. Caironi and M. Sommer, *Macromolecules*, 2019, **52**, 7251–7259.
- (35) D. Adamczak, A. Perinot, H. Komber, A. Illy, S. Hultmark, B. Passarella, W. L. Tan, S. Hutsch, D. Becker-Koch, C. Rapley, A. D. Scaccabarozzi, M. Heeney, Y. Vaynzof, F. Ortmann, C. R. McNeill, C. Müller, M. Caironi and M. Sommer, *J. Mater. Chem. C*, 2021, **9**, 4597–4606.
- (36) M. C. Scharber, D. Mühlbacher, M. Koppe, P. Denk, C. Waldauf, A. J. Heeger and C. J. Brabec, *Adv. Mater.*, 2006, **18**, 789–794.
- (37) C. McDowell, M. Abdelsamie, M. F. Toney and G. C. Bazan, *Adv. Mater.*, 2018, **30**, 1707114.

- (38) R. Steyrleuthner, R. Di Pietro, B. A. Collins, F. Polzer, S. Himmelberger, M. Schubert, Z. Chen, S. Zhang, A. Salleo, H. Ade, A. Facchetti and D. Neher, *J. Am. Chem. Soc.*, 2014, **136**, 4245–4256.
- (39) K. Zhou, R. Zhang, J. Liu, M. Li, X. Yu, R. Xing and Y. Han, *ACS Appl. Mater. Interfaces*, 2015, **7**, 25352–25361.
- (40) T. Earmme, Y.-J. Hwang, S. Subramaniyan and S. A. Jenekhe, *Adv. Mater.*, 2014, **26**, 6080–6085.
- (41) M. Schubert, B. A. Collins, H. Mangold, I. A. Howard, W. Schindler, K. Vandewal, S. Roland, J. Behrends, F. Kraffert, R. Steyrleuthner, Z. Chen, K. Fostiropoulos, R. Bittl, A. Salleo, A. Facchetti, F. Laquai, H. W. Ade and D. Neher, *Adv. Funct. Mater.*, 2014, **24**, 4068–4081.
- (42) E. Pavlopoulou, C. S. Kim, S. S. Lee, Z. Chen, A. Facchetti, M. F. Toney and Y.-L. Loo, *Chem. Mater.*, 2014, **26**, 5020–5027.
- (43) M. Schubert, D. Dolfen, J. Frisch, S. Roland, R. Steyrleuthner, B. Stiller, Z. Chen, U. Scherf, N. Koch, A. Facchetti and D. Neher, *Adv. Energy Mater.*, 2012, **2**, 369–380.
- (44) H. Kang, M. A. Uddin, C. Lee, K.-H. Kim, T. L. Nguyen, W. Lee, Y. Li, C. Wang, H. Y. Woo and B. J. Kim, *J. Am. Chem. Soc.*, 2015, **137**, 2359–2365.
- (45) Y. Lei, J. Sun, J. Yuan, J. Gu, G. Ding and W. Ma, *J. Mater. Sci. Technol.*, 2017, **33**, 411–417.
- (46) K. D. Deshmukh, R. Matsidik, S. K. K. Prasad, L. A. Connal, A. C. Y. Liu, E. Gann, L. Thomsen, J. M. Hodgkiss, M. Sommer and C. R. McNeill, *Adv. Funct. Mater.*, 2018, **28**, 1707185.
- (47) K. Rundel, Y. Shin, A. S. R. Chesman, A. C. Y. Liu, A. Welford, L. Thomsen, M. Sommer and C. R. McNeill, *J. Phys. Chem. C*, 2019, **123**, 12062–12072.
- (48) N. Wang, Y. Yu, R. Zhao, Z. Ding, J. Liu and L. Wang, *Macromolecules*, 2020, **53**, 3325–3331.
- (49) M. B. Upama, N. K. Elumalai, M. A. Mahmud, M. Wright, D. Wang, C. Xu and A. Uddin, *Sol. Energy Mater. Sol. Cells*, 2018, **176**, 109–118.
- (50) D. Trefz, Y. M. Gross, C. Dingler, R. Tkachov, A. Hamidi-Sakr, A. Kiriya, C. R. McNeill, M. Brinkmann and S. Ludwigs, *Macromolecules*, 2019, **52**, 43–54.
- (51) F. Jin, G. Ding, Y. Wang, J. Yuan, W. Guo, H. Yuan, C. Sheng, W. Ma and H. Zhao, *J. Phys. Chem. C*, 2017, **121**, 8804–8811.
- (52) Z.-G. Zhang, B. Qi, Z. Jin, D. Chi, Z. Qi, Y. Li and J. Wang, *Energy Environ. Sci.*, 2014, **7**, 1966.
- (53) X. Zhang, W. Li, J. Yao and C. Zhan, *ACS Appl. Mater. Interfaces*, 2016, **8**, 15415–15421.

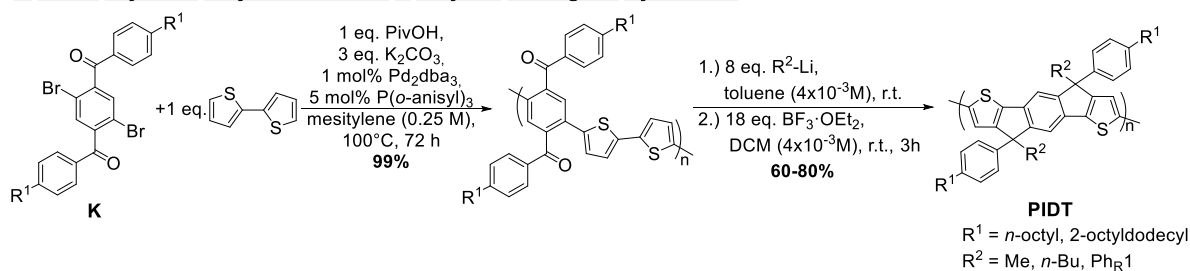
VI. Summary and outlook

In this thesis synthetic schemes towards IDT-based homo- and copolymers were explored in which all C-C coupling steps were achieved using C-H activation. A summary of the prepared materials and the synthetic pathways is shown in Scheme VI-1.

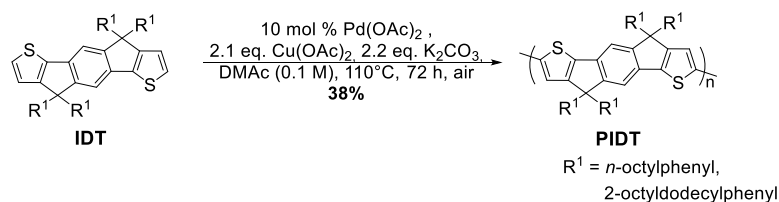
1. Monomer Synthesis (via Direct Arylation)



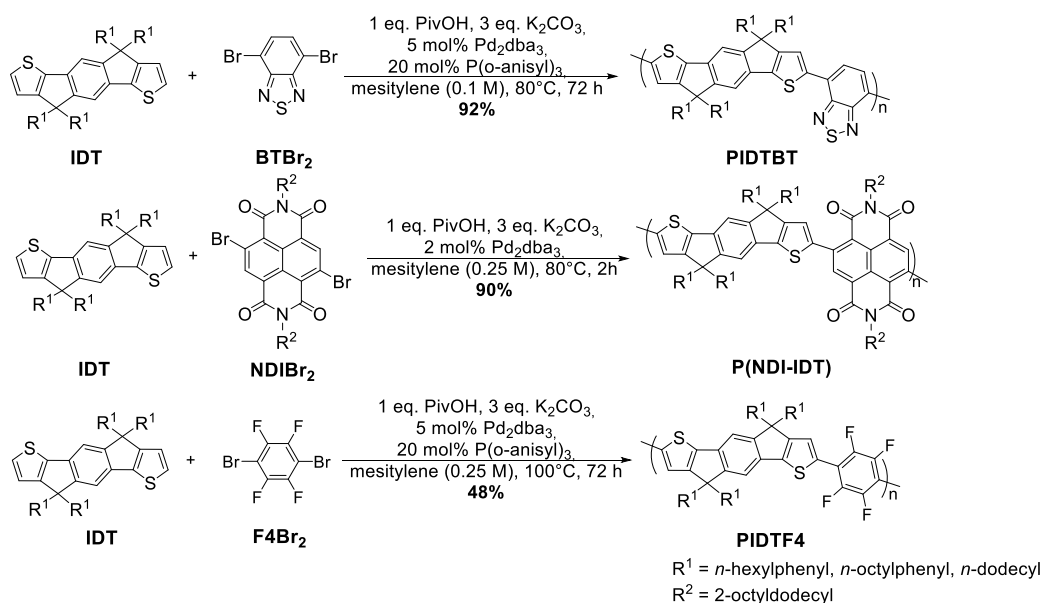
2. Direct Arylation Polycondensation & Polymer Analogous Cyclization



3. Oxidative Direct Arylation Polycondensation



4. Direct Arylation Polycondensation



Scheme VI-1. Overview of the IDT-based homo- and copolymers using C-H activation.

The ketone **K** was chosen as starting material for all reactions enabling the use of direct arylation since the usually used ester derivative is unstable under the given conditions for C-H activation. The reaction of the ketone **K** and thiophene was carried out in THF with PCy₃ Pd G2 as catalyst achieving a yield of 48% (Scheme VI-1). The following cyclization proceeds smoothly and the IDT monomer could be obtained after simple recrystallization from petroleum ether in high purity and yield as long as short *n*-alkyl chains are attached on the phenyl ring. When branched chains such as 2-octyldodecyl are used the final product is a wax and needs to be purified by column chromatography. The same strategy was also used to synthesize IDT-based homopolymers. In this case, the ketone was polymerized by DAP yielding polyketones as precursor polymer. The use of a P-ligand and a medium concentration of 0.25 M was necessary to obtain polyketones with M_n s up to 21 kg mol⁻¹ in high yields (Scheme VI-1). The branched alkyl chains on the phenyl ring ensure solubility during the following post-polymerization sequence. One advantage using this reaction pathway is the possibility to attach an asymmetric side chain pattern on the IDT unit. Depending on the choice of the Li compound IDT homopolymers with Me/2-octyldodecylphenyl, *n*-Bu/2-octyldodecylphenyl and 2-octyldodecylphenyl/2-octyldodecylphenyl side chain pattern in 60-80% yield were obtained. The progress of the cyclization was monitored by UV-vis and IR spectroscopy. Introduction of methyl and 2-octyldodecylphenyl as second side chain led to well-defined homopolymers without indication of any defect structures in UV-vis, IR and NMR spectroscopic analysis. However, the use of *n*-butyl lithium left traces of unreacted carbonyl groups in the IR spectrum of the cyclized polymer. Additionally, a hypsochromic shift of the absorption maximum was observed. To date, there are no detailed defect analyses of IDT-based (co)polymers. In order to get insight into the presence and nature of structural defects several synthetic and analytic attempts were made. However, neither model reactions nor preparation of appropriate model compounds could give conclusive information. The detection of potential defects by, for example, NMR analysis is quite challenging due to the rigid nature of IDT-based (co)polymers resulting in signal broadening and overlap with backbone signals. It could be assumed that possible side reactions occur by lithiation of thiophene end groups leading to branching and/or chain-chain coupling. In a second approach the cyclized IDT monomer was directly polymerized *via* oxidative direct arylation polycondensation. Symmetric substituted homopolymers were obtained in 38% yield when 10 mol% Pd(OAc)₂ as catalyst, Cu(OAc)₂ as oxidant, K₂CO₃ as base and DMAc as solvent were used. It is noteworthy that the polymerization does not need inert atmosphere since oxygen from air can act as co-oxidant.

Furthermore, it is possible to repeat polymerization on oligomer fractions and/or polymer chains under the same conditions due to predominant $-H$ termination enhancing molecular weights of the homopolymers. While spectroscopic properties are similar to their analogues prepared *via* polymer analogous reaction pathway, mobilities are significantly lower. In general, the mobilities are in the range 10^{-6} – 10^{-3} $\text{cm}^2 \text{V}^{-1} \text{s}^{-1}$ and can be correlated with the presence of unknown defect structures. Among them the ill-defined *n*-Bu/2-octyldodecylphenyl-PIDT showed the lowest performance.

In chapter III, the optimized conditions of the polymer analogous cyclization were transferred to PIDTBT copolymer synthesis. The synthesis of the corresponding polyketone by DAP is limited by the poor solubility despite of long branched side chains and hence, moderate M_n s of 11 kg mol^{-1} could be achieved. Cyclization led to PIDTBT copolymers with Me/2-octyldodecylphenyl and 2-octyldodecylphenyl/2-octyldodecylphenyl side chain pattern. Various analytic characterizations such as hypsochromically shifted absorption spectra, low absorption coefficients, bimodal SEC curves and low mobilities indicated structural defects of unknown nature. On the other hand, PIDTBT copolymers prepared by DAP yielded well-defined materials in high yields of over 90% and M_n s up to 38 kg mol^{-1} (Scheme VI-1). Due to broadening of the backbone signals in NMR spectra a detailed defect analysis was left out. The investigation of the side chain influence revealed that the length of the alkyl chain on the phenyl side chain did not impact the optical, thermal and electrical properties. All alkylphenyl-substituted PIDTBT copolymers show absorption maxima around 645 nm with sharp onsets. The DSC and GIWAXS measurements revealed an amorphous thin film morphology and glass transition temperatures around 90°C independent of the molecular weight. A similar independence on MW is observed for field-effect mobilities which are in the range of 0.02 – $0.04 \text{ cm}^2 \text{V}^{-1} \text{s}^{-1}$. In contrast, the alkyl-substituted PIDTBT copolymer demonstrates significantly different properties. The absorption spectrum displays a bathochromic shift of 20 nm. When transitioning into film a shift of 12 nm and the development of a pronounced shoulder around 630 nm indicate an increased order of the alkyl-substituted PIDTBT while the alkylphenyl-substituted PIDTBT exhibits a rather small shift of 8 nm. Electrochemical and theoretical analyses ascertained that the nature of the side chains have a greater impact on the HOMO energy levels of PIDTBT while the LUMO energy level remains largely unaffected. Further experiments reveal a weakly crystalline behavior and a lower energetic disorder of the alkyl-substituted PIDTBT leading to an order of magnitude higher hole mobilities compared to the alkylphenyl-substituted polymers.

In chapter IV, direct arylation polycondensation was adopted to the synthesis of an IDT-based n-type copolymer. Polymerization with NDIBr₂ led to defect-free copolymers with high M_n s up to 113 kg mol⁻¹ in high yields (Scheme VI-1). Usage of a phosphine ligand favors nucleophilic substitution of NDI-Br chain ends by pivalate resulting in –NDI-OH termination and low MWs. Without the addition of a ligand the polymers contain predominant –IDT-H end groups. P(NDI-IDT)s possess broad CT bands with absorption maxima around 728 nm and low optical band gaps of 1.5 eV. Compared to the n-type benchmark P(NDIT2) the P(NDI-IDT) polymers show a bathochromic shift of the CT band and a slightly higher lying LUMO energy level of -3.71 eV due to a stronger donor strength of IDT. However, the nature of the solvent as well as temperature did not alter the shape and intensity of the absorption bands featuring weak aggregation in solution. In films, the intensity of the CT band increases and a spectral shift of 40 nm can be observed due to planarization of the polymer backbone. Thermal annealing of the films causes slight changes of the CT band intensity. While annealing upon 100 °C results in an increase of the CT band intensity, annealing above the main chain melting temperature reduces the CT band intensity and causes a hypsochromic shift. Besides main chain melting (between 180 – 220 °C depending on molecular weight), the polymers show some weak side chain ordering around 60 °C. However, thin films are weakly crystalline with moderate mobilities on the order of 10⁻³ cm² V⁻¹s⁻¹, despite very low Urbach energies between 27 - 30 meV. Thermal annealing above main chain melting temperatures results in amorphous thin film morphologies, increased Urbach energies and a significant drop in field-effect mobilities. Compared to P(NDIT2), thin films show much weaker crystallinities and lower, chain length independent field-effect mobilities. This can be ascribed to the bulky hexylphenyl side chains in P(NDI-IDT) hindering main chain ordering and thus, interchain transport.

Chapter V contains results on all-PSCs made from IDT copolymers as donors. PIDTBT and PIDTF4 were blended with the naphthalene diimide copolymers PNDIT2 and PNDIBTz which were used as acceptors. After first test runs further optimizations were focused on PSCs containing PIDTBT:PNDIT2 blends as active layer. The devices showed high V_{oc} s up to 0.81 eV but decent J_{sc} s of maximum 0.78 mA cm⁻². The best performing devices were obtained with an 1.4:1 D/A weight ratio and chloroform/1-chloronaphthalene mixture as processing solvent. With increasing blend concentration and increased MW of the donor polymer PIDTBT the performance could be slightly enhanced. Nevertheless, a maximum PCE of 0.2% and EQE of 17% at 630 nm could be achieved. Further analysis reveal a low PL efficiency of under 70% pointing to inefficient charge transfer due to a poor blend film morphology.

To conclude, this thesis has explored a more atom-economic way towards preparation of p-type as well as n-type polymers based on IDT, which may be useful for their further development and commercialization of these materials for organic electronics. Furthermore, a detailed analysis and structure-function relationships have been provided as a fundament for future design of conjugated polymers.

In upcoming studies, introduction of a π -bridge and/or extension of the IDT backbone could be used to minimize steric hindrance. Furthermore, variation of the side chain length on the IDT unit or the use of a mixed side chain pattern (methyl/alkylphenyl) could enhance crystallinity of the materials. If these modified IDTs are copolymerized with NDI a new n-type polymer with improved π - π stacking and hence, charge transport properties could be created. This strategy could be also useful to improve the performance of IDT-based all-polymer solar cells. Devices containing an IDT-NDI copolymer with improved properties and an IDT-based donor polymer could promote a more favourable blend film morphology and enhance the performance. For the application of PIDTBT in all-polymer solar cells, in order to identify underlying mechanisms for the poor photovoltaic performance, a detailed study of the blend film morphology with different acceptor materials needs to be carried out. In addition, the use of an organic cathode interlayer such as PDINO and modified cell architectures such as inverted or tandem structures as well as the use of ternary blends should be analyzed. Replacement of PNDIT2 by an IDT-based small molecule acceptor could be another tool to construct high-performing organic solar cells based on PIDTBT.

VII. Acknowledgement

In the end, I would like to say thank you to all people who were part of this journey and supported this work.

First, I would like to express my gratitude to my supervisor *Prof. Dr. Michael Sommer* for giving me the chance to join his research group, providing his guidance and the granted freedoms throughout my career.

I am also thankful to *Prof. Dr. Ullrich Scherf* for agreeing to be reviewer of this thesis.

I wish to acknowledge the collaboration with *Dr. Hartmut Komber* and the research group of *Dr. Mario Caironi* who supported this work by providing NMR analyses and OFET measurements, respectively. I also thank *Wen Liang Tan* and *Dr. Christopher R. McNeill* as wells as *Dr. Oleksandr Dolynchuk* for GIWAXS measurements, *Sandra Hultmark* and *Prof. Dr. Christian Müller* for FSC measurements, *David Becker-Koch* and *Prof. Dr. Yana Vaynzof* for PDS measurements, *Sebastian Hutsch* and *Prof. Dr. Frank Ortmann* for DFT calculations, *Charlotte Rapley* and *Prof. Dr. Martin Heeney* for providing the C12-IDT monomer, *Maximilian Raisch* as well as *Raphael Hertel* for DSC measurements and *Dominik Stegerer* for TGA measurements. Further, I would like to thank *Prof. Dr. Carsten Deibel* for giving me the chance to work in his laboratories and *Olaf Müller-Dieckert* for his kind help and first instructions fabricating all-PSCs.

I would like to extend my special thanks to *Dr. Andreas Seifert* and our good-hearted soul of the group *Simone Kehr* who supported me in every respect and always had an open ear for me. I also wish to thank *Dr. Rukiya Matsidik*, *Dr. Simon Schmidt*, *Dr. Fritz Nübling*, *Dr. Yonghun Shin*, *Dominik Stegerer*, *Anna Illy*, *Caroline Schmidt*, *Markus Hönig*, *Patricia Godermajer*, *Hannah Buchheit* and *Maximilian Raisch* as well as all my other colleagues from Freiburg and Chemnitz who were at some point part of my journey. I enjoyed having lunch, drinking coffee, playing Skat and spending time with you outside the university.

Finally, I am deeply grateful to *my parents* and *my brother* for their lovely and unlimited support throughout so many years. Thank you!

VIII. Selbstständigkeitserklärung

Ich erkläre hiermit, dass ich die vorliegende Arbeit selbstständig und ohne Benutzung anderer als der angegebenen Quellen und Hilfsmittel angefertigt habe. Die den benutzten Hilfsmitteln wörtlich oder inhaltlich entnommenen Stellen habe ich unter Quellenangaben kenntlich gemacht. Die Arbeit hat in gleicher oder ähnlicher Form noch keiner anderen Prüfungsbehörde vorgelegen und ist auch noch nicht veröffentlicht worden.

Chemnitz, den

Desiree Adamczak

IX. Curriculum vitae

Personal Data

Name: Desiree Adamczak
Date of birth: 04.02.1991
Place of birth: Eberbach

Education

since 04/2017 Promotion (Prof. Dr. Sommer), Technische Universität Chemnitz

PhD thesis: „*Synthese von Indacenodithiophen-basierten Copolymeren mittels direkter C-H-Arylierungspolykondensation*“

10/2014–01/2017 Chemistry Master of Science, Albert-Ludwigs-Universität Freiburg

Master thesis: „*Synthese von Indacenodithiophen-Copolymeren mittels direkter C-H-Arylierungspolykondensation*“

09/2010–09/2014 Chemistry Bachelor of Science, Ruprecht-Karls-Universität Heidelberg

Bachelor thesis: „*Synthese von Matrixmaterialien für OLEDs*“

09/2001–06/2010 Abitur, Auguste-Pattberg-Gymnasium, Mosbach-Neckarelz

X. Publications and poster distributions

Published manuscripts

- (1) **"Indacenodithiophene homopolymers via direct arylation: direct polycondensation versus polymer analogous reaction pathways"**
D. Adamczak, H. Komber, A. Illy, A. Scaccabarozi, M. Caironi, M. Sommer, *Macromolecules*, **2019**, 52 (19), 7251-7259. DOI: [10.1021/acs.macromol.9b01269](https://doi.org/10.1021/acs.macromol.9b01269)
- (2) **"Influence of synthetic pathway, molecular weight and side chains on properties of indacenodithiophene-benzothiadiazole copolymers made by direct arylation polycondensation"**
D. Adamczak, A. Perinot, H. Komber, A. Illy, S. Hultmark, B. Passarella, W. L. Tan, S. Hutsch, D. Becker-Koch, C. Rapley, A. D. Scaccabarozi, M. Heeney, Y. Vaynzof, F. Ortmann, C. R. McNeill, C. Müller, M. Caironi, M. Sommer, *J. Mater. Chem. C*, **2021**, 9 (13), 4597-4606. DOI: [10.1039/D1TC00043H](https://doi.org/10.1039/D1TC00043H)

Submitted manuscripts

- (1) **"Temperature-dependent morphology-electron mobility correlations of naphthalene diimide-indacenodithiophene copolymers prepared via direct arylation polymerization"**
D. Adamczak, B. Passarella, H. Komber, D. Becker-Koch, O. Dolynchuk, S. B. Schmidt, Y. Vaynzof, M. Caironi, M. Sommer, **2021**.

Poster distributions

- (1) **"Indacenodithiophene Homo- and Copolymers with Asymmetric Side Chains via Direct Arylation Polycondensation"**
14th International Symposium on Functional π -Electron Systems in Berlin, 2019.
Thieme Chemistry Poster Prize.